

Measurements of Di-Jet $\pi^0 - h^\pm$ Correlations in Light-Heavy Ion Collisions at
RHIC-PHENIX

A dissertation presented to
the faculty of
the College of Arts and Science of Ohio University

In partial fulfillment
of the requirements for the degree
Doctor of Philosophy

Abinash Pun
August 2019
© 2019 Abinash Pun. All Rights Reserved.

This dissertation titled
Measurements of Di-Jet $\pi^0 - h^\pm$ Correlations in Light-Heavy Ion Collisions at
RHIC-PHENIX

by
ABINASH PUN

has been approved for
the Department of Physics and Astronomy
and the College of Arts and Science by

Justin E. Frantz
Associate Professor of Physics and Astronomy

Florenz Plassmann
Dean, College of Arts and Science

ABSTRACT

PUN, ABINASH, Ph.D., August 2019, Physics

Measurements of Di-Jet $\pi^0 - h^\pm$ Correlations in Light-Heavy Ion Collisions at RHIC-PHENIX (206 pp.)

Director of Dissertation: Justin E. Frantz

The possible presence of Quark-Gluon Plasma (QGP), the new state of matter created at the Relativistic Heavy Ion Collider (RHIC) and the Large Hadron Collider (LHC) in Au+Au and Pb+Pb collisions, is currently under investigation for smaller collisions systems such as light-heavy ions and even $p + p$. Long range angular correlations of particles produced in $p+\text{Pb}$, $p+\text{Au}$, $d+\text{Au}$, and ${}^3\text{He}+\text{Au}$, show evidence of QGP collective flow, but another signature, QGP-induced jet energy loss effects has not been identified. To address this situation, in this dissertation, a recently introduced observable R_I is employed in light-heavy ion collisions. R_I is derived from two-particle correlation method commonly used to study jet modification from energy loss in Au+Au.

π^0 -hadrons correlations are analyzed with R_I in ${}^3\text{He}+\text{Au}$, $d+\text{Au}$ and $p+p$. Modification of R_I in ${}^3\text{He}+\text{Au}$ is found, with suppression at high z_T and hints of enhancement at low z_T . This confirms the previous result of jet modification behavior in $d+\text{Au}$ R_I . When compared with $d+\text{Au}$, modifications in ${}^3\text{He}+\text{Au}$ qualitatively follow the system size dependence. R_I in ${}^3\text{He}+\text{Au}$ is more suppressed than in $d+\text{Au}$ at high z_T . The ratio of R_I in ${}^3\text{He}+\text{Au}$ to that in $d+\text{Au}$ at high z_T (>0.48) is more than 2σ below unity. Further simulation studies compared to previous works were done for checking possibilities of the cold nuclear matter effects mimicking the modification behavior observed in data. An intrinsic k_T effect from a new PYTHIA-8 study was found to be inconsistent with the ${}^3\text{He}+\text{Au}$ modifications. Also, the effects due to modifications in the nuclear parton distribution function (nPDF) from PYTHIA8+EPPS16 nPDF sets were found to be much smaller and qualitatively inconsistent with modification in R_I from data.

To my mom and dad

ACKNOWLEDGMENTS

First and foremost, I would like to extend my sincere gratitude to my advisor, Justin Frantz, for his constant guidance and unwavering support throughout my graduate life. I would not have come this far without his help and encouragement. Thank you for showing confidence and trust in my abilities even in the situation when I lost mine.

I would like to thank my dissertation committee members: Julie Roche, Zach Meisel and Ryan Fogt for taking out time from their busy schedule to be part of my dissertation committee and going through my work to make it better.

I would like to appreciate the whole PHENIX collaboration and the members for providing quality data for my analysis. I am very much thankful to the PHENIX HHJ working group for their honest feedback and suggestions throughout my analysis. I would also like to thank sPHENIX members, especially Jin Huang for helping me to learn about the simulation techniques.

I am grateful to the Department of Physics and Astronomy at Ohio University for accepting me as a graduate student and providing me the platform to pursue my research interest. Also, I am thankful to INPP (Institute of Nuclear and Particle Physics) at Ohio University for providing an environment (nuclear seminars, journal lunch, lunch with seminar speaker) to groom my knowledge in the field of nuclear physics and also for providing partial funding to me.

A special thank you to my senior group member, Bing Xia. My work is heavily based on the previous work done by Bing Xia. I have used many of his code frameworks as a starting point of my research work. Also, I very much appreciate my senior colleague, Tyler Danley, for walking me through the basic framework of PHENIX and ROOT during my initial days in research.

I am very much grateful to my "RK-2013" batch mates (Bishal, Rajib, Jerry, Oscar, Mamun, and Sudhanwa) for making my graduate life fun. I will always remember the late night homework parties we used to have in the bunker/computer lab of the Clippinger.

Also, I am extremely thankful to my former roommate, Bishal Bhattacharai, for encouraging and helping me to overcome the initial hurdles of graduate life.

I would like to appreciate all the NEPSA (Nepalese Student Association at OU) members for creating a homely environment. Keep the ball rolling NEPSAnians. Also, I have been very fortunate enough to befriend with Dr. Lara Wallace. Thank you so much, Lara for being very nice to me, helping me to improve my communication skills and advising me during my term in NEPSA.

Last but not least, I will always be grateful and indebted to my family. Didi, Venaju, Bhanja, and Bhanji, for unconditional support and love. My beautiful wife, for loving me even at my worst and supporting me during the last years of my hectic graduate life. My parents, for their selfless love and many sacrifices, to make the ground, the ground where I can stand and reach my goal.

TABLE OF CONTENTS

	Page
Abstract	3
Dedication	4
Acknowledgments	5
List of Tables	11
List of Figures	12
Table of Contents	19
 1 Introduction	20
1.1 History of Elementary Particles	20
1.2 The Standard Model	24
1.3 Quantum Electrodynamics (QED)	25
1.4 Quantum Chromodynamics (QCD)	27
1.4.1 Color Hypothesis and Confinement	28
1.4.2 Some Important Experiments	29
1.4.2.1 Evidence of Color (Electron Positron Annihilation)	30
1.4.2.2 Deep Inelastic Scattering (DIS)	32
1.4.2.3 Evidence of gluons	36
1.4.3 QCD Calculations	37
1.4.3.1 Running of α_s and Asymptotic Freedom	37
1.4.4 Perturbative QCD (pQCD) and Factorization	39
1.4.5 Lattice QCD (LQCD)	40
1.5 Quark Gluon Plasma (QGP)	41
1.6 Relativistic Heavy Ion Collision	43
1.7 Signatures of Quark Gluon Plasma	45
1.7.1 Hydrodynamic Flow	46
1.7.2 Jet Quenching	48
1.7.2.1 Nuclear Modification Factor (R_{AA})	49
1.7.2.2 Two Particle Correlation	50
1.7.2.3 Fragmentation Function Ratio	51
1.7.3 Quarkonia	53
1.7.4 Strangeness Enhancement	53
1.7.5 Constituent Quark Number Scaling	53
1.8 Cold Nuclear Matter Effects	54
1.8.1 Nuclear Modification of Parton Distribution	55
1.8.2 k_T Effect (k_T broadening)	57
1.8.3 Cronin Effect (p_T Broadening)	57

1.8.4	Gluon Saturation	58
1.8.5	Radiative Energy Loss	59
1.9	Speculations in Light-Heavy Ion Collision	59
1.9.1	Long Range Two-Particle Correlation	59
1.9.2	Engineering of Geometry	61
1.9.3	Jet Modification in $d+Au$	62
1.10	Statement of Purpose	63
2	The Experiment	64
2.1	The Relativistic Heavy Ion Collider	64
2.2	PHENIX	65
2.2.1	Magnets	66
2.2.2	Global Detectors	67
2.2.2.1	Beam-Beam Counters (BBCs)	68
2.2.2.2	Zero-Degree Calorimeters (ZDC)	69
2.2.3	Central Arms	70
2.2.3.1	Drift Chamber (DC)	70
2.2.3.2	Pad Chamber (PC)	72
2.2.3.3	Ring-Imaging Cherenkov (RICH) Detector	72
2.2.3.4	ElectroMagnetic Calorimeter(EMCal)	73
2.2.3.4.1	Lead-Scintillator (PbSc) Calorimeter	74
2.2.3.4.2	Lead-Glass (PbGl) Calorimeter	75
2.2.4	Forward Arms	75
2.3	Data Acquisition and Trigger Systems in PHENIX	75
2.3.1	Minimum Bias (MB) Trigger	78
2.3.2	EMCAL/RICH Trigger (ERT)	79
2.4	Centrality Determination in PHENIX	80
2.5	Reconstruction of Charged Tracks in PHENIX	82
2.6	EMCal Clustering in PHENIX	83
3	Data Preparation	85
3.1	Data Selection	85
3.2	Run Selection	85
3.3	Event Selection	86
3.4	Particle Selection	87
3.4.1	Photon Identification and Selection	87
3.4.2	π^0 Trigger	90
3.4.3	Charged Hadron Tracks	91
4	Analysis Details	93
4.1	Two particle Correlation	93
4.1.1	Acceptance Correction and Event Mixing	94
4.1.2	Two-Source Model	95
4.1.3	Background Level (b_0)	97
4.1.3.1	Zero Yield At Minimum (ZYAM)	97

4.1.3.2	Absolute Normalization Method (ABS)	98
4.2	Jet Pair Quantification	98
4.2.1	Per-trigger Yield Nuclear Modification Factor (I_{AA})	98
4.2.2	Double Ratio (R_I)	99
4.2.3	Corrections to R_I	101
4.2.3.1	Rapidity Acceptance Correction	101
4.2.3.2	Bleeding Correction	104
4.2.3.3	ERT Trigger Turn-on Cross-check	105
4.3	Error Analysis	106
4.3.1	Uncertainty from Mis-Constructed (Fake) π^0 Combinatorics	107
4.3.2	Uncertainty from ZYAM	109
4.3.3	Uncertainty from Bleeding correction	110
4.3.4	Uncertainty from $R_{\Delta\eta}$	110
4.3.5	v_3 Contribution	111
4.3.6	Tabulation of Uncertainty Sizes	112
5	Results and Discussions	114
5.1	Baseline Measurement: $p+p$	114
5.1.1	Correlation Function and Jet Function	114
5.2	${}^3\text{He}+\text{Au}$ Results	115
5.2.1	Correlation Function and Jet Function	115
5.2.2	Double Ratio (R_I)	117
5.3	Previous Result of $d+\text{Au}$	118
5.4	Re-analysis of $d+\text{Au}$	118
5.5	Comparison of $d+\text{Au}$ and ${}^3\text{He}+\text{Au}$	120
5.5.1	Comparison With Previous $d+\text{Au}$ Result	120
5.5.2	Comparison with Combined $d+\text{Au}$ Result	122
5.6	Analysis of Statistical Significance of Shape Modifications	123
5.7	Interpretation of The Result	127
5.7.1	PYTHIA 8	128
5.7.2	Intrinsic k_T Study	129
5.7.3	Nuclear Modification of Parton Distribution Function (nPDF)	132
5.7.4	Additional Previous Simulation Studies in $d+\text{Au}$	135
5.7.4.1	Quark Gluon Jet Mixing	135
5.7.4.2	HIJING	137
5.7.5	Concluding Remarks and Small System Eloss Calculation Outlook	139
6	Summary and Outlook	141
6.1	Summary	141
6.2	Outlook	142
6.2.1	Cu+Au and Peripheral Au+Au	142
6.2.2	sPHENIX	144
References		148

Appendix A: Jargon in Relativistic Heavy Ion Collisions	157
Appendix B: 2-Particle Correlation Mathematics	161
Appendix C: sPHENIX EMCal Simulation Design and Correlation Studies	165
Appendix D: Copy Rights	177

LIST OF TABLES

Table	Page
1.1 Predicted values of ratio cross-sections of hadrons to muon pairs production from the electron-positron annihilation for different energy regimes. The m_c , m_b and m_t are the masses of charm quark, bottom quark and top quark respectively	31
2.1 Physical parameters of Lead-Scintillator (PbSc) and Lead-Glass (PbGl) calorimeters. The table is adapted from [1].	77
3.1 A summary of PHENIX data sets used for analysis. The integrated luminosity is taken from [2].	85
4.1 The size of the bleeding effect correction on the awayside in 0-20% d+Au collisions (The unit of p_T is GeV/c). The table is taken from [3].	105
4.2 Uncertainties and their Contributions for R_I in $^3\text{He}+\text{Au}$ collisions at $\sqrt{s_{NN}} = 200$ GeV.	113
6.1 The number of nucleons participating in collisions, $\langle N_{part} \rangle$, corresponding to centrality bins for different collision species. The values are collected from [4–7].	143

LIST OF FIGURES

Figure	Page
1.1 The elementary particles in the Standard Model. The figure is taken from [8]. Courtesy European Organization for Nuclear Research, CERN.	24
1.2 A basic interaction vertex of QED (Left). A typical example of QED process; $e^-e^- \rightarrow e^-e^-$ (Right).	26
1.3 Basic interaction vertices of QCD. Left figure shows the vertex for interaction between quarks via gluons and other two figures shows the gluon self-interaction.	27
1.4 Steps of hadronization. The Figure is adapted from [9].	29
1.5 The experimental measurement of R as a function of \sqrt{s} . The figure is taken from [10]. The copyright permission for the figure is attached in Figure D.1.	31
1.6 Electron-nucleon inelastic scattering. The scattering of electron off the proton results into the bunch of hadrons (X) along with scattered electron.	32
1.7 Evolution of F_2 with Q^2 for different values of x. The figure is taken from [10]. The copyright permission for the figure is attached in Figure D.1.	35
1.8 The proton PDFs from NNLO NNPDF3.0 global analysis [11] at $Q^2 = 10 \text{ GeV}^2$ (left) and $Q^2 = 10^4 \text{ GeV}^2$ (right). The figure is taken from [10]. The copyright permission for the figure is attached in Figure D.1.	36
1.9 Feynman diagram for annihilation of electron-positron into quark anti-quark pairs (left) and into quark, anti-quark and gluon (right).	36
1.10 The measurements of α_s as a function of energy scale, Q. The figure is taken from [10]. The world average of the α_s at the Z boson mass scale is also shown in the figure. The copyright permission for the figure is attached in Figure D.1.	38
1.11 Diagram showing the three elements of pQCD factorization: parton distribution functions, partonic cross sections and fragmentation functions. The figure is taken from [12]. The copyright permission for the figure is attached in Figure D.2.	40
1.12 The light hadron spectrum of from LQCD calculations. The solid circles are results. Horizontal lines and bands are the experimental values with their decay widths. The combination of statistical and systematic errors are shown by vertical error bars. The figure is taken from [13]. The copyright permission for the figure is attached in Figure D.3.	41
1.13 Energy density (left figure) and pressure (right figure) normalized by T^4 as a function of temperature (T) on number of lattice points (N_t) in temporal direction. The Stefan-Boltzmann (SB) limit are indicated by an arrow in both figures. The figures are taken from [14]. Copyright permission for the figures is attached in Figure D.4.	42
1.14 QCD phase diagram mapping out different phases of nuclear matter expected to exist. The lines in the diagram are just an educational guess. The figure is taken from [15]. Courtesy Brookhaven National Laboratory. The copyright permission to use the figure is attached in Figure D.5 and Figure D.6.	43
1.15 Schematic of stages in relativistic heavy ion collisions. The figure is taken from [16].	44

1.16 Left: The almond shaped interaction region for a non-central collision is formed by participant nucleons. The green grid is reaction plane. Beam direction is along the z-axis and blue regions are spectator nucleons. Right: Momentum anisotropy of final state particles due to non-central collision. Figure is taken from [17]. The copyright permission for the figure is attached in Figure D.7. Courtesy PHENIX collaboration.	46
1.17 Comparison of STAR and PHENIX measurements of elliptic flow for different particle species with hydrodynamic models prediction. The figure is taken from [18]. The copyright permission for this figure is attached in Figures D.8 and D.9.	47
1.18 R_{AA} vs. p_T in central $Au + Au$ collision at $\sqrt{s_{NN}} = 200\text{GeV}$ for direct photon (blue), π^0 (orange) and η (red). This figure is taken from [19]. The copyright permission for this figure is attached in Figure D.10.	49
1.19 Di-hadron azimuthal correlations for $p+p$ (black), $d+Au$ (red) and $Au+Au$ (blue) collisions in STAR. Trigger particles with $4 < p_T^{trig} < 6 \text{ GeV}$ and associated particles with $2 < p_T^{assoc} < p_T^{trig} \text{ GeV}$ are used for correlation. This figure is taken from [20]. The copyright permission for the figure is shown in Figure D.11	51
1.20 The fragmentation function ratio of most central $Pb+Pb$ collisions to $p+p$ collisions. This figure is taken from [21]. The copyright permission for this figure is attached in Figure D.12.	52
1.21 Enhancement of production of strange baryon as a function of mean number of participating nucleons in nucleus-nucleus collisions $< N_{part} >$. The figure is taken from [22] (An article available under the terms of the Creative Commons Attribution 3.0 License).	54
1.22 Elliptic flow, v_2 , vs transverse momentum and kinetic energy before (left two plots) and after (right two plots) scaled with number of quarks. The figures are taken from [18]. The copyright permission for this figure is attached in Figures D.8 and D.9.	55
1.23 Different modification regions for parton distribution functions . The figure is taken from [23]. The copyright permission for the figure is shown in Figure D.13.	56
1.24 The nuclear modification factor as a function of p_T . The red and green points are of $d+Au$ collisions while blue points are of $Au+Au$ collisions. The figure is taken from [20]. The copyright permission for the figure is attached in Figure D.14.	58
1.25 Two-particle correlations in $\Delta\eta - \Delta\phi$ measured in (a) $Pb+Pb$ collisions at 2.76 TeV (b) $p+Pb$ collisions at 5.02 GeV and (c) $p+p$ collisions at 13 TeV. The peaks in figures (b) and (c) are truncated for proper visualization. The figures (a) and (b) are taken from [24]. The copyright for the figures are attached in Figure D.15. The figure (c) is taken from [25], which is available under the terms of the <i>Creative Commons Attribution 3.0 License</i> .	60

1.26 Measured flow coefficients (v_2 , v_3) as a function of p_T for a) $p+\text{Au}$ b) $d+\text{Au}$ and c) ${}^3\text{He}+\text{Au}$ at $\sqrt{s_{NN}} = 200$ GeV in 0-5% centrality. The black solid sphere (diamond) are measured v_2 (v_3). The solid red and dashed blue curves represent SONIC & iEBE-VISHNU hydrodynamic model predictions respectively. Also, the dotted green curve represents the postdictions of flow coefficients from initial-state momentum correlations. The figure is taken from [26]. The copyright permission for the figure is attached in Figure D.16.	61
1.27 The R_I as a function of z_T measured for $d+\text{Au}$ collisions at $\sqrt{s_{NN}} = 200$ GeV in centrality 0-20%. The figure is taken from [3]. Courtesy Bing Xia.	62
 2.1 Relativistic Heavy Ion Collider (RHIC) complex at Brookhaven National Lab (BNL). The figure is taken from [27]. Courtesy Brookhaven National Laboratory. The copyright permission to use the figure are attached in Figure D.5 and Figure D.6.	64
2.2 Beam view (left) and side view (right) of PHENIX detector configuration for Run12. The figure is taken from [17]. The copyright permission for the figure is attached in Figure D.7. Courtesy PHENIX collaboration.	65
2.3 Line drawings of the PHENIX magnets. The cut away is to show the interior structures. The beam line of the colliding beams are shown by arrows. The figure is taken from [28]. The copyright permission for the figure is attached in Figure D.17.	66
2.4 Magnetic field lines in PHENIX with central magnetic coils in the combined (++) mode. The figure is taken from [17]. The copyright permission for the figure is attached in Figure D.7. Courtesy PHENIX collaboration.	67
2.5 Left: A single element of BBC consisting of a PMT and quartz radiator. Middle: One of the two BBCs consisting of 64 PMTs and radiators. Right: BBC installed around the beam pipe [29].	68
2.6 Schematics of BBCs. The two BBCs (North and South) are at distance 288.9 cm. Collision is supposed to occur around the middle of two BBCs.	68
2.7 Installation of north and south ZDCs (red blocks) along the beam axis. The figure is taken from [30]. The copyright permission for the figure is attached in Figure D.18.	69
2.8 DC frame. The figure is taken from [31]. The copyright permission for the figure is attached in Figure D.19 and Figure D.20.	71
2.9 Left: Side view of layout of wire arrangement within one sector of DC. Right: Top view of U, X and V wire orientation. The figure is taken from [31]. The copyright permission for the figure is attached in Figure D.19 and Figure D.20.	71
2.10 The expanded geometry of the PC1. The figure is taken from [32]. The copyright permission for the figure is attached in Figure D.21.	73
2.11 The cutaway view of PbSc calorimeter module. The figure is taken from [1]. The copyright permission for the figure is attached in Figure D.22.	74
2.12 The exploded view of PbGl calorimeter super-module. The figure is taken from [1]. The copyright permission for the figure is attached in Figure D.22.	76
2.13 Schematic representation of flow of PHENIX data.	78
2.14 The method for EMCAL Trigger. The figure is taken from [33].	79

2.15 Cartoon showing the correlation between the final state observable N_{ch} and quantities (b , N_{part}) calculated from Glauber. The figure is taken from [34]. The copyright permission for the figure is attached in Figure D.23 and Figure D.24.	81
2.16 Left: The total energy deposited in ZDC vs total charge detected in BBC, “clock method”. Right: Charge distribution of BBC, “BBC only method” Each bin contains same number of events for both figures. The figures are taken from [35].	82
2.17 Reconstruction of charged track using DC with Combinatorial Hough Transform (CHT) technique [36]. The larger circle is defined by DC reference radius and the smaller circles represents hits from particles along its trajectory.	83
3.1 Left: The ERT and Minimum Bias (MB) π^0 spectrum for ${}^3\text{He}+\text{Au}$ collisions at $\sqrt{s_{NN}}=200$ GeV. Right: The ratio of ERT to MB π^0 trigger yield. The blue vertical line is at 5 GeV.	86
3.2 Left two columns: All hits in the eight sectors of EMCAL for ${}^3\text{He}+\text{Au}$ collisions. Right two columns: Photon hits after applying hot/dead maps. In each panel, X-axis represents the tower position along beam axis while the Y-axis represents the tower height. Each bin represents individual tower and the color density profile shows the hits in the tower.	89
3.3 Left two columns: All hits in the eight sectors of EMCAL for Run16 $d+\text{Au}$ collisions. Right two columns: Photon hits after applying hot/dead maps. In each panel, X-axis represents the tower position along beam axis while the Y-axis represents the tower height. Each bin represents individual tower and the color density profile shows the hits in the tower.	89
4.1 Trigger and partner particle pairs from back to back scattering parton.	94
4.2 The decomposition of correlation function into jet and background pairs with background level b_0 [37]. The copyright permission for the figure is attached in Figure D.25	96
4.3 Schematic of how individual v_n components cancel in R_I	100
4.4 Function of $\Delta\eta$ Correction	102
4.5 Nearside Width for 0 - 20% Centrality	103
4.6 NS $R_{\Delta\eta}$ corrs	104
4.7 Left: The ratio of π^0 spectrum of Run14 ${}^3\text{He}+\text{Au}$ ERT to that of $p+p$. The blue vertical line is at 5 GeV. Right: The ratio of re-weighted π^0 spectrum of Run14 ${}^3\text{He}+\text{Au}$ ERT to π^0 spectrum of $p+p$	106
4.8 π^0 invariant mass distribution for ${}^3\text{He}+\text{Au}$ in 0-20 % centrality bin. Red line: Gaussian+line fit to data. Black line: Straight line fit for background estimation. Green line: Gaussian fit after background subtraction. Signal (S) is found by integrating the green line in 2σ from the peak (in between two vertical magenta lines). Background is found by integration of black line in the same interval.	108

4.9	${}^3\text{He}+\text{Au}$ R_I with and with out flow vs z_T . Note in this plot other corrections are not applied. The flow estimations come from 0-20% Au+Au where we expect the high p_T flow, which is driven by energy loss to be smaller, and thus this test should substantially overestimate the effects of flow. Because of the high jet signal to background in ${}^3\text{He}+\text{Au}$ due to still having relatively small total multiplicity, the effects are negligible as in $d+\text{Au}$	111
4.10	The relative difference (absolute value) in R_I with and with out the over-estimated flow vs z_T . Red line is fit value over low z_T range.	112
5.1	π^0 -hadrons correlation function (PHENIX Preliminary approved) for Run15 $p+p$ collisions. The red line is the fit for the data and the blue line is the background level from ZYAM method. Trigger p_T bins: [5.0 - 7.0, 7.0 - 9.0] GeV/c running from top to bottom. Partner p_T bins: [0.6 - 1.0, 1.0 - 2.0, 2.0 - 3.0, 3.0 - 5.0 and 5.0 - 7.0] GeV/c running from left to right.	114
5.2	π^0 -hadrons jet function for Run15 $p+p$ collisions. The jet function doesn't include any correction due to single particle efficiency. The trigger p_T bins used are [5.0 - 7.0, 7.0 - 9.0] GeV/c which runs from top to bottom. The partner p_T bins used are [0.6 - 1.0, 1.0 - 2.0, 2.0 - 3.0, 3.0 - 5.0 and 5.0 - 7.0] GeV/c which runs from left to right.	115
5.3	π^0 -hadrons correlation function (PHENIX Preliminary approved) for Run14 ${}^3\text{He}+\text{Au}$ collisions. The red line is the fit for the data and the blue line is the background level from ZYAM method. Trigger p_T : [5.0 - 7.0, 7.0 - 9.0] GeV/c running from top to bottom. Partner p_T bins: [0.6 - 1.0, 1.0 - 2.0, 2.0 - 3.0, 3.0 - 5.0 and 5.0 - 7.0] GeV/c running from left to right.	116
5.4	π^0 -hadrons jet function for Run14 ${}^3\text{He}+\text{Au}$ collisions. The jet function doesn't include any corrections due to single particle efficiency. Trigger p_T bins: [5.0 - 7.0, 7.0 - 9.0] GeV/c running from top to bottom. Partner p_T bins: [0.6 - 1.0, 1.0 - 2.0, 2.0 - 3.0, 3.0 - 5.0 and 5.0 - 7.0] GeV/c running from left to right.	116
5.5	(PHENIX Preliminary Version) R_I in Run14 ${}^3\text{He}+\text{Au}$. The red line is the straight line fit for $z_T > 0.45$. The vertical bars represent statistical errors while the boxes represent systematic uncertainties.	117
5.6	The R_I as a function of z_T measured for $d+\text{Au}$ collisions at $\sqrt{s_{NN}} = 200$ GeV in centrality 0-20%. The vertical bars represent statistical errors while the boxes represent systematic uncertainties. The figure is taken from [3]. Courtesy Bing Xia.	118
5.7	R_I as a function of z_T for 0-20% Run16 (left) and Run8 (right) $d+\text{Au}$ at $\sqrt{s_{NN}} = 200$ GeV. The vertical bars represent statistical errors while the boxes represent systematic uncertainties.	119
5.8	R_I as a function of z_T for combined (Run8 + Run16) $d+\text{Au}$ at $\sqrt{s_{NN}} = 200$ GeV. The vertical bars represent statistical errors while the boxes represent systematic uncertainties.	119
5.9	(PHENIX Preliminary Version) Comparison of R_I of preliminary Run8 $d+\text{Au}$ and that of Run14 ${}^3\text{He}+\text{Au}$. The black color is for the ${}^3\text{He}+\text{Au}$ and blue color for the $d+\text{Au}$. The vertical bars represent statistical errors while the boxes represent systematic uncertainties.	120

5.10 (PHENIX Preliminary Version) Ratio of Away side to near side per-trigger yield of preliminary Run8 d +Au and that of Run14 ${}^3\text{He}$ +Au. This is the same as the Ratio of the R_I 's themselves, when the same $p+p$ reference is used. The ${}^3\text{He}$ +Au R_I is two sigma smaller than that of d +Au.	121
5.11 Left: Comparison of R_I of combined (Run8 +Run16) d +Au and that of Run14 ${}^3\text{He}$ +Au. The black color is for the ${}^3\text{He}$ +Au and magenta color for the d +Au. Right: Ratio of R_I in ${}^3\text{He}$ +Au to that in combined d +Au.	122
5.12 Ratio of R_I in ${}^3\text{He}$ +Au to that in d +Au. The red line represents constant fit over full range of z_T	123
5.13 The R_I of d +Au (left) and ${}^3\text{He}$ +Au (right) fitted with first degree of polynomial in full range of z_T . The magenta dotted line represents the fit.	124
5.14 The R_I of d +Au (left) and ${}^3\text{He}$ +Au (right) fitted with zeroth degree of polynomial in full range of z_T . The magenta dotted line represents the fit.	125
5.15 Away side per-trigger yield modification from π^0 -hadron correlations in 0-10% Pb-Pb collisions at $\sqrt{s_{NN}} = 2.76$ TeV. The figure is taken from [38] and is available under the <i>Creative Commons Attribution License</i>	127
5.16 Distribution of k_T for $p+p$ and d +Au collisions at $\sqrt{s_{NN}} = 200$ GeV. The figure is taken from [39]. The copyright permission for the figures is attached in D.27.	129
5.17 The modification in R_I due to the different k_T settings in PYTHIA-6.	130
5.18 Modification of R_I with realistic k_T (left) and with exaggerated k_T value as a function of hadron p_T for trigger bin $5 < p_T < 7$ GeV/c. Both of the k_T options could not reproduce the original modification of R_I	131
5.19 The modification in R_I due to nPDF from EPPS09 in d +Au. The uncertainties in EPS09 nPDF sets are shown in shaded area.	132
5.20 The jet functions from PYTHIA-8 simulation. The black points corresponds to the $p+p$ collisions with default NNPDF2.3 QCD+QED LO PDF set without any nuclear modification. The red points corresponds to the jet function of He+Au collisions with EPPS16 nPDF set.	134
5.21 The modification in R_I due to nPDF from EPPS16. The uncertainties in EPPS16 nPDF sets are shown in shaded area. The box represents the uncertainty due to EPPS16 error sets.	135
5.22 2D density plot for Q^2 as a function of x for triggered events in PYTHIA-8+EPPS16 study. $x \approx 0.02 \sim 0.03$ and $Q^2 \approx 30 \sim 50$ (GeV/c) 2 corresponds to the most probable events. The lower cut in Q^2 is due to the phase space cut in the transverse momenta in 2 \rightarrow 2 processes.	136
5.23 Nuclear modification of parton distribution functions with EPPS16 of Au (left) and He (right) at $6 \leq Q \leq 7$ GeV/c.	136
5.24 Left: Modification in R_I from PYTHIA d +Au collisions considering conversion of all quark jets (q) into gluon jets (g). Right: The modification in R_I due to double conversion ($q \leftrightarrow g$). The figures are taken from [3].	137
5.25 The η distribution for charged hadrons (left) and π^0 triggers (right) from HIJING simulation. The red line is for $p+p$ collisions while black line is that for central d +Au collisions. The figure is taken from [3].	138

5.26 Left: Modification in R_l from HIJING $d+\text{Au}$ simulations with realistic $k_T = 2.0 \text{ GeV}/c$ and PYTHIA-6 $p+p$ simulations with realistic $k_T = 2.8 \text{ GeV}/c$. Right: The modification in R_l from HIJING simulations with default $k_T = 0.44 \text{ GeV}/c$ for both $d+\text{Au}$ and $p+p$. The figures are taken from [3].	139
5.27 R_{pA} for charged hadrons as a function of p_T at $\sqrt{s_{NN}} = 5.02 \text{ TeV}$. The data points are from $p+\text{Pb}$ collisions in ALICE and different lines represents result from calculations. (a) The dotted line shows the calculations for the energy loss in $p+p$. The dotted dashed line shows the EKS98 [40] correction to nPDF. The solid and dashed lines shows the energy loss in $p+\text{Pb}$ with and without considering energy loss in $p+p$. The multiple lines are due to different considerations in theory calculations. (b & c) are same as (a) but for different radius of fireball in $p+\text{Pb}$ collisions. The figure is taken from [41]. The copyright permissions for the figure are attached in Figure D.28 and Figure D.29.	140
6.1 Left: Arbitrary suppression of R_l at high z_T for different collision systems as a function of N_{part} . Right: Average R_{AA} for charged hadrons of $8 < p_T < 20 \text{ GeV}/c$ as a function of centrality bins in $\text{Pb}+\text{Pb}$ collisions at $\sqrt{s_{NN}} = 5.02 \text{ TeV}$. The solid black line shows the model prediction from HG-PYTHIA. HG-PYTHIA is PYTHIA-based model superimposing events incoherently without nuclear modification. The right figure is taken from [42] and is available under the terms of <i>Creative Commons Attribution License</i>	144
6.2 Current outline of the proposed sPHENIX detector. The figure is taken from [43] and the figure is available under the terms of <i>Creative Commons Attribution-NonCommercial-No Derivatives License</i>	145
A.1 Pseudorapidity (η) vs polar angle (θ). The normal polar angle (90°) corresponds to zero pseudorapidity.	157
A.2 Cartoon illustration of collision geometry. The green grid plane is the reaction plane with two nuclei colliding along z-axis.	159
C.1 Electromagnetic Calorimeter subsystem of sPHENIX. The figure is taken from [44].	166
C.2 Electromagnetic Calorimeter subsystem of sPHENIX. The figure is taken from [44].	167
C.3 Illustration of CMS Island algorithm. The figure is taken from [45].	168
C.4 π^0 cluster splitting fraction with respect to the opening angle of two decaying photons. Here "withv1" corresponds to the PHENIX clustering algorithm while "withoutv1" corresponds to the simple contiguous algorithm.	169
C.5 Reconstructed energy vs truth (primary) energy for single photon simulation in three different clustering algorithm. The dashed line is where the reconstructed energy is equal to the truth or primary energy.	170
C.6 Reconstructed energy vs truth (primary) energy for embedded photon simulation in two different clustering algorithms. The dashed line is where the reconstructed energy is equal to the truth or primary energy.	171

C.7	Reconstructed vs. Primary energy for single photon simulation using PHENIX clustering algorithm.	172
C.8	Patterns of low energy clusters in the single photon GEANT4 simulation. The pattern matches with the fiber positions, tower boundary and sector boundary.	172
C.9	The low energy clusters before (right) and after (left) 9^0 tilt. Note: the number of events in the left figure is large compared to that in right figure.	173
C.10	Pictorial illustration of ZEMC.	174
C.11	Reconstruction efficiency as a function of ZEMC.	175
C.12	Blackhole energy just after the EMCAL position.	175
C.13	Reconstruction efficiency without (left) and with (right) including blackhole energy.	176
D.1	The permission to use Figure 1.5, 1.7, 1.8 and 1.10	178
D.2	The permission to use Figure 1.11	179
D.3	The permission to use Figure 1.12	180
D.4	The permission to use Figure 1.13	181
D.5	The permission to use Figure 1.14 and Figure 2.1. Part 1 of 2.	182
D.6	The permission to use Figure 1.14 and Figure 2.1. Part 2 of 2.	183
D.7	The permission to use Figure 1.16, Figure 2.2 and Figure 2.4	184
D.8	The permission to use Figure 1.17 and 1.22 (part1 of 2).	185
D.9	The permission to use Figure 1.17 and 1.22 (part2 of 2).	186
D.10	The permission to use Figure 1.18	187
D.11	The permission to use Figure 1.19.	188
D.12	The permission to use Figure 1.20.	189
D.13	The permission to use the Figure 1.23	190
D.14	The permission to use Figure 1.24.	191
D.15	The permission to use figure (c) of Figure 1.25.	192
D.16	The permission to use Figure 1.26.	193
D.17	The permission to use Figure 2.3.	194
D.18	The permission to use Figure 2.7.	195
D.19	The permission to use Figure 2.8 and Figure 2.9. Part 1 of 2.	196
D.20	The permission to use Figure 2.8 and Figure 2.9. Part 2 of 2.	197
D.21	The permission to use Figure 2.10.	198
D.22	The permission to use Figure 2.11 and Figure 2.12.	199
D.23	The permission to use Figure 2.15. Part 1 of 2.	200
D.24	The permission to use Figure 2.15. Part 2 of 2.	201
D.25	The permission to use Figure 4.2	202
D.26	The permission to use Figure 4.4	203
D.27	The permission to use Figure 5.16	204
D.28	The permission to use Figure 5.27. Part 1 of 2.	205
D.29	The permission to use Figure 5.27. Part 2 of 2.	206

1 INTRODUCTION

"The laws of nature should allow the existence of intelligent beings that can ask about the laws of nature."

- Anthropomorphic principle,

What are the most fundamental constituents of matter? How do those tiny fundamental particles weave the ordinary, real world that we could observe and how did they first appear in the evolution of our universe? Human beings have always been interested to study about nature and its laws in the most fundamental level to get the answers for above questions.

At a time about microseconds after the birth of the universe, the universe was in a state called Quark-Gluon plasma, QGP (described in Section 1.5). All of the particles in the present Universe root back to the QGP state. This dissertation presents an analysis to help better understand the properties of the QGP, which is ultimately connected to finding out the answers of the aforementioned questions.

1.1 History of Elementary Particles

Early Days:

Ancient Greek philosophers speculated there was an "Atom" (Greek: *atomos*, meaning "uncuttable") as the most fundamental constituent of matter. After the discovery of electron by J.J. Thomson (1897), he proposed "plum pudding model" of an atom in 1904. According to the model, an atom consists of electrons suspended in a heavy positively charged paste. Ernest Rutherford (1909) carried out a scattering experiment of alpha particles into thin gold foils which lead to a change from Thomson's model. Rutherford described an atom having very dense positively charged nucleus surrounded by negatively charged lighter electrons. He gave the name "proton" to the nucleus of lightest atom i.e. hydrogen. Neil Bohr (1914) proposed the famous planetary concept of atoms where the electrons circulates protons like planets circulating around the nuclear "sun" in a fixed orbit. The

peculiarity of the weight of the next heavy atom after hydrogen, helium (four times heavier than hydrogen), was solved by James Chadwick when he discovered electrically neutral "neutron" inside the nucleus of atom. Until this time, it was only the electron, the proton and the neutron, which made up matter.

Origin of Quantum Realm:

Planck (1900) proposed an idea about the quantization of energy of electromagnetic radiation while explaining the spectrum of black-body radiation. According to him, electromagnetic radiation came in the discrete packets of energy. Einstein (1905) used the idea of Planck to explain the *photoelectric effect*. The photoelectric effect is the phenomenon of release of electrons from metal surface when struck by light. Einstein explained this phenomenon by proposing the idea of a particle nature of light. According to him, light comes in the discrete packets called the *photon* which has zero mass. The idea of photon was further confirmed with an experiment of scattering of a photon with a particle at rest, by Compton (1923). In the Quantum field theory of electrodynamics, QED (explained in Section 1.3.), the interaction between the two charges can be explained by considering the exchanges of photons between them. In other words, the photon is treated as a quanta of the electromagnetic field.

What holds the nucleus together?

In-spite of the Coulomb repulsion between the protons, they are tightly bound with neutrons inside the nucleus of atom. There must be some kind of short range force stronger than electromagnetic repulsion, which holds the protons and neutrons inside the nucleus. Hence it got the name, *strong force*. Yukawa (1934) explained the strong force by proposing a theory with the assumption of some kind of field in between protons and neutrons. According to him, the field results due to the exchange of a particle between the nucleons. He called the mediating particle, *meson* because its predicted mass lied in between electron and proton mass. Anderson and Neddermeyer (1937) observed a particle having similar

properties of Yukawa's meson during the study of cosmic rays. Further study of the cosmic ray particles revealed discrepancies with the Yukawa particle. The discrepancies were soon resolved in 1946 by Powell and his group. They found that the cosmic ray particles were of two kinds; *pion* and *muon*. The pion was the actual Yukawa's meson while muon was heavier version of electron.

Myriad of particles

With the advancement in theory and experiments, many other elementary particles were discovered over a period of time. Explaining the relativistic quantum particles by Dirac (1927) leaded into the negative energy solutions of wave equation. This eventually lead to the theoretical prediction of the existence of antiparticles. Anderson in 1931, experimentally found the positron, an antiparticle counterpart of electron. A problem of missing energy in the nuclear beta decay theoretically demanded the existence of another neutral particle, the *neutrino*. The existence of neutrinos were verified experimentally by Cowan and Reines (Mid 1950s) from the experiments in Savannah River nuclear reactor [46]. The neutrino produced in beta decay was found to be associated with the electron. Later on, another neutrino associated with the muon was also discovered. The electron- and muon- associated neutrinos and their antiparticle counterparts were kept in a family, called *Leptons*.

After the discovery of Yukawa's meson, Rochester and Butler (1947) discovered a new neutral meson particle, the K^0 (kaon) decaying into two new sets of meson particles π^+ and π^- . After that many mesons including K^+ , η , ω , ρ were discovered. Andersen's group at Cal Tech.(1950) discovered a neutral particle, the Λ , heavier than the proton which decays into a p^+ and π^- . The Λ was classified into the *Baryon* family along with proton and neutron. Soon after the discovery of Λ , other particles belonging to baryon family including Σ' s, Δ' s and Ξ' s were discovered. These newly discovered mesons and baryons were produced copiously and decayed slowly and hence got the name *strange particles*. With growing number of the particles, it became urgency for the particle physicists to find a periodic table

for the elementary particles. Murry Gell-Mann (1961) came up with *Eightfold way* [47] to classify those elementary particles with arrangements that followed geometrical patterns according to their charge and strangeness.

The Quark Model:

The geometrical patterns in the Eightfold way classification of hadrons (which is a collective term for meson and baryon) demanded explanation. Gell-Mann and Zweig (1964) independently put forward the idea that all of the hadrons are in turn composed of elementary constituents called *quarks* [48]. According the model, there were three flavors of quarks; up (u, charge = +2/3, strangeness = 0), down (d, charge = -1/3, strangeness = 0) and strange (s, charge = -1/3, strangeness = -1) with their antiparticle counterparts. These three quarks and their antiquarks followed combination rules to form the hadrons.

1. Baryons are made up of three quarks.
2. Mesons are made up of one quark and one antiquark.

The Eightfold way of classification of hadrons was explained very well by the quark model but there were some problems. Since the quarks are fermions (spin 1/2), there is a violation of Pauli's exclusion principle while combining quarks of same flavor. O.W. Greenberg (1964) proposed the three color flavors (red, green and blue) of each quarks to solve the problem [49]. Another problem at that time for the quark model was that there was no experimental evidence of individual quark. A hypothesis of *quark confinement* (which will be discussed further below) was put forward to explain this unavailability of free quarks.

In 1974, the discovery of the J/ψ meson [50] came to rescue for the quark model. This meson was independently discovered by two groups, one in Brookhaven Lab (group led by Ting) and another in SLAC (group led by Burton Richter). The J/ψ was exceptionally heavy for a meson (nearly three times than proton), electrically neutral and had relatively longer lifetime. The existence of the J/ψ meson can be explained by the quark model

by introducing a new flavor of quark, charm (c)—which can then make the meson with the corresponding anti-quark (\bar{c}) flavor. Because of its contribution to support the quark model and other reasons, the discovery of the J/ψ meson is now taken as the start of the *November Revolution* when many aspects of the current Standard Model were introduced and/or became accepted. The discovery of J/ψ also proved the longtime speculation of symmetry between the leptons and quarks family (four in each.) This symmetry was even expanded after the discovery of tau lepton & its neutrino and top quark & bottom quark.

1.2 The Standard Model

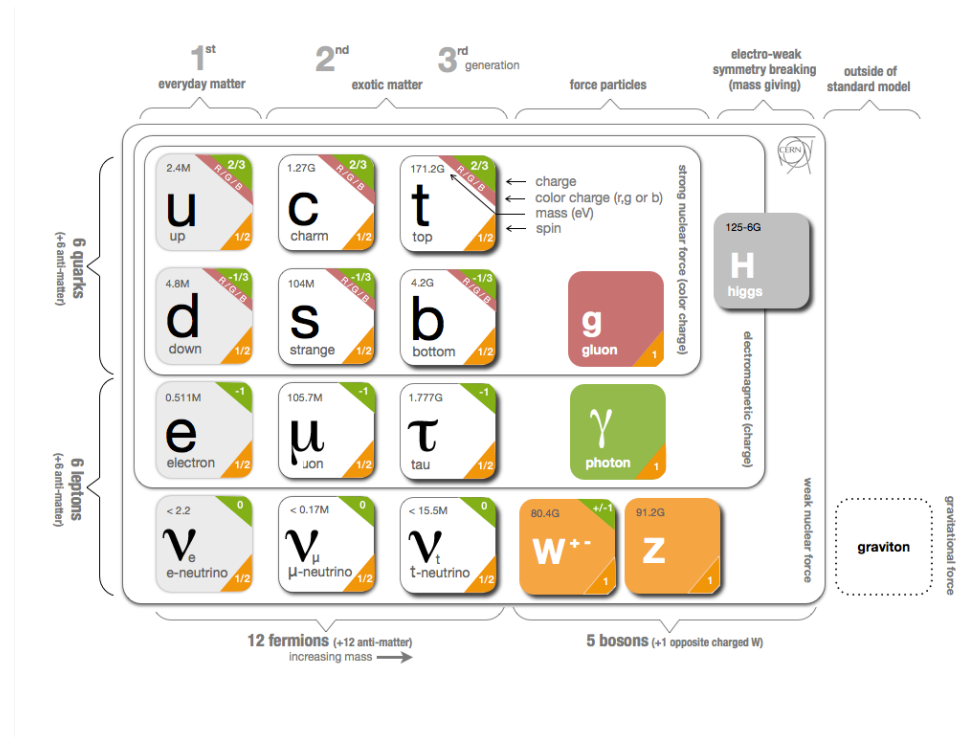


Figure 1.1: The elementary particles in the Standard Model. The figure is taken from [8]. Courtesy European Organization for Nuclear Research, CERN.

The Standard Model (SM) [10], developed in early 1970's, is a theoretical framework for describing the constituents of matter and their interactions with each other. According to the SM, the elementary particles belongs to three families; quarks, leptons, and mediating

bosons. The Standard Model consists of fermions with a half integer value of spin and bosons with an integer value of spin. Fermions consist of six quarks and six leptons forming all known matter, while bosons are force carriers in the interaction of matter. Figure 1.1 shows the elementary particles in the SM.

The SM successfully describes the three out of four fundamental forces; electromagnetic, weak, and strong. The gravitational force is not described by the SM. If it were, the mediating boson would be called the graviton. The SM is a $SU(3) \otimes SU(2) \otimes U(1)$ theory which refer to different mathematical *groups* which define part of the underlying mathematical structure. The SM successfully explains and correctly predicts most of the elementary physics but there are still some unanswered questions. The explanation of masses of quarks & leptons, quantum theory of gravity, the obvious matter - antimatter asymmetry in the detectable matter in the universe, and dark matter are some of the questions the SM is yet to explain.

In the next sections, I introduce more details about some of the main components of the SM, which can be described as a collection of three Quantum Field Theories (QFT's that describe the Electromagnetic, Strong Nuclear, and Weak Nuclear forces in a unified way). These are respectively called Quantum Electrodynamics (QED), Quantum Chromodynamics (QCD), and Quantum Flavor Dynamics (QFD). Both QED and QCD are especially relevant to this thesis, especially QCD which is main focus of the whole field of Nuclear Physics in general.

1.3 Quantum Electrodynamics (QED)

Quantum Electrodynamics (QED) is a quantum field theory of the electromagnetic interactions mediated by exchange of photons. In classical electromagnetism, the force arises from a potential $V(\vec{r})$ (more fully a "four-vector" potential $A_\mu = (V, \vec{A})$) acting instantaneously at a distance. In QED, forces are described by the exchange of field quanta called photons. A basic interaction vertex for QED can be represented with a

Feynman diagram¹ as shown in Figure 1.2. Feynman diagrams are very useful tools in



Figure 1.2: A basic interaction vertex of QED (Left). A typical example of QED process; $e^-e^- \rightarrow e^-e^-$ (Right).

the particle physics. The transition matrix element, input in *Fermi's Golden Rule*² to get the transition rate, can be calculated with the help of the Feynman diagram of the process. The QED interaction is a three point vertex of gauge boson (photon) and incoming & outgoing fermions. Each interaction is associated with coupling constant(g) which enters any calculation as an overall multiplicative factor g . The coupling constant determines the strength of fundamental interaction between gauge boson and a fermion.

Transition amplitude (M) $\propto g$; for one vertex

$$\text{Transition rate} \propto |M|^2 \propto g^2$$

A dimensionless constant, α ($\propto g^2$), is introduced for the sake of convenience. The α is sometimes itself called coupling constant. For QED,

$$\alpha = \frac{e^2}{4\pi\epsilon_0\hbar c} \simeq \frac{1}{137}$$

¹ A Feynman diagram is a pictorial representation of a process corresponding to a particular transition amplitude [51]. Transition amplitude for all the processes (annihilation, decay, scattering, absorption, emission) can be described by Feynman Diagrams. In Feynman diagrams, fermions are represented with solid lines with arrows and bosons are with wavy or dashed lines. Time flows from left to right (or upward) in Feynman diagram.

² Fermi-Golden rule: Transition rate = $\frac{2\pi}{\hbar}|M|^2(\text{phase} - \text{space})$. Where, M is amplitude (matrix element) containing all the dynamical information. The *phase - space* , also called density of final states, contains only kinematic information.

which is same as "fine structure constant" which shows up in the description of fine structure of atomic spectra. Energy, momentum, charge, fermion flavor and parity are conserved in QED vertices. The contribution of the exchanged particle in the transition matrix element is introduced as the "propagator term".

$$\begin{aligned} \text{Propagator term: } & \frac{1}{q^2 - m_x^2} \\ & : \frac{1}{q^2}, \text{ for QED} \end{aligned}$$

where q is four momentum and m_x is mass of exchanged virtual particle. The exchanged virtual particles do not have the mass of physical particle. They are not directly detectable but their effects can be observed through the forces they mediate. The QED is proven to be one of the most precise theories in physics.

1.4 Quantum Chromodynamics (QCD)

Quantum Chromodynamics is a fundamental field theory describing the strong interactions mediated by exchange of *gluons*. This theory is developed with the same framework of QED with some crucial differences. One of the most important differences is, unlike photon in QED, the gluons can self interact with themselves in QCD, which leads to many of the odd properties of QCD, including the concept of color confinement explained in the next section. The basic QCD interaction vertices predicted from the requirement of SU(3) local gauge invariance are as shown in Figure 1.3.

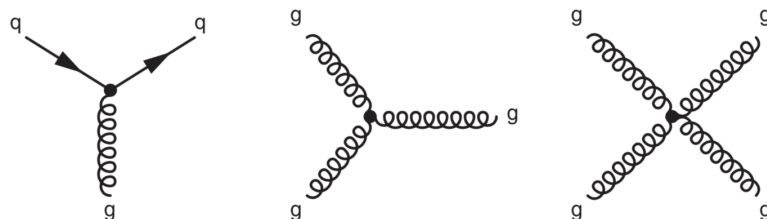


Figure 1.3: Basic interaction vertices of QCD. Left figure shows the vertex for interaction between quarks via gluons and other two figures shows the gluon self-interaction.

1.4.1 Color Hypothesis and Confinement

In QCD, there are three "color" charges, red (r), blue (b) and green (g) unlike the single electric charge in QED. The gluons only couple to the particles with non-zero color charge. Quarks have color charge and hence couple with gluons while leptons are color neutral and don't couple with gluons. The anti-quarks carry the opposite color charge to quark; \bar{r} , \bar{b} and \bar{g} . In addition to solving the problem of violation of Pauli's exclusion principle in hadrons with combination of same quarks, the color hypothesis has much experimental evidence (explained in Section 1.4.2.1.).

Even though there are many experimental evidences for the existence of quarks, there is no direct detection of free quarks. This non-observation of the free quark can be explained with a hypothesis called *color confinement*. According to this hypothesis, "Colored objects are always confined to color singlet states and no objects with non-zero color charge can propagate as free particle" [9]. The concept of the color confinement has not been analytically proven yet. But calculations of Lattice QCD, a version of the QCD theory described below, exhibits the confinement behavior and confirm that qualitatively it can be described as gluon-gluon self interaction. The phenomenological potential for the strong interaction for explaining the concept of confinement can be written as,

$$V_s = -\frac{4}{3} \frac{\alpha_s(r)}{r} + kr, \quad (1.1)$$

where k , is constant determining the field energy per unit length. The first term in the right hand-side of the Equation (1.1) is similar to the Coulomb potential and dominates at small distance r . Whereas, the second term dominates at larger distance and hence confines the quark and gluons inside hadrons.

Hadronization and Jets

The Figure 1.4 shows the qualitative description of the hadronization. The quark and anti-quark (or quark and gluon) pairs produced in any interactions tend to travel back to back in the center of mass frame. During this process, the color field is restricted to

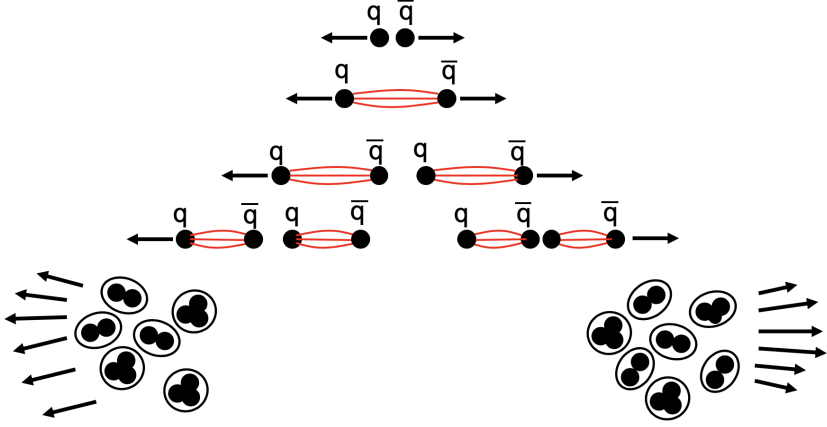


Figure 1.4: Steps of hadronization. The Figure is adapted from [9].

the shape of a tube due to attractive interaction between gluons. The energy stored in the tube increases linearly as the separation increases. The separation increases until the energy stored in the color field is sufficient to form a new $q\bar{q}$ pairs instead of allowing the propagating quarks or gluons to continue to simply increase the strength of the field by continuing to move apart. This process continues until the relative momentum of quarks is sufficiently moderated to form colorless bound state hadrons. This process is called hadronization or fragmentation. This results into two jets of hadrons following the initial direction of respective quark or anti-quark [52]. Thus, the quarks and gluons produced in high energy collisions are detected as jets of hadrons in the detectors.

1.4.2 Some Important Experiments

In this subsection, I explain some important QED and QCD experiments which helped to build the theory of QCD.

1.4.2.1 Evidence of Color (Electron Positron Annihilation)

For annihilation of electron-positron pairs into muon-anti-muon pairs, the total QED cross-section [9] can be written as in Equation (1.2).

$$\sigma(e^+e^- \rightarrow \mu^+\mu^-) = \frac{4\pi\alpha^2}{3s}, \quad (1.2)$$

where α is QED coupling constant and s is square of center of mass energy of collision.

The electron-positron can also annihilate to form quark-anti-quark pairs. Applying the same approach, the total cross-section corresponding to the production of the quark pairs can be written as in Equation (1.3).

$$\sigma(e^+e^- \rightarrow q\bar{q}) = 3 \times \frac{4\pi\alpha^2}{3s} \times Q_q^2, \quad (1.3)$$

where the factor "3" is introduced assuming the three possible color combination of final state $q\bar{q}$ ($g\bar{g}$, $r\bar{r}$ & $b\bar{b}$) and Q_q is quark charge. This final state of quarks cannot be observed because the strong interaction acts as soon as they are produced. And the color field established in between the quarks pair is energetic enough to produce additional quark-anti-quark pairs. Hence jets of hadrons are observed as final state instead of simply a $q\bar{q}$ pair. We cannot differentiate the quarks directly because of the conversion of quarks into hadrons. So, we consider the inclusive hadron cross-section, $\sigma(e^+e^- \rightarrow \text{hadrons})$, which to the first order is simply the sum of individual cross-sections.

$$\sigma(e^+e^- \rightarrow \text{hadrons}) \simeq \sum \sigma(e^+e^- \rightarrow q\bar{q}), \quad (1.4)$$

The ratio of hadronic cross-section to that of muon pairs from the electron-positron collisions can be written as in Equation (1.5).

$$R \equiv \frac{\sigma(e^+e^- \rightarrow \text{hadrons})}{\sigma(e^+e^- \rightarrow \mu^+\mu^-)} \simeq 3 \sum Q_i^2. \quad (1.5)$$

The value of R for different energy regimes are tabulated in Table 1.1. For different energy regions, the ratio is simple ratios of whole numbers. Since a new channel opens up with

Table 1.1: Predicted values of ratio cross-sections of hadrons to muon pairs production from the electron-positron annihilation for different energy regimes. The m_c , m_b and m_t are the masses of charm quark, bottom quark and top quark respectively .

Predicted value of R	Energy region	Quarks involved
$R = 3[(2/3)^2 + 2(1/3)^2] = 2$	$\sqrt{s} < 2m_c \simeq 3.7 \text{ GeV}$	u, d, s
$R = 2 + 3(2/3)^2 = 10/3$	$3.7 < \sqrt{s} < 2m_b \simeq 10 \text{ GeV}$	u, d, s, c
$R = 10/3 + 3(1/3)^2 = 11/3$	$10 < \sqrt{s} < 2m_t \simeq 350 \text{ GeV}$	u, d, s, c, b

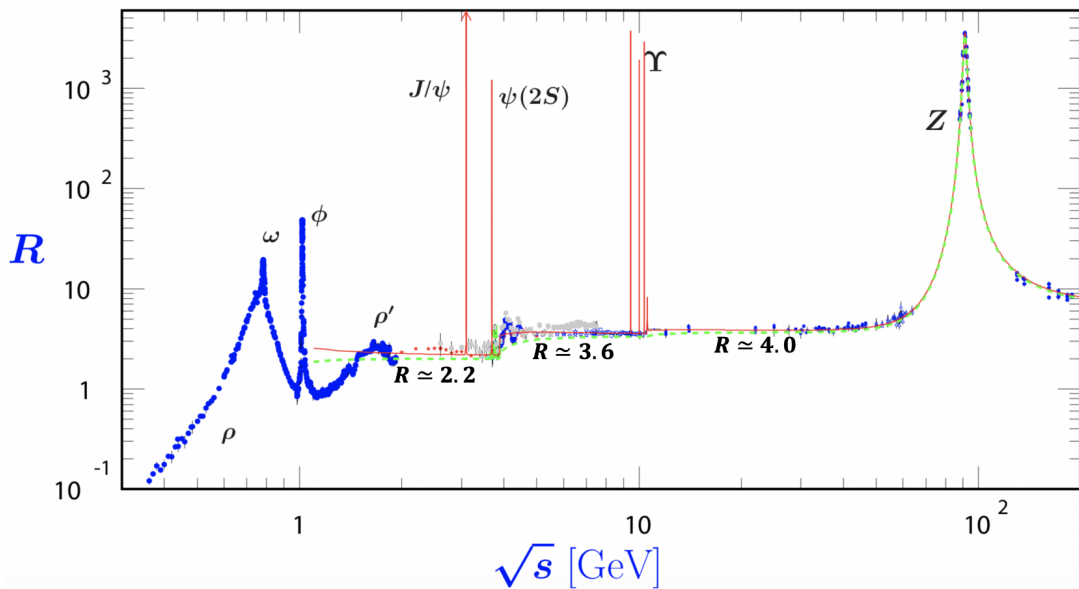


Figure 1.5: The experimental measurement of R as a function of \sqrt{s} . The figure is taken from [10]. The copyright permission for the figure is attached in Figure D.1.

heavier quarks, there is a step in the ratio at each new energy threshold corresponding to each higher quark mass.

The experimental values for the ratio (R) as a function of center of mass energy of collision is as shown in Figure 1.5. The ratio (R) obtained from the experiments shows

the gross features of the theory prediction. It also includes the small steps at the quark thresholds. This consistency in the value of R justifies the introduction of factor "3" in the hadronic cross-section and hence provides a solid evidence of presence of color in quarks. The small deviation of R can be explained by corrections derived in a form of the QCD theory called perturbative QCD, which is the regime of QCD in which the most common kind of field-theory-based analytical calculations can be made. The peaks in the Figure 1.5 are due to the resonant production of bound $q\bar{q}$ pairs.

1.4.2.2 Deep Inelastic Scattering (DIS)

Since the electron is a point particle and we know electromagnetic interactions very well, it can be used as an ideal probe to study the internal structure of nucleons. Elastic scattering of electrons provides the information about the charge and magnetic moment distribution of nucleons in terms of form factors. The elastic cross-section decreases with q^2 (four momentum squared of exchanged virtual photon). At moderate high value of q^2 , inelastic process produces excited states of target proton having same quantum numbers. This process is called resonance. At high q^2 beyond the resonance region, the target proton breaks up into multiple hadrons. In this case, the photon interacts with the charged constituents of the target protons.

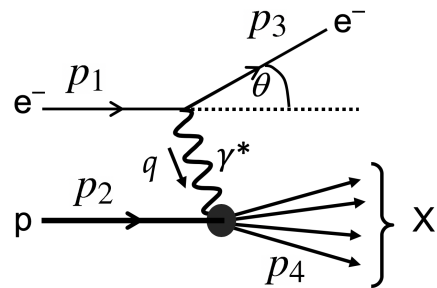


Figure 1.6: Electron-nucleon inelastic scattering. The scattering of electron off the proton results into the bunch of hadrons (X) along with scattered electron.

Kinematic variables:

$*Q^2 \equiv -q^2$, Negative four-momentum squared of virtual photon

$*\nu \equiv \frac{p_2 \cdot q}{M_p} = E_1 - E_3$, the energy lost by electron

$*\text{Bjorken } x: x \equiv \frac{Q^2}{2p_2 q} = \frac{Q^2}{2M_p \nu}$, fraction of momentum carried by *parton*³

$*\text{In-elasticity: } y \equiv \frac{p_2 \cdot q}{p_2 \cdot p_1}$, fraction of energy lost by the electron in scattering process.

Structure Functions:

The electron proton inelastic scattering ($\text{ep} \rightarrow \text{eX}$) cross section mediated by the exchange of virtual photon can be written as in Equation (1.6) [9].

$$\frac{d^2\sigma}{dxdQ^2} = \frac{4\pi\alpha^2}{Q^4} \left[\left(1 - y - \frac{M_p^2 y^2}{Q^2} \right) \frac{F_2(x, Q^2)}{x} + y^2 F_1(x, Q^2) \right], \quad (1.6)$$

where the $F_i(x, Q^2)$'s are the *structure functions* related to inner structure of target proton. In the deep inelastic region, $Q^2 \gg m_p^2 y^2$ ($Q^2 \geq 1\text{GeV}$, "infinite momentum frame") the Equation (1.6) reduces to

$$\frac{d^2\sigma}{dxdQ^2} = \frac{4\pi\alpha^2}{Q^4} \left[(1 - y) \frac{F_2(x, Q^2)}{x} + y^2 F_1(x, Q^2) \right], \quad (1.7)$$

The experimental studies in Stanford Linear Accelerator revealed some interesting properties about the structure functions. In Bjorken limit ($Q^2 \rightarrow \infty$, $\nu \rightarrow \infty$ and constant x), the structure functions are mostly independent of Q^2 . This is called *Bjorken scaling*.

$$F_2(x, Q^2) \rightarrow F_2(x) \text{ and } F_1(x, Q^2) \rightarrow F_1(x),$$

This means no matter how large the momentum is transferred, the resolution doesn't increases. Thus, the Bjorken scaling leads to the fact that there must be some constituents with no substructures inside a proton. This is a clear evidence of the parton (quark) model. Furthermore, the two structure functions are found to be related as

$$F_2(x) = 2xF_1(x).$$

³ Feynman coined the term "parton" to describe the parts of protons before quark model was fully accepted.

This relation is called *Callan-Gross relation* and it reflects the fact that the partons carry spin 1/2. Due to scattering from spin half Dirac particles the magnetic moment is directly related to the charge.

Scaling Violations:

DIS at different values of Q^2 and x were performed at HERA⁴ in Hamburg, Germany. The structure functions measured from experiments in HERA (H1+ZEUS) along with some earlier measurements in various facilities are as shown in Figure 1.7. From the figure, although the structure function is fairly constant for wide range of x values, it is evident that the scaling of structure functions is not exact. For small values of x , the structure functions increases significantly with increase in Q^2 . This implies the increase in number of low- x quarks (quarks with small momentum fraction) with increase in Q^2 . This violation of scaling can be explained by QCD theory by considering the contribution from virtual gluons enriching the number of quarks at the lower x values. Thus, the scaling violation of structure function provides a solid ground for the validation of QCD.

Parton Distribution Function (PDF):

Inside a proton, the quarks interact with each other via exchange of gluons. This results into the distribution of quark momenta within the proton and can be expressed in terms of *parton distribution function*. In deep inelastic regime, the Bjorken x is the fraction of momentum of the proton carried by stuck quark. Hence the momentum distribution of the quarks inside the proton can be extracted from the measurement of the structure function, $F_2(x)$. The structure function can be related to PDF as

$$F_2(x) = x \sum Q_i^2 f_i(x), \quad (1.8)$$

where f_i is the PDF of i^{th} quark for proton and Q_i is its corresponding charge. From the DIS experimental measurements of structure functions, the quarks inside the protons found to be carrying only $\sim 54\%$ of proton's momentum. Thus this is an early indirect evidence

⁴ Hadron-Electron Ring Accelerator operated by Deutsches Elektronen-Synchroton (DESY) laboratory

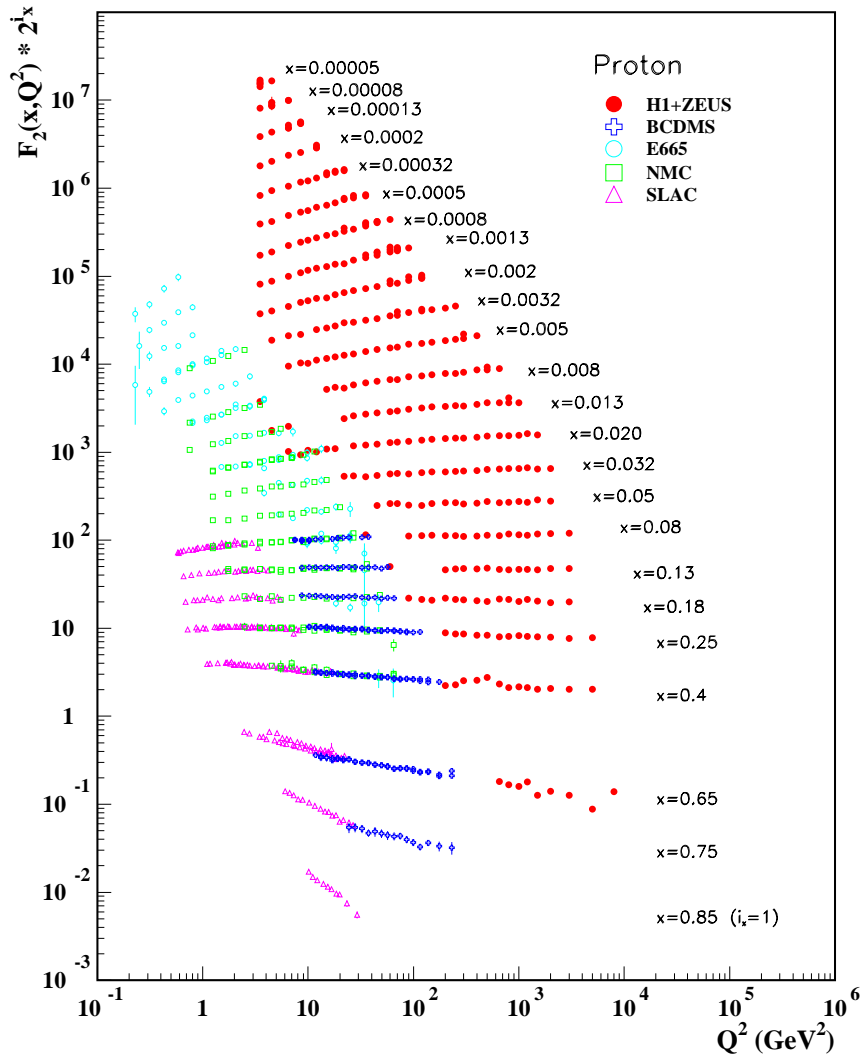


Figure 1.7: Evolution of F_2 with Q^2 for different values of x . The figure is taken from [10].
The copyright permission for the figure is attached in Figure D.1.

of existence of gluons. Since gluon is charge neutral it doesn't take part in QED interaction and hence can not be observed from DIS experiments. The parton distribution functions for proton from various other experiments along with DIS is shown in Figure 1.8.

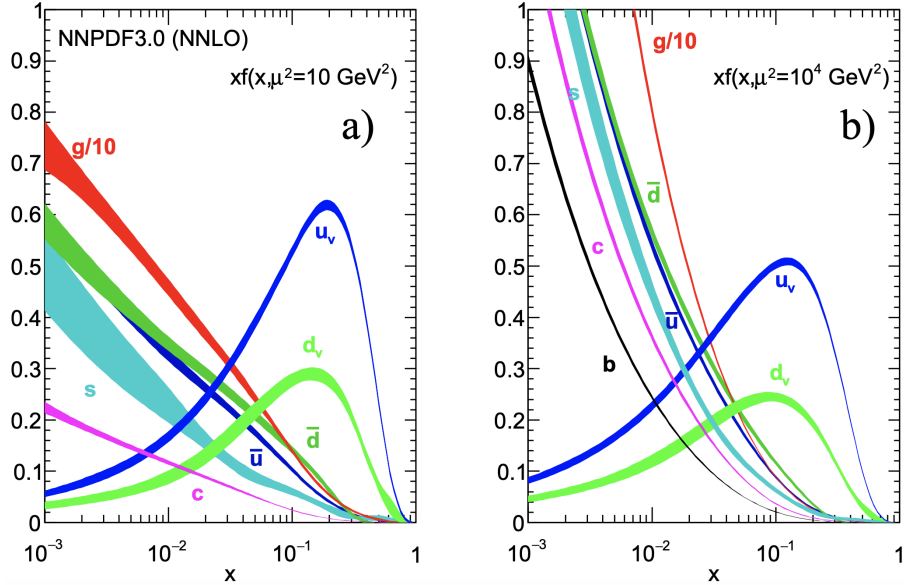


Figure 1.8: The proton PDFs from NNLO NNPDF3.0 global analysis [11] at $Q^2 = 10 \text{ GeV}^2$ (left) and $Q^2 = 10^4 \text{ GeV}^2$ (right). The figure is taken from [10]. The copyright permission for the figure is attached in Figure D.1.

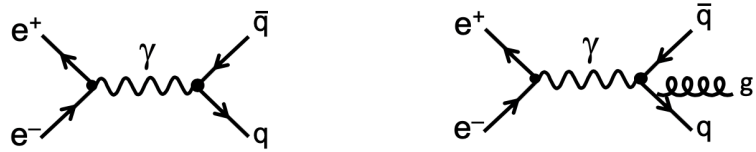


Figure 1.9: Feynman diagram for annihilation of electron-positron into quark anti-quark pairs (left) and into quark, anti-quark and gluon (right).

1.4.2.3 Evidence of gluons

As described in the Section 1.4.1, the two back to back jets of hadrons are observed as final state particles in case of $e^+ + e^- \rightarrow q + \bar{q}$ process. But the events with 3 jets were also observed in the electron-positron annihilation process. This appearance of the third jet can be explained by QCD process: $e^+ + e^- \rightarrow q + \bar{q} + \text{gluon}$. The gluon radiated

(gluon bremsstrahlung) from the outgoing quark is responsible for the third jet. Thus, the appearance of the third jet in electron-positron annihilation provides evidence for the existence of gluons.

1.4.3 QCD Calculations

The Lagrangian of QCD can be expressed as [10],

$$L = \sum_q \bar{\psi}_{q,a} (i\gamma^\mu \partial^\mu \delta_{ab} - g_s \gamma^\mu t_{ab}^C A_\mu^C - m_q \delta_{ab}) \psi_{q,b} - \frac{1}{4} F_{\mu\nu}^A F^{A\mu\nu}, \quad (1.9)$$

where repeated indices are summed over. The $\psi_{q,a}$ are quark-field spinors for a quark of flavor q and mass m_q . a is color index which runs from 1 to 3. The γ^μ are Dirac γ -matrices. The A_μ^C gives the gluon fields, where C runs from 1 to 8 (representing 8 types of gluons). This term appears in the QCD Lagrangian because of the self interacting nature of gluons. The t_{ab}^C ($\equiv \lambda_{ab}^C/2$, Gell-Mann matrices) are eight 3×3 matrices, which are the generators of the SU(3) group. The term g_s is related to QCD coupling constant ($\alpha_s = \frac{g_s^2}{4\pi}$). And, the $F_{\mu\nu}^A$ is the field tensor given as,

$$F_{\mu\nu}^A = \partial_\mu A_\nu^A - \partial_\nu A_\mu^A - g_s f_{ABC} A_\mu^B A_\nu^C. \quad (1.10)$$

where f_{ABC} are the structure constants of the SU(3) group.

1.4.3.1 Running of α_s and Asymptotic Freedom

The scale (energy scale of the interaction) dependent QCD coupling constant is determined by re-normalization⁵ group equation,

$$Q^2 \frac{\partial \alpha_s}{\partial Q^2} = \beta(\alpha_s), \quad (1.11)$$

From one loop approximation,

$$\alpha_s(Q^2) = \alpha_s(\mu^2) \frac{1}{1 + \alpha_s(\mu^2) b \ln(\frac{Q^2}{\mu^2})}, \quad (1.12)$$

⁵ Re-normalization: Technique used in quantum field theories to take care of the infinities arising when dealing with beyond the leading order Feynman diagrams. Generally, immeasurable bare quantities are introduced to absorb those infinities.

where μ is re-normalization scale and

$$b = \frac{11N_c - 2n_f}{12\pi}.$$

N_c is the number of colors and n_f is number of quarks flavors at the energy scale (Q). Unlike in QED (where the coupling constant increases with momentum transfer), the Equation (1.12) shows the decrease of α_s with the momentum transfer Q^2 , referred as running of strong coupling constant. Following two scenarios come into play in case of QCD;

1. Just like in QED, vacuum polarization creates quark-antiquark loops in gluon propagator which shield the color charge of the target.
2. Unlike in QED, the coupling of gluons between themselves introduces gluon loops, which reinforces the color charge of the target instead of shielding it.

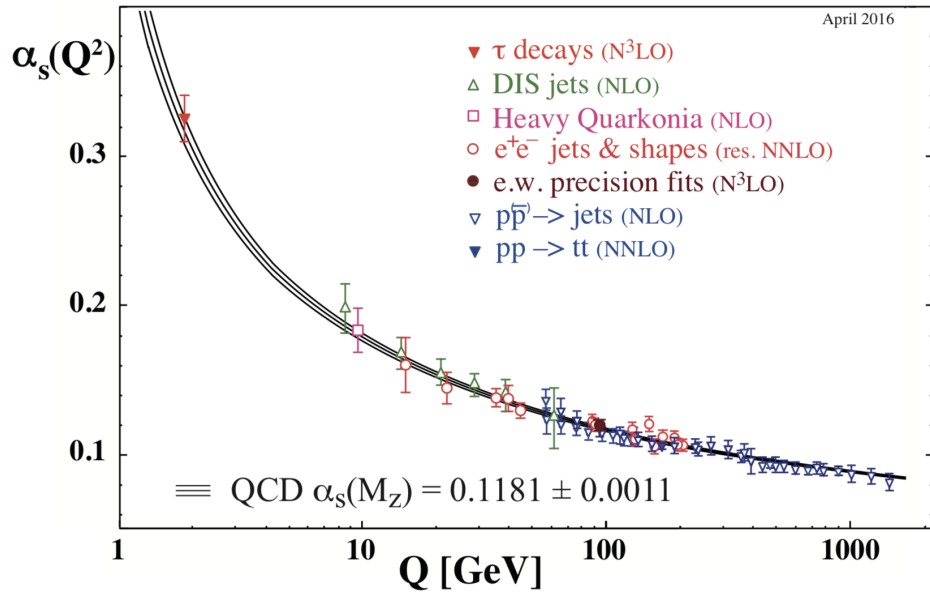


Figure 1.10: The measurements of α_s as a function of energy scale, Q . The figure is taken from [10]. The world average of the α_s at the Z boson mass scale is also shown in the figure. The copyright permission for the figure is attached in Figure D.1.

Therefore, as the distance (decrease the momentum transfer) between the target quarks is increased, the quark-antiquark loops shield the color charge and decrease the coupling between the target while the gluon loops have the opposite effect. Because of the large number of gluons and their zero mass, gluon loop dominates the strong vacuum polarization. Thus the coupling constant increases with increase in distance (decrease in momentum transfer). The world measurements of α_s as a function of momentum transfer as shown in Figure 1.10 are in very good agreement with the QCD calculations. Because of the nature of the coupling strength in QCD, quarks behave like a free particle (de-confined) at a very small length scale (very high energy scale). This characteristic is known as *asymptotic freedom*.

1.4.4 Perturbative QCD (pQCD) and Factorization

Since the α_s decreases with increase in the momentum transfer, just a few Feynman diagrams after leading order are enough to describe any process at high momentum transfer (where $\alpha_s \ll 1$) precisely enough. This perturbation method, where the higher order correction term can be neglected, is valid for all the regions in QED (because of small coupling constant) while for QCD, it is only valid for high momentum transfer region i.e. hard scattering processes.

According to a "factorization theorem" [53], the cross section of hard scattering in a nuclear collision involving jets of hadrons as final state particles factorizes into three basic parts; parton distribution function, partonic cross sections and fragmentation functions. The cross section of A and B nuclei colliding into final state hadrons is given as Equation (1.13).

$$\begin{aligned} d\sigma_{AB \rightarrow h} &= \text{Initial State nPDF} \otimes \text{pQCD} \otimes \text{Final State} \\ &= \sum_{a,b,c} \int dx_a dx_b dz f_a(x_a) f_b(x_b) d\hat{\sigma}_{ab \rightarrow c}(x_a, x_b, Q^2) D_c^h(z), \end{aligned} \quad (1.13)$$

where $f(x)$ s are the parton distribution functions and can be measured from DIS process. The Bjorken x is the momentum fraction of the colliding particles carried by each colliding partons (a, b). The $d\hat{\sigma}$ is differential partonic cross section. It describes the binary collisions

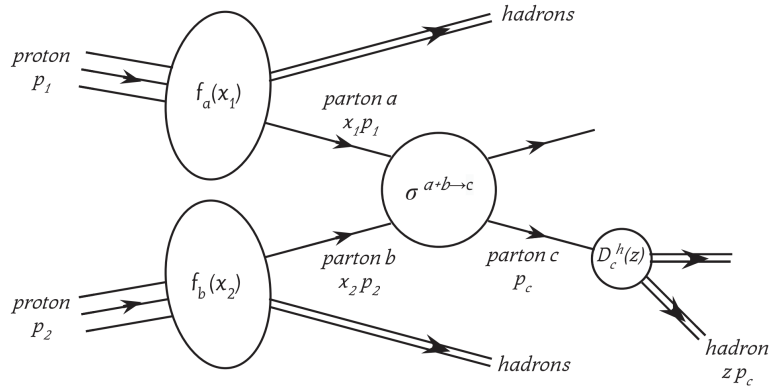


Figure 1.11: Diagram showing the three elements of pQCD factorization: parton distribution functions, partonic cross sections and fragmentation functions. The figure is taken from [12]. The copyright permission for the figure is attached in Figure D.2.

between partons and can be calculated from the corresponding Feynman diagrams. The last term, $D_c^h(z)$, is the *fragmentation function*. This represents the probability for an outgoing parton (c) to yield a hadron (h) with momentum fraction, $z \equiv p_h/p_c$. The p_h and p_c are the momentum of hadron and parton respectively.

1.4.5 Lattice QCD (LQCD)

The QCD coupling constant is large ($\alpha_s \sim 1$) at low energy scales. So, the perturbation approach can not be used for QCD process in this energy regime. Hence Lattice QCD theory of QCD is used which doesn't require the perturbative approach. In Lattice QCD, the quantum mechanical calculations are made by replacing space-time continuum by a mesh of equidistant discrete points, similar to crystal lattice. Color fields are restricted on the site of lattice while gluons fields are included on the links, and the configuration of QCD is calculated like a Monte Carlo simulation. As the lattice spacing goes on decreasing ($a \rightarrow 0$), the continuous space-time is recovered. The divergences inherent in perturbative QCD are regularized by introducing a lower limit on momentum transfer of the order of $1/a$. The calculations in lattice QCD requires tremendous computing resource and advance

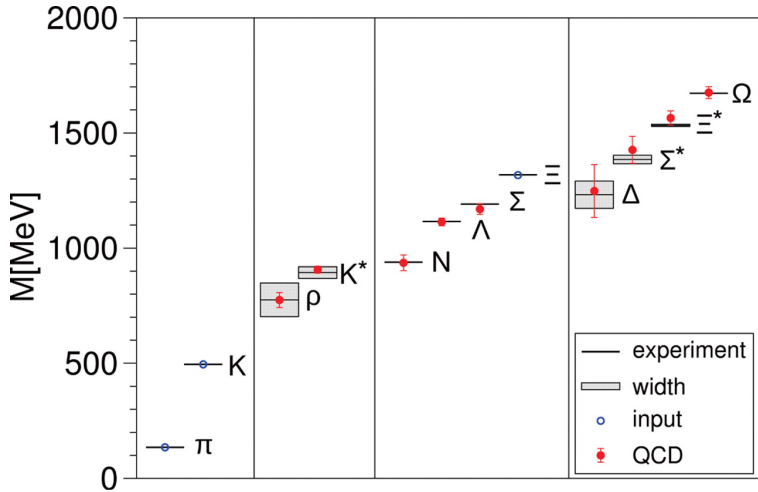


Figure 1.12: The light hadron spectrum of from LQCD calculations. The solid circles are results. Horizontal lines and bands are the experimental values with their decay widths. The combination of statistical and systematic errors are shown by vertical error bars. The figure is taken from [13]. The copyright permission for the figure is attached in Figure D.3.

computational techniques. Lattice QCD calculations correctly predicts the masses of light hadrons as shown in Figure 1.12.

1.5 Quark Gluon Plasma (QGP)

We already discussed about how the quarks are always confined in the hadrons no matter how much we try to separate them and how they behave like free particle at very high energy scale. So, what would happen when temperature and baryon density are increased towards the asymptotic freedom limit? At high enough temperature or pressure, it was predicted that the hadrons dissolves into a new state of matter where the quarks and gluons become relevant degree of freedom [54]. This state of nuclear matter is later on called, *Quark Gluon Plasma* (QGP). According to STAR collaboration, “The QGP is a locally (thermally) equilibrated state of matter in which quarks and gluons are deconfined from hadrons, so that color degrees of freedom become manifest over nuclear, rather than nucleonic volumes” [55].

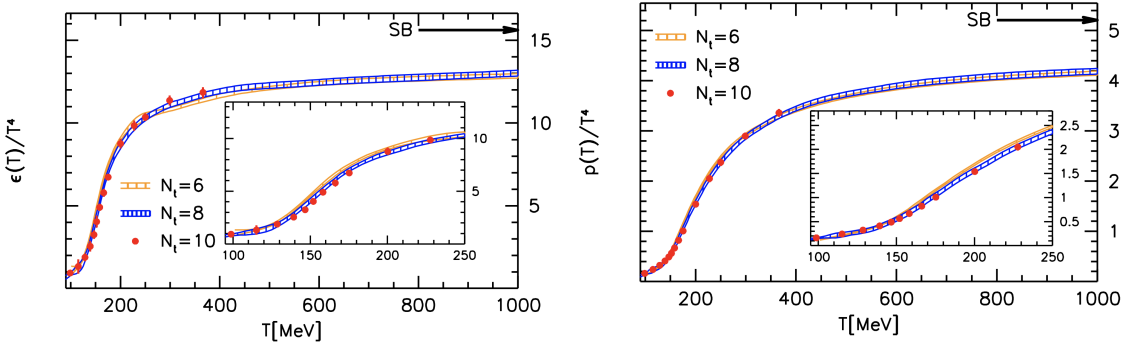


Figure 1.13: Energy density (left figure) and pressure (right figure) normalized by T^4 as a function of temperature (T) on number of lattice points (N_t) in temporal direction. The Stefan-Boltzmann (SB) limit are indicated by an arrow in both figures. The figures are taken from [14]. Copyright permission for the figures is attached in Figure D.4.

Lattice calculations predicting this transition from confined to deconfined matter in QCD are shown in Figure 1.13. Both the energy density (ϵ) and pressure (p) show sudden rise at critical temperature $T_c \approx 170$ MeV ($\approx 10^{12}$ K) indicating an increase in degree of freedom or entropy because in the Stefan-Boltzmann limit, the quantity plotted can be directly related the numbers of types of constituents of the matter, which is much more for the quarks and gluons rather than hadrons. The critical temperature corresponds to the energy density $\epsilon_c \approx 1 \text{ GeV}/\text{fm}^3$, which is an order of magnitude greater than that of normal nuclear matter. The plateaus of both energy density and pressure lie just below the Stefan-Boltzmann limits of an ideal quark/gluon gas ie from quark/gluon state counting. This indicates the system is strongly coupled instead of being a non-interacting ideal gaseous state.

A schematic phase diagram of nuclear matter over a range of temperature and baryon chemical potential is as shown in Figure 1.14. The exact order of the phase transition is not known yet. The phase transition for low baryon densities and high temperature is expected to be of second order while at high densities and lower temperature it is expected to be of

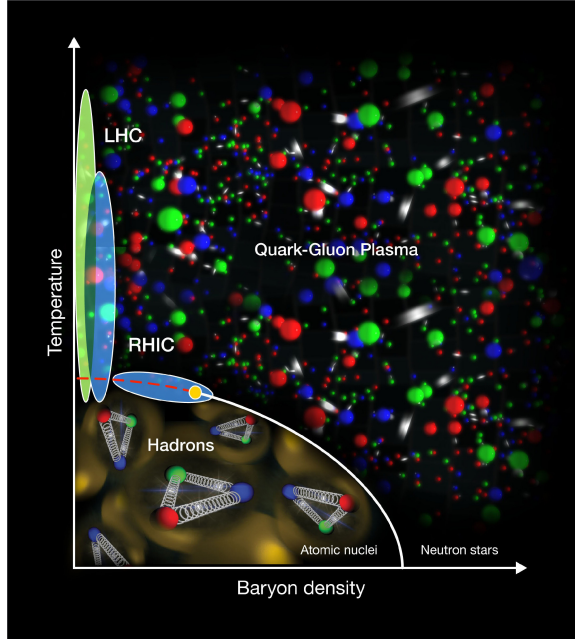


Figure 1.14: QCD phase diagram mapping out different phases of nuclear matter expected to exist. The lines in the diagram are just an educational guess. The figure is taken from [15]. Courtesy Brookhaven National Laboratory. The copyright permission to use the figure is attached in Figure D.5 and Figure D.6.

first order. Exact positions of the critical points and critical lines are yet to be determined. The quantitative mapping of the QCD phase diagram is an active ongoing research area.

1.6 Relativistic Heavy Ion Collision

The kinematic variables and the jargon used to describe the heavy ion collisions are discussed in Appendix [A].

As discussed before, the quark-gluon plasma or QGP is considered as a primordial form of matter, which existed for only a few microseconds after the birth of the Universe, and it is the root of various elements in the present Universe. Due to the lots of backgrounds from later stages of the Big-Bang, it is not possible to trace back the signals of QGP from the early universe. However, the condition to produce such a state of matter can be achieved

by relativistic (near the light-speed) collisions of heavy ions⁶ with accelerators. These collisions are sometimes called "little bang"'s. In such collisions, the colliding nuclei are Lorentz-contracted in the shape of "pancakes". For center-of-mass energy per nucleon greater than 10 GeV, the high energy density and high temperature with low baryon density condition is achieved to form QGP. The Large Hadron Collider (LHC) at CERN and the Relativistic Heavy Ion Collider (RHIC) are two current accelerators capable of such collisions to produce QGP. The stages of relativistic heavy ion collision are shown in Figure 1.15; initial state, thermalization, QGP, hadronization, hadron gas and freeze-out.

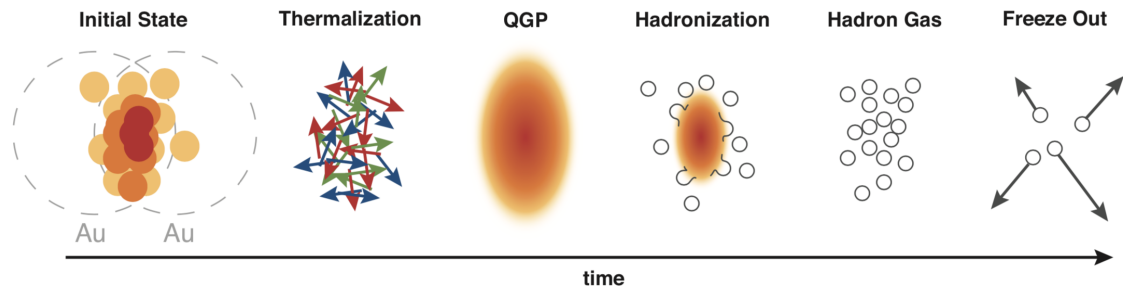


Figure 1.15: Schematic of stages in relativistic heavy ion collisions. The figure is taken from [16].

The *initial state* refers to the information of nucleons of colliding nuclei. The initial state of the colliding nucleons has an important role in the deposition of initial energy and its subsequent evolution. Among many different methods to construct initial state, the Glauber model [34] and the Color Glass Condensate [56] models are two commonly used ones.

In the collision process, the two colliding nuclei pass through each other within very short time scale ($\sim 0.1 fm/c$). A large amount of energy is deposited in the colliding region producing a high-energy-density fireball (sometimes, called *glasma* [56]). The energy deposition is localized but not thermalized. After that, multiple interactions of partons

⁶ Heavy atomic nuclei obtained by stripping electrons from atoms.

in the fireball thermalizes itself into a state of QGP. The QGP then expands, cools down, gets diluted and eventually undergoes hadronization. In heavy-ion collision, hadronization takes place via two different process; *recombination* and *fragmentation*. Recombination occurs when colored partons in deconfined phase get combined with each other to form colorless bound hadrons. The hadronization from the fragmentation of high p_T partons into jets of hadrons is already discussed in section 1.4.1, and similar fragmentation processes are expected to occur down to rather low energy. Thus formed hadrons, if produced in sufficient density, can also behave collectively and hence are called *hadron gas*. These stages of evolution can be explained by relativistic fluid dynamics [57], commonly called "hydro", along with the QCD equation of state extending for hadronic and partonic phases [58] taken from Lattice QCD calculations.

Finally, as expansion increases, collisions between the hadrons drop. *Chemical freeze out* occurs once inelastic collisions of hadrons ceases. After the chemical freeze out, there will be no change in hadronic composition. Finally, *kinetic freeze out* occurs once the elastic collisions of hadrons ceases and the hadrons travel through the detectors to be detected as final state particles. The Boltzmann equation in relativistic transport theory can be used to explain this stage of evolution in heavy ion collisions [59].

1.7 Signatures of Quark Gluon Plasma

As the QGP formed in heavy-ion collisions lasts for very brief amount of time ($\sim 5\text{--}10\text{ fm}/c$) and is of a few femtometers in diameter, it is difficult to observe. One mostly has to do the study of final state particles detected in detectors to extract the properties of the QGP. Many signatures of QGP have been observed from the data of heavy ion collisions. Among them, elliptic flow and jet quenching are the most important and also most relevant to this analysis. In the following sections are descriptions of those two signatures along with some other commonly studied signatures in heavy ion field.

1.7.1 Hydrodynamic Flow

Flow is the collective expansion of particles produced in the collision, usually referring to flow of the QGP before it hadronizes into final state particles. The azimuthal anisotropy of particle production in non-central collision can be explained with the anisotropic flow of QGP medium. A non-central collision has an almond-shaped transverse overlapping region where the energy deposition is not azimuthally symmetric. When the system expands, particles moving "in-plane" (in the "reaction plane" which is the plane containing the two colliding centers of masses at all times before the collision) are boosted compared to the out-of plane due to the difference in pressure gradient. This is illustrated in Figure 1.14. Thus, anisotropy in the initial state geometry drives final state momentum space anisotropy. The azimuthal distribution of particles produced with respect to the reaction plane can be expressed in a Fourier expansion [60] as:

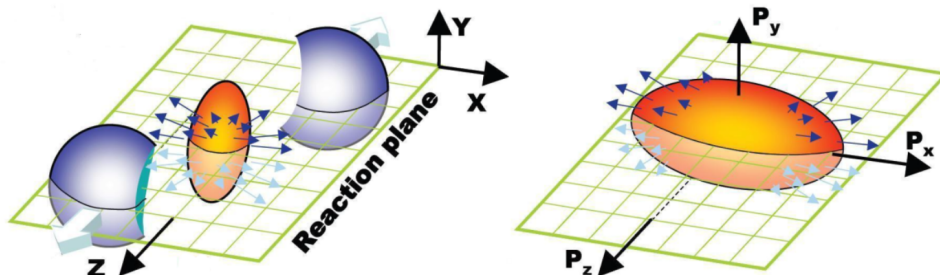


Figure 1.16: Left: The almond shaped interaction region for a non-central collision is formed by participant nucleons. The green grid is reaction plane. Beam direction is along the z-axis and blue regions are spectator nucleons. Right: Momentum anisotropy of final state particles due to non-central collision. Figure is taken from [17]. The copyright permission for the figure is attached in Figure D.7. Courtesy PHENIX collaboration.

$$E \frac{d^3N}{d^3p} = \frac{d^2N}{2\pi p_T dp_T dy} \left(1 + \sum_{n=1}^{\infty} 2v_n \cos[n(\phi - \Phi_R)] \right), \quad (1.14)$$

where ϕ is the azimuthal angle, E the energy, p the momentum, p_T the transverse momentum, y the rapidity and Φ_R the reaction plane angle. The rapidity is defined as $y = \frac{1}{2} \ln \left(\frac{E+p_z}{E-p_z} \right)$, with p_z being longitudinal momentum. The high relativistic equivalent of rapidity is pseudorapidity (η). Since the differences in y and in η are Lorentz invariant, the difference is used to measure the angles between the particles boosted along the beam direction. The reaction plane is defined by the impact parameter (in the X-direction in this case) and beam axis (Z-direction) as shown in Figure 1.16. The sine terms in the Fourier expansion disappear due to reflection symmetry with respect to reaction plane. The Fourier coefficients are given as:

$$v_n(p_T, y) = \langle \cos[n(\phi - \Phi_R)] \rangle. \quad (1.15)$$

The average in Equation (1.15) is taken for the particles in the (p_T, y) bin. These flow

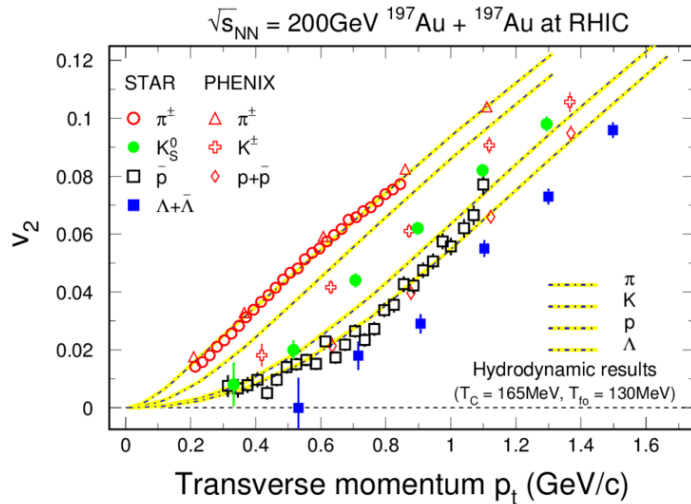


Figure 1.17: Comparison of STAR and PHENIX measurements of elliptic flow for different particle species with hydrodynamic models prediction. The figure is taken form [18]. The copyright permission for this figure is attached in Figures D.8 and D.9.

coefficients, v_n , depend on the colliding nuclei's mass, species of particle & their transverse

momentum, beam energy and rapidity (y). The first harmonic coefficient, v_1 , is called direct or radial flow while second harmonic coefficient, v_2 , is called *elliptic flow*, v_3 is called *triangular flow*. Elliptic flow, v_2 , is most dominant among the coefficients. Some v_n have components that are on average even or odd behavior in rapidity. For these components, typically v_n is an odd (even) function rapidity if n is odd (even), so for example much of the v_1 coefficient vanishes at mid-rapidity regions. The PHENIX and STAR⁷ measurements of v_2 for different particle species as a function of p_T are as shown in Figure 1.17. The v_n measurements are successfully described by the hydrodynamical model calculations [61]. This confirms the formation of an almost perfect liquid (meaning having nearly zero viscosity), which is also a signature of the QGP due to its strongly-interacting nature.

Due to fluctuations in the positions of nucleons in each collision, instead of estimating the actual reaction plane angle itself, "event plane" angles which vary with each harmonic are estimated and used in Equation 1.15. These angles are defined as:

$$\Psi_n = \frac{1}{n} \left(\tan^{-1} \frac{\sum_i w_i \sin(n\phi_i)}{\sum_i w_i \cos(n\phi_i)} \right), \quad (1.16)$$

where w_i is the weight factor and the summation is over i th particle. The particle p_T is often used as weight factor.

1.7.2 Jet Quenching

In relativistic heavy ion collisions, the hard scattering of partons occurs before the formation of the QGP. High transverse momentum partons from the hard scattering, are typically produced in back-to-back directions in the center-of-mass reference frame then fragment into collimated sprays of hadrons, called jets. The interaction of jets and the dense nuclear medium leads to jet energy loss. Thus, the production of such jets in heavy ion collisions are found to be suppressed compared to that in proton-proton collisions. This phenomenon of suppression of jet, also known as jet quenching, provides an important evidence of dense matter (i.e. QGP) created in heavy ion collisions. There are many jet

⁷ Both PHENIX and STAR are experiments at RHIC (Relativistic Heavy Ion Collider) in Brookhaven National Lab and are described in section 2.1 of "The Experiment" chapter.

reconstructing algorithms available to extract jets from the beds of background. Standard algorithms such as the *Anti- k_t algorithm* [62] and ones newly developed for Heavy Ion collisions such as the *Gaussian filter algorithm* [63] are commonly used in the heavy ion community.

1.7.2.1 Nuclear Modification Factor (R_{AA})

One of the most important and commonly used observables of jet quenching is the suppression of the single inclusive hadron yield at high p_T in nucleus-nucleus collisions as compared to that in proton-proton collisions. Such nuclear modification effect can be quantified in terms of the nuclear modification factor, R_{AA} , as in Equation (1.17).

$$\begin{aligned} R_{AA} &= \frac{\text{Yield in AA}}{\langle N_{coll} \rangle \text{ Yield in pp}} \\ &= \frac{d^2N/dp_T dy_{AA}}{\langle N_{coll} \rangle_{AA} d^2N/dp_T dy_{pp}} \end{aligned} \quad (1.17)$$

where $\langle N_{coll} \rangle$ is the mean number of nucleon-nucleon collisions in a single nucleus-

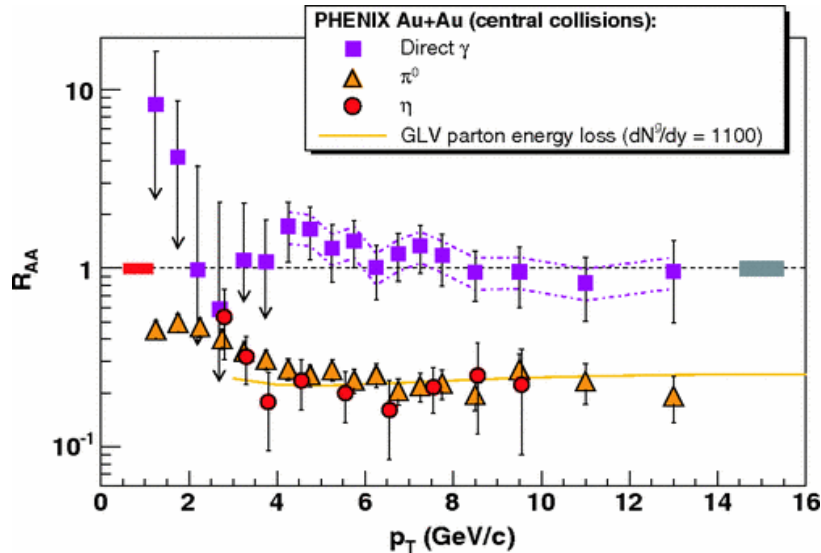


Figure 1.18: R_{AA} vs. p_T in central $Au + Au$ collision at $\sqrt{s_{NN}} = 200\text{GeV}$ for direct photon (blue), π^0 (orange) and η (red). This figure is taken from [19]. The copyright permission for this figure is attached in Figure D.10.

nucleus collision. It is related to the inelastic cross-section for nucleon-nucleon collision (σ_{NN}) and nuclear thickness function ($< T_{AB} >$) as in Equation 1.18.

$$< N_{coll} >_{AA} = < T_{AA} > \times \sigma_{NN}, \quad (1.18)$$

$< T_{AA} >$ and $< N_{coll} >_{AA}$ are extracted from Glauber Model of Monte Carlo simulation [64].

The R_{AA} is expected to be unity above certain p_T (i.e. hard scattering regime), if the nucleus-nucleus collision is simply a superposition of the nucleon-nucleon collisions. In Figure 1.18, the high p_T yield of π^0 and η shows suppression by around a factor of 5 while direct photon yields show no suppression. This indicates the presence of QGP medium in Au+Au collision. i.e. the partonic jets interact with colored medium causing the energy loss. The non-suppression of direct photons can be taken from the fact that they only interact electromagnetically and hence they don't interact with QGP.

1.7.2.2 Two Particle Correlation

The two particle correlation method is extensively used in this analysis. The details of this method is explained in Section 4.1. The following is very brief description of the method.

With the consideration of two back to back jets, the correlation between the two final state particles can be used to study the jet quenching behavior in heavy ion collisions. In this method, the distribution of two final state particles (trigger and partner) are studied relative to their azimuthal angular difference. Among the two particles, the trigger particle is chosen to have relatively higher p_T than second partner particle . Due to the back-to-back jets, distribution of particles is expected to form peaks around the azimuthal difference of 0 and π . The Figure 1.19 shows the di-hadron correlations for different collision systems at STAR. The near side peaks (around $\Delta\phi = 0$) in Figure 1.19 are present in all the systems while the away side peak (around $\Delta\phi = \pi$) is clearly suppressed for the Au+Au. This shows the evidence of the QGP in Au+Au system.

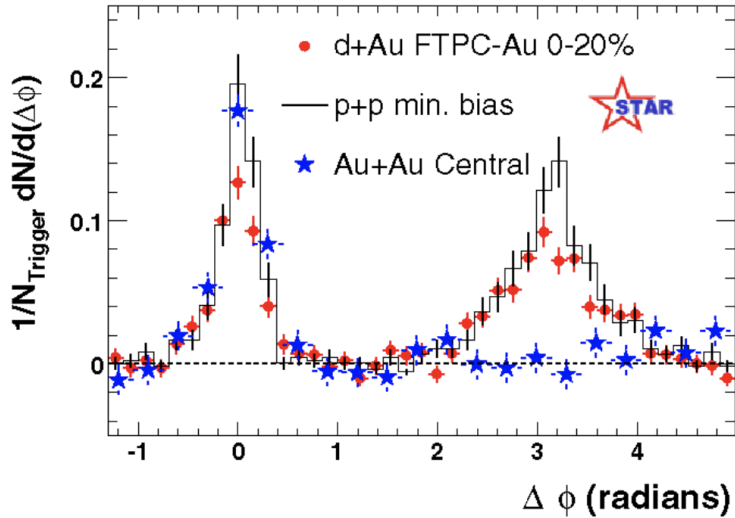


Figure 1.19: Di-hadron azimuthal correlations for $p+p$ (black), $d+Au$ (red) and $Au+Au$ (blue) collisions in STAR. Trigger particles with $4 < p_T^{trig} < 6$ GeV and associated particles with $2 < p_T^{assoc} < p_T^{trig}$ GeV are used for correlation. This figure is taken from [20]. The copyright permission for the figure is shown in Figure D.11

1.7.2.3 Fragmentation Function Ratio

Even-though the R_{AA} measurement of reconstructed jets confirms the jet quenching due to the medium, study of jet substructures is needed to find out how do the jets interact with medium. The fragmentation function ratio helps to find out how the jet fragmentation is affected by the medium. The fragmentation function (introduced in section 1.4.4) can be defined as in Equation 1.19.

$$D(z) = \frac{1}{N_{jet}} \frac{dN_h}{dz} \quad (1.19)$$

where $z = p_T^{hadron}/p_T^{jet}$ is the momentum fraction carried out by hadron fragmenting from the jet. The fragmentation function measurement helps to probe the inner structures of jets. It usually depends very little on the producing collision system and is only a property of the outgoing source parton. But in the QGP, fragmenting partons lose energy via radiation while traversing the medium and hence fragment at lower energy which creates a deficit

of both jets and possibly high z fragments, and an enhancement of low z fragments. Thus the modification of the fragmentation function of heavy ion collisions compared to proton-proton collision gives the evidence of presence of QGP in the heavy ion collisions.

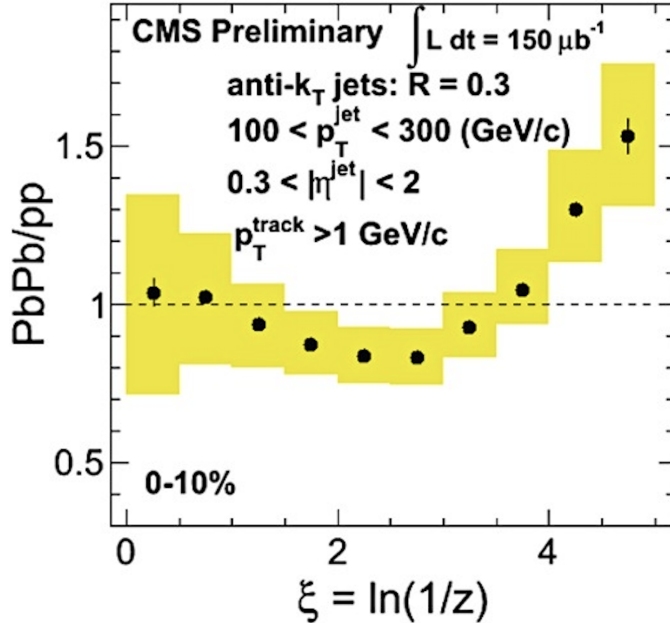


Figure 1.20: The fragmentation function ratio of most central Pb+Pb collisions to $p+p$ collisions. This figure is taken from [21]. The copyright permission for this figure is attached in Figure D.12.

The Figure 1.20 shows the CMS⁸ measurement of ratio of fragmentation function in Pb+Pb to that in $p+p$. The ratio is plotted as a function of $\xi = \ln(1/z)$ for the better visualization in low z region. The ratio shows the slight enhancement in low ξ , suppression in medium ξ and large enhancement in high ξ . The small enhancement in low ξ is thought to be due to the bias of jet reconstructing algorithms towards the non-suppressed jets or otherwise different quark-gluon averaging in the A+A jet sample. The high and medium ξ modification are due to the medium modification, suppression and enhancement, described above.

⁸ Compact Muon Solenoid detector at Large Hadron Collider (LHC)

1.7.3 Quarkonia

Quarkonium is a meson of heavy quark and its own anti-quark. Charmonium ($c\bar{c}$, also called J/ψ meson) and Bottomonium ($b\bar{b}$) are two families of quarkonium. The quarkonia are produced in early stage of heavy ion collisions. Due to the screening of strong interaction in a deconfined medium, the quarkonia states are dissociated. Thus, the suppression of production of quarkonia in heavy ion collisions compared to $p+p$ collisions [65] is taken as the signature of QGP. In addition, there are several quarkonium states with very different binding energies. These various quarkonium states dissociates in the sequence of their binding energies given a certain distribution of thermal energy of the QGP. Thus, this sequential melting of the quarkonium states could be considered as a "thermometer" of the medium.

1.7.4 Strangeness Enhancement

In QGP, the temperature is high enough for the abundant production of strange quark and its anti-quark. Also, large gluon density favors the gluon fusion leading to the production of strange quark and anti-quark pairs ($gg \rightarrow s\bar{s}$). Therefore, the production of strange particles is enhanced in the relativistic heavy ion collision compared to the nucleon-nucleon collisions. The strangeness enhancement in heavy ion collisions in ALICE and STAR experiments is shown in Figure 1.21. The production of strange baryons (Ω , Ξ and Λ) increases as the mean number of participating nucleons increases.

1.7.5 Constituent Quark Number Scaling

The universal curve of elliptic flow for all of mesons and baryons when scaled with quark number implies that the hydrodynamic flow originates at the quark level and hence proves the deconfinement. This scaling also proves the fragmentation (at high p_T) and recombination (at medium p_T) methods of hadronization in relativistic heavy ion collisions. The Figure 1.22 shows the constituent quark number scaling of elliptic flow for different hadrons from STAR and PHENIX experiments. The left two plots show two groups of

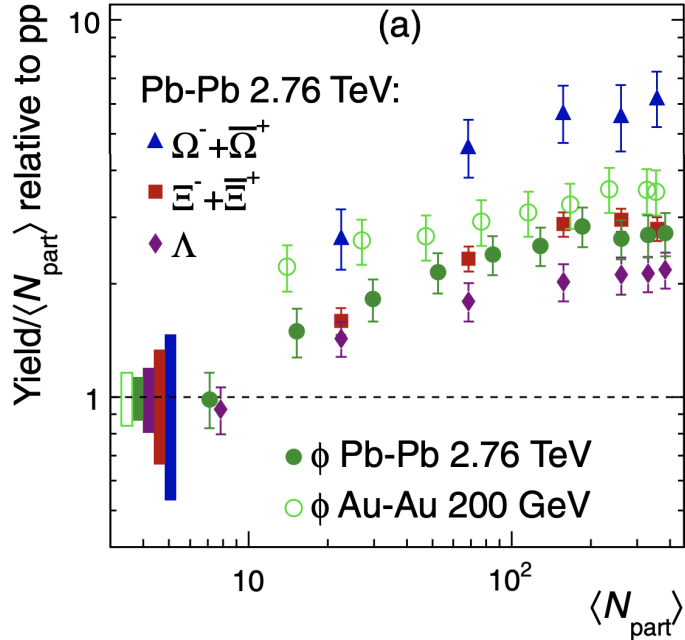


Figure 1.21: Enhancement of production of strange baryon as a function of mean number of participating nucleons in nucleus-nucleus collisions $\langle N_{part} \rangle$. The figure is taken from [22] (An article available under the terms of the Creative Commons Attribution 3.0 License).

hadrons (baryon and meson) while after scaling the two groups fall into a single group as shown in right two plots.

1.8 Cold Nuclear Matter Effects

The quark-gluon plasma (QGP) is believed to be absent in normal proton-proton ($p+p$) collisions. Thus, $p+p$ collisions are analyzed and used as a baseline measurement with respect to heavy ion collisions, where QGP is believed to be formed. Light-heavy ion collisions like proton-gold ($p+Au$) or deuteron-gold ($d+Au$), where the energy density was traditionally considered to be too low to create QGP, are also studied. These light-heavy ion collisions and $p+p$ collisions are also called *small system collisions*. This study helps to isolate any influences on the final observables due to additional nuclear matter effects

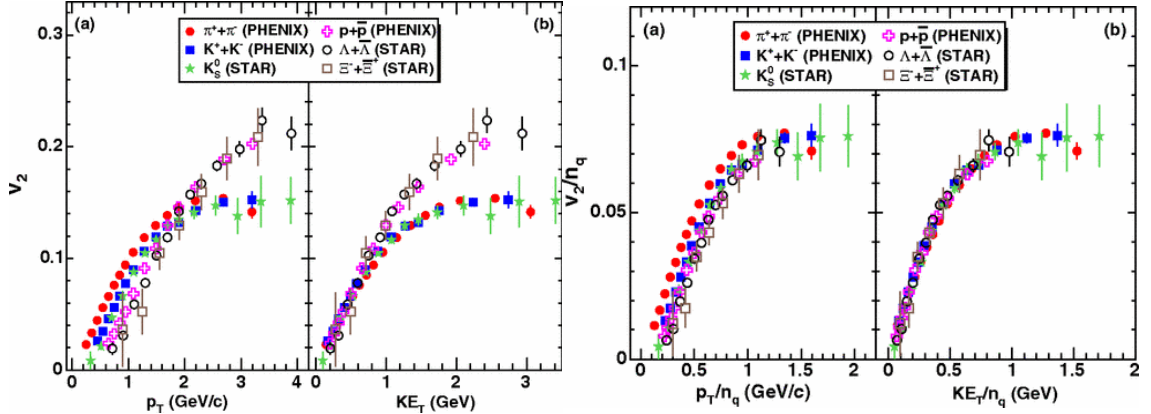


Figure 1.22: Elliptic flow, v_2 , vs transverse momentum and kinetic energy before (left two plots) and after (right two plots) scaled with number of quarks. The figures are taken from [18]. The copyright permission for this figure is attached in Figures D.8 and D.9.

compared to $p+p$ collision. All of those effects are called "cold nuclear matter" effects and the collisions were originally considered "control" experiments to the more usual A+A large heavy ion collisions. Generally, $p+Au$ in RHIC and $p+Pb$ in LHC are still taken mostly as such control experiments. However as will be shown, related to one of the main goals of this thesis, recently some QGP-like effects have been observed in light-heavy systems.

1.8.1 Nuclear Modification of Parton Distribution

We already discussed about the parton distribution function (PDF) of nucleons in Section 1.4.2.2. But, the PDF of a nucleus is not just the sum of the PDFs from the constituent nucleons. The modification of the nuclear parton distribution function (nPDF) can be quantified by the ratio of PDF of the nucleus to that of the proton as in Equation (1.20).

$$R_i^A(x, Q^2) = \frac{f_i^A(x, Q^2)}{f_i(x, Q^2)}, \quad (1.20)$$

where, $f_i(x, Q^2)$ is the PDF of parton of flavor i inside free proton and $f_i^A(x, Q^2)$ is the PDF of parton flavor i inside a nucleus with atomic mass number A .

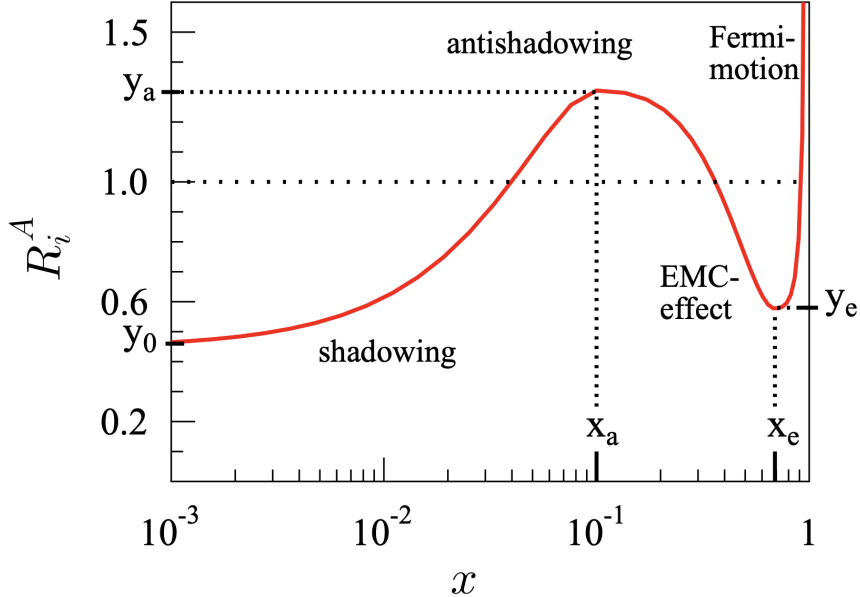


Figure 1.23: Different modification regions for parton distribution functions . The figure is taken from [23]. The copyright permission for the figure is shown in Figure D.13.

- **Shadowing Effect:**

At low- x region ($x \lesssim 0.04$), parton densities of nucleus is suppressed relative to the free proton. This phenomenon is called the *shadowing effect*. This effect is probably due to the destructive interference between the wave function of partons in different nucleons. Because of gluon abundance at low- x , shadowing effect is more pronounced for gluons.

- **Anti-shadowing Effect**

At intermediate- x region ($0.04 \lesssim x \lesssim 0.3$), parton densities of nucleus is enhanced relative to the free proton. This phenomenon is called *anti-shadowing effect*. This effect is probably due to the constructive interference between the wave functions of partons in different nucleons.

- **EMC Effect**

In the region of $0.3 \lesssim x \lesssim 0.8$, there is decrease of $R_i^A(x, Q^2)$. This phenomenon is called *EMC effect*. This effect was first observed by Eurpeon Muon Collaboration (EMC) in scattering of muon from iron and deuterium [66]. Despite of various attempts to explain the EMC effect, the full reason for the EMC effect is still unknown, but recent measurements show that it is most-likely related to something called Short Range Correlations (SRC) between nucleons.

- **Fermi Motion**

In the region $x \gtrsim 0.8$, there is abrupt increase in $R_i^A(x, Q^2)$. This phenomenon is called *Fermi motion*. This effect is due to the Fermi motion of the constituent nucleons inside nucleus [67].

1.8.2 k_T Effect (k_T broadening)

For leading order scattering of partons ($f_1 + f_2 \rightarrow f'_1 + f'_2$) in QCD, the two outgoing partons should be back to back. But there is an inherent acoplanarity between the outgoing partons due to higher order effects, such as the finite size of nucleons. This is called k_T effect. This will ultimately cause the acoplanarity in the produced dijet. The intrinsic transverse momentum of the scattered partons is found to be at least ~ 300 MeV/C [68]. The additional gluon radiation in beyond leading order will increase the value of acoplanarity further. Since the parton transverse momentum increases from the multiple scattering within nucleus, the mean value of p_T sum of outgoing partons ($\langle k_T \rangle$) is found to be proportional to length traversed in nucleus. Thus $\langle k_T \rangle \propto L \propto A^{1/3}$, with A being the mass number of nucleus.

1.8.3 Cronin Effect (p_T Broadening)

The production of hadrons in $p+A$ collisions at the moderate p_T region ($2 \lesssim p_T \lesssim 6$ GeV/c) was found to be enhanced compared to $p+p$ collision [69]. This effect is called the *Cronin effect*. The multiple scattering of partons within a nucleus before hard scattering is believed to be the reason behind the enhancement of intermediate p_T hadrons. This

enhancement leads to the suppression in low p_T particles. The Figure 1.24 shows the

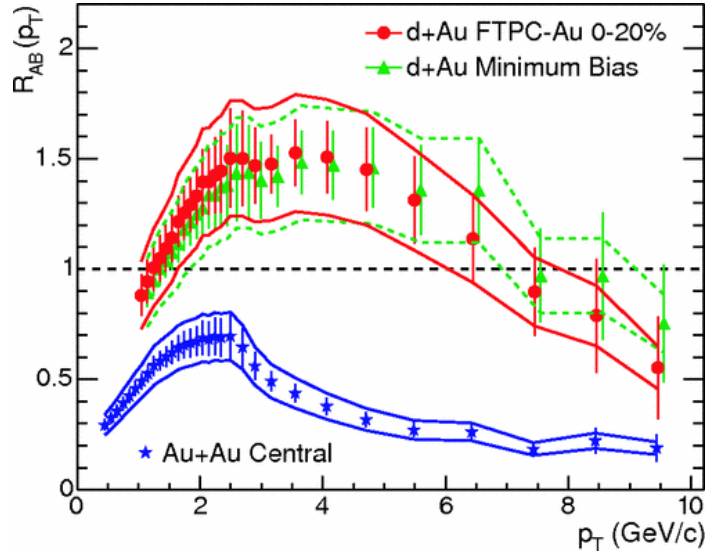


Figure 1.24: The nuclear modification factor as a function of p_T . The red and green points are of d +Au collisions while blue points are of Au+Au collisions. The figure is taken from [20]. The copyright permission for the figure is attached in Figure D.14.

nuclear modification factor for most central (0-20%) d +Au and Au+Au collisions. The enhancement at intermediate p_T regions are clearly observed for both collision systems.

1.8.4 Gluon Saturation

The gluon contribution increases as we go towards the smaller longitudinal momentum fraction, x , as shown in Figure 1.8. Beyond certain threshold of momentum transfer, the gluon density is so large that they likely to overlap and become non-resolvable and fused due to their self-interaction. In other words, the gluon saturation has to occur. This threshold of momentum transfer is called saturation scale, Q_s . This saturation scale varies with mass number (A) as $Q \sim \frac{A^{1/3}}{x^{0.3}}$ [70]. An effective field theory called color glass condensate (CGC) is supposed to explain the QCD for small x below Q_s . This saturation of gluon in colliding nucleus is believed to cause some suppression in the nuclear modification factor (R_{AA}) and other modifications.

1.8.5 Radiative Energy Loss

The radiative energy loss refers to the loss in energy due to the radiation or exchange of gluons in the medium [71]. This energy loss can occur in two different cases; initial state energy loss, final state energy loss. The initial state energy loss occurs before hard scattering when the incoming parton radiates while traversing medium. This initial state energy loss causes the decrease in x -value of incoming partons and hence shifts the parton distribution (to the left) relative to $p+p$ collision. The final state energy loss occurs when outgoing partons or fragmented hadrons radiate energy while traversing through medium. Thus this is the mechanism for the jet suppression effects of the QGP mentioned previously. This final state radiative energy loss is equivalent to the change in the fragmentation function. The initial state energy loss is calculated to be very small in comparison to expected final state effects in heavy ion collisions.

1.9 Speculations in Light-Heavy Ion Collision

As discussed in the section 1.8, the small-heavy ion collision systems (or simply called small system collisions) are analyzed to study cold nuclear matter effects. Since the heavy ion collision involves both cold and hot (QGP) nuclear matter effect, the study of small system collisions are taken as control experiments to extract the properties of hot QGP effects in heavy ion collisions. However, the observation of some important signatures of the QGP in such small system collisions has raised questions about our understanding of QGP and cold nuclear matter effects. The following are some of the observations seen in the small system collisions which need more explanations and investigations.

1.9.1 Long Range Two-Particle Correlation

Azimuthal distribution of the final state particles due to the anisotropy in initial state geometry has been already discussed as one of the signatures of QGP in section 1.7.1. This effect clearly appears in the final state two-particle correlations in η and ϕ as in part (a) of Figure 1.25 for Pb+Pb collisions. In the figure, the distribution of particles around $\Delta\phi \simeq \pi$

corresponds to awayside jet. The distribution over the range of $\Delta\eta$ in awayside is due to the different momentum fraction x of the scattering partons. Also, the distribution around $(\Delta\eta, \Delta\phi) \simeq (0,0)$ is due to the final state particles from same jets. The near side ($\Delta\phi \simeq 0$) distribution extending over the large pseudorapidity range is known as *ridge*. The presence of such ridge in heavy ion collisions are can be explained with the effect of initial state flow effect, in particular the elliptic flow (v_2).

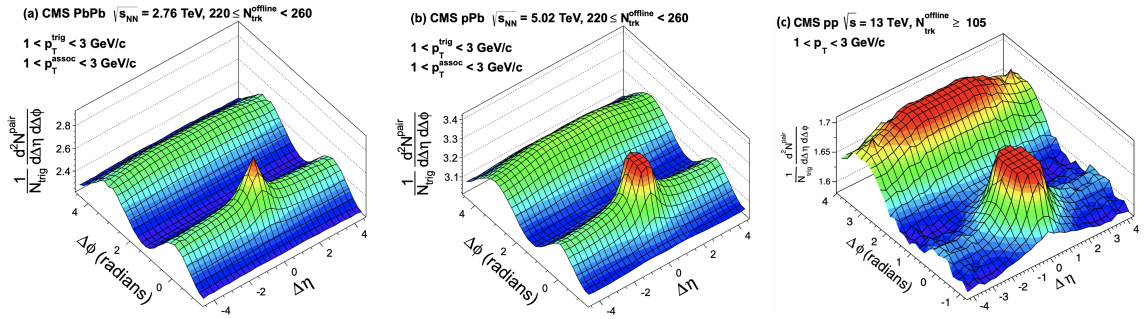


Figure 1.25: Two-particle correlations in $\Delta\eta - \Delta\phi$ measured in (a) Pb+Pb collisions at 2.76 TeV (b) p +Pb collisions at 5.02 TeV and (c) p + p collisions at 13 TeV. The peaks in figures (b) and (c) are truncated for proper visualization. The figures (a) and (b) are taken from [24]. The copyright for the figures are attached in Figure D.15. The figure (c) is taken from [25], which is available under the terms of the *Creative Commons Attribution 3.0 License*.

In two-particle correlation of small system collisions, only the distribution around $(\Delta\eta, \Delta\phi) \simeq (0,0)$ with no ridges is expected in near side. The part (b) of Figure 1.25 shows the two particle correlations in p +Pb collisions at 5.02 TeV. The figure clearly shows the unexpected ridge structure in near-side similar to that in Pb+Pb. A less pronounced but similar ridge structure appears in high multiplicity p + p collisions at 13 TeV as shown in part (c) of Figure 1.25. Analysis of long range angular correlations in d +Au at PHENIX also shows similar collective behavior [72]. The origin of these observations of collective flow in small system collisions need more explanation and investigation in order to find out

whether it has origin same as in heavy ion collisions i.e. QGP (final state effect) or it is resulted due to some cold nuclear initial state effects.

1.9.2 Engineering of Geometry

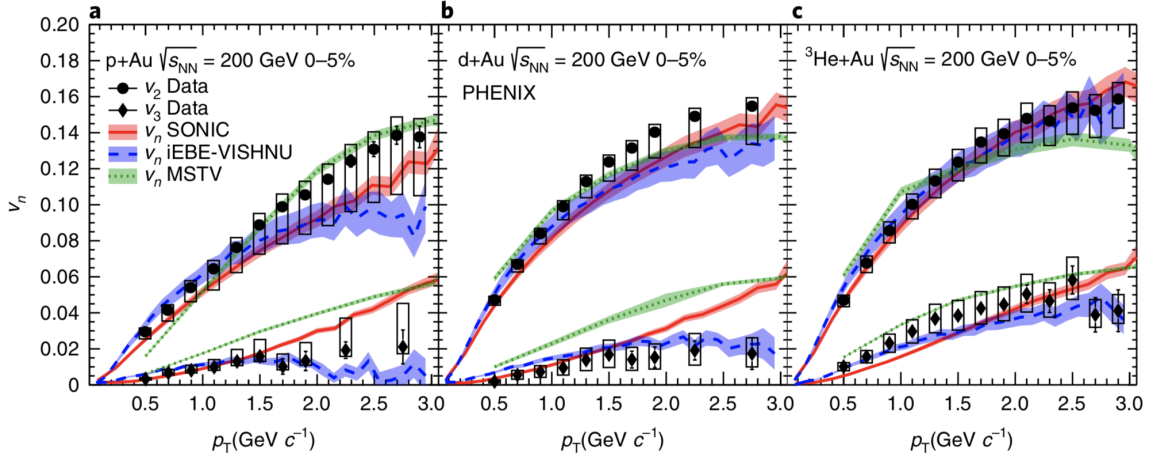


Figure 1.26: Measured flow coefficients (v_2 , v_3) as a function of p_T for a) $p\text{-Au}$ b) $d\text{-Au}$ and c) ${}^3\text{He}\text{-Au}$ at $\sqrt{s_{NN}} = 200 \text{ GeV}$ in 0-5% centrality. The black solid sphere (diamond) are measured v_2 (v_3). The solid red and dashed blue curves represent SONIC & iEBE-VISHNU hydrodynamic model predictions respectively. Also, the dotted green curve represents the postdictions of flow coefficients from initial-state momentum correlations. The figure is taken from [26]. The copyright permission for the figure is attached in Figure D.16.

After the observations of collectivity in small system collisions, high energy community has been trying to find its theoretical and experimental explanation. Recently in PHENIX [26], different asymmetric collisions with different geometries were analyzed to impart different shape of initial energy density distribution. The three asymmetric collisions are a) $p\text{-Au}$ b) $d\text{-Au}$ and c) ${}^3\text{He}\text{-Au}$. The p is supposed to have spherical, d - elliptical and ${}^3\text{He}$ - triangular shape of collision geometry. If the QGP is produced for long enough

in those collisions, then the flow coefficients measured should be directly correlated to the intrinsic collision geometry. This method is also known as *geometry engineering*.

The Figure 1.26 shows the measurements of flow coefficients (v_2 , v_3) for $p+\text{Au}$, $d+\text{Au}$ and ${}^3\text{He}+\text{Au}$. The measured elliptical flow coefficients follows the order; $v_2^{d+\text{Au}} \sim v_2^{{}^3\text{He}+\text{Au}} > v_2^{p+\text{Au}}$. Also, the triangular flow follows the order; $v_3^{{}^3\text{He}+\text{Au}} > v_3^{d+\text{Au}} \sim v_3^{p+\text{Au}}$. The greater value of tri-angularity in ${}^3\text{He}+\text{Au}$ and ellipticity in $d+\text{Au}$ clearly suggest strong correlation between the initial geometry and final flow patterns. The ordering and the value of measured flow coefficients closely matches hydro-dynamical theory calculations. This observation strongly indicates the formation of tiny QGP droplets in those small system collisions.

1.9.3 Jet Modification in $d+\text{Au}$

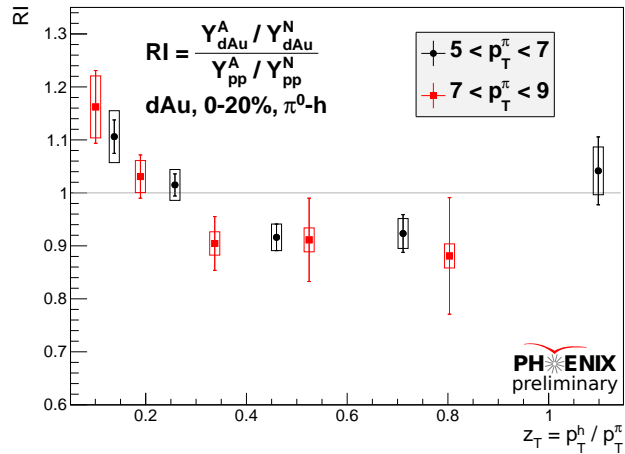


Figure 1.27: The R_I as a function of z_T measured for $d+\text{Au}$ collisions at $\sqrt{s_{NN}} = 200$ GeV in centrality 0-20%. The figure is taken from [3]. Courtesy Bing Xia.

The previous two sections deal with the collective behavior of the medium produced during the collisions. Even if the QGP is produced in the small system collisions, it may be too small to produce any modification in the behavior of jets. Bing Xia [3] and the group

of Justin Frantz at Ohio University proposed a very sensitive two-particle correlation, R_I (described in detail in section 4.2.2), to study the possible jet modification behavior in small system.

Figure 1.27 shows the R_I from π^0 -hadron correlation as a function of z_T for $d+\text{Au}$ collisions at PHENIX. The R_I shows enhancement in low z_T and suppression in high z_T . This behavior is qualitatively similar to the energy loss behavior in heavy-ion collisions. This behavior couldn't be explained by hydrodynamics study nor by nPDF simulation study [3]. These measurements are expanded in this dissertation and their interpretations will be discussed extensively in the later parts of this dissertation.

1.10 Statement of Purpose

Though the heavy ion community unanimously agrees in the presence of flow behavior in the small system collisions, they are still skeptical about the presence of jet modification due to energy loss from QGP medium. However, the modification explained in Section 1.9.3 is the smoking gun worth looking into for more details. One would like to confirm the jet modification result in Section 1.9.3 with another small system. In this analysis, we present the π^0 -hadrons correlations analysis for next bigger system i.e. ${}^3\text{He}+\text{Au}$ collisions from PHENIX detector to check the consistency of the results obtained from $d+\text{Au}$ collisions. We use the new baseline $p+p$ collisions from 2015 runs with improved statistics than previously used 2006 runs. We also cross check the 2008 $d+\text{Au}$ data set with new 2016 $d+\text{Au}$ data set and combine them.

2 THE EXPERIMENT

2.1 The Relativistic Heavy Ion Collider

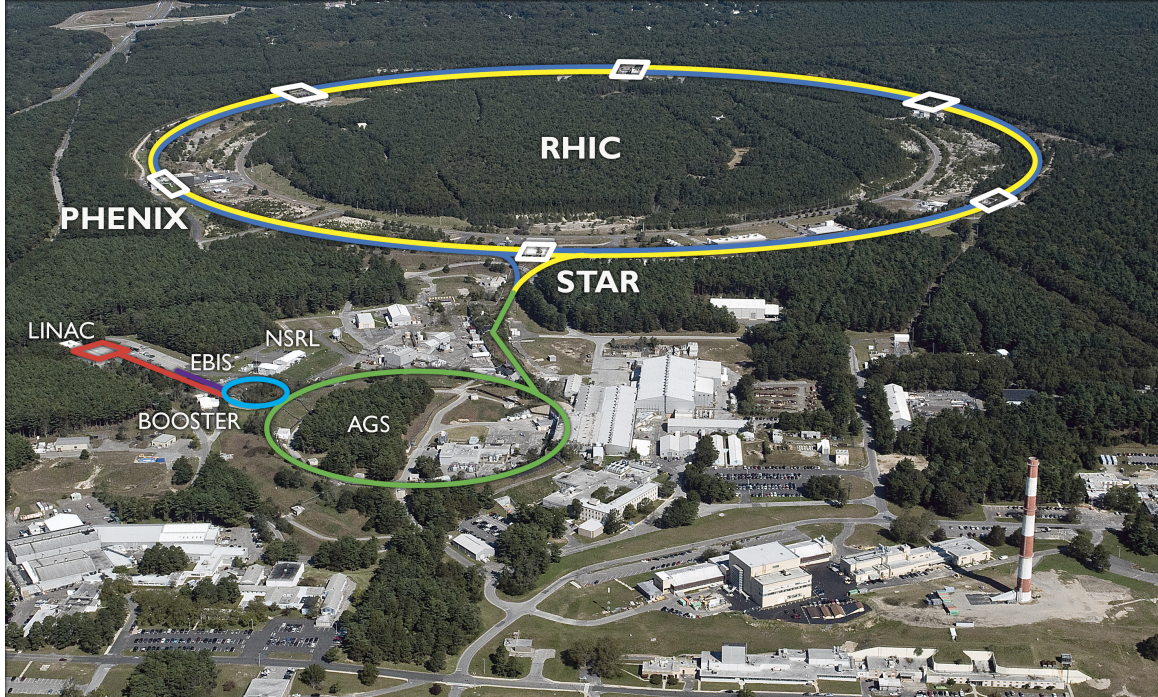


Figure 2.1: Relativistic Heavy Ion Collider (RHIC) complex at Brookhaven National Lab (BNL). The figure is taken from [27]. Courtesy Brookhaven National Laboratory. The copyright permission to use the figure are attached in Figure D.5 and Figure D.6.

The Relativistic Heavy Ion Collider (RHIC) [73] at Brookhaven National Lab (BNL) in Upton, New York, USA is the first dedicated heavy ion collider in the world. It is also the only collider capable of colliding two high-energy beams of spin-polarized protons. RHIC started its operation in 2000. RHIC consists of two counter-circulating beam lines with circumference of ~ 3.8 km [73]. The beam lines intersect at six different sites so that the ions can collide. RHIC can collide a wide range of ion species (from proton to Uranium) at varying energies. There are four different experimental halls along the beam lines, viz.:

PHOBOS, BRAHMS, STAR⁹ and PHENIX. PHOBOS, BRAHMS and PHENIX have been already decommissioned after successfully completing their scientific mission. Only the STAR detector is currently in operation, while a new experiment in the former PHENIX Experimental Hall, sPHENIX, is being constructed. The analysis in this thesis is based on the data collected from PHENIX detector during years of 2008, 2014, 2015 and 2016.

2.2 PHENIX

The Pioneering High Energy Nuclear Interaction eXperiment (PHENIX) is designed to study the properties of the QGP phase with the help of leptonic and photonic measurements as well as to study the spin structure of protons. PHENIX consists a number of detector subsystems dedicated to do specific things such as characterizing collision events, tracking of charged particles as well as identifying and measuring the energy and momentum of the particles produced during collision. PHENIX consists broadly of global detectors close to beam line and four spectrometers or arms; two central and two forward as shown in Figure 2.2.

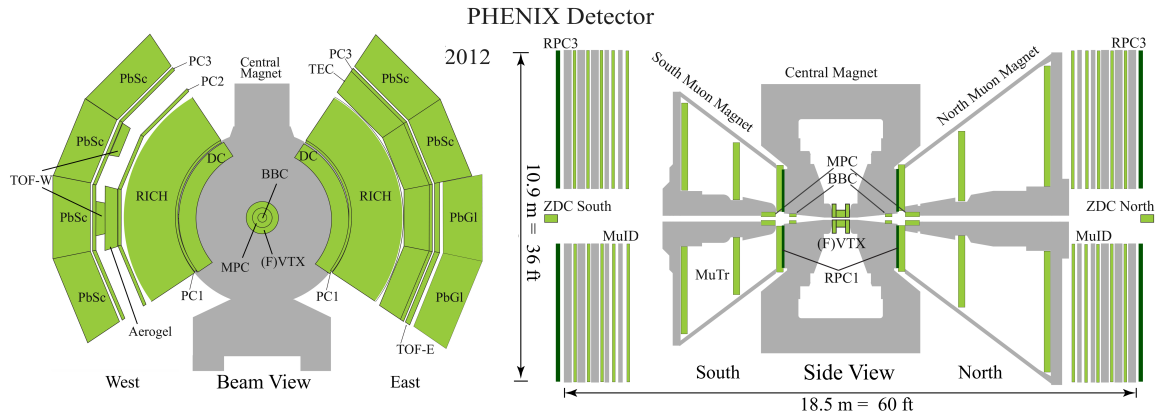


Figure 2.2: Beam view (left) and side view (right) of PHENIX detector configuration for Run12. The figure is taken from [17]. The copyright permission for the figure is attached in Figure D.7. Courtesy PHENIX collaboration.

⁹ PHOBOS: named after greek god. BRAHMS: Broad RAne Hadron Magnetic Spectrometers Experiment. STAR: Solenoidal Tracker at RHIC

The two central arms are centered at zero rapidity and in the range $|\eta| \leq 0.35$ and with total $\pi/2$ coverage in azimuth. The two forward arms have full azimuth coverage and are located at each end of central arms.

2.2.1 Magnets

Magnets are not detectors themselves, but it is nearly impossible to imagine any particle detectors without magnets. The magnets bend the direction of the charged particles into curved arcs so that their momentum and charge can be measured in desired detectors through the arc curvature which for a given setting of magnetic field strength will by the Lorentz force law be proportional to the momentum. There are three magnet systems in PHENIX: a Central Magnet for the central arm and two forward magnets for the north & south muon arms. The line drawing of the PHENIX magnets is shown in Figure 2.3 Solenoid coils in the forward magnets produce radial magnetic field for muon analysis. In

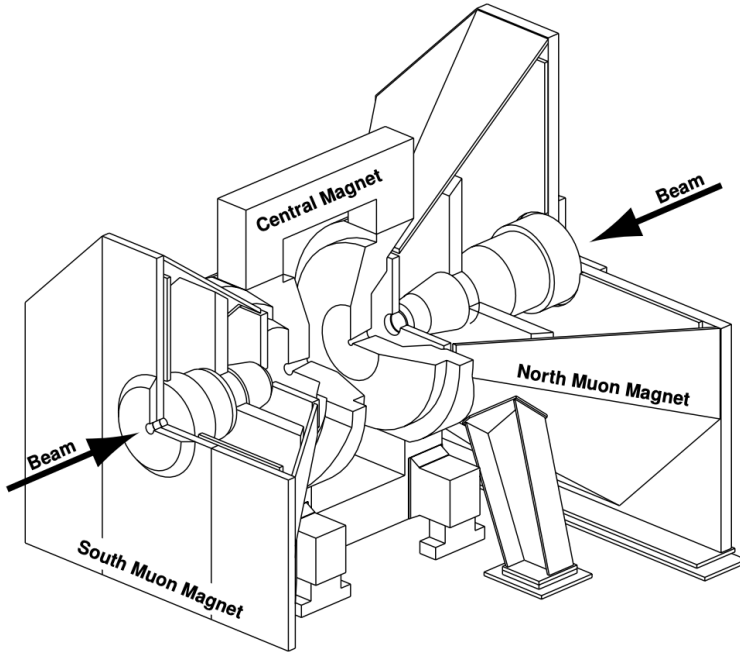


Figure 2.3: Line drawings of the PHENIX magnets. The cut away is to show the interior structures. The beam line of the colliding beams are shown by arrows. The figure is taken from [28]. The copyright permission for the figure is attached in Figure D.17.

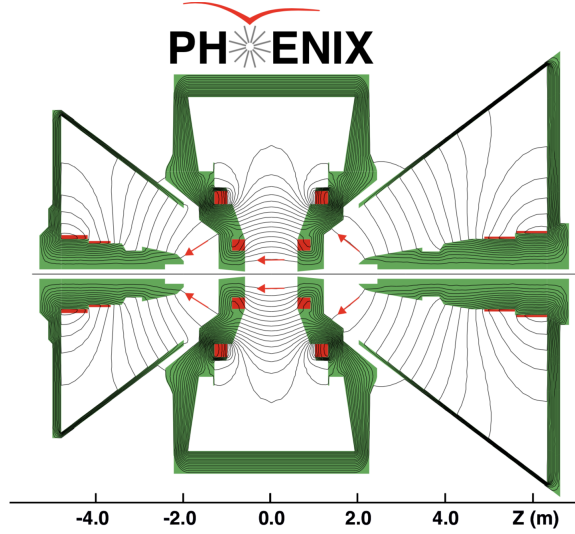


Figure 2.4: Magnetic field lines in PHENIX with central magnetic coils in the combined (++) mode. The figure is taken from [17]. The copyright permission for the figure is attached in Figure D.7. Courtesy PHENIX collaboration.

the central magnet systems, there are two pairs of concentric coils which create axial field in the central arms. They can be operated separately (+ or -), together (++) or in opposite configuration (+-). The magnetic field lines for the PHENIX magnetic systems with two central magnetic coils in combined (++) mode is shown in Figure 2.4. The central magnet is 9 meters tall weighing around 500 tons. The central magnetic system has the acceptance of $|\eta| < 0.35$.

2.2.2 Global Detectors

Global detectors help to characterize the general nature of each collision. The initial time, vertex (location of collision), and multiplicity (number of particles) of interactions are determined with the help of global detectors. The Zero-Degree Calorimeter (ZDC) and the Beam-Beam Counters (BBC) are global detectors in PHENIX.

2.2.2.1 Beam-Beam Counters (BBCs)

There are two identical BBC [74] counters on both sides (144cm on North and South) of the collision point along the beam axis. This covers the pseudorapidity range $3.0 < \eta < 3.9$ over the full 2π azimuth. Each of the BBCs comprises 64 one-inch mesh dynode photo multiplier tubes (PMTs) which measures the Cherenkov light from the charged particles passing through the quartz radiators in front of each PMT as shown in Figure 2.5.



Figure 2.5: Left: A single element of BBC consisting of a PMT and quartz radiator. Middle: One of the two BBCs consisting of 64 PMTs and radiators. Right: BBC installed around the beam pipe [29].

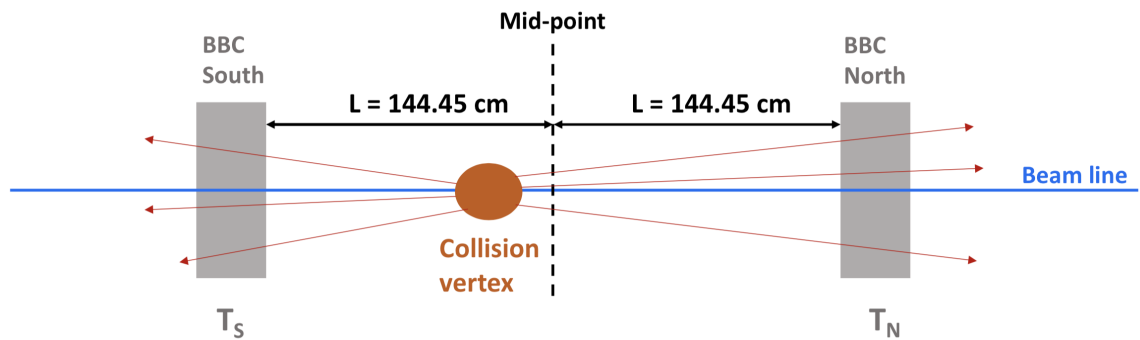


Figure 2.6: Schematics of BBCs. The two BBCs (North and South) are at distance 288.9 cm. Collision is supposed to occur around the middle of two BBCs.

The schematics of BBC is shown in Figure 2.6. The BBC helps to measure the initial time of collision or time zero (T_0) for the collision with excellent timing resolution of about 52 ± 4 ps [74].

$$T_0 = \frac{T_S + T_N}{2} - \frac{2L}{c} + t_{offset}, \quad (2.1)$$

where T_S (T_N) is average time for south (North) BBC and t_{offset} is intrinsic time offset of particles produced in collision. This initial time can be used to measure the particle's time of flight (TOF). The BBC also helps to determine vertex of the collisions along the beam axis with the resolution of about 1 cm [74].

$$z_{vertex} = \frac{T_S - T_N}{2} + z_{offset}, \quad (2.2)$$

where z_{offset} is intrinsic z -position offset. The tracking subsystems use the collision vertex as a origin point.

2.2.2.2 Zero-Degree Calorimeters (ZDC)

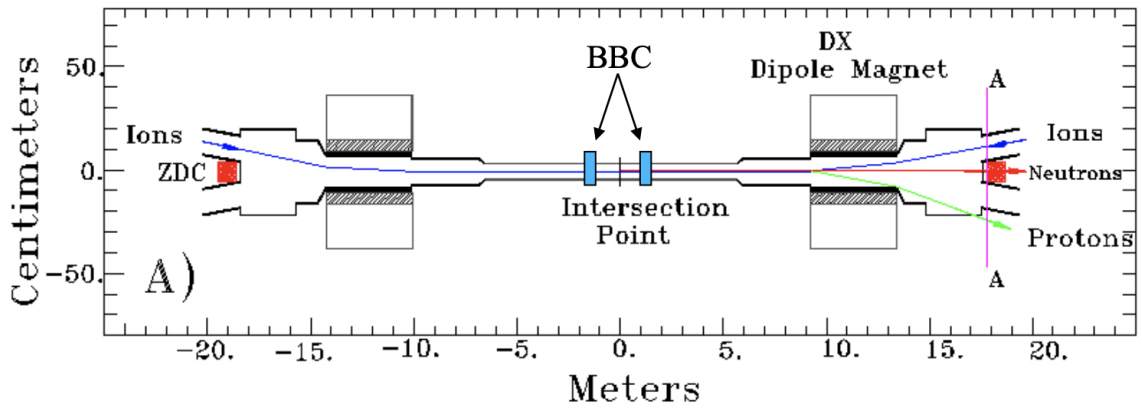


Figure 2.7: Installation of north and south ZDCs (red blocks) along the beam axis. The figure is taken from [30]. The copyright permission for the figure is attached in Figure D.18.

There is a pair of small ZDC [75] detectors, each of them located behind the dipole magnets around 18m from the interaction point. The dipole magnets steer the remnant beam out of the experimental detector region. The ZDCs are hadronic calorimeters which

detect grazing (spectator) neutrons with respect to beam axis. The ZDCs along with BBCs are used for event-by-event characterization. Also, the coincidence signals on both detectors are used for the monitoring of luminosity.

2.2.3 Central Arms

The two central arms are centered at zero rapidity and surrounded by two central magnets. These magnets provide axial magnetic field parallel to beam line. They are in the range $|\eta| \leq 0.35$ and with total $\pi/2$ coverage in azimuth. The sub-detector systems for tracking, measuring energy and identifying particles are arranged in these two central arms.

The Drift Chambers (DCs), Pad Chambers (PCs) are used for charged particle tracking while measurement of photons and electrons is given by the Electromagnetic Calorimeter (EMCAL). The Ring Imaging Cherenkov Counters (RICH) and Time of Flight (TOF) detectors are used for particle identification.

2.2.3.1 Drift Chamber (DC)

There are two identical cylindrical shaped Drift Chambers [31] in the innermost part of both east and west central arms. They are located in 2 to 2.4 m from and 2 m along the beam axis. The acceptance of DC is 90° , each for east and west, in the ϕ , ± 0.35 in pseudorapidity and ± 1.25 m in the beam axis. The main purpose of the DC is measure the trajectories of charged particles in $r\text{-}\phi$ direction which can be used to determine the momentum of particles and the invariant mass of particle pairs.

Each of the DCs is a close volume with titanium frame along the azimuthal and beam-axis limit while Five-mil Al-mylar windows in the radial limit. Each frame is divided into 20 equal sectors and in each sectors, there are six wire modules (X1, U1, V1, X2, U2 AND V2) positioned radially as shown in Figure 2.9. Also, each of the modules consists 80 wires. The region between the wires contains mixture of argon and ethane. The ionization of the gas due to the charged particles releases electrons and those electrons drift along the electric field lines. The distance between the location where the electrons is produced due

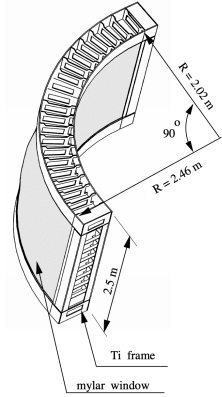


Figure 2.8: DC frame. The figure is taken from [31]. The copyright permission for the figure is attached in Figure D.19 and Figure D.20.

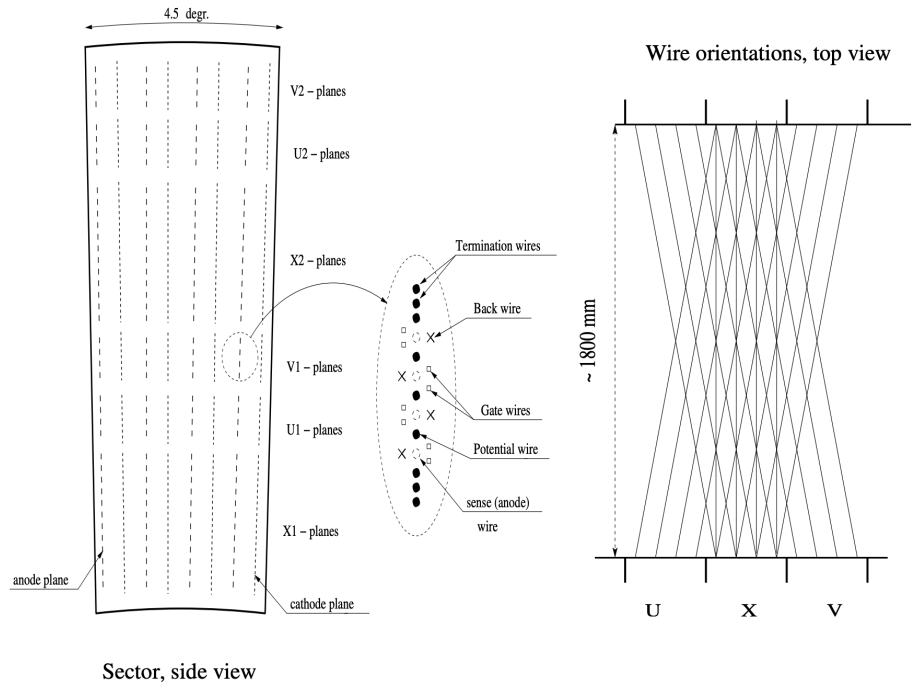


Figure 2.9: Left: Side view of layout of wire arrangement within one sector of DC. Right: Top view of U, X and V wire orientation. The figure is taken from [31]. The copyright permission for the figure is attached in Figure D.19 and Figure D.20.

to passage of charged particles and anode wires are determined by the arrival time and drift velocity. The X wires are parallel to beam axis and can measure tracks in r- ϕ plane. U and V wires are placed with a small stereo angle (6°) relative to X wires and are used to measure z-positions of the track.

2.2.3.2 Pad Chamber (PC)

The main purpose of the Pad Chamber [32] is to provide the track information and check the redundancy with DCs. There are five Pad Chambers; two PC1s, a PC2 and two PC3s. They are multi-wire proportional chambers filled with a mixture of argon and ethane gas. PC1 is located in between RICH and DC in both east and west arm. The PC2 layer is installed behind RICH of west arm only. The PC3 is installed in front of EMCAL in both arms.

Each of the Pad Chambers is made out of two flat cathode panels (pixelated and solid) and an anode wire electrode in between them as shown in Figure 2.10. The three interleaved pixels define a cell. Signals from at least three pixels is required to be considered as a valid hit.

The PC1 measures the z-coordinates of track which can be used to confirm the hit in the DC and hence helping to reconstruct track. The PC3 is used to crosscheck the charged particles flying into the EMCAL. This helps to rule out the charge particles produced from secondary interaction after outside the DC. Only PC1 and PC3 are used for this analysis.

2.2.3.3 Ring-Imaging Cherenkov (RICH) Detector

Ring-Imaging Cherenkov (RICH) [76] is primarily used to identify the electrons produced in PHENIX experiment. RICH is located just outside PC1 in both of the central arms. When a charged particle passes through a medium with phase velocity greater than that of light in that medium, it emits electromagnetic radiation called the Cherenkov radiation. RICH works on the principle of Cherenkov radiation. RHIC uses carbon dioxide (CO_2) at 1 atm. pressure with refractive index 1.000410 as a medium. CO_2 has Cherenkov

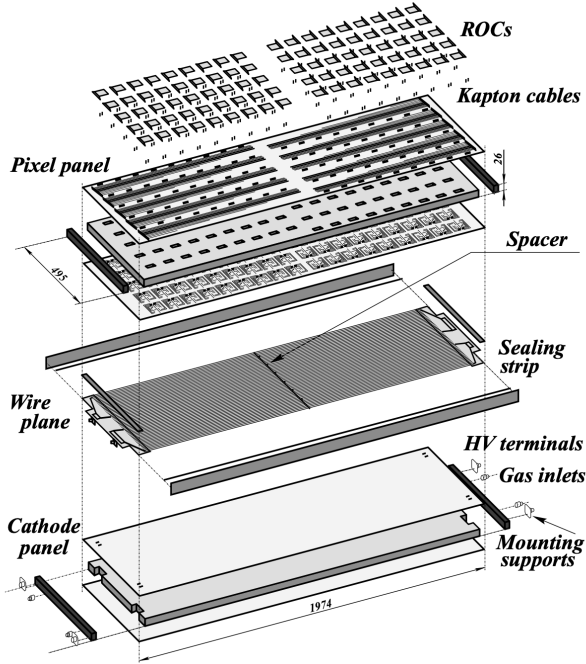


Figure 2.10: The expanded geometry of the PC1. The figure is taken from [32]. The copyright permission for the figure is attached in Figure D.21.

threshold of 4.65 GeV/c for pions and 18 MeV/c for electrons. Spherical mirrors in the RICH reflects Cherenkov light produced by charged particles onto photomultiplier tubes (PMTs). Thus the charged particles can be distinguished from electron by looking at the radius of the PMTs it collects the light on. Thus RICH helped us to veto the electrons from the tracks of charged hadrons with momentum below 5 GeV/c.

2.2.3.4 ElectroMagnetic Calorimeter(EMCal)

In PHENIX, the spatial position and energy of photons and electrons produced are measured with help of Electromagnetic Calorimeter (EMCal) [1]. The electrons and photons interact with EMCal materials via well-understood QED process (mainly bremsstrahlung and pair production) and produces shower of secondary particles with progressively degraded energy. The energy deposited by the charged particles of the shower can be detected in the form of charge or light.

Two types of EMCAL are used in PHENIX, viz.; lead scintillator sampling calorimeters (PbSc) and lead glass cherenkov calorimeter (PbGl). The west arm consists four sectors of PbSc calorimeters while the East arm consists of two sectors of PbSc and two sectors of PbGl. The PbSc has better linearity and is optimized for high timing resolution while the PbGl has better granularity and is optimized for high energy resolution.

2.2.3.4.1 Lead-Scintillator (PbSc) Calorimeter

PbSc is a shashlik type sampling calorimeter. A module is the basic building block for a calorimeter. The module of PbSc calorimeter is as shown in Figure 2.11.

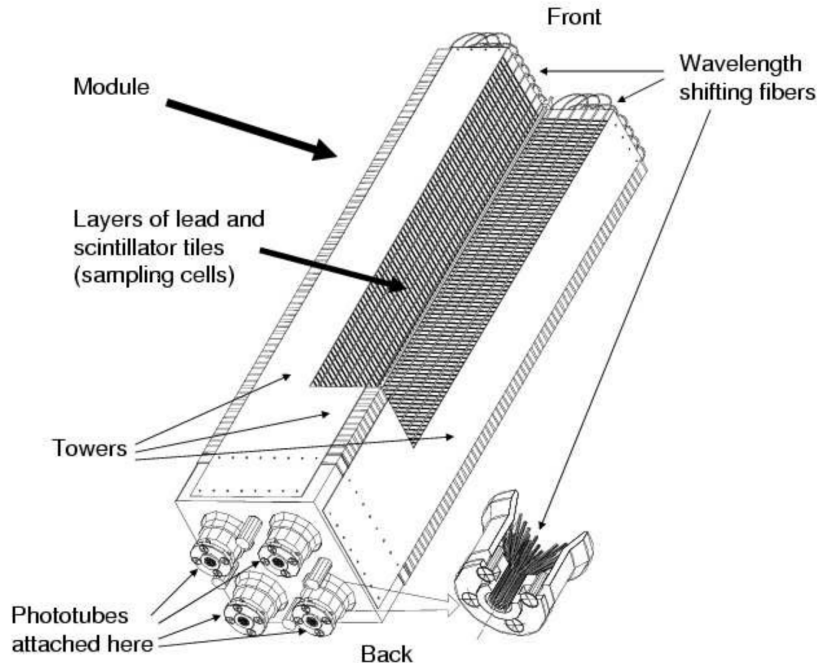


Figure 2.11: The cutaway view of PbSc calorimeter module. The figure is taken from [1]. The copyright permission for the figure is attached in Figure D.22.

Each PbSc module consists of four (2x2) towers and each tower contains sixty six sampling cells consisting of alternating tiles of Pb and scintillator. The cells are optically connected by wavelength shifting fibres to collect light to photo-tubes at the back of towers.

Thirty six (6x6) modules are attached together to form a super-module and eighteen (3x6) super-modules are further grouped to make a sector. The energy resolution for the PbSc calorimeter is given by

$$\frac{\sigma_E^{PbSc}}{E} = \frac{8.1\%}{\sqrt{E(GeV)}} \oplus 2.1\%, \quad (2.3)$$

where the first term in right hand side of Equation (2.3) is stochastic term due to the fluctuations related to the physical development of shower and second term is constant term due to intrinsic non-uniformities. The noise contribution is corrected in the resolution.

2.2.3.4.2 Lead-Glass (PbGl) Calorimeter

The PbGl is basically a Cherenkov detector. It consists of lead, glass and lead oxide as a homogeneous medium. An array of twenty four (6x4) Lead-Glass module forms a super-module as shown in Figure 2.12. A super-module is a self-contained detector based on a set of 3 different LEDs¹⁰. One hundred and ninety two super-modules again group together to form a sector.

The energy resolution for the PbGl calorimeter is given by

$$\frac{\sigma_E^{PbGl}}{E} = \frac{(5.9 \pm 0.1)\%}{\sqrt{E(GeV)}} \oplus (0.8 \pm 0.1)\%. \quad (2.4)$$

The physical parameters of the PbSc and PbGl calorimeters are as shown in Table 2.1.

2.2.4 Forward Arms

There are two forward arms (north and south) with muon tracker (MuTr), muon identifier (MuID) and muon piston calorimeter (MPC). These detectors are used for the measurement of muons which is used to study J/Ψ , Ψ' and lighter mesons. None of these detectors are used in the analysis of this dissertation.

2.3 Data Acquisition and Trigger Systems in PHENIX

In order for subsystems of PHENIX to work in sync with each other while doing some specific measurements independently, the granules and partitions mechanism was

¹⁰ LED: Light Emitting Diodes

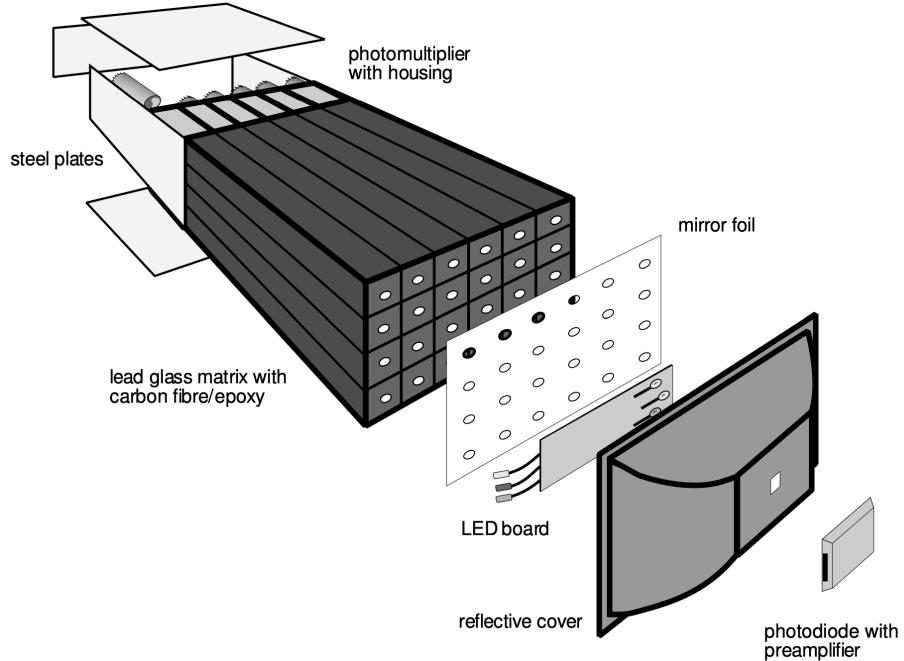


Figure 2.12: The exploded view of PbGl calorimeter super-module. The figure is taken from [1]. The copyright permission for the figure is attached in Figure D.22.

developed for data acquisition (DAQ) in PHENIX. A granule is a minimum combination of DAQ hardware sufficient for data production while partition is a combination of granules which works as a unit.

The schematic representation of the flow of PHENIX data is as shown in Figure 2.13. The Front-End Modules (FEM) process the input signals and store the results in digital (BBC, ZDC,..) or analog (EMC, RICH,..) memory units. Local Level Trigger (LL1) uses the data from part of subsystems (BBC, ADC, EMC, RICH,..) and do some fast analysis. The result from this analysis is sent to Global level-1 (GL1) trigger for final decision making. GL1 then checks some trigger logic and fires trigger. The data in FEM corresponding to the triggers are then sent to Data Collection Module (DCM). According to Granules → Partitions mapping, the Event Builder (EvB) combines the data from DCMs

Table 2.1: Physical parameters of Lead-Scintillator (PbSc) and Lead-Glass (PbGl) calorimeters. The table is adapted from [1].

Parameter	PbSc	PbGl
Geometry:		
No. of sectors	6	2
Size of sector surface	$(4 \times 2) \text{ m}^2$	$(4 \times 2) \text{ m}^2$
Super-modules per sector	18 (6×3)	192 (16×12)
Modules per Super-module	36 (6×6)	24 (6×4)
Towers per Modules	4 (2×2)	1
Tower $\eta \times \phi$ coverage	0.001×0.001	0.008×0.008
Radiation Length (X_0)	2.02 cm	2.8 cm
Moliere Radius	3.0 cm	3.68 cm
Interaction Length	44.2 cm	38.0 cm
Critical Energy		16 MeV
Active (Tower) Depth	37.5 cm ($18 X_0$)	40.0 cm ($14 X_0$)

into Partition Event Packet. The Level-2 trigger analyzes the events and the desired events are accumulated and then sent to HPSS¹¹ and are stored on tapes.

Trigger System

In PHENIX, the ions are collided in the rate as high as several MHz. Saving data from all of the events requires huge space and it is often too time-consuming to process all of them. Furthermore, most of these events contain already known and therefore uninteresting physics. So, we need to select the data for the physics we are interested in. The condition required to record data collection for an event during a collision is called a *trigger*. The

¹¹ High Performance Storage System

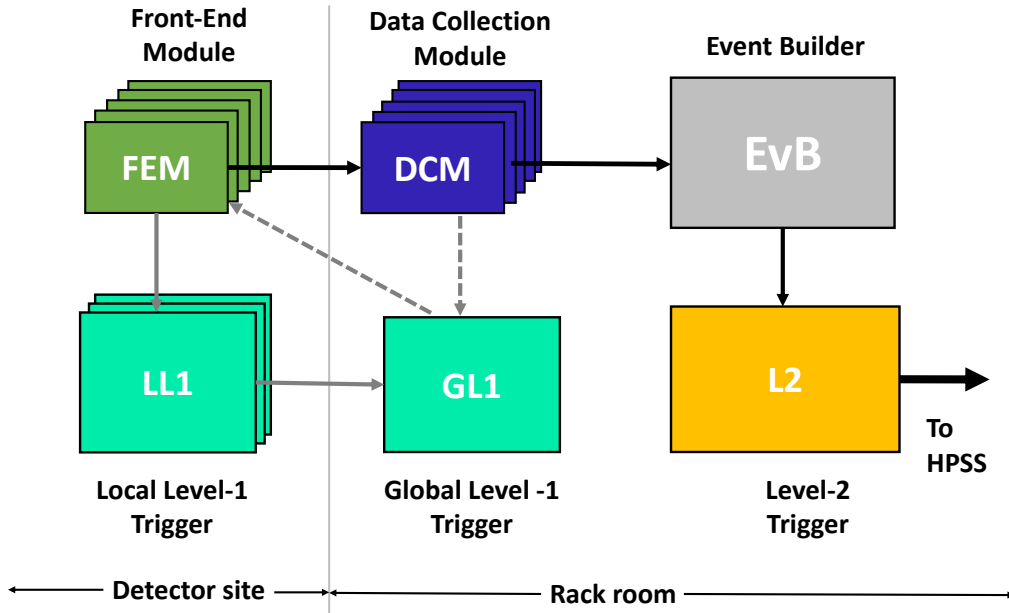


Figure 2.13: Schematic representation of flow of PHENIX data.

trigger condition differs based on the physics we are interested to draw from the data. There are two levels of trigger conditions applied in PHENIX; Level-1 (LVL1) and Level-2 (LVL2). LVL1 makes the decision on each beam crossing by processing the reduced data from a part of detector subsystems in parallel. The LVL2 makes a fast analysis and decides if the data which passed the LVL1 trigger to be stored or discarded. Two different Level-1 triggers are applied for the analysis in this thesis.

2.3.1 Minimum Bias (MB) Trigger

BBC helps to determine the Minimum Bias (MB) trigger by finding out the collision vertex. It defines the minimum signal system that is considered the “minimum bias” way to define that an collision event actually occurred. The conditions for MB trigger differ with collision species. The following are the three different types of MB trigger.

1. Normal trigger: Triggers events with $z_{vertex} < |30|$ cm.
2. Narrow vertex trigger: Triggers events with $z_{vertex} < |10|$ cm.

3. No vertex trigger: Triggers events with any coincidence between the north and south BBC.

2.3.2 EMCAL/RICH Trigger (ERT)

The EMCAL/RICH Level-1 trigger (ERT) requires events with electrons and high p_T photons to be triggered. The ERT trigger is set by the conditions in the Ring Imaging Cherenkov (RICH) detector and Electromagnetic Calorimeter (EMC). Energy sums of groups of EMCAL towers, called trigger tiles, are used for photon triggers. If the energy sum in the trigger tiles is greater than threshold energy, the event is triggered to be written. For electron triggers, both EMCAL and RICH data are used.

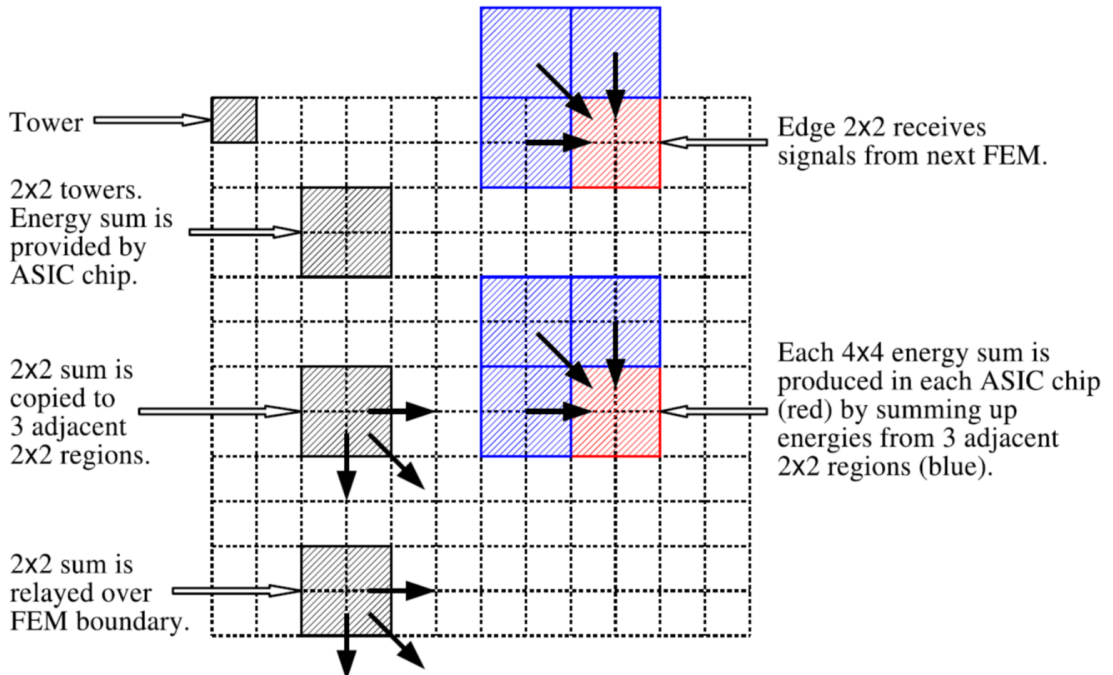


Figure 2.14: The method for EMCAL Trigger. The figure is taken from [33].

The method to select an ERT event is as shown in Figure 2.14. An ASIC chip sums the energies in 2×2 towers. Then a FEM reads the information of 6×6 ASIC chips (from 12×12 towers). So, there are 36 energy sums produced per FEM. To take care of the inefficiency

for particle hitting in the border 2×2 towers, the energy sum of 4×4 towers is formed from four 2×2 energy sum. One FEM obtains the 36 4×4 energy sum signals. Thus, the ERT trigger decision is made by comparing each 4×4 energy sum as well as 2×2 energy sum. Three trigger thresholds are applied in 4×4 energy sum; ERT $4 \times 4A$, ERT $4 \times 4B$ and ERT $4 \times 4C$ and one in ERT 2×2 . The ERT $4 \times 4B$ has highest trigger threshold while ERT $4 \times 4C$ has lowest. The values of thresholds depend on collision energy and species.

2.4 Centrality Determination in PHENIX

The impact parameter for the heavy ion collision is too small ($\sim 10^{-15}$ m) to measure. So, centrality is used to quantify the extent of overlap between the nuclei during the collisions. The more central the collision, the smaller is the impact parameter. Centrality is defined as a mapping of the number of particles produced in an event, such that the centrality value in percent on average represents the percentage of events with multiplicity equal to or smaller than this value. With the help of the Glauber Model [34], the centrality class is used to extract the number of participating nucleons (N_{part}), the number of colliding nucleons (N_{coll}) and the impact parameter of a collision. Typically a measured distribution like per event charge multiplicity (dN_{evt}/dN_{ch}) for an ensemble of event is compared with the distribution obtained from Glauber calculations. The Figure 2.15 shows the correlation between the integrated distribution of per-event charge multiplicity with Glauber calculations. The centrality classes, shown by vertical dashed lines in Figure 2.15, are determined by binning the distribution based upon the fraction of the total integral. Then, the mean values of Glauber quantities are calculated for each centrality bins.

In the PHENIX experiment, there are two different ways to determine centrality class; the “clock method” and the “BBC only method”. In the “clock method”, BBC and ZDC are used to determine the centrality class of a collision. The charge collected in the BBC depends upon the number of participating nucleons and the energy deposited in the ZDC depends upon the number of neutrons coming from the colliding nuclei. In peripheral collisions, few charged particles are produced in mid-rapidity region while large numbers

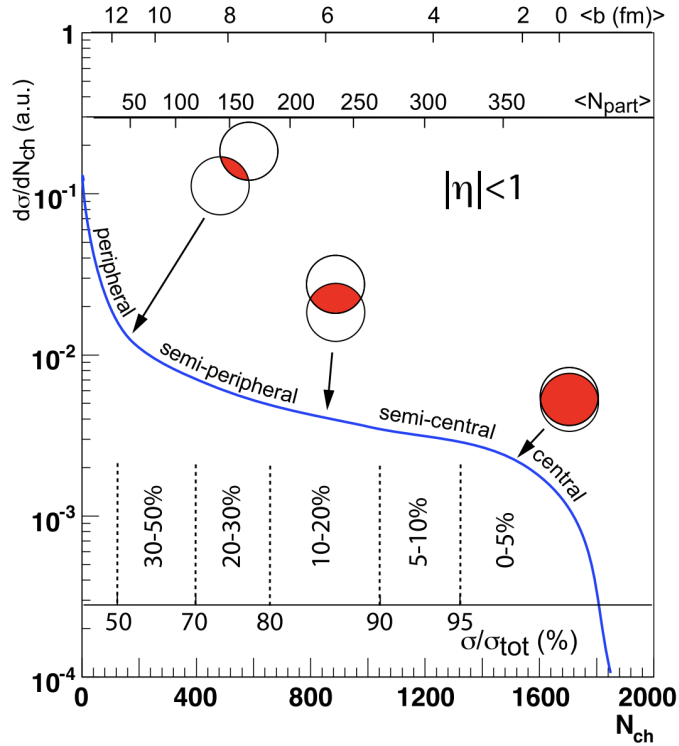


Figure 2.15: Cartoon showing the correlation between the final state observable N_{ch} and quantities (b , N_{part}) calculated from Glauber. The figure is taken from [34]. The copyright permission for the figure is attached in Figure D.23 and Figure D.24.

of spectator neutrons reach the ZDC. While in case of the most central collisions, larger number of charged particle are produced in mid rapidity region while a fewer number of spectator neutrons reach the ZDC. Based on this fact, the centrality class of the collision is determined as illustrated on the left in Figure 2.16. Each red and blue bins on the left in Figure 2.16 are of 5 %, the most central being in the right most side. The radial division of the bins on the left in Figure 2.16 looks like a clock, hence the name.

In the “BBC only” method, the charge distribution in BBC are divided into percentiles as shown on the right in Figure 2.16. The blue and red colors are centrality classes with interval of 5 %. The most central bin starts from right hand side.

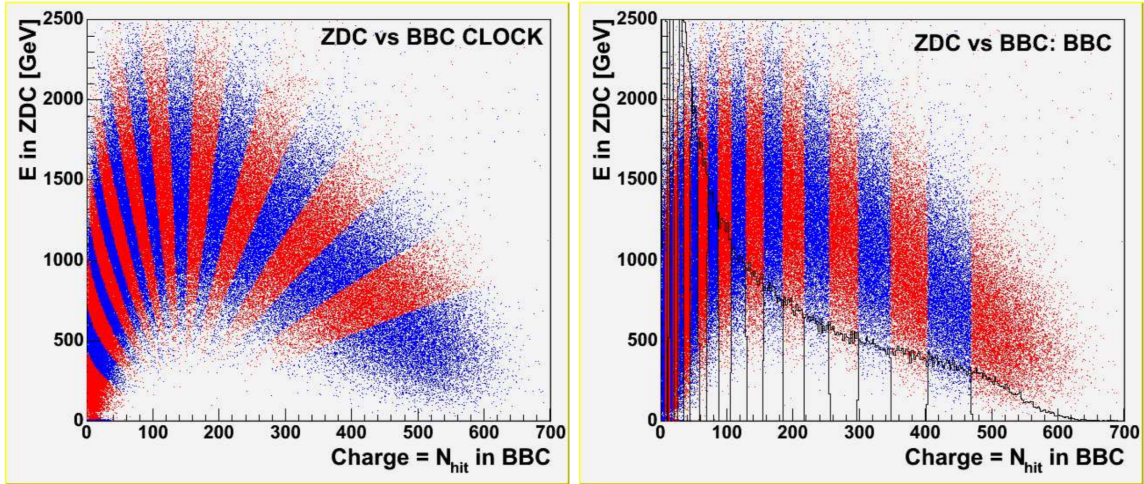


Figure 2.16: Left: The total energy deposited in ZDC vs total charge detected in BBC, “clock method”. Right: Charge distribution of BBC, “BBC only method” Each bin contains same number of events for both figures. The figures are taken from [35].

2.5 Reconstruction of Charged Tracks in PHENIX

The Drift Chamber (DC) and Pad Chamber (PC1) are used to reconstruct the trajectory of the charged particles produced in collision. The construction of track candidates is done in the DC using pattern recognition based on the Combinatorial Hough Transform (CHT) [36] while hits on PC1 are used to confirm the track candidates.

The charged particles produced at the collision vertex get bent by the field of central magnets and enters the DC. The momentum and charge of the particle determine the extent of bending. ϕ - α pairs are used to describe tracks in DC as shown in Figure 2.17. ϕ is polar angle at the intersection of the track with a “reference radius” at the mid-radius of drift chamber while α is the inclination angle of the track at that point. The CHT technique assumes the tracks are straight lines within DC. In this technique, all the (ϕ, α) -combinations from hits are calculated, then binned, and searched for the maxima. The hits corresponding to a track lead to a peak while random pairs of hits from different tracks

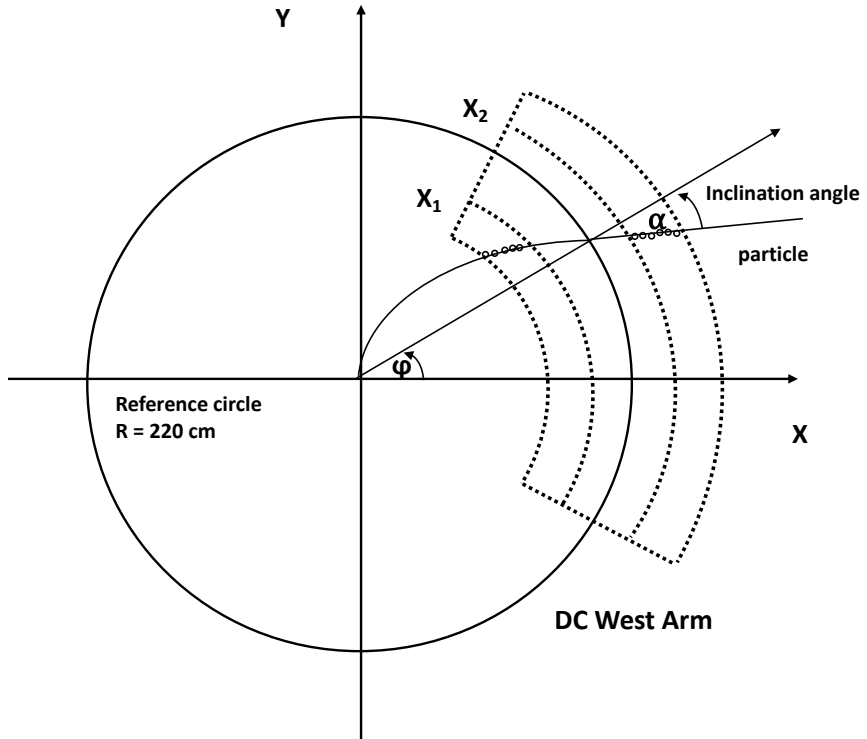


Figure 2.17: Reconstruction of charged track using DC with Combinatorial Hough Transform (CHT) technique [36]. The larger circle is defined by DC reference radius and the smaller circles represents hits from particles along its trajectory.

leads to a flat background in $(\phi-\alpha)$ feature space. Thus constructed candidates of tracks are then matched with PC1 hits.

2.6 EMCAL Clustering in PHENIX

The production and multiple scattering of electrons and positrons away from shower axis are mainly responsible for the transverse size of an electromagnetic shower. Measurement of this transverse size of shower integrated over the full shower depth is expressed in terms of Moliere Radius (R_M). The Moliere Radius is characterized by a radiation length and atomic number of the matter. Generally, about 90 % of the shower

energy is contained in a cylinder of radius of $1 R_M$. Thus most of the showers in PHENIX experiment stretch up to two, or more than two, towers. Also, a single tower might contain more than one showers. To separate these showers, a sophisticated clustering algorithm is needed. The following is the brief outline of the PHENIX clustering algorithm.

1. Find a cluster: A cluster is a group of adjacent towers each with a energy above a noise threshold.
2. Find the local maxima of the cluster: Local maxima are modules above certain peak threshold with maximum amplitude in the 3×3 tower region surrounding it. There may be may be more than one local maxima.
3. A fit is performed with one shower shape fit function with floating parameters per local maximum each of which then defines a "peak area". If there is a tower with contribution from two or more peak areas, the tower energy divided into each peak areas according to the parameterized shower profile for each peak fit function.
4. Redefining the cluster area as "core cluster" by the towers which all but 2% of energy sum in the belonging peak area.

3 DATA PREPARATION

This chapter includes the information about the data, selection criteria of π^0 trigger particles and charged tracks used in this dissertation.

3.1 Data Selection

The data sets taken from PHENIX experiment at RHIC are used for the purpose of this research. Since our goal is to study the light heavy ion collision, we are analyzing the ${}^3\text{He}+\text{Au}$ and $d+\text{Au}$ systems with reference to $p+p$ data. The run year, beam energy, integrated luminosity for the data under analysis are summarized in Table 3.1.

Table 3.1: A summary of PHENIX data sets used for analysis. The integrated luminosity is taken from [2].

Run Year	Beam Species	Beam Energy $\sqrt{s_{NN}}$ (GeV)	Integrated Luminosity
2014	${}^3\text{He}+\text{Au}$	200	134 nb^{-1}
2015	$p+p$	200	382 pb^{-1}
2016	$d+\text{Au}$	200	289 nb^{-1}

3.2 Run Selection

Quality assurance (QA) of each run is done to take care of temporary detector issues before the run is considered for further analysis. Run quality assurance (QA) is done by scanning for problems in DC/PC and EMCAL sectors. The good run list of Run14¹² ${}^3\text{He}+\text{Au}$ are taken from PHENIX internal Analysis Note 1297 [77] and that of Run15 $p+p$ are taken from PHENIX internal Analysis Note 1269 [78]—both of these notes performed analysis to estimate and confirm stability of the EMCAL and tracking.

¹² Run x means run taken during 2000+ x AD. Here, Run14 means runs taken during 2014.

3.3 Event Selection

Events are selected by applying cuts in the z-vertex with $|z_{vertex}| < 30$ cm. The 0-20% centrality of ${}^3\text{He}+\text{Au}$ & $d+\text{Au}$ and all centrality bins of $p+p$ are taken for the analysis. Each photon used to construct high $p_T \pi^0$'s are checked to make sure that they fired one of the three Level 1 gamma triggers (A,B,C) which are all used together. EMCal Rich Triggers (ERT) data sets are used. For the ERT data sets used, it was checked the 5 GeV trigger threshold we use is above or near the efficient turn-ons of the triggers.

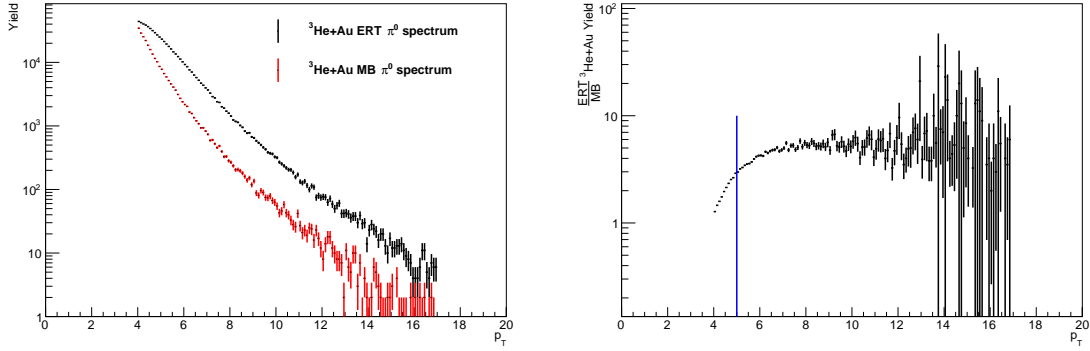


Figure 3.1: Left: The ERT and Minimum Bias (MB) π^0 spectrum for ${}^3\text{He}+\text{Au}$ collisions at $\sqrt{s_{NN}}=200$ GeV. Right: The ratio of ERT to MB π^0 trigger yield. The blue vertical line is at 5 GeV.

The ratio of π^0 trigger spectrum in ${}^3\text{He}+\text{Au}$ collisions for ERT and MB data sets is shown in right of the Figure 3.1. The ratio shows the ERT trigger is not fully efficient till 6-7 GeV. To first order, trigger efficiency cancels when we make per-trigger-yield, but there is second order effect in the observable we are interested. The effect of the turn-on region in ${}^3\text{He}+\text{Au}$ was found to be negligible. The details about this study are explained in Section 4.2.3.3.

3.4 Particle Selection

In the two particle correlation method (described in Section 4.1.), the angular correlation between trigger and partner particles is studied. The ideal particle for trigger (in this context, trigger does not mean an actual Level-1 trigger described previously) is the direct photon since direct photons originate from initial hard scattering with no flow effects and their color-neutrality allows them to have virtually no interaction with the QGP. However, the measurement of direct photons suffers from low statistics. The larger modification effects on di-jet-related triggers are more ideal when searching for potentially small effects in the smaller light-heavy ion collisions. For these reasons, π^0 particles are taken as trigger for this study. Due to the 98.8 % branching ratio of $\pi^0 \rightarrow \gamma + \gamma$ and precise energy, position resolution, and fast triggering (via the ERT trigger previously discussed) of the PHENIX EMCal detectors, π^0 is the obvious choice in PHENIX. Charged hadrons suffer from too-poor resolution, high backgrounds at high p_T , and no possible Level-1 triggering. However, at low p_T , π^0 has lots of combinatorial ($\gamma + \gamma$) backgrounds and thus aren't ideal to be used as partner particle. Since there is very high statistics, low background, and excellent resolution of charged hadrons in low p_T regions, they are chosen to be an ideal candidate as partner particle.

3.4.1 Photon Identification and Selection

Photon Identification

- Shower Shape cut: $\chi^2 < 3$, or dispersion cut for PbGl standard dispersion cut.

The photons interact electromagnetically with EMCal material to produce electromagnetic showers. The electromagnetic showers are short, slim and regular while hadronic showers are penetrating, wide and irregular. The electromagnetic showers are distinguished from the hadronic showers with the help of shower shape cut; $\chi^2 < 3$. Where the χ^2 is defined in Equation (3.1).

$$\chi^2 = \sum_i \frac{E_i^{pred} - E_i^{meas}}{\sigma_i^2} \quad (3.1)$$

where σ^2 is variance of predicted energy function.

$$\sigma^2 = A \cdot E_i^{pred} \left(1 + B \sqrt{E_{tot}} \sin^4 \alpha \right) \left(1 - \frac{E_i^{pred}}{E_{tot}} \right) + q(E_{tot}) \quad (3.2)$$

- Charged Hadron Veto: $r_{emc-pc3}^{veto} < 8.0$

Even after the shower shape cut, there might be contribution of hadrons which are a background for the photon measurement. Those showers are further ruled out with help of the charged hadron veto. For each cluster, the associate particle hits in Pad Chamber (PC3) is found and $r_{emc-pc3}^{veto}$ is calculated as in Equation (3.3). Anything with $r_{emc-pc3}^{veto} < 8.0$ cm is ruled out.

$$r_{emc-pc3}^{veto} = \sqrt{dx_{emc-pc3}^2 + dy_{emc-pc3}^2 + dz_{emc-pc3}^2} \quad (3.3)$$

Photon Selection

- p_T : $5 \leq p_T \leq 20$ GeV/c
- Hot/dead tower maps

For this analysis, we choose photons with $1 \leq p_T \leq 20$ GeV/c. The problematic towers of electromagnetic calorimeter should be excluded from the analysis. This is done by finding out the hot/dead maps of each sector of EMCAL and excluding those towers in the maps. Hot towers are continually, or too-often, signaling towers of the electromagnetic calorimeter while dead towers are unresponsive ones. For generating the hot/dead maps, we plot the distribution of hits in each tower for each sector. Then, we choose the boundary to cut off tails of the distribution manually. The hits of photons for ${}^3\text{He}+\text{Au}$ before and after the hot/dead map applied are shown in Fig. 3.2.

- Fiducial cut: $|Z_{EMC}| < 155.0$ cm

The EMCAL towers in the edge of sector can have improperly reconstructed clusters and poor calibration. These clusters are ruled out with the help of fiducial cut.

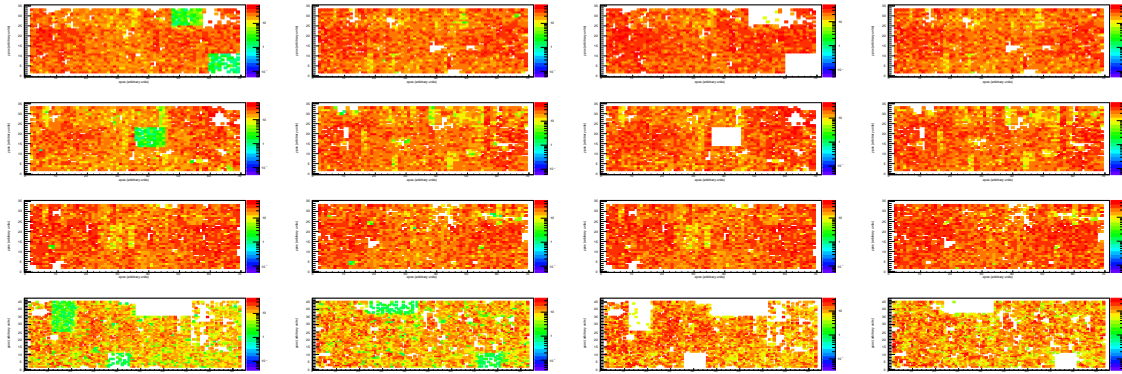


Figure 3.2: Left two columns: All hits in the eight sectors of EMCal for ${}^3\text{He} + \text{Au}$ collisions. Right two columns: Photon hits after applying hot/dead maps. In each panel, X-axis represents the tower position along beam axis while the Y-axis represents the tower height. Each bin represents individual tower and the color density profile shows the hits in the tower.

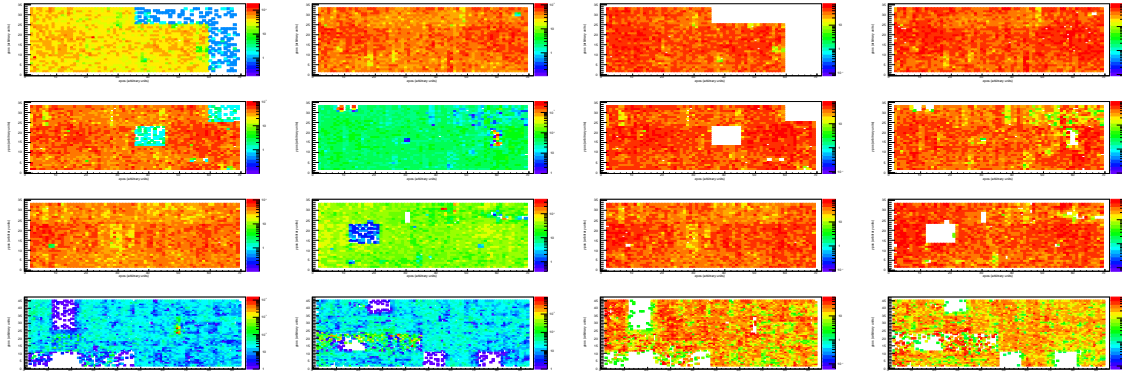


Figure 3.3: Left two columns: All hits in the eight sectors of EMCal for Run16 $d + \text{Au}$ collisions. Right two columns: Photon hits after applying hot/dead maps. In each panel, X-axis represents the tower position along beam axis while the Y-axis represents the tower height. Each bin represents individual tower and the color density profile shows the hits in the tower.

3.4.2 π^0 Trigger

- $p_T: 4 \leq p_T \leq 17 \text{ GeV}/c$

The π^0 s with $4 \leq p_T \leq 17 \text{ GeV}/c$ are selected as trigger particles. The upper limit is taken because the two π^0 photons become merged into one tower on average due to the relativistic boost of the parent pion, and thus can no longer be separately distinguished.

- Invariant mass: $0.12 \leq m_{\gamma\gamma} \leq 0.16 \text{ GeV}/c^2$.

The mass of π^0 is 0.134 GeV. The π^0 s are reconstructed by the invariant mass of photon pairs as:

$$m_{\gamma_1\gamma_2} = \sqrt{2E_{\gamma_1}E_{\gamma_2}(1 - \cos(\phi_{\gamma_1\gamma_2}))}, \quad (3.4)$$

where $\phi_{\gamma_1\gamma_2}$ is the opening angle between the two photons and E_{γ_1} (E_{γ_2}) is the energy of photon 1 (2). The reconstructed invariant mass of the photon pairs falling in the mass window of [120, 160] MeV are selected as π^0 in this analysis.

- Arm: same Arm
- $E_{\gamma_1}, E_{\gamma_2} > 1 \text{ GeV}$
- Asymmetry cut: $4 < E_{\pi^0} < 5.45$ and $\frac{E_{\gamma_1} - E_{\gamma_2}}{E_{\gamma_1} + E_{\gamma_2}} > 0.15 + 0.85 \left[\frac{E_{\pi^0} - 4}{1.25} \right]^2$

Photon pairs from same π^0 are likely to remain in same arm and in same sector of EMCAL. So, we require the condition for the photon pairs to be in same sector. There are lots of low- p_T photons which pair up with high- p_T photons to satisfy the invariant mass condition of the π^0 . These combinatorial background due to the combination of high p_T photon and low energy soft photon are reduced to a negligible level by requiring that two photons are above 1 GeV. For the cases with high combinatorial background (for e.g. central Au+Au), extra cautious is taken by applying an asymmetry (α) cut. The α is defined as follows:

$$\alpha = \left| \frac{E_{\gamma_1} - E_{\gamma_2}}{E_{\gamma_1} + E_{\gamma_2}} \right| \quad (3.5)$$

The threshold of the asymmetry cut can depend upon the centrality of the event and the energy of photons. However, this cut has not been applied in this analysis. The details about the asymmetry cut can be found in the reference [79, 80].

3.4.3 Charged Hadron Tracks

The Drift Chamber (DC) and Pad Chamber (PC1) are used to reconstruct the trajectory of the charged particles produced in collision as described previously. We choose tracks that have hits in PC1 and can be matched to tracks in the drift chamber.

- $0.5 \leq p_T \leq 10 \text{ GeV}/c$
- Track quality == 63 || 31

The charged hadrons with $0.5 \leq p_T \leq 10 \text{ GeV}/c$ are selected as partner particles in this study. The background discussed previously for charged tracks above 5 GeV/c is greatly reduced for events already containing a verified trigger π^0 . In this analysis, standard DC track quality bit-pattern is required to be either 63 or 31. Quality 63 is the highest quality which requires hits in X1, X2 wires and a unique UV and PC1 hit. Quality 31 is the second highest quality which requires hits from X1, X2 wires and a non unique PC1 hit.

- RICH ring veto ($n0 \leq 0$ cut)

Charged hadrons with p_T less than 4.65 GeV/c are not able to radiate Cherenkov light in RICH detector. Thus, $n0 \leq 0$ ($n0$: number of rings) cut can be used to reject electrons for tracks below 5 GeV/c by requiring no Cherenkov rings.

- PC3 and EMCal matching re-calibration.

The tracks reconstructed from DC and PC1 hit are projected to PC3. We also have a cut on the signalized distance between the projection point from DC/PC1 to PC3 and PC3 hit points in order to cut out high momentum false tracks. The matching window is determined by a Gaussian fit of the distribution of distance between the projection point

and PC3 hit positions. Then mean and sigma of the distances between projected point from DC/PC1 and hit on PC3 are found in the ϕ and z directions. For each track, this is defined as

$$\sigma\phi = \frac{d\phi - \langle d\phi \rangle}{\sigma_{d\phi}}, \quad \sigma z = \frac{dz - \langle dz \rangle}{\sigma_{dz}}, \quad (3.6)$$

where $d\phi$ is the distance in ϕ , dz is the distance in z , the angle brackets denote average over all tracks and $\sigma_{d\phi, dz}$ is the standard deviation in the average. We accept tracks with $\sqrt{\sigma\phi^2 + \sigma z^2} \leq 2$ in the PC3. The same procedure can be repeated for the EMCal matching re-calibration when the PC3 is replaced by the EMCal.

4 ANALYSIS DETAILS

4.1 Two particle Correlation

As we already discussed in Section 1.7.2, jet quenching is the one of the most important signatures of the QGP. These jets can be identified using standard jet reconstruction algorithms (Anti- k_t algorithm, Cone algorithm, Gaussian filter algorithm etc.). Due to the limited acceptance of PHENIX detector and overwhelming production of background particles in low energy jets in RHIC energy, it is very challenging to reconstruct jets with high purity.

In hard scattering occurring near the surface of the system, the jet from parton corresponding to shorter pathlength will be relatively unmodified in compared to the jet from the other parton which has to transverse a longer path in medium. This fact can be exploited to study the jet quenching behavior by analyzing the angular correlations between two final state jet-particle pairs. Thus this method can be called the surface biased method. In this two particle correlation method, a particle with high p_T is selected and the distribution of other associated particles is studied as function of the azimuthal angle difference ($\Delta\phi$) and pseudorapidity difference ($\Delta\eta$). Due to the limited acceptance in pseudorapidity in PHENIX, this analysis includes the correlation only in azimuthal angle difference. Typically the trigger particle belongs to the jet with shortest pathlength within QGP. Associated particles coming from the same jet as the triggers are called the nearside jet make a Gaussian-like distribution around $\Delta\phi \sim 0$ while the associated particles belonging to opposite side jet ("awayside" jet) make a Gaussian-like distribution around $\Delta\phi \sim \pi$.

Due to the incomplete azimuth coverage of the PHENIX detector, even isotropic production of the particles will show two peak structures at $\Delta\phi \sim 0$ and $\Delta\phi \sim \pi$. To take care of this limited acceptance of the detector, mixed events are generated by pairing up the trigger of one event to the partner of another event. The ratio of the same-event to

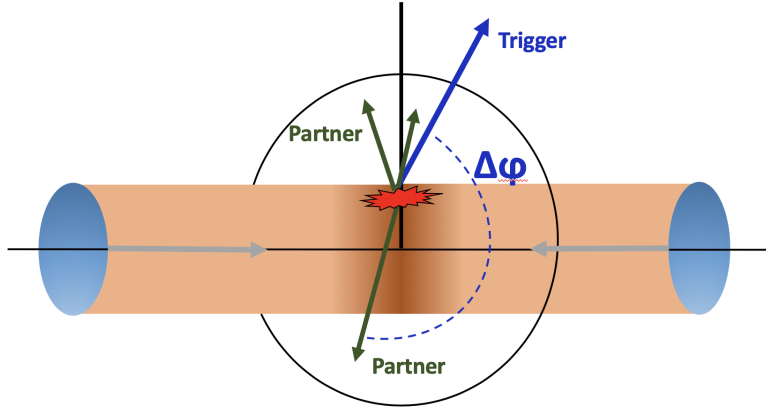


Figure 4.1: Trigger and partner particle pairs from back to back scattering parton.

the mixed-event pair distribution cancels out the detector acceptance effects leaving behind the physical correlation only. Thus, the correlation function, $C(\Delta\phi)$,

$$C(\Delta\phi) \propto \frac{N_{same}^{AB}(\Delta\phi)}{N_{mix}^{AB}(\Delta\phi)}, \quad (4.1)$$

where N_{same}^{AB} is the total trigger(A)-partner(B) pair from same events while N_{mix}^{AB} is that from mixed events. There are different methods of normalizing the Equation (4.1). This analysis implements the most common method of normalization where the same- and mixed-event event pair distribution have equal integrals.

$$C(\Delta\phi) = \frac{\frac{d\langle n_{same}^{AB} \rangle}{d\Delta\phi} / \int \frac{d\langle n_{same}^{AB} \rangle}{d\Delta\phi} d\Delta\phi}{\frac{d\langle n_{mix}^{AB} \rangle}{d\Delta\phi} / \int \frac{d\langle n_{mix}^{AB} \rangle}{d\Delta\phi} d\Delta\phi}. \quad (4.2)$$

where $\langle n_{same}^{AB} \rangle$ ($\langle n_{mix}^{AB} \rangle$) is number of measured pairs per event for same (mixed) events. Some more mathematical details related to the correlation function are in Appendix [B].

4.1.1 Acceptance Correction and Event Mixing

As stated before, the limited azimuthal acceptance of PHENIX detector and dead or inefficient areas of the detector can be removed by creating mixed events. The mixed events are created by pairing up the triggers of one event to the partners of another event.

For this analysis, the ERT data sets are mixed with MinBias data set for proper acceptance correction and better background estimation since most important parts of the combinatoric background and acceptance correction are where the jet is paired with random particles from the underlying event. The correlation in such generated mixed events is only due to the same detector acceptance. Thus dividing same event pair distribution to mixed pair distribution cancels out the pair detector acceptance effects leaving only the physical correlation. Hence the definition of correlation function in Equation (4.2).

The acceptance correction $Acc(\Delta\phi)$ for the particle pairs can be defined as,

$$\frac{d\langle n_{same}^{AB} \rangle}{d\Delta\phi} = \frac{\frac{d\langle n_{same}^{AB} \rangle}{d\Delta\phi}}{Acc(\Delta\phi)}, \quad (4.3)$$

where the $\langle n_{same}^{AB} \rangle$ ($\langle n_{mix}^{AB} \rangle$) is true (measured) number of pairs per event. Thus the acceptance correction is found to be (details in Appendix [B].)

$$Acc(\Delta\phi) = \frac{d\langle n_{mix}^{AB} \rangle}{d\Delta\phi} \frac{\epsilon_{mix}^{AB}}{\langle n_{mix}^{AB} \rangle} \int d\Delta\phi, \quad (4.4)$$

with

$$\epsilon_{mix}^{AB} = \kappa \epsilon^A \epsilon^B. \quad (4.5)$$

where, κ is the pair cut survival probability, which can be taken as being approximately equal to unity for this analysis. Also, the ϵ is the particle detection efficiency. The integration range in the RHS of Equation (4.4) depends on the range of measurement ($\int d\Delta\phi = \pi$ for "folded" measurements, and occasionally $\int d\Delta\phi = 2\pi$).

4.1.2 Two-Source Model

One of the important benefits from two particle correlation is that the contribution from jets and flow can be separated. According to a commonly used *two source model*, the same-event pair distribution is the sum of the distribution due to the particle pairs from hard scattering partons (jet pairs) and that due to the combinatorial background pairs from anisotropic flow production of particles relative to the reaction plane. Thus,

$$\frac{dn_{same}^{AB}}{d\Delta\phi} = \frac{dn_{jet}^{AB}}{d\Delta\phi} + \frac{dn_{comb}^{AB}}{d\Delta\phi}, \quad (4.6)$$

where variable n is counts per event. In terms of per trigger yield,

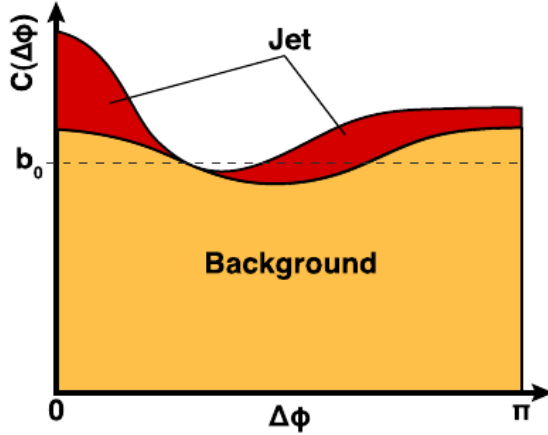


Figure 4.2: The decomposition of correlation function into jet and background pairs with background level b_0 [37]. The copyright permission for the figure is attached in Figure D.25

$$\frac{1}{n^A} \frac{dn_{same}^{AB}}{d\Delta\phi} = \frac{1}{n^A} \left[\frac{dn_{jet}^{AB}}{d\Delta\phi} + \frac{dn_{comb}^{AB}}{d\Delta\phi} \right]. \quad (4.7)$$

The per trigger yield (PTY) is used to divide out to first order the effects of different trigger efficiency for different triggers. The combinatorial background term is due to the pairs of flowing soft particles each following the distribution given by Equation (4.8).

$$\frac{dn_{comb}^{AB}}{d\Delta\phi} \propto \left[1 + \sum_{n=1}^{\infty} \langle 2v_n^A v_n^B \rangle \cos(n\Delta\phi_{AB}) \right], \quad (4.8)$$

where v_n 's are the flow coefficients. The elliptical coefficient (v_2) dominates the flow contribution. In the two particle correlation method, it is not necessary to determine reaction plane for each event. Now, proceeding with some substitution in Equation (4.7) leads (details in Appendix [B]) to the working equation,

$$C(\Delta\phi_{AB}) = J(\Delta\phi_{AB}) + b_0 \left[1 + \sum_{n=1}^{\infty} \langle 2v_n^A v_n^B \rangle \cos(n\Delta\phi_{AB}) \right]. \quad (4.9)$$

The jet function, $J(\Delta\phi_{AB})$, is the fraction of the correlation function from only jet-jet pairs. The second term in the RHS of Equation (4.9) is from background contribution, which is described by a Fourier series. The b_0 is the combinatorial background level which normalizes the contribution of combinatorial pairs to the correlation function.

4.1.3 Background Level (b_0)

In order to extract the jet signal in two particle correlations, we need to determine the combinatorial background. There are different methods to find the background level (b_0) given by Equation (4.10). In this analysis, the ZYAM method is implemented to find the background level,

$$b_0 = \frac{\langle n_{bg}^{AB} \rangle}{\langle n_{same}^{AB} \rangle}. \quad (4.10)$$

The ZYAM method is described in the next section.

4.1.3.1 Zero Yield At Minimum (ZYAM)

In the ZYAM [37] method, there is assumed to be a region or point where the jet contribution to the correlation function is negligible, which is approximately the case around $\Delta\phi = \pi/2$. Apart from the assumption of independent sources for the jet and background correlations, the validity of ZYAM requires 1) approximate vanishing of jet contribution yield in one or more points and 2) correlation sample which is sufficiently well-sampled to determine a stable and precise minimum value.

In heavy ion collisions at high p_T ($\geq 4GeV$) or in small systems, the near-side and away-side jet peaks are well separated with background dominated broad region between them. Thus, ZYAM is an ideal method to determine the background level in those systems. This method might over-subtract the background if the jet contribution is significant near the ZYAM point. Also, this method might under-subtract if the statistics are too low.

4.1.3.2 Absolute Normalization Method (ABS)

The absolute normalization method (ABS) [37] uses the direct calculation of quantities in Equation (4.10) for the determination of background level. In the ABS method, the background is assumed to be combinatorial in nature and the background pair production rate is ideally equal to the product of the single particle production rates i.e. $\langle n_{bg}^{AB} \rangle = \langle n^A \rangle \langle n^B \rangle$. Thus,

$$b_0^{ideal} = \frac{\langle n^A \rangle \langle n^B \rangle}{\langle n_{same}^{AB} \rangle}, \quad (4.11)$$

However, there is a multiplicity correlation due to the dependence of $\langle n^A \rangle$ and $\langle n^B \rangle$ on the centrality of the event. This multiplicity effect is corrected by a scale factor, ξ , given by Equation (4.12).

$$\xi = \frac{\langle n^A n^B \rangle}{\langle n^A \rangle \langle n^B \rangle}, \quad (4.12)$$

Also, by taking care of the effect of pair multiplicity due to rejection of pairs with small separation, the final working equation is given as,

$$b_0 = \xi \frac{\kappa \langle n^A \rangle \langle n^B \rangle}{\langle n_{same}^{AB} \rangle}. \quad (4.13)$$

Because we effectively make no explicit pair cuts, κ can be taken as 1.

4.2 Jet Pair Quantification

4.2.1 Per-trigger Yield Nuclear Modification Factor (I_{AA})

The $\Delta\phi$ -integrated per-trigger yield (Y) for the near- and away-side regions can be used to characterize the modification of jets. The per-trigger yield nuclear modification factor, I_{AA} , is introduced for the comparative study of those yields between Au+Au and $p+p$ collisions.

$$I_{AA} = \frac{Y^{AA}}{Y^{pp}} = \frac{\int_{\Delta\phi_1}^{\Delta\phi_2} \left(\frac{1}{n_A} \frac{dn^{AB}}{d\Delta\phi} \right)_{AA} d\Delta\phi}{\int_{\Delta\phi_1}^{\Delta\phi_2} \left(\frac{1}{n_A} \frac{dn^{AB}}{d\Delta\phi} \right)_{pp} d\Delta\phi}, \quad (4.14)$$

I_{AA} might be of near- or away-side depending upon the integration range. Since I_{AA} is the ratio of per-trigger yield, no scaling is required as in R_{AA} . The yield roughly represents

the number of particles produced per jet. Thus the yield is expected to be same in $p+p$ collisions as in Au+Au collisions if there is no modification. So, any deviation of I_{AA} from unity represents modification of jets due to the presence of medium. Typically a large suppression of the away-side I_{AA} due to the QGP energy loss/quenching of the away-side jet is found in Au+Au collisions. Along with this overall suppression level, at certain low energy ranges for partner particles, an enhancement of I_{AA} is found to occur which is also thought to be part of the energy loss process, in that the energy that is lost must eventually reappear nearby the jet in the form of low energy particles. Generally, the observables for jet pair quantification are plotted as a function of a variable, $z_T \equiv \frac{p_T^{partner}}{p_T^{trigger}}$. The z_T is defined to approximate z in fragmentation function, $D_c^h(z)$ defined in Section 1.4.4 which is known to be approximately universal, that is, independent of jet energy.

4.2.2 Double Ratio (R_I)

The large systematic errors in I_{AA} is one of the main drawbacks in the study of possible jet modification in the light-heavy ion collision where the suppression levels could be very small. The double ratio, R_I , of away to near side yield first used in the analysis of Bing Xia [3] and the Ohio University group of Justin Frantz substantially decreases the systematic errors. The R_I is defined as,

$$R_I \equiv \frac{Y_{away}^{AA}/Y_{near}^{AA}}{Y_{away}^{pp}/Y_{near}^{pp}}. \quad (4.15)$$

Because in Au+Au, it is known that energy loss jet suppression modifies the near-side very little due to the surface bias effect (surviving high p_T triggers more likely from surface since these are not suppressed or less suppressed—which was described previously), then essentially inserting the nearside into I_{AA} to obtain R_I does not alter the values of R_I compared to I_{AA} , or does so very little. But taking the double ratio and choosing to integrate over whole hemispheres, results in a number of benefits which substantially reduce the systematic errors. The benefit of using R_I can be itemized as follows;

- **No need or virtually no sensitivity to single partner hadron efficiency:** The major source of systematic error in I_{AA} is due to the single particle detection efficiency. Since the single particle efficiency is same for the near-side ($|\Delta\phi| = 0$ to $|\Delta\phi| = \pi/2$) and away-side ($|\Delta\phi| = \pi/2$ to $|\Delta\phi| = \pi$) regions, no single partner hadron efficiency is needed, and the systematic error due to the single particle efficiency is removed completely in the ratio R_I . (The trigger single efficiency is of course canceled by the per trigger yields).
- **Little or no sensitivity to v_n except for v_1 :** The integration of per-trigger yield in the near-side as well as in the away-side in the full $\pi/2$ region, completely cancels out the contribution of even v_n . This is because on each $\pi/2$ interval, once ZYAM is subtracted, the modulations have equal positive and negative contributions. The contribution of the odd v_n in those two regions decreases with an increase in harmonic order n : for $n \geq 3$, the number of oscillations in each $\pi/2$ interval is high enough to also have a strong cancellation of positive and negative contributions post-ZYAM. This is described schematically Figure 4.3.

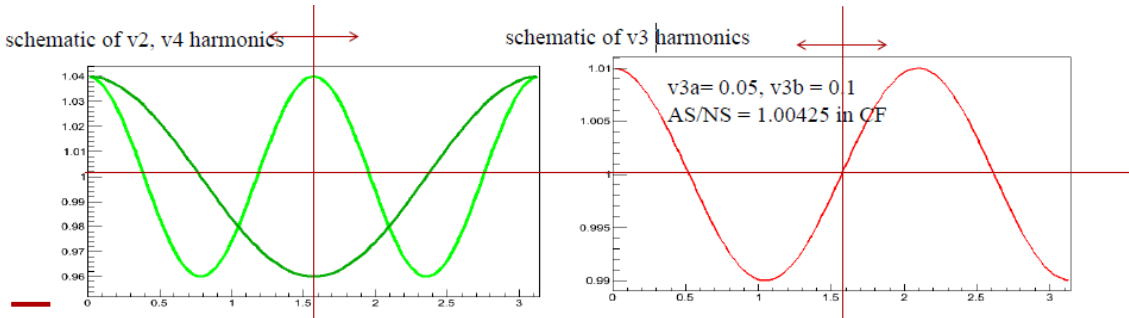


Figure 4.3: Schematic of how individual v_n components cancel in R_I .

Thus we find that in the small systems, all contributions except v_1 can be neglected.

- **Low sensitivity on ZYAM/Background Normalization:** Because the level of background (b_0) subtracted to go from jet function (JF) $J(\Delta\phi)$ or correlation function

(CF) $C(\Delta\phi)$ contributes equally to the near-side and away-side integration region, there is also a much reduced sensitivity to exact value of b_0 . Thus the systematic due to this notorious source is also much smaller than for I_{AA} —so much so that even in Au+Au as long as b_0 is chosen in the right neighborhood, the propagated systematic from any imperfection in this subtraction level, will be relatively negligible.

- **Theory/Interpretation Advantage (Low sensitivity to "background" potential theoretical modifications in overall cross sections):** This advantage of R_I has to do with using the per-trigger yields and ratio of shape regions. Any competing "background" non-energy loss like effect that results from a modification of the overall cross section of di-jets will generally affect R_I only at higher orders because they will affect both jets/sides of the correlation equally, and hence cancel in the ratio to first order. For example known nuclear modifications to the previously discussed parton distribution functions will generally cancel out, as we will see in the final interpretations of our results in a later section.

4.2.3 Corrections to R_I

4.2.3.1 Rapidity Acceptance Correction

Since the effects we are looking at here are small (10-15% suppression/enhancement), we need to consider the η acceptance correction along with the ϕ acceptance correction. The correction factor for the η acceptance is derived based on the assumption that the angular jet width is the same in $\Delta\phi$ and $\Delta\eta$. The near side correction factor can be written as [81],

$$R_{\Delta\eta} = \frac{1}{\frac{1}{\sqrt{2\pi\sigma_N^2}} \int_{-0.7}^{0.7} \exp\left(-\frac{\Delta\eta}{2\sigma_N^2}\right) acc(\Delta\eta) d\Delta\eta}, \quad (4.16)$$

where $acc(\Delta\eta) = (0.7 - |\Delta\eta|)/0.7$ is PHENIX pair acceptance function in $|\Delta\eta|$ obtained by convolving two flat distributions in $|\Delta\eta| < 0.35$. The $acc(\Delta\eta)$ has triangular shape. The

away-side correction factor can be written as [81],

$$R_{\Delta\eta} = \frac{2(0.7)}{\int_{-0.7}^{0.7} acc(\Delta\eta)d\Delta\eta} = 2. \quad (4.17)$$

For R_I , this factor cancels, so only the correction for the near-side's matters. The function of $\Delta\eta$ correction for the nearside (NS) derived in [81], is shown in Figure 4.4—this depends on the NS width so if the widths in $x+Au^{13}$ vs. $p+p$ are different a small correction needs applied to RI, which is the ratio of the correction for $x+Au$ vs $p+p$. For both away-side jet yields, the correction is simply 2, so there is no effect (i.e. ratio of corrections = $2/2 = 1$).

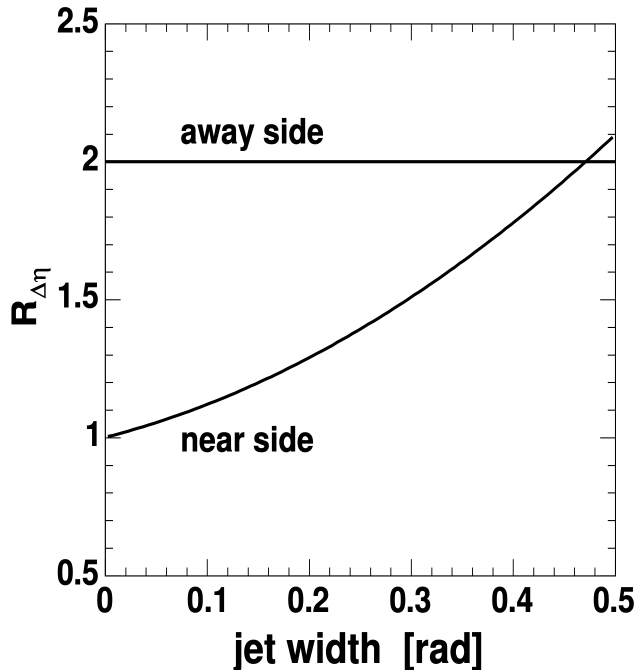


Figure 4.4: The function of the $\Delta\eta$ correction, vs width, which is close to a linear function for nearside and constant (2) for away-side. This figure is taken from [81]. The copyright permission for the use of the figure is attached in Fig D.26.

The $\Delta\eta$ correction in nearside jet yields depends on the width of the nearside jet. The width of the nearside jet is not affected by the uncertainty due to the π^0 combinatorics.

¹³ $x+Au$: x implies a small nucleus. For eg. p , d , 3He , etc.

It is determined by fitting the jet function with two Gaussian plus a pedestal background. The nearside Gaussian peak widths are shown as an example in Figure 4.5. These plots show a subtle modification in the d +Au collisions, and for x+Au collisions we assume the same possibility of slightly different peak widths (recent p +Au results from the Michigan group [82] show explicitly that the widths are modified in that system, so this behavior is now confirmed and should be considered the expectation for d +Au and ${}^3\text{He}+\text{Au}$).

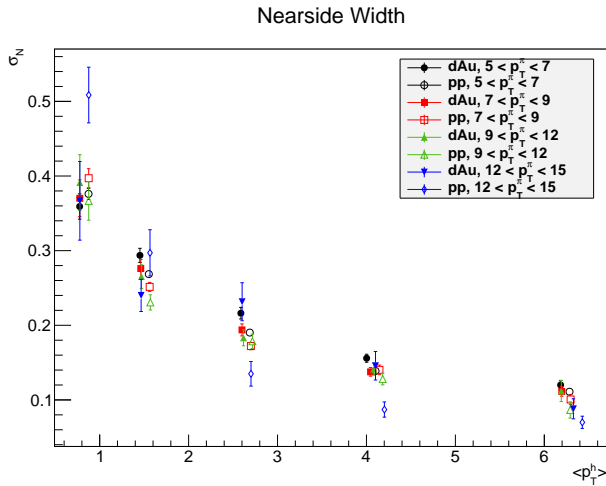


Figure 4.5: Nearside width for 0-20% centrality d +Au and $p+p$ used for $R_{\Delta\eta}$ from Gaussian fits. The p_T^h values for $p+p$ are shifted to the right by 0.1. The figure is taken from [3]. Courtesy Bing Xia.

In Figure 4.6, the size of the $R_{\Delta\eta}$ correction is shown for the case of d +Au. Since as previously stated, our R_I observable is only sensitive to the ratio of the $p+p$ to x+Au corrections. Thus, in the figure only the ratio of the $p+p$ to x+Au ($p+p$ to d +Au in this case) matters, so for each grouping of points, the ratio of the two points with the same colors. Thus the correction is never larger than a few percent level for the two trigger bins 5-7/7-9 GeV, trigger bins which are focused on. The uncertainties are usually even smaller as will be tabulated in the next section, although for the lowest associated p_T bin, we use conservative error estimation that results in a uncertainty that is generally larger than the

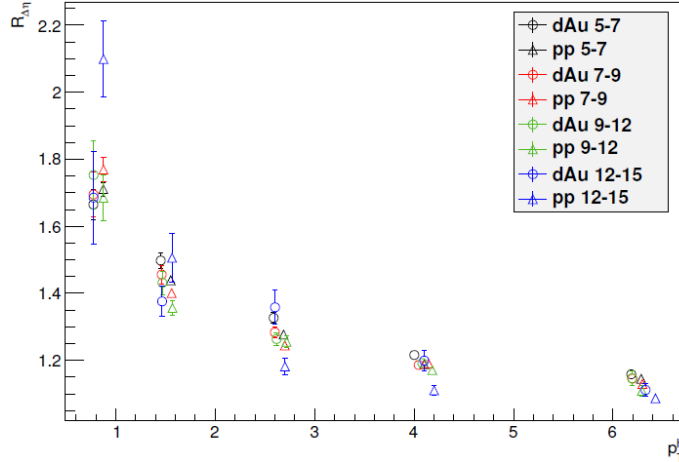


Figure 4.6: Actual Nearside $R_{\Delta\eta}$ corrections for $d+\text{Au}$. Although the actual size of the correction ranges from 1.2-1.4, for the R_I observable, only the ratio of the $p+p$ to $x+\text{Au}$ correction($p+p$ to $d+\text{Au}$ in this case) matters, so for each grouping of points, the ratio of the two points with the same colors. Thus the R_I correction is generally very small, on the percent level. The figure is taken from [3].

size of the correction. We believe that this is due to the fit in that bin having non-Gaussian shape and could be reduced, which we can investigate further for the final published result.

4.2.3.2 Bleeding Correction

Another small correction which depends on the widths of the peaks in the correlation functions is the peak "bleeding correction". The tail of the near (away)-side Gaussian peaks could extend to the away (near) side. This is called "bleeding effect". The bleeding effect in near (away) side yield is taken care by adding its Gaussian tail which is leaked to away (near) side and subtracting the Gaussian tail from away (near) side. We have used $\pi/2$ as the integration range, which is the mid point of away (π) and near (0) side peak. The bleeding correction for nearside and awayside yield is done as in Equation (4.18) and

Equation (4.19).

$$Y_N = \int_0^{\pi/2} JF(\Delta\phi) d\Delta\phi - \int_0^{\pi/2} Gaus_A(\Delta\phi) d\Delta\phi + \int_{\pi/2}^{\pi} Gaus_N(\Delta\phi) d\Delta\phi, \quad (4.18)$$

$$Y_A = \int_{\pi/2}^{\pi} JF(\Delta\phi) d\Delta\phi - \int_{\pi/2}^{\pi} Gaus_N(\Delta\phi) d\Delta\phi + \int_0^{\pi/2} Gaus_A(\Delta\phi) d\Delta\phi. \quad (4.19)$$

The first terms in the Equation (4.18) and (4.19) are from the histograms. The last two terms in the equations are calculated from the fitted Gaussian function. The size of the bleeding effect correction in R_I for the original d +Au measurement is shown in Table 4.1. Considering larger yields, the effect of correction is very small.

Table 4.1: The size of the bleeding effect correction on the awayside in 0-20% d+Au collisions (The unit of p_T is GeV/c). The table is taken from [3].

%	$0.6 < p_T^h < 1$	$1 < p_T^h < 2$	$2 < p_T^h < 3$	$3 < p_T^h < 5$	$5 < p_T^h < 7$
$5 < p_T^\pi < 7$	2.54	0.783	0.161	0.0103	2.87e-4
$7 < p_T^\pi < 9$	0.97	0.22	5.78e-3	2.62e-4	1.77e-05
$9 < p_T^\pi < 12$	0.25	0.025	7.17e-4	2.14e-4	4.43e-07
$12 < p_T^\pi < 15$	1.4	0.0137	0.0207	6.93e-06	1.99e-09

4.2.3.3 ERT Trigger Turn-on Cross-check

As mentioned in Section 3.3, the ERT trigger in case of ${}^3\text{He}+\text{Au}$ is not fully efficient until $\sim 6\text{-}7$ GeV/c. To the first order, the trigger efficiency cancels when we make per-trigger-yield. But for the R_I , there is a second order effect since R_I contains ${}^3\text{He}+\text{Au}$ to $p+p$ ratio. The left of the Figure 4.7 shows the π^0 trigger ratio for Run14 ${}^3\text{He}+\text{Au}$ to Run15 $p+p$ collisions. The trigger turn-on for Run15 $p+p$ and Run14 ${}^3\text{He}+\text{Au}$ are different. This implies, mean p_T of trigger will be slightly different between those runs. If the difference

is big enough then it needs correction. For this, we did a study by weighting the triggers in Run14 ${}^3\text{He}+\text{Au}$ with respect to Run15 $p+p$ while filling the histograms.

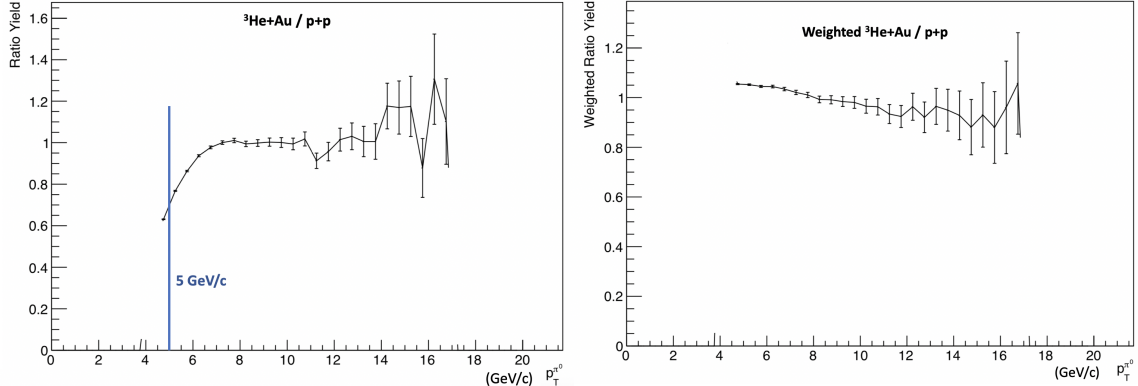


Figure 4.7: Left: The ratio of π^0 spectrum of Run14 ${}^3\text{He}+\text{Au}$ ERT to that of $p+p$. The blue vertical line is at 5 GeV. Right: The ratio of re-weighted π^0 spectrum of Run14 ${}^3\text{He}+\text{Au}$ ERT to π^0 spectrum of $p+p$.

The π^0 trigger ratio for Run14 ${}^3\text{He}+\text{Au}$ to Run15 $p+p$ collisions after re-weighting is shown in the right of Figure 4.7. The re-weighted spectra are little over corrected. Even after this re-weighting, there is negligible change in R_I . In this analysis, we have used the re-weighted π^0 spectra of ${}^3\text{He}+\text{Au}$ to produce the results.

4.3 Error Analysis

In this analysis, the uncertainties associated with each measured variable are different, especially for R_I , where most of the systematic are cancelled out, completely or mostly. In R_I , any uncertainty from efficiency is cancelled entirely. Some of other systematic uncertainties are correlated with each other, which dramatically reduce the size of systematic uncertainty. The uncertainties deserve a separate section in any measurement, inside or outside physics. Here is a list of uncertainties considered in this analysis.

- Statistical uncertainty

- Uncertainty from the mis-constructed π^0 combinatorics
- Uncertainty from ZYAM
- Uncertainty from the bleeding correction
- Uncertainty from $R_{\Delta\eta}$
- Uncertainty from v_3 contribution

The statistical uncertainty is treated by ROOT. The rests are the systematic uncertainties.

4.3.1 Uncertainty from Mis-Constructed (Fake) π^0 Combinatorics

The contribution of the mis-constructed π^0 in R_I can be quantified using the signal to background ratio and side band yields. The background (B) is found by linearly fitting the invariant mass distribution of π^0 in 2σ interval and taking the integral of the fit. Then, the background is subtracted from the distribution and integral of Gaussian fit of the remaining distribution is taken to find out the signal (S). The measured per trigger yield in jet function can be written as,

$$Y^{meas} = \frac{S.Y^{\pi^0} + B.Y^{fake}}{S + B}, \quad (4.20)$$

The contribution due to true π^0 can be written as,

$$Y^{\pi^0} = Y^{meas} + \frac{1}{S/B} (Y^{meas} - Y^{fake}), \quad (4.21)$$

And,

$$\begin{aligned} \frac{Y^{\pi^0}}{Y^{meas}} &\equiv r = 1 + \frac{1}{S/B} \frac{(Y^{meas} - Y^{fake})}{Y^{meas}}, \\ &= 1 + \frac{1}{S/B} \delta r. \end{aligned} \quad (4.22)$$

where,

$$\delta r = \frac{(Y^{meas} - Y^{fake})}{Y^{meas}}.$$

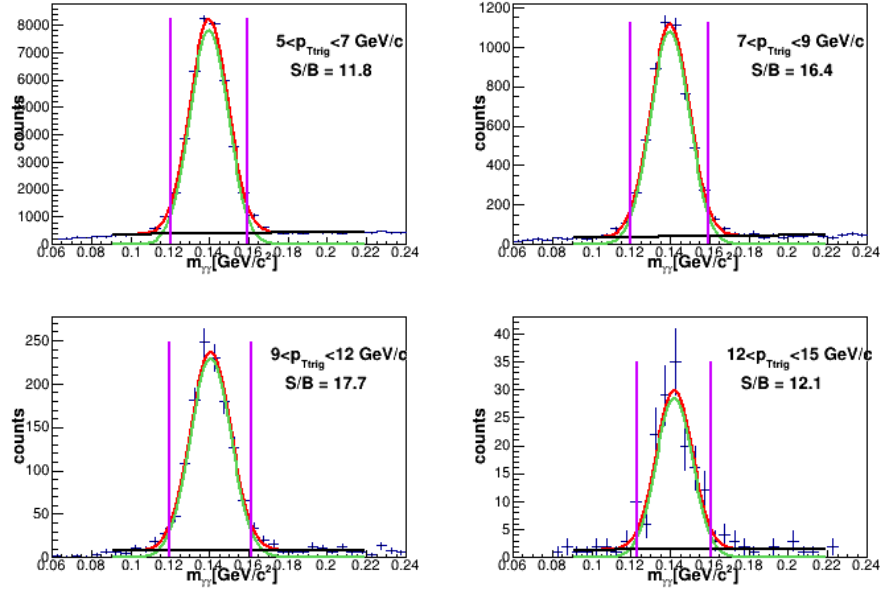


Figure 4.8: π^0 invariant mass distribution for ${}^3\text{He} + \text{Au}$ in 0-20 % centrality bin. Red line: Gaussian+line fit to data. Black line: Straight line fit for background estimation. Green line: Gaussian fit after background subtraction. Signal (S) is found by integrating the green line in 2σ from the peak (in between two vertical magenta lines). Background is found by integration of black line in the same interval.

Thus, the ratio of away side to near side can be approximated up to first order as;

$$\begin{aligned} \frac{r_{\text{away}}}{r_{\text{near}}} &= \frac{1 + \frac{1}{S/B} \delta r_{\text{away}}}{1 + \frac{1}{S/B} \delta r_{\text{near}}}, \\ &\simeq \left(1 + \frac{1}{S/B} \delta r_{\text{near}}\right) \left(1 - \frac{1}{S/B} \delta r_{\text{away}}\right), \\ &\simeq 1 + \frac{1}{S/B} (\delta r_{\text{away}} - \delta r_{\text{near}}). \end{aligned} \quad (4.23)$$

For the mis-constructed π^0 systematic, we assign the size of this uncertainty as 100% of the relative size of π^0 combinatorics correction, using side-bands. As discussed before these are negligible due to the small S/B in the small systems. The corrections are usually uncorrelated with others in most of the quantities I list, however, they are correlated in R_I . They are both subtracted in near and away side peaks, which make the effect less in R_I . The

relative size of this systematics in x+Au and $p+p$ is calculated by Equation 4.24.

$$\frac{\Delta RI}{RI} = \frac{1}{S/B} \left| \frac{\Delta Y_{\pi^0}^A}{Y^A} - \frac{\Delta Y_{\pi^0}^N}{Y^N} \right|, \quad (4.24)$$

where,

$$\Delta Y_{\pi^0}^{A(N)} = Y^{meas} - Y^{fake}.$$

is correction from π^0 combinatorics in away (near) side yields in x+Au and $Y^{A(N)}$ is measured yield in away (near) side.

The fake π^0 yield is estimated by the combination of per-trigger yields taken from triggers in the two side-bands (trigger photon pairs with invariant mass in the side bands). For this analysis, the $d+$ Au side band triggered yields are used to estimate the size of the fake π^0 per-trigger yields in ${}^3\text{He}+\text{Au}$ (to construct the ΔY 's), but with the ${}^3\text{He}+\text{Au}$ S/B levels applied, which are slightly worse.

- low band: $0.065 \text{ GeV} \leq m_{\gamma\gamma} \leq 0.115 \text{ GeV}$
- high band: $0.165 \text{ GeV} \leq m_{\gamma\gamma} \leq 0.200 \text{ GeV}$

4.3.2 Uncertainty from ZYAM

The uncertainty of the ZYAM level is determined by the size of the b_0 parameter error from fit during ZYAM procedure. Consider δ as the error in fit in the ZYAM level, then the near to away side yield ratio can be written as,

$$\begin{aligned} y &= \frac{a + c\delta}{b + d\delta} \\ &= \frac{a}{b} \frac{1 + \frac{c}{a}\delta}{1 + \frac{d}{b}\delta} \\ &\approx \frac{a}{b} \left(1 + \frac{c}{a}\delta\right) \left(1 - \frac{d}{b}\delta\right) \\ &\approx \frac{a}{b} \left[1 + \left(\frac{c}{a} - \frac{d}{b}\right)\delta\right] \end{aligned} \quad (4.25)$$

where c and d are the integration range for near and away side respectively. In our case, integration range is $\pi/2$ for both since the yields are integrated in $0 - \pi/2$ and $\pi/2 - \pi$. Since

the R_I is the double ratio, the systematic error in the R_I due to ZYAM can be quantified as;

$$\sigma_{R_I}^{ZYAM} = R_I \times \sqrt{\left[\left(\frac{\pi/2}{Y_{xAu}^A} - \frac{\pi/2}{Y_{xAu}^N} \right)^2 \times (\delta_{xAu}^{ZYAM})^2 + \left(\frac{\pi/2}{Y_{pp}^A} - \frac{\pi/2}{Y_{pp}^N} \right)^2 \times (\delta_{pp}^{ZYAM})^2 \right]} \quad (4.26)$$

The reason we combine $p+p$ and $x+\text{Au}$ as the root of sum of squares because we believe the uncertainty of b_0 in $p+p$ and $x+\text{Au}$ fitting are uncorrelated with each other.

4.3.3 Uncertainty from Bleeding correction

The half of the bleeding correction itself is taken as uncertainty due to the bleeding effect. The corrections in the lowest p_T bins, ($5-7 \times 0.6-1$) GeV/c, needs a careful treatment since the correction is relatively large in those bins. The effect due to the bleeding correction for $p+p$ and ${}^3\text{He}+\text{Au}$ ($d+\text{Au}$) are similar because the jets have similar shape and width in those systems. Since R_I is the double ratio of ${}^3\text{He}+\text{Au}$ ($d+\text{Au}$) to $p+p$, the effect due to the bleeding correction partially get cancelled. Also, while taking care of bleeding effect, the loss in one side is added to another side and vice versa. Thus, the bleeding correction is not exactly independent variable. The propagation of the uncertainties of the fitted width could be better estimate for the uncertainty due to bleeding correction. For this dissertation, we have used the half value of correction itself as a conservative estimate.

4.3.4 Uncertainty from $R_{\Delta\eta}$

The uncertainty in R_I due to the $\Delta\eta$ acceptance correction is evaluated from the functions shown Figure 4.4. As already mentioned, the away-side yield is not affected due to η acceptance. Thus the uncertainty in R_I is only due to the acceptance correction in nearside yield. Thus the uncertainty of $R_{\Delta\eta}$ is obtained by varying the near side width by error from the fitting. Then the error is propagated to the nearside yield and then in R_I . As the uncertainty in ${}^3\text{He}+\text{Au}$ and $d+\text{Au}$ are treated as uncorrelated, the uncertainty in R_I is calculated as the square root of sum of the squares of those uncertainties.

The size of the uncertainties usually a few percent, is tabulated in Table 4.2 at the end of this section and is discussed above during the discussion of the correction $R_{\Delta\eta}$ itself. In

particular the relatively large uncertainty on the lowest z_T point is conservative, and may be investigated further, e.g. when the results are finalized.

4.3.5 v_3 Contribution

The results for both $d+\text{Au}$ (following the previous analysis) and now also ${}^3\text{He}+\text{Au}$ don't include any flow subtraction due to the estimation that flow effects are small in the small-system ${}^3\text{He}+\text{Au}$, and also because no v_2, v_3 measurements with sufficient precision are available for ${}^3\text{He}+\text{Au}$. As systematic check, we used $\text{Au}+\text{Au}$ v_3/v_2 in the ${}^3\text{He}+\text{Au}$ system. This should also provide a recheck of the $d+\text{Au}$ results since flow effects which enter the two particle correlations results only through the combinatoric background subtraction of the pedestal, depend on the relative size of the background which is smaller in $d+\text{Au}$ than ${}^3\text{He}+\text{Au}$. As the high $p_T v_n$ due to energy loss should substantially smaller in

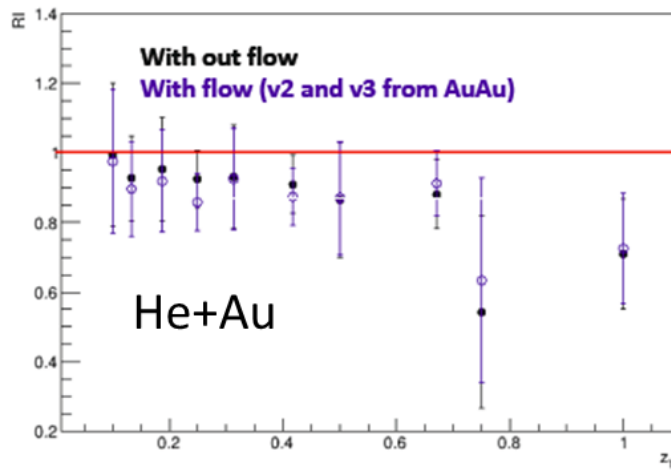


Figure 4.9: ${}^3\text{He}+\text{Au}$ R_l with and without flow vs z_T . Note in this plot other corrections are not applied. The flow estimations come from 0-20% $\text{Au}+\text{Au}$ where we expect the high p_T flow, which is driven by energy loss to be smaller, and thus this test should substantially overestimate the effects of flow. Because of the high jet signal to background in ${}^3\text{He}+\text{Au}$ due to still having relatively small total multiplicity, the effects are negligible as in $d+\text{Au}$.

${}^3\text{He}+\text{Au}$ compared to $\text{Au}+\text{Au}$, this test should exaggerate size of v_n effects. We measured

the average of relative difference between with and without the use of v_2 and v_3 as shown in Figure 4.9. We conservatively took 2.0 % as the total systematics due to this effect.

On the relative difference plot, Figure 4.10, statistical error bars are only estimated by the size of the difference in the error bar between the two cases—this should be an underestimate—in lieu of exactly accounting for the overlap in statistics in the two samples. The fit value for over the lowest z_T points where the effect should be the largest and where statistical precision is best, yields an average deviation of about 2%. Even though some points have larger deviation, we use this value, 2%, as the systematic for all points, considering again that we are using the over-exaggerated Au+Au flow values.

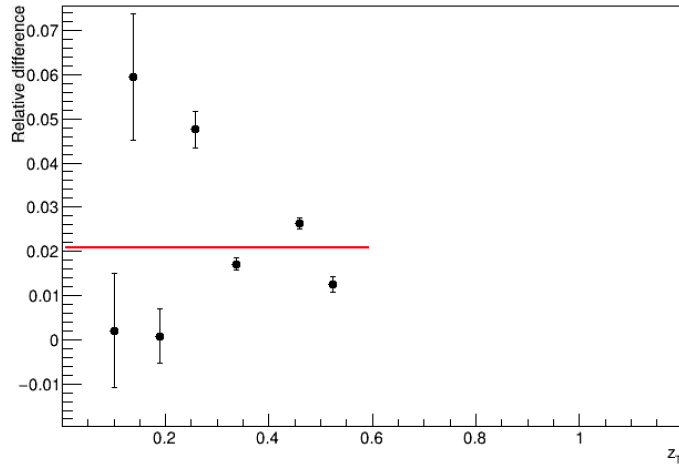


Figure 4.10: The relative difference (absolute value) in R_I with and with out the overestimated flow vs z_T . Red line is fit value over low z_T range.

4.3.6 Tabulation of Uncertainty Sizes

The percentage contribution the three previously discussed uncertainties in R_I for $^3\text{He}+\text{Au}$ are tabulated in Table 4.2. For $d+\text{Au}$ the uncertainty sizes are similar,

Table 4.2: Uncertainties and their Contributions for R_I in ${}^3\text{He}+\text{Au}$ collisions at $\sqrt{s_{NN}} = 200 \text{ GeV}$.

Uncertainty	%	$0.6 < p_T^h < 1$	$1 < p_T^h < 2$	$2 < p_T^h < 3$	$3 < p_T^h < 5$	$5 < p_T^h < 7$
ZYAM	$5 < p_T^\pi < 7$	0.33	0.28	0.18	0.20	0.19
	$7 < p_T^\pi < 9$	0.37	0.31	0.17	0.12	0.71
Bleeding	$5 < p_T^\pi < 7$	1.15	0.13	0.03	3.72e-06	2.16e-07
	$7 < p_T^\pi < 9$	1.05	0.03	1.72e-05	2.9e-07	5.05e-10
Delta Eta	$5 < p_T^\pi < 7$	2.03	2.38	1.41	1.02	1.83
	$7 < p_T^\pi < 9$	2.93	4.03	2.01	1.66	2.76

5 RESULTS AND DISCUSSIONS

5.1 Baseline Measurement: $p+p$

To extract the possible effects from medium in light-heavy ion collisions, nucleon-nucleon ($p+p$) collisions are used as baseline comparison. In this analysis, we use Run15 $p+p$ data at $\sqrt{s_{NN}} = 200$ GeV from PHENIX with using the ERT Photon triggers. The excellent statistics for this run of $p+p$ helps to improve the previous ratio plots from previous analyses of $d+\text{Au}$ in addition to the new ${}^3\text{He}+\text{Au}$ and $d+\text{Au}$ reanalyses as well.

5.1.1 Correlation Function and Jet Function

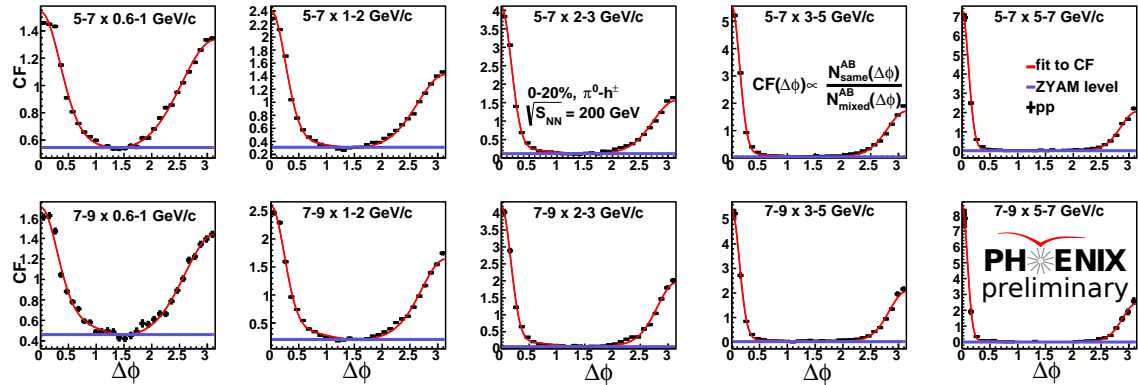


Figure 5.1: π^0 -hadrons correlation function (PHENIX Preliminary approved) for Run15 $p+p$ collisions. The red line is the fit for the data and the blue line is the background level from ZYAM method. Trigger p_T bins: [5.0 - 7.0, 7.0 - 9.0] GeV/c running from top to bottom. Partner p_T bins: [0.6 - 1.0, 1.0 - 2.0, 2.0 - 3.0, 3.0 - 5.0 and 5.0 - 7.0] GeV/c running from left to right.

Figure 5.1 shows the PHENIX preliminary approved π^0 -hadron correlation function for $p+p$ collisions at PHENIX in 2015. The result shows two clear peaks around 0 and π azimuthal angular difference for each trigger and partner bins. The blue line shows the ZYAM level. The ZYAM level is obtained without considering the flow effects.

This ZYAM level is subtracted from the correlation function to get jet function shown in Figure 5.2. As we are only interested in the R_I observable, which only involves the Away-side/Near-side ratio, and thereby exactly cancels efficiency and other corrections, these have no corrections applied for the shown jet functions. Excellent statistics were observed for all trigger and partner p_T bins in the jet functions as shown in Figure 5.2.

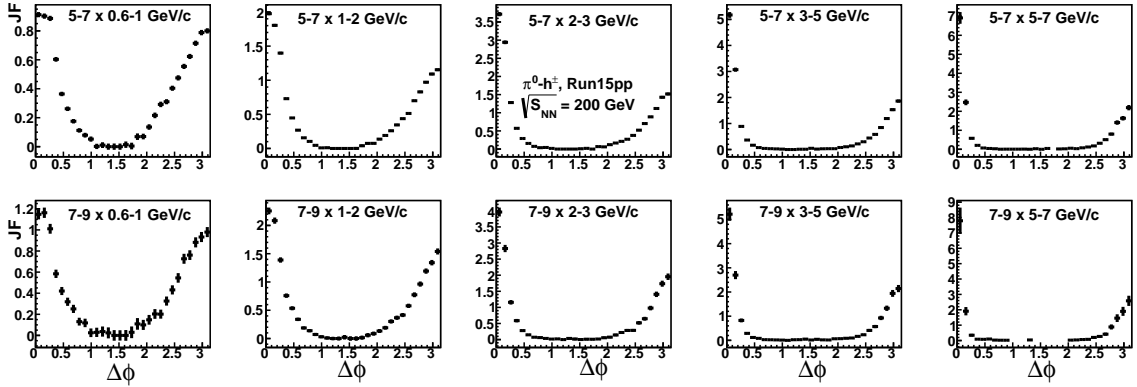


Figure 5.2: π^0 -hadrons jet function for Run15 $p+p$ collisions. The jet function doesn't include any correction due to single particle efficiency. The trigger p_T bins used are [5.0 - 7.0, 7.0 - 9.0] GeV/c which runs from top to bottom. The partner p_T bins used are [0.6 - 1.0, 1.0 - 2.0, 2.0 - 3.0, 3.0 - 5.0 and 5.0 - 7.0] GeV/c which runs from left to right.

5.2 ${}^3\text{He}+\text{Au}$ Results

Since our main goal is to confirm the jet modification behavior seen in $d+\text{Au}$ [3], we analyze ${}^3\text{He}+\text{Au}$ which is next bigger system after $d+\text{Au}$. The 0-20% centrality triggered and EMcal-Rich (ERT) data sets of ${}^3\text{He}+\text{Au}$ at $\sqrt{s_{NN}} = 200$ GeV are analyzed.

5.2.1 Correlation Function and Jet Function

The Figure 5.3 shows our PHENIX preliminary approved π^0 -hadron correlation function for Run14 ${}^3\text{He}+\text{Au}$ collisions at $\sqrt{s_{NN}} = 200$ GeV. The result shows two peaks around 0 and π azimuthal angular difference for each trigger and partner bins. The blue line

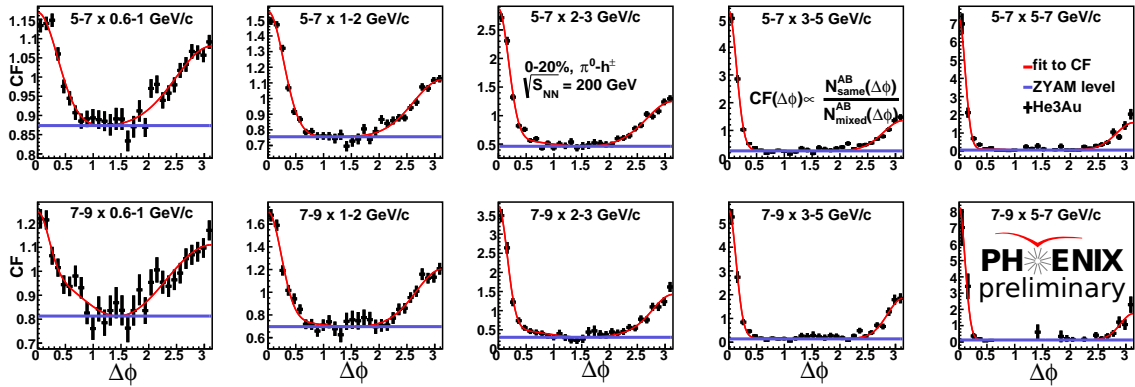


Figure 5.3: π^0 -hadrons correlation function (PHENIX Preliminary approved) for Run14 ${}^3\text{He} + \text{Au}$ collisions. The red line is the fit for the data and the blue line is the background level from ZYAM method. Trigger p_T : [5.0 - 7.0, 7.0 - 9.0] GeV/c running from top to bottom. Partner p_T bins: [0.6 - 1.0, 1.0 - 2.0, 2.0 - 3.0, 3.0 - 5.0 and 5.0 - 7.0] GeV/c running from left to right.

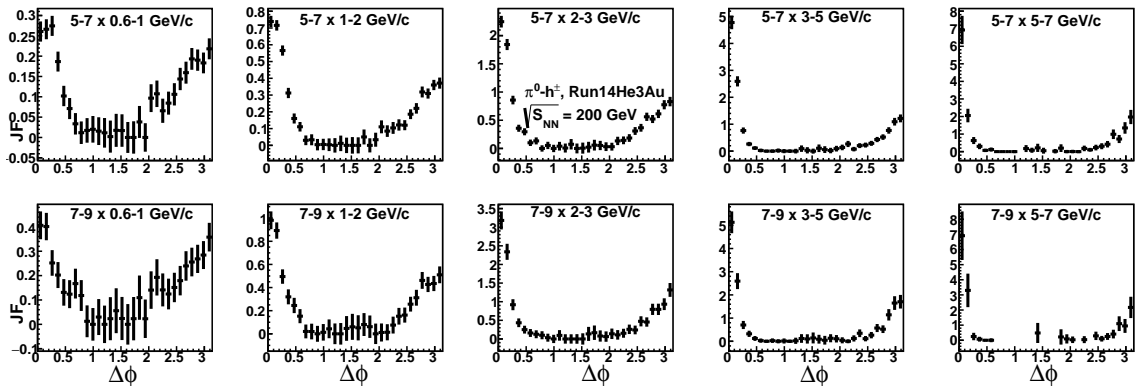


Figure 5.4: π^0 -hadrons jet function for Run14 ${}^3\text{He} + \text{Au}$ collisions. The jet function doesn't include any corrections due to single particle efficiency. Trigger p_T bins: [5.0 - 7.0, 7.0 - 9.0] GeV/c running from top to bottom. Partner p_T bins: [0.6 - 1.0, 1.0 - 2.0, 2.0 - 3.0, 3.0 - 5.0 and 5.0 - 7.0] GeV/c running from left to right.

in the Fig. 5.3 shows the ZYAM level. The ZYAM level is obtained without considering the flow effects. This level is subtracted from the correlation function to get the jet function as shown in Fig. 5.4. Just like in baseline $p+p$ collisions, as we are only interested in the RI observable, which only involves the Away-side/Near-side ratio, and thereby exactly cancels efficiency and other corrections, these have no corrections applied for the shown jet functions. The relatively poor statistics in low partner p_T bins is observed as shown in the Figure 5.4.

5.2.2 Double Ratio (R_I)

The PHENIX preliminary approved result for the double ratio of Run14 ${}^3\text{He}+\text{Au}$ with Run15 $p+p$ baseline is shown in Figure 5.5. The R_I shows significant suppression at high

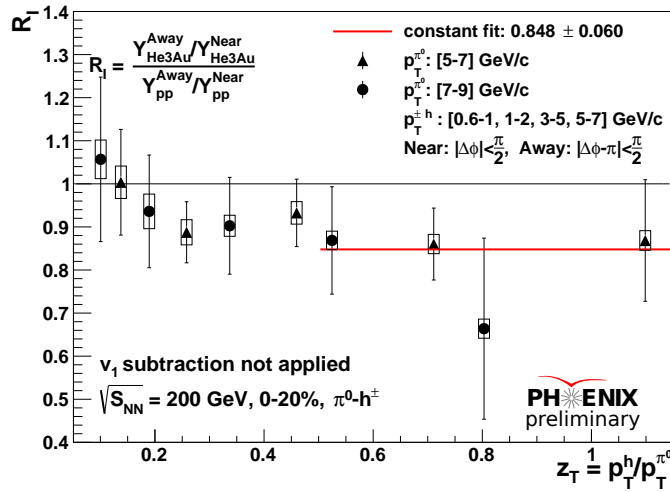


Figure 5.5: (PHENIX Preliminary Version) R_I in Run14 ${}^3\text{He}+\text{Au}$. The red line is the straight line fit for $z_T > 0.45$. The vertical bars represent statistical errors while the boxes represent systematic uncertainties.

z_T and with less statistical significance a shape that could be consistent with a rise at low z_T similar to the previous $d+\text{Au}$ and all $\text{Au}+\text{Au}$ results. In other words it confirms the previous $d+\text{Au}$ preliminary results.

5.3 Previous Result of $d+\text{Au}$

Figure 5.6 shows the R_I from the previous study of π^0 -hadron correlations from $d+\text{Au}$ at $\sqrt{s_{NN}} = 200$ GeV [3]. The result uses Run6 $p+p$ at $\sqrt{s_{NN}} = 200$ GeV as baseline measurement. The R_I clearly shows high z_T suppression and low z_T enhancement behavior. This result could not be reproduced by various simulation study of cold nuclear matter effects. This result is the main motivation for our ${}^3\text{He}+\text{Au}$ analysis.

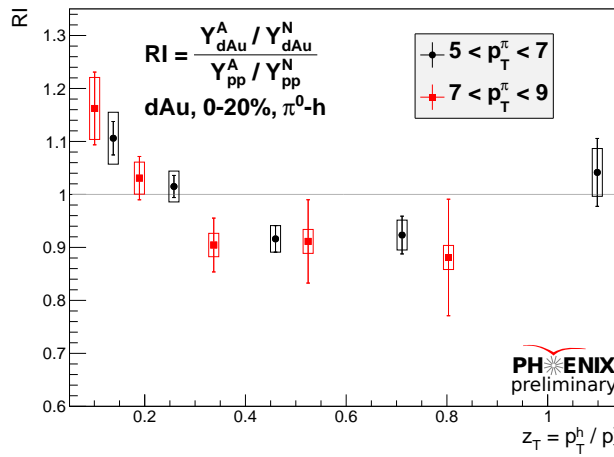


Figure 5.6: The R_I as a function of z_T measured for $d+\text{Au}$ collisions at $\sqrt{s_{NN}} = 200$ GeV in centrality 0-20%. The vertical bars represent statistical errors while the boxes represent systematic uncertainties. The figure is taken from [3]. Courtesy Bing Xia.

5.4 Re-analysis of $d+\text{Au}$

Since we are comparing the $d+\text{Au}$ and ${}^3\text{He}+\text{Au}$ result, it is better to have the same framework of codes and $p+p$ baseline for both systems of collisions. So, we reanalyzed old Run8 $d+\text{Au}$ and new Run16 $d+\text{Au}$ with new Run15 $p+p$ baseline and also combined them. The R_I for 0-20% centrality of Run16 and Run8 $d+\text{Au}$ at $\sqrt{s_{NN}} = 200$ GeV is shown in Figure 5.7. Despite having poorer statistical precision, Run16 $d+\text{Au}$ shows consistently

similar behavior as previous Run8 d +Au. The re-analyzed Run8 d +Au result matches with the previous result except small differences in low z_T due to better cut optimization.

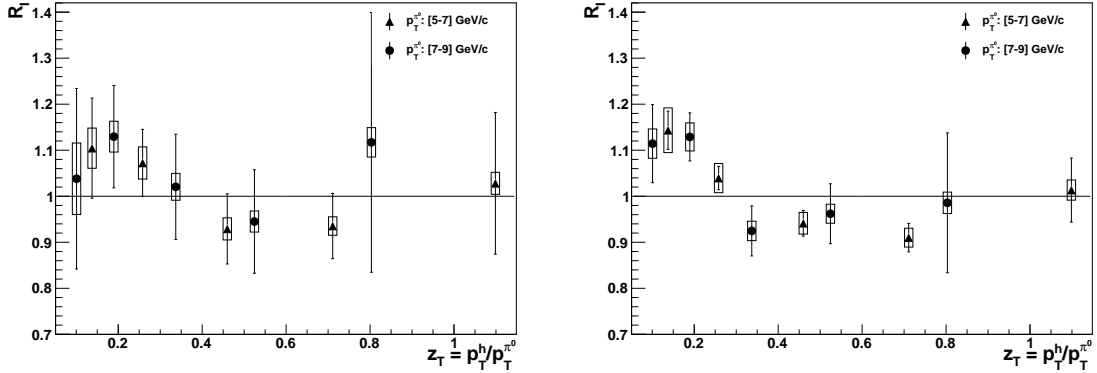


Figure 5.7: R_I as a function of z_T for 0-20% Run16 (left) and Run8 (right) d +Au at $\sqrt{s_{NN}} = 200$ GeV. The vertical bars represent statistical errors while the boxes represent systematic uncertainties.

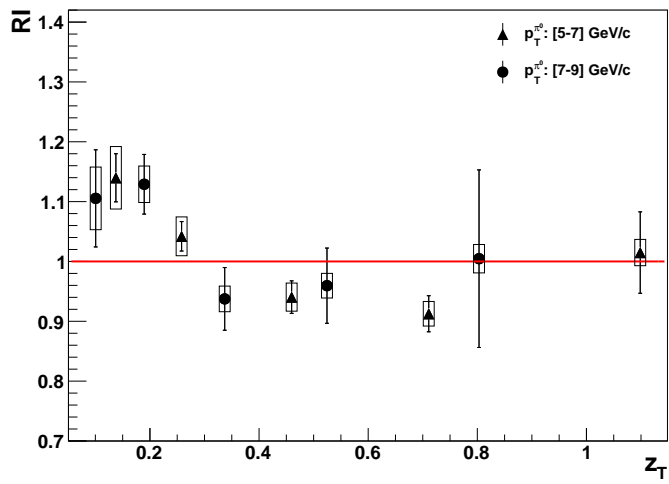


Figure 5.8: R_I as a function of z_T for combined (Run8 + Run16) d +Au at $\sqrt{s_{NN}} = 200$ GeV. The vertical bars represent statistical errors while the boxes represent systematic uncertainties.

The R_I for 0-20% centrality of combined Run8 and Run16 d +Au at $\sqrt{s_{NN}} = 200$ GeV is shown in Figure 5.8. The results were combined at the R_I level itself, since differences in single particle efficiencies which we do not currently derive between the two Runs would prevent us from combining at a lower level. The Particle Data Group method for combining the results based only on their statistical errors (since systematic errors are generally negligible) is used for the combination.

5.5 Comparison of d +Au and $^3\text{He}+\text{Au}$

5.5.1 Comparison With Previous d +Au Result

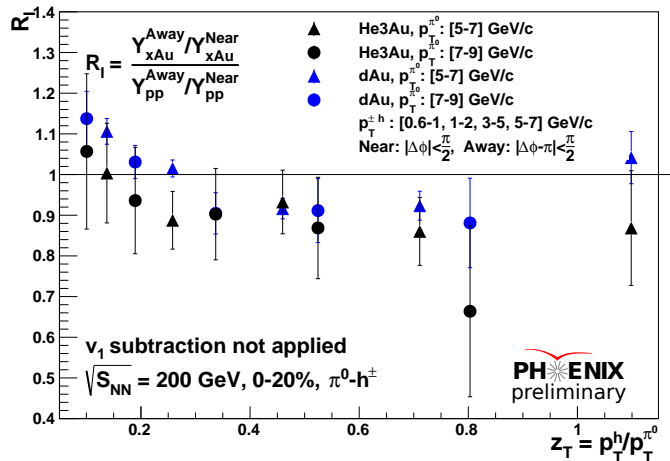


Figure 5.9: (PHENIX Preliminary Version) Comparison of R_I of preliminary Run8 d +Au and that of Run14 $^3\text{He}+\text{Au}$. The black color is for the $^3\text{He}+\text{Au}$ and blue color for the d +Au. The vertical bars represent statistical errors while the boxes represent systematic uncertainties.

The PHENIX approved preliminary R_I comparison from previously approved Run8 d +Au (PHENIX preliminary) and from new $^3\text{He}+\text{Au}$ are plotted together in Figure 5.9. The comparison clearly shows the similarity between the two results, confirming the d +Au behavior, especially with high significance, the high z_T suppression. The comparison

also shows qualitatively that the ${}^3\text{He}+\text{Au}$ suppression is larger than for $d+\text{Au}$, which demonstrates a scaling with nuclear size.

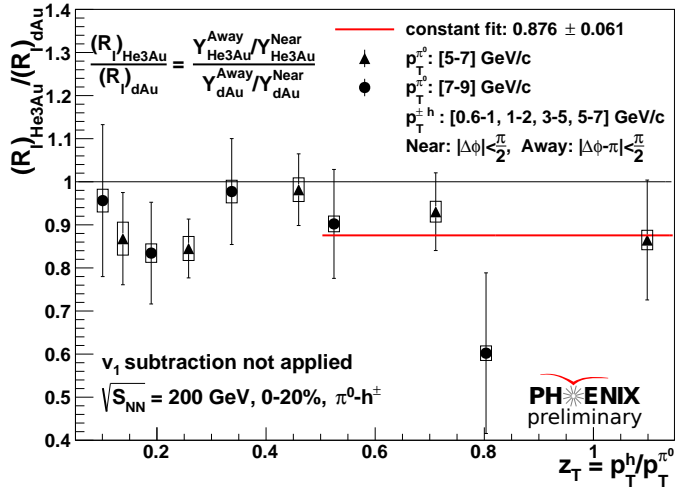


Figure 5.10: (PHENIX Preliminary Version) Ratio of Away side to near side per-trigger yield of preliminary Run8 $d+\text{Au}$ and that of Run14 ${}^3\text{He}+\text{Au}$. This is the same as the Ratio of the R_I 's themselves, when the same $p+p$ reference is used. The ${}^3\text{He}+\text{Au}$ R_I is two sigma smaller than that of $d+\text{Au}$.

Since by using the old preliminary $d+\text{Au}$ RI, we cannot use the new higher statistics $p+p$ reference, in order to better show the significance of the difference between ${}^3\text{He}+\text{Au}$ and $d+\text{Au}$ (which shows that the suppression of ${}^3\text{He}+\text{Au}$ follows the ordering one would expect from Energy Loss, i.e. larger system, larger suppression) we use the direct ratio of the ${}^3\text{He}+\text{Au}$ AS/NS ratio divided by the $d+\text{Au}$ AS/NS: this is numerically the same as the ratio of ${}^3\text{He}+\text{Au}$ to $d+\text{Au}$ R_I 's if the same $p+p$ reference is used. Alternatively one may view this ratio as being exactly like R_I , but with using $d+\text{Au}$ instead of $p+p$ as the reference. Since this ratio cancels completely the common $p+p$ statistical errors inherent in the side by side comparisons of R_I before, it shows that in fact the effect of ${}^3\text{He}+\text{Au}$ being more suppressed than $d+\text{Au}$ has more than 2-sigma than significance. For example

the interesting suppression level in the high z_T region is 0.87 ± 0.06 times smaller than the $d+\text{Au}$ suppression level.

5.5.2 Comparison with Combined $d+\text{Au}$ Result

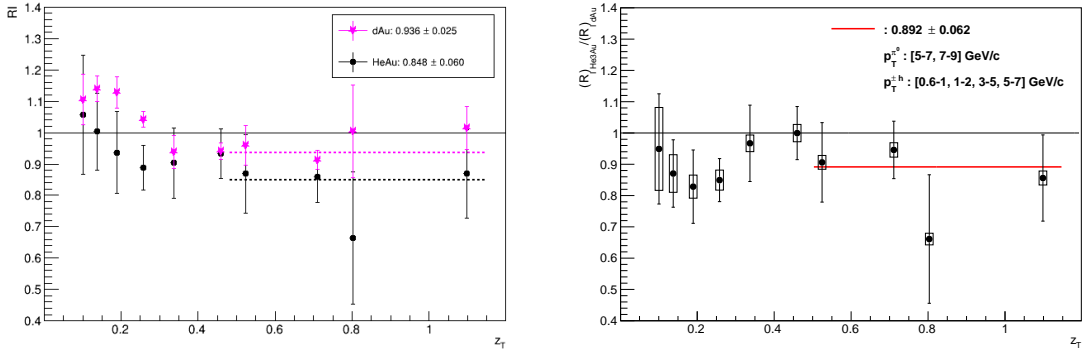


Figure 5.11: Left: Comparison of R_I of combined (Run8 +Run16) $d+\text{Au}$ and that of Run14 ${}^3\text{He}+\text{Au}$. The black color is for the ${}^3\text{He}+\text{Au}$ and magenta color for the $d+\text{Au}$. Right: Ratio of R_I in ${}^3\text{He}+\text{Au}$ to that in combined $d+\text{Au}$.

Both $d+\text{Au}$ and ${}^3\text{He}+\text{Au}$ have good statistical significance in showing suppression at high z_T . From a basic standpoint, the main effect of the suppression in $d+\text{Au}$ is confirmed with ${}^3\text{He}+\text{Au}$ which is the main message. Similar to A+A jet energy loss, the suppression increases with system size, i.e. ${}^3\text{He}+\text{Au}$ is more suppressed than $d+\text{Au}$. From the right plot of Figure 5.11, the suppression level in ${}^3\text{He}+\text{Au}$ at the high z_T region is 0.892 ± 0.062 times smaller than the combined $d+\text{Au}$ suppression level. The difference between this figure and Figure 5.10 is that this version, with the combined Run8+Run16 $d+\text{Au}$ re-analysis, will be the final version that will be in the soon-coming PHENIX publication. The result is virtually the same as the PHENIX Preliminary result in Figure 5.10 but with just slightly less than 2-sigma significance of being less than 1, as opposed to the PHENIX Preliminary, which was slightly greater than 2-sigma significance. However, with the final result in hand, another statistical significance with potentially equal or better importance can be evaluated.

This is that if the shapes of the d +Au and $^3\text{He}+\text{Au}$ are approximately equal everywhere, as they appear to be consistent with, then we can actually use the entire z_T range including also the low z_T points, to evaluate the statistical significance of the $^3\text{He}+\text{Au}$'s higher suppression level (lower R_I) than the d +Au's. The result is shown in Figure 5.12. There we can see that the fit to the finalized ratio across all z_T is 0.89 ± 0.034 . This means that the statistical significance of the greater suppression in He+Au is actually more like 3-sigma, since this is the value on-average for the whole measurement.

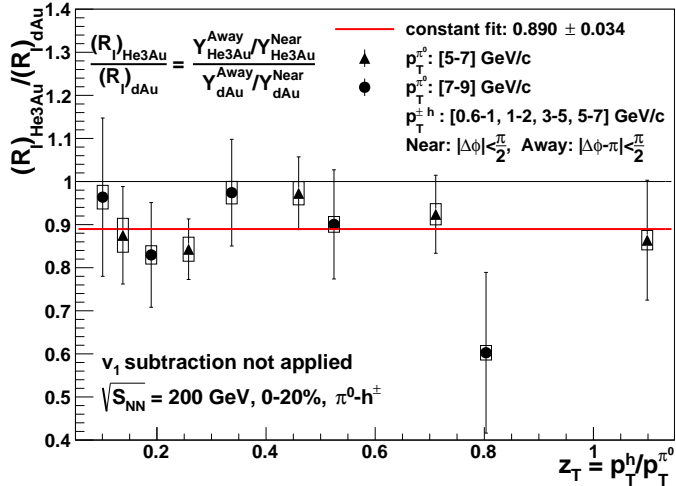


Figure 5.12: Ratio of R_I in $^3\text{He}+\text{Au}$ to that in d +Au. The red line represents constant fit over full range of z_T .

5.6 Analysis of Statistical Significance of Shape Modifications

Previous analysis of the d +Au in the previous result of Bing's thesis [3] showed that the rise at low z (R_I going above to higher values eventually exceeding 1 for low z_T values) has strong statistical significance. In this section we aim to re-evaluate that significance in light of the changes made in our re-analysis, albeit they only affect essentially the lowest z_T point primarily—still this is an important point for this comparison. Also, it appears that the $^3\text{He}+\text{Au}$ does not have statistical precision to confirm that aspect of the result, although

there is also a net rise so it qualitatively looks similar, and it certainly could be consistent with a rise of the similar size as seen in d +Au. So, also in this section we would like to evaluate the actual statistical significance for these statements to see how valid they are, and also to get a quantitative understanding of by how much the statistics would likely need improved if we would wish to make a stronger statement.

"By eye", an important point is that one must be careful to compare the rise region between the two systems, because in judging the relative rise, one must take into account that the ${}^3\text{He}+\text{Au}$ is starting from a more suppressed value. As Tyler Danley's recent photon-hadron results [83] indicate, taking the overall suppression level of jets into account is important in judging the amount of enhancement, thus it is the relative difference of the low z_T vs. the high z_T behavior that matters—the relative size of the low z_T rise. This is the key to what follows, where we make a rough estimate of the statistical significance of the above statements.

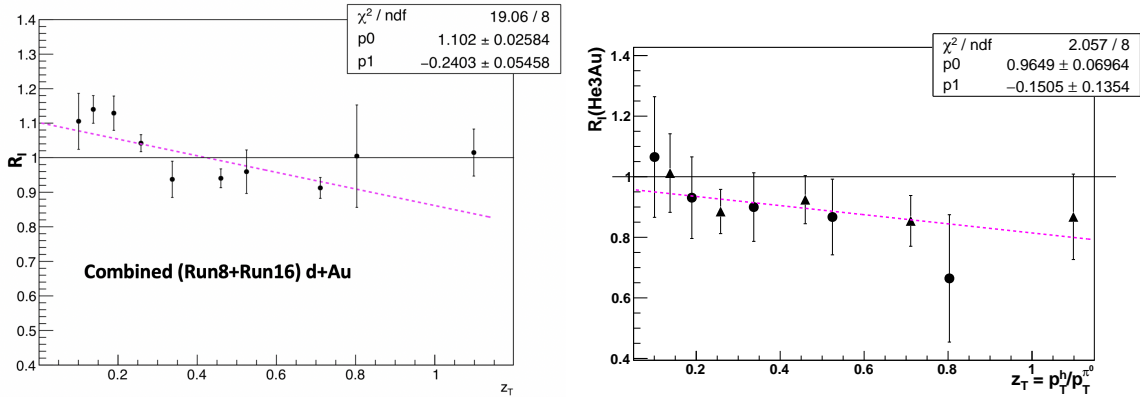


Figure 5.13: The R_I of d +Au (left) and ${}^3\text{He}+\text{Au}$ (right) fitted with first degree of polynomial in full range of z_T . The magenta dotted line represents the fit.

In order to study the statistical significance of the shape modification, we do two short studies. Here we will start with the more qualitative one, and then explain the more rigorous one. For the first qualitative study, we first fitted R_I with first degree polynomial, a straight

line with potentially non-zero slope, as shown Figure 5.13. This is not exactly the expected shape for the R_I from any known effect (which we cannot know a priori what such effects might look like) but it does qualitatively capture the two main effects, a low z_T enhancement and/or relative to a high z_T suppression. As the figure shows, for $d+\text{Au}$, the slope of the fit is 6σ away from 0 *i.e.* flat while it is only 1σ away for ${}^3\text{He}+\text{Au}$. Thus by this metric, the $d+\text{Au}$ is highly non-flat/non-constant in shape. This is because while the chi2 for the fit could probably be made better by restricting the fit ranges, it would be obviously get much worse for smaller slope values— how much worse will be explored in the more rigorous test below. By this metric also, we see that our "by eye" guess that the shape seems to qualitatively rise at low z_T is actually true, but only with 1-sigma significance. The fit to the ${}^3\text{He}+\text{Au}$ also tells however that comparing the $d+\text{Au}$ non-flat shape to that of ${}^3\text{He}+\text{Au}$'s, as admittedly is only approximately captured in this fit function choice through the slope value, tells us also that the $\text{He}+\text{Au}$ shape is consistent with that of $d+\text{Au}$ within one sigma. This is because the slope of $\text{He}+\text{Au}$ is -0.15 ± 0.14 while that of $d+\text{Au}$ is -0.24 ± 0.04 .

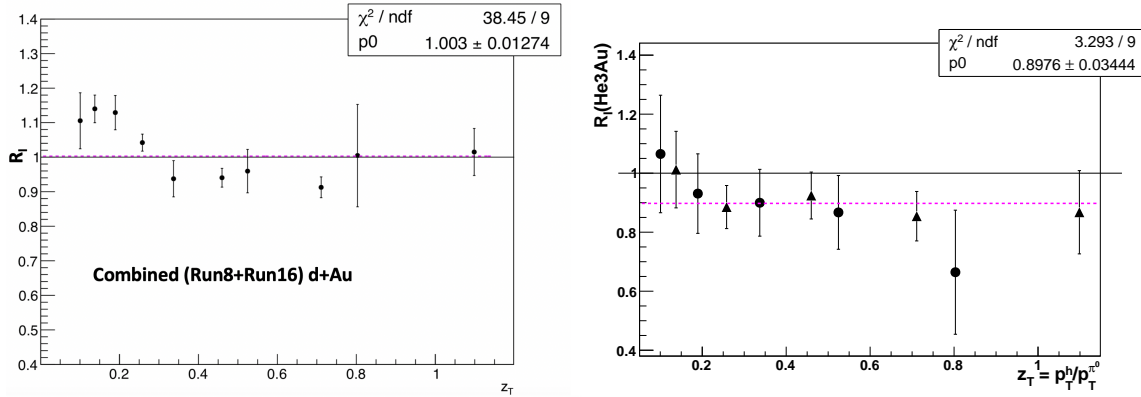


Figure 5.14: The R_I of $d+\text{Au}$ (left) and ${}^3\text{He}+\text{Au}$ (right) fitted with zeroth degree of polynomial in full range of z_T . The magenta dotted line represents the fit.

A p-value test is another way to quantify some of the above considerations more rigorously, albeit with less information about how the actual shape parameters might

compare. In Figure 5.14 the same main result R_t plots are fitted now to a constant function (in root a "pol0") and the p-value is evaluated, mainly as another way to quantify how *non-flat* the finalized d +Au result is. This is the most important purpose of this section since we want to confirm that even after the changes made during the reanalysis of the d+Au, this important shape feature still remains present with high statistical significance. The p-value of the fit shown to the d +Au is calculated to be $< .00001$. This means we can reject the hypothesis with greater than 99.99 % confidence. Hence can conclude that the modification behavior in d+Au can not be explained with zeroth degree of polynomial. Not surprisingly the He+Au fit is on the other hand well consistent with the flat fit function, the p-value of this figure's fit being 0.95137, only slightly less than the fit for the slope fit.

5.7 Interpretation of The Result

The analysis of the modification behavior of R_I in $^3\text{He}+\text{Au}$ and re-analysis in $d+\text{Au}$ now confirms the previous result [3] of jet modification behavior in $d+\text{Au}$. Also, the modifications qualitatively follow the system size dependence. Both $d+\text{Au}$ and $^3\text{He}+\text{Au}$ results are qualitatively similar to the per-trigger yield modification, I_{AA} , measurements in heavy ion collisions. The Figure 5.15 shows the away-side I_{AA} from π^0 -hadron correlations

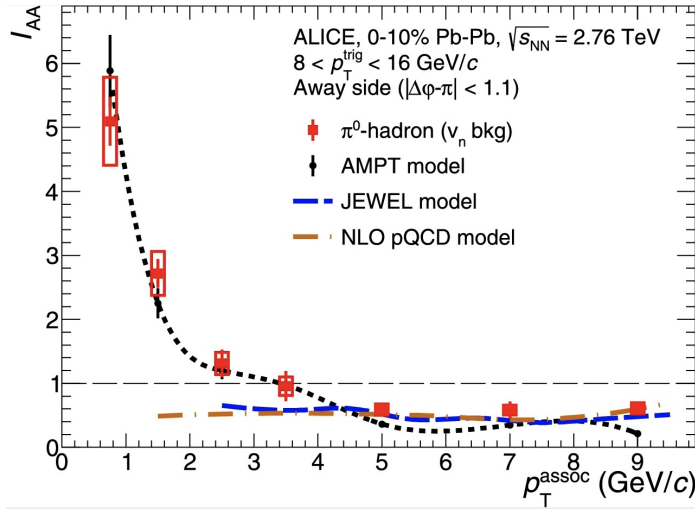


Figure 5.15: Away side per-trigger yield modification from π^0 -hadron correlations in 0-10% Pb-Pb collisions at $\sqrt{s_{NN}} = 2.76$ TeV. The figure is taken from [38] and is available under the *Creative Commons Attribution License*.

for Pb+Pb collisions. There is rise in I_{AA} for low p_T^{assoc} (transverse momentum of associated/partner particle) and suppression in high p_T^{assoc} . This modification behavior in I_{AA} is qualitatively similar to that in R_I from $d+\text{Au}$ and $^3\text{He}+\text{Au}$ collisions. The I_{AA} in the Figure 5.15 is compared with different energy loss models; AMPT [84], JEWEL [85] and pQCD calculation [86]. All of the three energy loss models explain the suppression behavior at high p_T^{assoc} and hence proves the idea of parton energy loss in the QGP medium. AMPT model explains the low p_T^{assoc} as well, which is contributed to the fact that the high p_T particles appear as soft particles as a result of energy loss. The qualitative similarity

between the R_J s in small system collisions and I_{AA} adds support to the speculation that the modification might be from the energy loss due to the presence of QGP.

Apart from the energy loss in the QGP medium, various cold nuclear might effects might be responsible for the modifications behavior in R_J . We have done some Monte Carlo simulation studies to constrain the possible origin of modification behavior from the cold nuclear matter effects. The non-zero k_T value in hard scattering could lead to jet imbalance in the mid-rapidity region and then deviates the R_J value from unity. We have done study on the effect of the k_T in our observable by taking realistic and exaggerated values. Also, the modification of parton distribution functions in the nucleus as opposed to the proton from which they are dervied could have some contribution to the modification behavior in R_J . We have studied this effect with EPPS16 nPDF sets. In the following sections, I describe the details of my cold nuclear matter simulation studies and also give brief overview of previous simulation studies done by Xia [3].

5.7.1 PYTHIA 8

*PYTHIA*¹⁴ is a tool developed by a group in Lund University to generate the events of high-energy collisions [87, 88]. It is typically optimized for generating events of hadron-hadron collisions. However, it also provides interfaces to various external programs and utilities for range of studies in high energy sector. Several known sets of physics models are incorporated in PYTHIA to simulate the evolution of complex final state particles from few-body hard process. It includes library containing hard physics from Standard Model (SM) and some even from Beyond the Standard Model (BSM) though these are not turned on for this study. It also includes different models for soft particle production, beam remnants that don't participate in hard scattering, particle decays, hadronization and multiparton interactions.

¹⁴ PYTHIA is named after high priestess of the Temple of Apollo at Delphi, who was also known as *Oracle of Delphi*.

PYTHIA 6 version was used for the previous simulation study of $d+\text{Au}$ results. This analysis uses new updated version of PYTHIA; *PYTHIA 8* [88]. This new version of PYTHIA is based on the C++ interface unlike previous versions which were based on FORTAN. PYTHIA 8 is up-to-date with decay data and PDFs, contains new SM and BSM processes and has improved underlying event and hard scattering in diffractive systems incorporated. Also it has been tuned to reproduce extensive new datasets, such as the LHC $p+p$ collisions, which did not exist when PYTHIA 6 was written.

5.7.2 Intrinsic k_T Study

As already discussed in the Section 1.8, k_T is the net transverse momentum of the two jets produced in a single 2→2 jet process. Ideally, the k_T should be zero on average as scattering partons has only longitudinal momentum along the beam direction. But, the inherent transverse momentum of the scattering partons leads to the non-zero value of k_T . The STAR measurement of k_T [39], integrated over all 10-20 GeV/c di-jet measurement in $d+\text{Au}$ and $p+p$ is shown in Figure 5.16. The k_T in $d+\text{Au}$ is measured to be 1σ greater

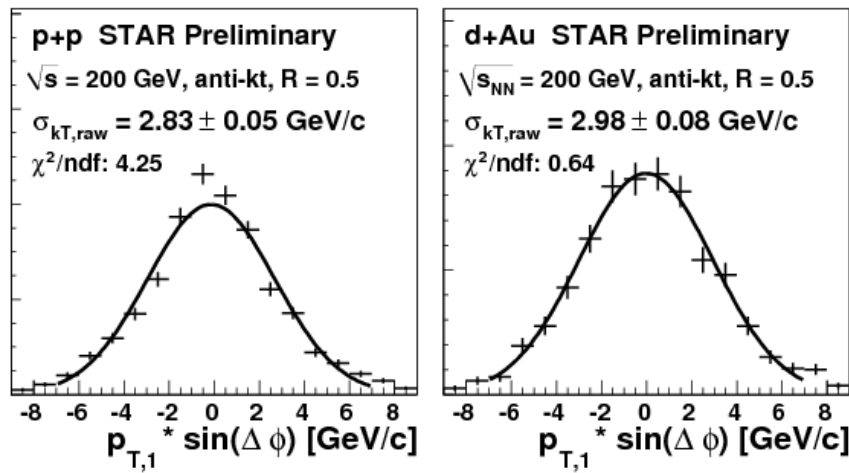


Figure 5.16: Distribution of k_T for $p+p$ and $d+\text{Au}$ collisions at $\sqrt{s_{NN}} = 200$ GeV. The figure is taken from [39]. The copyright permission for the figures is attached in D.27.

than that in $p+p$. The study of k_T effect for $d+\text{Au}$ was done with PYTHIA-6 to test if it can mimic the modification behavior in R_I of $d+\text{Au}$. The modification of R_I as a function of hadron p_T for trigger bin $5 < p_T < 7 \text{ GeV}/c$ is shown in Figure 5.17. This study also concluded none of the k_T combinations can reproduce the original modification behavior in R_I of $d+\text{Au}$.

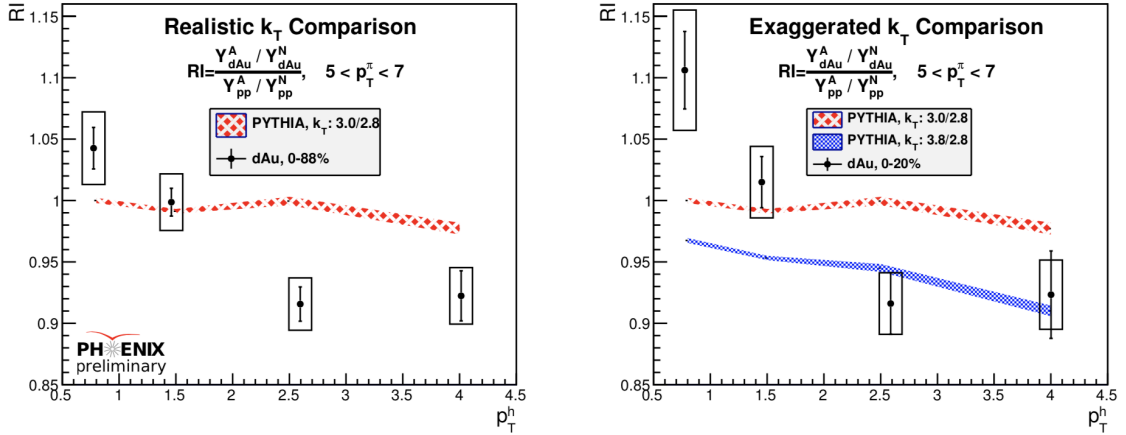


Figure 5.17: The modification in R_I due to the different k_T settings in PYTHIA-6.

Updated k_T study

PYTHIA-8 is used to study the effect of intrinsic k_T in ${}^3\text{He}+\text{Au}$ collisions. For this, PYTHIA-8 was initialized for $p+p$ collisions at $\sqrt{s_{NN}} = 200 \text{ GeV}$. All the hard QCD processes were turned on. The π^\pm along with π^0 were chosen as trigger to increase the statistical precision. The charged hadrons were chosen as partners. The threshold for trigger and partner particles are set to $5 \text{ GeV}/c$ and $0.5 \text{ GeV}/c$ just as in data analysis. Also, the rapidity range of $-0.35 \leq \eta \leq +0.35$ was taken to match the PHENIX acceptance. Since the lower trigger p_T bins would have larger effect of the k_T , which is known to be a constant average value as a function only of center of mass scattering energy of the nucleons, we studied the lowest trigger p_T bin i.e. $5 < p_T < 7 \text{ GeV}/c$.

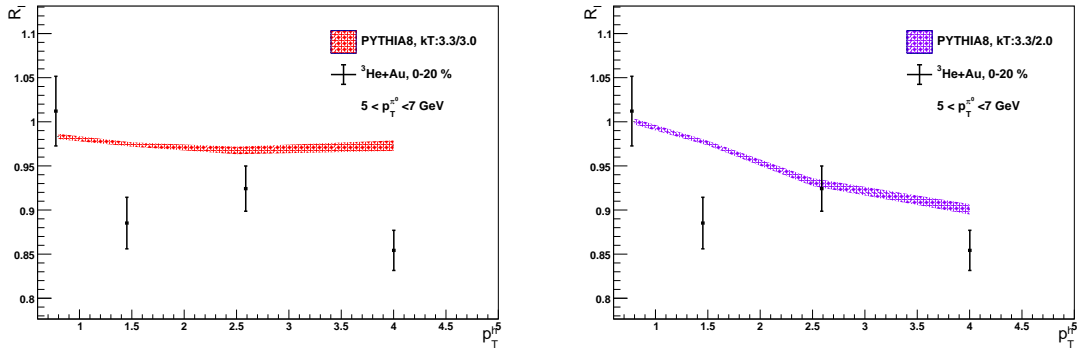


Figure 5.18: Modification of R_L with realistic k_T (left) and with exaggerated k_T value as a function of hadron p_T for trigger bin $5 < p_T < 7$ GeV/c. Both of the k_T options could not reproduce the original modification of R_L .

The modifications in R_L due to k_T effects expected for ${}^3\text{He}+\text{Au}$ collision due to different values of k_T are shown in Figure 5.18. The realistic value of $k_T = 2.8$ GeV/c for $p+p$ is taken from STAR measurement. The realistic value for He+Au is taken as 3.3 GeV/c based on the value of $d+\text{Au}$ STAR measurement. To take of the worst case scenario, the value of k_T corresponding to regular $p+p$ was exaggerated to be as low as 2.0 GeV/c. The left figure shows the modification due to realistic value of k_T as obtained from STAR measurement while right figure shows the modification due to over exaggerated value of k_T . The realistic k_T case doesn't show any kind of modification behavior. Even though the exaggerated one shows trend similar to the original R_L , the suppression level is small compared to original one. From this study, we can conclude that the k_T effect though might have certain role in producing potentially part of the modification, is not the main source of the modification—the realistic sized effects are much smaller than the real He+Au modification seen, and they have the wrong qualitative overall shape.

5.7.3 Nuclear Modification of Parton Distribution Function (nPDF)

Nuclear modifications of parton distribution functions as discussed in Section 1.8 can also produce some modification behavior in jet observables. There are different sets of nuclear PDFs available which are compiled from different data. The previously analyzed $d+Au$ result was compared with EPS09 [89] nuclear PDF sets. The trigger, partner and η

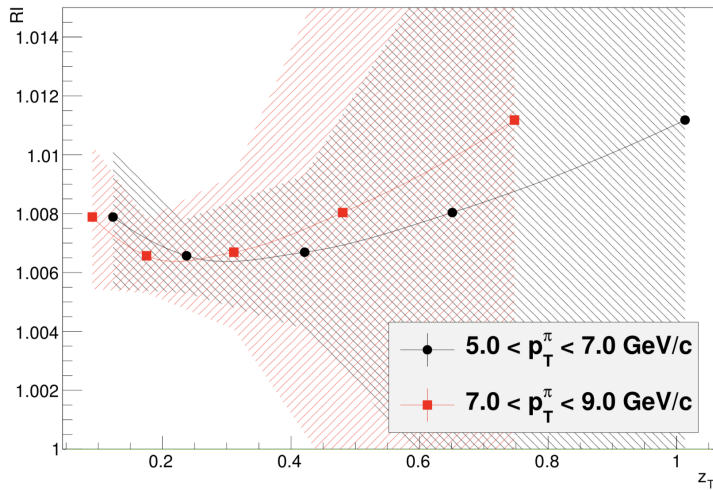


Figure 5.19: The modification in R_l due to nPDF from EPPS09 in $d+Au$. The uncertainties in EPS09 nPDF sets are shown in shaded area.

acceptance settings were similar as in current nPDF study. The default PDF set in PYTHIA-6 is CTEQ5L [90]. CTEQ5L doesn't include any nuclear modification. A similar approach as in PYHIA-8+EPPS16 study was implemented which is explained in more detail below. The modification in R_l from the study is shown in Figure 5.19. The EPS09 study does not show any suppression in simulation. Hence the modification of R_l from $d+Au$ data could not be explained by EPS09 study.

Updated nPDF Study

In this analysis, we use new nPDF data set called EPPS16 [91]. EPPS16 is next to leading order (NLO) nuclear PDFs. Compared to EPS09, EPPS16 includes new

data from neutrino-nucleus deep-inelastic scattering, pion-nucleus Drell-Yan process and dijet production in LHC $p+\text{Pb}$ collisions. In EPPS16, there is no longer assumption of flavor-blind nuclear modification for valence and sea quarks. It considers a full flavor decomposition for quarks and hence reduces the theoretical bias. Also, there are 40 error sets available in EPPS16 compared to 30 of EPS09.

In the EPPS16 study with PYTHIA-8, we turn on all the default hard QCD scattering. Similar to the k_T study, the π^\pm along with π^0 were chosen as trigger to increase the statistical precision and the charged hadrons were chosen as partners. The threshold for trigger and partner particles were set to 5 GeV/c and 0.5 GeV/c just as in data analysis. Also, the rapidity range of $-1.0 \leq \eta \leq +1.0$ was taken instead of PHENIX acceptance ($-0.35 \leq \eta \leq +0.35$) to increase the statistical significance. The PYTHIA-8 has NNPDF2.3 QCD+QED LO [92] as default PDF set without any modification. We basically run $p+p$ at $\sqrt{s_{NN}} = 200$ GeV with PYTHIA-8 and use the EPPS16 functions to calculate the nuclear modification factors for the He and Au. We used ${}^4\text{He}$ grid file while using EPPS16 for helium since ${}^3\text{He}$ grid file was not available. In private communication with the authors of EPPS16 they suggested that we should not expect ${}^4\text{He}$ to behave very differently as ${}^3\text{He}$ with approximately negligible differences¹⁵. These modification values for each partons are used as weight when histogramming the He+Au cross-sections from $p+p$. The uncertainties of EPPS16 are evaluated by finding out the standard deviation of difference between the mean set and all other 40 error sets. The jet functions caused by nuclear modifications are as shown in Figure 5.20. The modification has greater effect in the larger partner p_T bins.

The modification in R_I due to the nuclear modification in parton distribution obtained from EPPS16 nPDF sets is shown in Figure 5.21. The R_I modification of He+Au collisions from the PYTHIA+EPPS16 simulation shows small enhancement instead of any kind of suppression. Most importantly the effects are very small in the few percent range (note the

¹⁵ The grid file for ${}^3\text{He}$ is not made available from the EPPS16 authors. The grid file of ${}^4\text{He}$ is used instead as suggested by the authors.

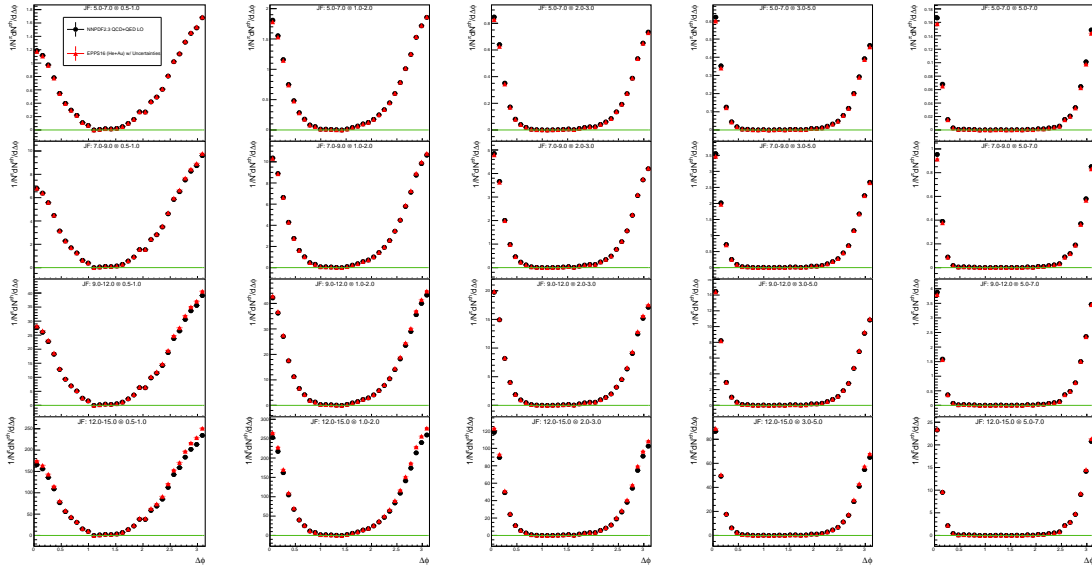


Figure 5.20: The jet functions from PYTHIA-8 simulation. The black points corresponds to the $p+p$ collisions with default NNPDF2.3 QCD+QED LO PDF set without any nuclear modification. The red points corresponds to the jet function of He+Au collisions with EPPS16 nPDF set.

y-axis range). The modification from EPPS16 is very negligible and inconsistent with the behavior we saw in Figure 5.5. For the explanation of this non-modification behavior in simulation, we plotted x vs. Q^2 for the triggered events as shown in Figure 5.22. From the figure, we can find that the events with $x \approx 0.02 \sim 0.03$ and $Q^2 \approx 30 \sim 50$ (GeV/c) 2 are most probable events. The range of the x corresponds to the region in between the shadowing and anti-shadowing effect. The Figure 5.23 shows the modification for parton distribution functions as a function of x for Au and He obtained from EPPS16 nPDF sets. In the most probable Q and x region, all the parton modification factors for both He and Au are close to unity. Thus, the PYTHIA+EPPS16 nPDF study could not explain the modification behavior of R_I from central He+Au collisions.

As noted in the previous Analysis section about the advantages of the R_I observable, lack of similar effects due to nPDF modifications are not surprising given the R_I 's

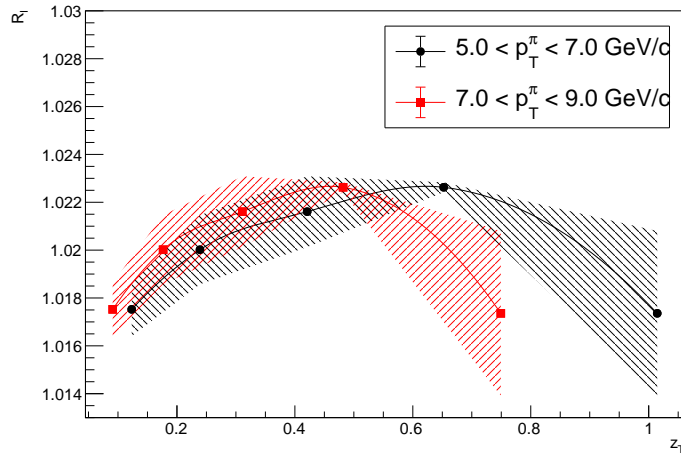


Figure 5.21: The modification in R_I due to nPDF from EPPS16. The uncertainties in EPPS16 nPDF sets are shown in shaded area. The box represents the uncertainty due to EPPS16 error sets.

definition. nPDF modifications are changes in the x weighting in the full QCD factorization integrations that produce changes to the overall cross section of di-jets, *i.e.* both jets in a given event. Since we are taking the ratio of away-side to near-side jet regions in R_I the nPDF modifications largely cancel.

5.7.4 Additional Previous Simulation Studies in $d+\text{Au}$

Apart from the k_T and nPDF, couple of more simulation studies were done in previous works to check if they could reproduce the modification behavior in $d+\text{Au}$ data. The following is the brief revisit of the previous simulation studies done by Xia [3].

5.7.4.1 Quark Gluon Jet Mixing

Jets from gluons are known to be broader and softer than that from quarks. If the production of gluon jets from $d+\text{Au}$ collisions is more compared to that from $p+p$ collisions, it could possibly cause some modification in R_I observable. However, PYTHIA

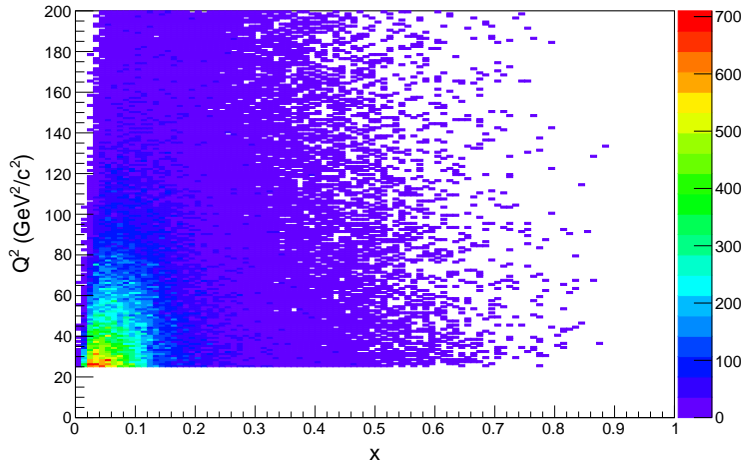


Figure 5.22: 2D density plot for Q^2 as a function of x for triggered events in PYTHIA-8+EPPS16 study. $x \approx 0.02 \sim 0.03$ and $Q^2 \approx 30 \sim 50$ (GeV/c) 2 corresponds to the most probable events. The lower cut in Q^2 is due to the phase space cut in the transverse momenta in 2 \rightarrow 2 processes.

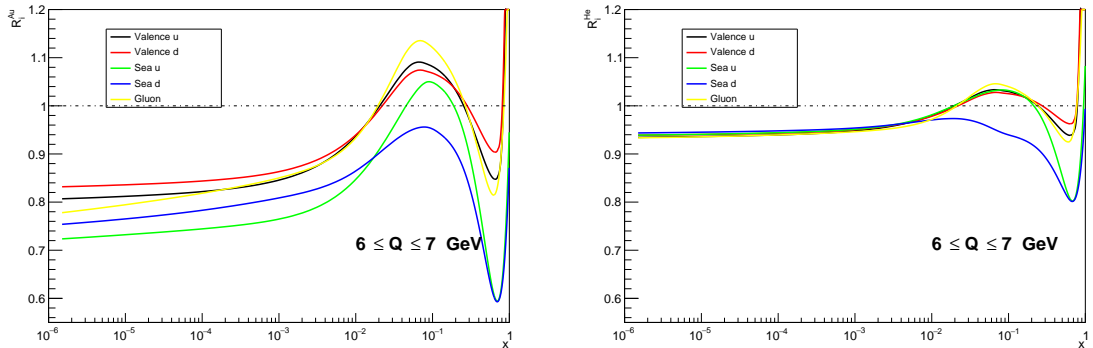


Figure 5.23: Nuclear modification of parton distribution functions with EPPS16 of Au (left) and He (right) at $6 \leq Q \leq 7$ GeV/c.

study of $p+p$ vs. $p+n$ collisions didn't show any difference to support the fact that more gluons jets are produced in $d+Au$.

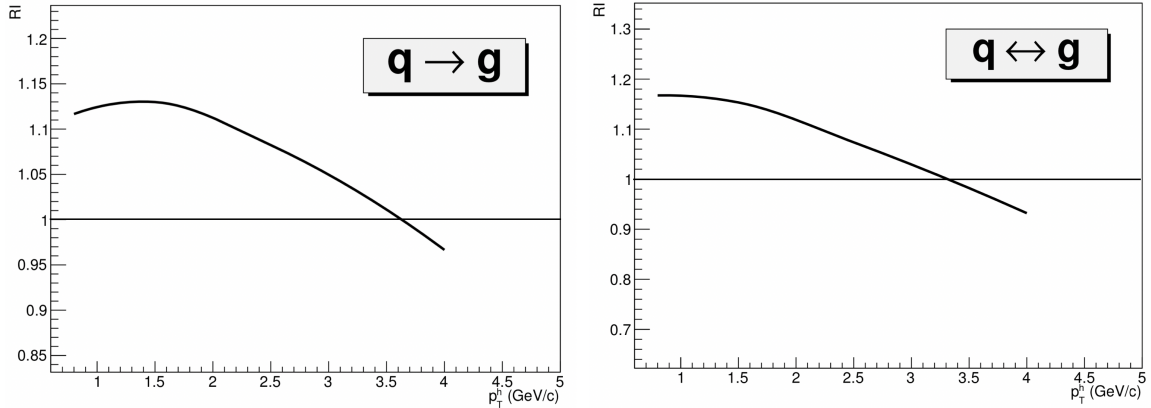


Figure 5.24: Left: Modification in R_L from PYTHIA d +Au collisions considering conversion of all quark jets (q) into gluon jets (g). Right: The modification in R_L due to double conversion ($q \leftrightarrow g$). The figures are taken from [3].

For the study of effect of increased gluon jets, the extreme scenario was considered where all the quark jets are converted into the gluon jets without affecting the original gluon jets. With this consideration, the modification in R_L is shown in left figure of Figure 5.24. It shows enhancement in low z_T with no suppression in high z_T . The modification behavior is not consistent with the measured R_L . Thus, even the over-exaggerated assumption of the quark jet conversion could not produce the original modification in R_L . An unlikely situation where substantial number of quark and gluon jets get converted into each other was also studied. The modification in R_L due to this "double conversion" is shown in right figure of Figure 5.24 which is also not consistent with the R_L from d +Au data.

5.7.4.2 HIJING

HIJING¹⁶ is an event generator for high energy hadronic and nuclear collisions [93–96]. It is a Monte-Carlo program, which is basically designed to simulate all known nuclear effects in hard scattering, including multiple jets and particle production, QGP-like jet quenching in high energy hadronic and nuclear collisions (although this feature is largely

¹⁶ HIJING: Heavy Ion Jet INteraction Generator

out of date with current Eloss calculations so we did not use it). PYTHIA subroutines and Lund jet fragmentation schemes are used in HIJING.

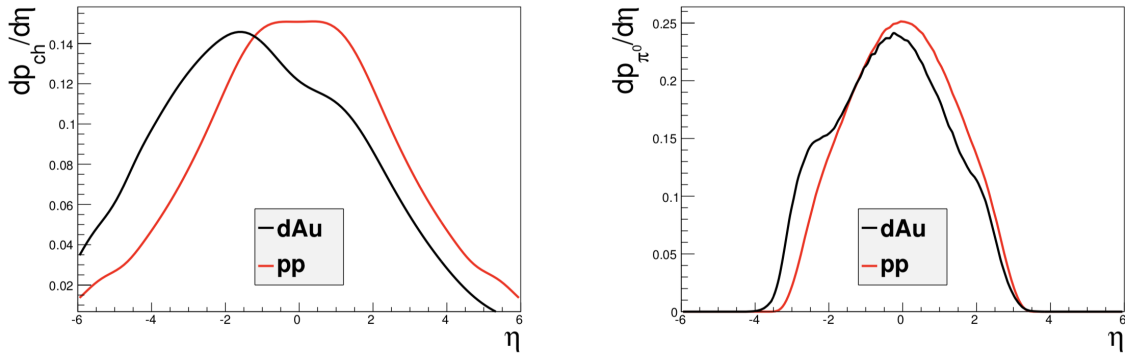


Figure 5.25: The η distribution for charged hadrons (left) and π^0 triggers (right) from HIJING simulation. The red line is for $p+p$ collisions while black line is that for central $d+Au$ collisions. The figure is taken from [3].

In order to study the cold nuclear matter effects from $d+Au$, jet quenching was turned off in HIJING. The collision parameter $0 < b < 5$ fm was used for the simulation study of central $d+Au$ collisions. Unlike the original data set, the HIJING produces uneven η distribution as shown in Figure 5.25. No action was taken to make the distribution flat as in data. The effect of uneven distribution can be taken as extreme case where the R_I might be effected even more.

HIJING doesn't have interface for changing the hard scattering parton's k_T value. The HIJING default value of k_T for the remnants is set to 0.44 GeV/c. To study the k_T effect with HIJING, the k_T of remnants was varied. Apart from the default value, the simulation was done for $k_T = 1.2$ GeV/c, 2.0 GeV/c and 2.8 GeV/c. The systematic changes in jet widths and I_dA values were studied to tune the k_T value to the realistic one. From the study, the best matched value for $d+Au$ collisions was found to be 2.0 GeV/c. This realistic k_T value in $d+Au$ HIJING simulation and PYTHIA-6 $p+p$ simulation with k_T value of 2.8 GeV/c are used in the study of modification in R_I . The left figure of Figure 5.26 shows

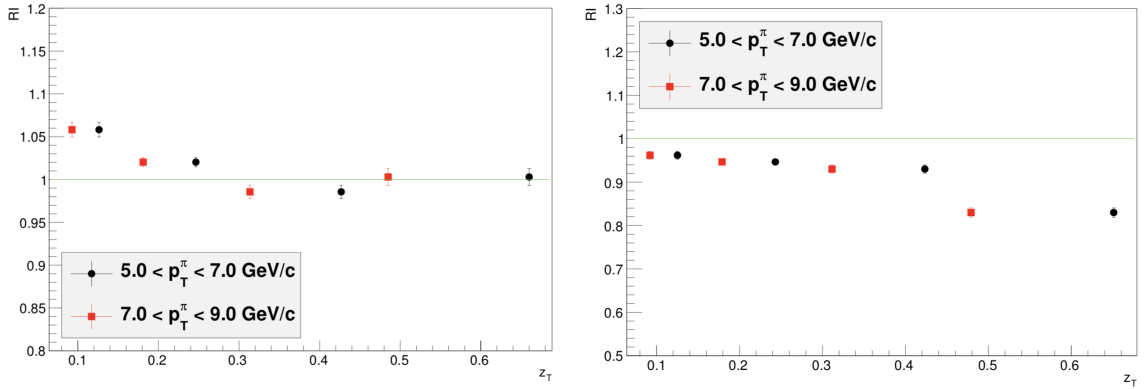


Figure 5.26: Left: Modification in R_L from HIJING $d+\text{Au}$ simulations with realistic $k_T = 2.0 \text{ GeV}/c$ and PYTHIA-6 $p+p$ simulations with realistic $k_T = 2.8 \text{ GeV}/c$. Right: The modification in R_L from HIJING simulations with default $k_T = 0.44 \text{ GeV}/c$ for both $d+\text{Au}$ and $p+p$. The figures are taken from [3].

the modification behavior in R_L with realistic k_T settings in HIJING+PYTHIA while the right figure shows the one with default k_T settings in HIJING. From both of the plot, it was concluded that the HIJING simulation study of $d+\text{Au}$ is unable to produce the modification behavior of R_L from data.

5.7.5 Concluding Remarks and Small System Eloss Calculation Outlook

The result in ${}^3\text{He}+\text{Au}$ now confirms the modification behavior observed in previous result of $d+\text{Au}$. The simulation studies of cold nuclear matter effects were unable to reproduce the modifications of R_L in ${}^3\text{He}+\text{Au}$ and $d+\text{Au}$. The updated study of intrinsic k_T effect with the help of PYTHIA-8 reproduced some qualitative similarities but very small modification behavior than from the data. From the updated nPDF study, the modification obtained is very small and in the opposite direction of the modification from data. Also, the previous study of the HIJING could not reproduce the result in $d+\text{Au}$. Furthermore, the collective flow is also not able to explain the result. All of these points are making a potentially strong case for at least the consideration of possible energy loss in QGP medium

for small collision system. However, there are not much theoretical work done in the small system QGP energy loss.

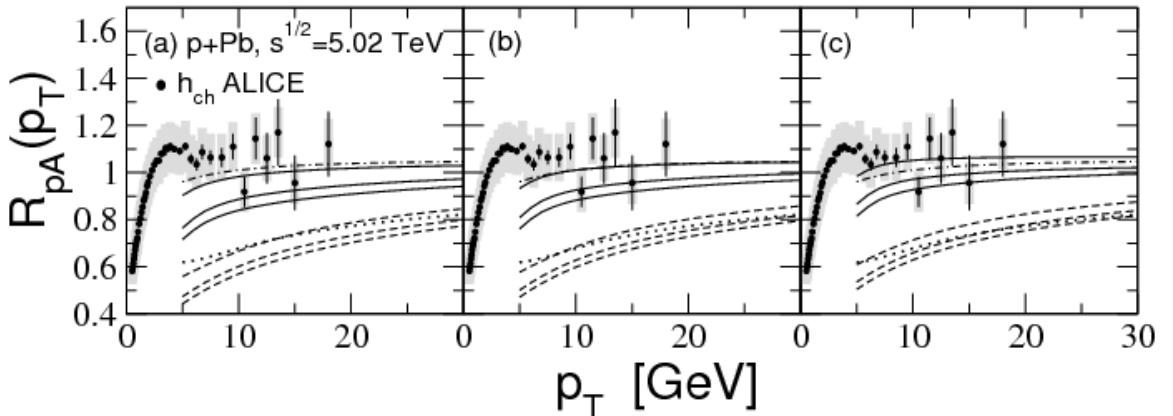


Figure 5.27: R_{pA} for charged hadrons as a function of p_T at $\sqrt{s_{NN}} = 5.02$ TeV. The data points are from $p+Pb$ collisions in ALICE and different lines represents result from calculations. (a) The dotted line shows the calculations for the energy loss in $p+p$. The dotted dashed line shows the EKS98 [40] correction to nPDF. The solid and dashed lines shows the energy loss in $p+Pb$ with and without considering energy loss in $p+p$. The multiple lines are due to different considerations in theory calculations. (b & c) are same as (a) but for different radius of fireball in $p+Pb$ collisions. The figure is taken from [41]. The copyright permissions for the figure are attached in Figure D.28 and Figure D.29.

Figure 5.27 shows the theory comparison of energy loss in small system with $p+Pb$ data from ALICE¹⁷ [41]. There are multiple assumptions applied in the calculation (hence multiple curves) and some of those qualitatively agrees with $p+Pb$ data. Our results with more sensitive observable are now pretty well studied and it should be a motivation for theorist to do similar kind of calculations to determine the possible explanation behind the modification behavior. We are in communication with a high energy theory group from Rutgers University (Jacquelyn Noronha-Hostler) for the calculation but the result is not expected to be completed by the time of the publication of this dissertation.

¹⁷ ALICE: A Large Ion Collider Experiment at LHC (Large Hadron Collider)

6 SUMMARY AND OUTLOOK

6.1 Summary

The π^0 -hadron correlations in Run14 ${}^3\text{He}+\text{Au}$, Run15 $p+p$ and Run16 $d+\text{Au}$ at $\sqrt{s_{NN}} = 200 \text{ GeV}$ were analyzed. A two particle correlation jet observable, double ratio (R_I), for Run14 ${}^3\text{He}+\text{Au}$ was measured with respect to the baseline of Run15 $p+p$. The measured double ratio in Run14 ${}^3\text{He}+\text{Au}$ was compared with the previously measured Run8 $d+\text{Au}$ result. The Run8 $d+\text{Au}$ was also reanalyzed with same code frame work and $p+p$ baseline and combined with Run16 $d+\text{Au}$ result.

The R_I from π^0 -hadron correlation in ${}^3\text{He}+\text{Au}$ collision shows significant suppression at high z_T and with less statistical significance a shape that could be consistent with a rise at low z_T of previous $d+\text{Au}$ and $\text{Au}+\text{Au}$ results. The comparison of R_I in ${}^3\text{He}+\text{Au}$ and in $d+\text{Au}$ collisions clearly shows the similarity between the two results, confirming the $d+\text{Au}$ behavior, especially with high significance, the high z_T suppression. The comparison also shows qualitatively that the ${}^3\text{He}+\text{Au}$ suppression is larger than for $d+\text{Au}$, which demonstrates a hint of scaling with nuclear size. In order to better show the significance of the difference between ${}^3\text{He}+\text{Au}$ result and previous $d+\text{Au}$ result, we used the direct ratio of the ${}^3\text{He}+\text{Au}$ AS/NS ratio divided by the $d+\text{Au}$ AS/NS: this is numerically the same as the ratio of ${}^3\text{He}+\text{Au}$ to $d+\text{Au}$ R_I 's if the same $p+p$ reference is used. This ratio completely cancels the common $p+p$ statistical errors inherent in the side by side comparisons of R_I . The ratio shows the effect of ${}^3\text{He}+\text{Au}$ being more suppressed than $d+\text{Au}$ has more than 2-sigma significance. For example the interesting suppression level in the high z_T region is 0.87 ± 0.06 times smaller than the $d+\text{Au}$ suppression level.

We also analyzed Run16 $d+\text{Au}$ as a crosscheck of the previous Run8 $d+\text{Au}$ result. The result from Run16 $d+\text{Au}$ is consistent with the previous Run8 $d+\text{Au}$ result. We also reanalyzed Run8 $d+\text{Au}$ to have same framework of codes and $p+p$ baseline as in ${}^3\text{He}+\text{Au}$ result. The re-analyzed results from Run8 and Run16 were combined. Since differences in single particle efficiencies which we do not currently derive between the two Runs would

prevent us from combining at a lower level, the results were combined at the R_l level itself. From a basic standpoint, the main effect of the suppression in $d+\text{Au}$ is confirmed with ${}^3\text{He}+\text{Au}$ which is the main message. Similar to A+A jet energy loss the suppression increases with system size, i.e. ${}^3\text{He}+\text{Au}$ is more suppressed than $d+\text{Au}$ although this statement only has about 1.3 sigma statistical significance.

Simulation studies were done for checking possibilities of the cold nuclear matter effects mimicking the modification behavior observed in data. The effect of intrinsic k_T was studied with the help of PYTHIA-8. Two sets including realistic and exaggerated values of k_T s for $p+p$ and ${}^3\text{He}+\text{Au}$ were implemented. But both sets of k_T was unable to reproduce the modification in R_l from data. The effects due to modification of nuclear parton distribution function (nPDF) were studied using PYTHIA-8+EPPS16 nPDF data sets. This study too could not reproduce the modification behavior in R_l from data. The previous simulation studies of quark gluon jet mixing and HIJING without quenching effect also could not reproduce the modification behavior.

For the theory study, we are in touch with a high energy theory group led by Jacquelyn Noronha-Hostler at Rutgers University. The group is interested to study for the energy loss behavior in small system collisions. But the study could not be completed by the time of the publication of this dissertation.

6.2 Outlook

In this section, we discuss some works which can be done in future to move ahead the analysis we have done for this dissertation.

6.2.1 Cu+Au and Peripheral Au+Au

We also had a look in the very peripheral centrality bins of Au+Au and Cu+Au collisions where the system sizes should be comparable to d+Au and He+Au. The analysis on those systems could give some context for what one might expect from the results

from the size of jet energy loss effects as we approach the smaller multiplicities probed by ${}^3\text{He}+\text{Au}$ and $d+\text{Au}$.

The number of participating nucleons (N_{part}) corresponding to the different centrality bins of the $d+\text{Au}$, ${}^3\text{He}+\text{Au}$, $\text{Cu}+\text{Au}$ and $\text{Au}+\text{Au}$ are tabulated in the Table 6.1. From

Table 6.1: The number of nucleons participating in collisions, $\langle N_{part} \rangle$, corresponding to centrality bins for different collision species. The values are collected from [4–7].

Collision Species	Centrality %	Number of Participants $\langle N_{part} \rangle$	$\sigma_{N_{part}}$
$d+\text{Au}$	0-20	16.26	
${}^3\text{He}+\text{Au}$	0-20	22.497	
$\text{Au}+\text{Au}$	50-55	53.16	4.96
	55-60	40.96	4.48
	60-65	30.77	3.91
	65-70	22.64	3.40
	70-75	16.17	2.80
	75-80	11.15	2.19
	80-93	5.60	0.81
$\text{Cu}+\text{Au}$	0-20	154.80	4.14
	20-40	80.37	3.29
	40-50	43.26	2.98
	50-60	26.79	2.56
	60-70	15.22	2.01
	70-80	7.86	1.49
	80-93	3.76	0.79

Table 6.1, we can see that there is good overlapping of the number of participants in small

system collisions (d +Au and ^3He +Au) with the peripheral centrality bins of Cu+Au and Au+Au. It would be very interesting to analyze those overlapping centrality bins of Au+Au and Cu+Au and the bins where the energy loss suppression turns off. The left figure of Figure 6.1 shows the comparison of projected statistical uncertainties for arbitrary high z_T suppression for the R_I modifications across different collision systems while the right figure shows average R_{AA} for charged hadrons versus centrality in Pb+Pb collisions in ALICE. It would be interesting to find out how the finalized version of the left figure would be in compare to the figure in the right.

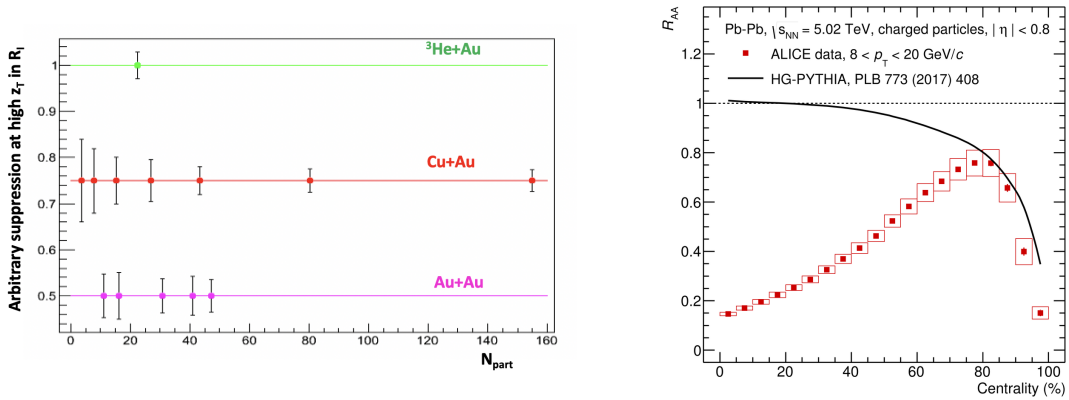


Figure 6.1: Left: Arbitrary suppression of R_I at high z_T for different collision systems as a function of N_{part} . Right: Average R_{AA} for charged hadrons of $8 < p_T < 20 \text{ GeV}/c$ as a function of centrality bins in Pb+Pb collisions at $\sqrt{s_{NN}} = 5.02 \text{ TeV}$. The solid black line shows the model prediction from HG-PYTHIA. HG-PYTHIA is PYTHIA-based model superimposing events incoherently without nuclear modification. The right figure is taken from [42] and is available under the terms of *Creative Commons Attribution License*.

6.2.2 sPHENIX

sPHENIX [97] is a proposed state-of-art jet and Upsilon detector to succeed PHENIX experiment at RHIC. The "s" in the name stands for the strongly interacting particles. sPHENIX is being designed to probe the jets, Upsilon(Υ s), jet correlations and heavy

flavor hadrons. Even after the discovery of the QGP and its properties, the emergence of the QGP properties from the from its point-like constituent particles (quarks and gluons) remains to be unraveled. The sPHENIX detector is expected to achieve the 2015 U.S. Nuclear Physics Long Range Plan's [98] goal to resolve the microscopic structure of QGP and determine temperature dependence of transport coefficients and the color screening length in the QGP.

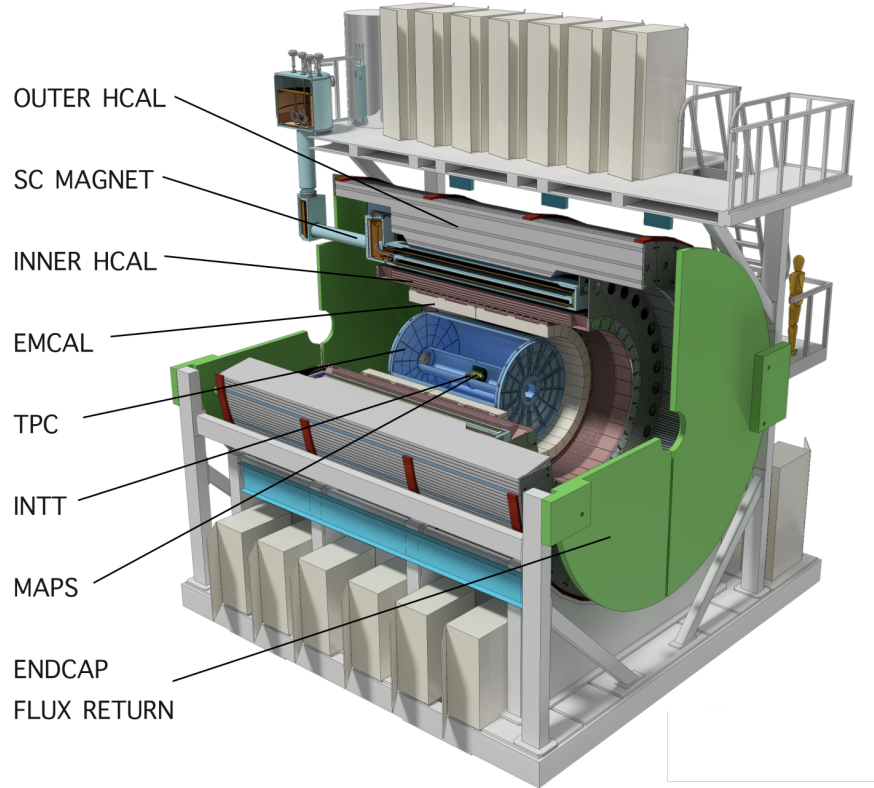


Figure 6.2: Current outline of the proposed sPHENIX detector. The figure is taken from [43] and the figure is available under the terms of *Creative Commons Attribution-NonCommercial-No Derivatives License*.

The current design for the proposed sPHENIX detector is shown in Figure 6.2. It has the acceptance of $|\eta| < 1.1$ and full azimuth coverage. A 3.5m long superconducting solenoid, previously used in BaBar experiment at SLAC (Stanford Linear Accelerator

Center), would be used to produce magnetic field of 1.5 Tesla to tracking system, electromagnetic calorimeter and inner hadronic calorimeter. Although not included in this thesis, as part of ancillary work related to this thesis, I participated extensively in sPHENIX software development and design studies which is summarized in the Appendix C.

Tracking System

The tracking system will have three subsystems; Monolithic Active Pixel Sensors (MAPs), Intermediate Silicon Strip Tracker (INTT) and compact Time Projection Chamber (TPC). This high resolution tracking system will be designed to separate the upsilon states and do the high precision jet structure measurement.

Calorimeter System

The calorimetry of sPHENIX consists of two Hadronic Calorimeters (HCAL) and one ElectroMagnetic Calorimeter (EMCAL). The EMCAL is in between the tracking system and an inner HCAL. It is made of scintillating fibres embedded in the Tungsten powder and epoxy. The readouts are made of silicon. The EMCAL segmentation is 0.025×0.025 for $\Delta\eta \times \Delta\phi$. The electrons and photons produce showers in the EMCAL and deposit its energy. The EMCAL helps for the identification of electron which is very important for the Υ states measurements. The photon measurements help to measure the photon jet events required to analyze the photon-jet correlations. Approximately projective towers are being studied to use for improving the electron-pion separation.

There are two hadronic calorimeters proposed for the sPHENIX detector. The inner HCAL is just inside the magnetic system while outer HCAL is just outside. The HCALs are made of alternating layers of steel plates and scintillating fibers. The energy of hadrons are measured with the help of HCALs. Also, the HCAL together with EMCAL are used to reconstruct the energy of jets.

Lots of efforts in hardware and simulations are being made to optimize the design of the detector to reach its goal. Prototypes of detectors are being made in different Labs and

collaborator institutions and are being tested at the Fermilab Test Beam Facility (FTBF). It has recently mostly passed the PD-2/3¹⁸ [99] review from the Department Of Energy (DOE) and thus is approved for construction. sPHENIX is expected to be installed by 2022 and start taking high statics nucleon-nucleon, nucleon-nucleus and nucleus-nucleus data from 2023. During this dissertation work, I contributed several simulation studies of the sPHENIX EMCAL to the sPHENIX Collaboration which are described in the Appendix C.

¹⁸ PD-2/3: Project Decision -2 out of 3

REFERENCES

- [1] L. Aphecetche *et al.*, Nuclear Instruments and Methods in Physics Research Section A: Accelerators, Spectrometers, Detectors and Associated Equipment **499**, 521 (2003), the Relativistic Heavy Ion Collider Project: RHIC and its Detectors.
- [2] “RUN OVERVIEW OF THE RELATIVISTIC HEAVY ION COLLIDER,” <http://www.agsrhichome.bnl.gov/RHIC/Runs/>, accessed: 2017-07-21.
- [3] B. Xia, $\pi^0 - h^\pm$ Jet Correlation in $d+Au$ Collisions at $\sqrt{s_{NN}} = 200$ GeV, Ph.D. thesis, Ohio University (2014).
- [4] R. Wei *et al.*, “Glauber Calculations of Centrality Dependent Variables in Au+Au at $\sqrt{s_{NN}} = 200$ GeV,” (2009), PHENIX internal Analysis Note 768.
- [5] J. Nagle *et al.*, “PHENIX Run-08 $d+Au$ 200 GeV Centrality Categorization: Addendum,” (2013), PHENIX internal Analysis Note 1087.
- [6] J. Mithcell *et al.*, “Centrality Calibration and Glauber Model Calculations for the Run-12 200 GeV Cu+Au Dataset,” (2014), PHENIX internal Analysis Note 1078.
- [7] J. Nagle, “PHENIX Run-14 ${}^3\text{He}+Au$ 200 GeV Centrality Categorization,” (2017), PHENIX internal Analysis Note 1207.
- [8] A. Purcell, , 10 (2012), Go on a particle quest at the first CERN webfest.
- [9] M. Thomson, *Morden Particle Physics* (Cambridge University Press, Newyork, NY, 2013).
- [10] C. Patrignani *et al.* (Particle Data Group), Chin. Phys. C **40**, 100001 (2016).
- [11] J. Rojo *et al.*, Journal of Physics G: Nuclear and Particle Physics **42**, 103103 (2015).
- [12] A. Adare *et al.* (PHENIX), Phys. Rev. **D90**, 012007 (2014), arXiv:1402.6296 [hep-ex].

- [13] S. Dürr *et al.*, Science **322**, 1224 (2008).
- [14] S. Borsànyi *et al.*, J. High Energ. Phys. **77** (2010).
- [15] K. M. Walsh, “Supercomputing the Transition from Ordinary to Extraordinary Forms of Matter,” <https://www.bnl.gov/newsroom/news.php?a=24281> (2013).
- [16] M. P. McCumber, *Measurements of Fast Parton Interactions with Hot Dense Nuclear Matter via Two-Particle Correlations at PHENIX*, Ph.D. thesis, Stony Brook University (2009).
- [17] “PHENIX photos & drawings,” <https://www.phenix.bnl.gov/WWW/run/drawing/>, accessed: 2017-06-16.
- [18] M. Oldenburg, Journal of Physics G: Nuclear and Particle Physics **31** (2004).
- [19] S. S. Adler *et al.* (PHENIX Collaboration), Phys. Rev. C **75**, 024909 (2007).
- [20] J. Adams *et al.* (STAR Collaboration), Phys. Rev. Lett. **91**, 072304 (2003).
- [21] Y. Mao, Nuclear Physics A **932**, 88 (2014), Hard Probes 2013.
- [22] B. Abelev *et al.* (ALICE Collaboration), Phys. Rev. C **91**, 024609 (2015).
- [23] K. Eskola, H. Paukkunen, and C. Salgado, Journal of High Energy Physics **2009**, 065 (2009).
- [24] S. Chatrchyan *et al.*, Physics Letters B **724**, 213 (2013).
- [25] V. Khachatryan *et al.* (CMS Collaboration), Phys. Rev. Lett. **116**, 172302 (2016).
- [26] C. Aidala *et al.* (PHENIX), Nature Phys. **15**, 214 (2019).
- [27] “Relativistic Heavy Ion Collider,” <https://www.flickr.com/photos/brookhavenlab/7979381212/in/album-72157613690851651/>, accessed: 2017-05-17.

- [28] S. Aronson *et al.*, Nuclear Instruments and Methods in Physics Research Section A: Accelerators, Spectrometers, Detectors and Associated Equipment **499**, 480 (2003), The Relativistic Heavy Ion Collider Project: RHIC and its Detectors.
- [29] T. Nakamura, “Introduction to PHENIX Beam Beam Counter (BBC),” https://www.phenix.bnl.gov/phenix/WWW/intro/detectors/focus/focus_bbc.pdf (2002).
- [30] M. Chiu *et al.*, “RHIC Zero Degree Calorimeter,” https://www.phenix.bnl.gov/phenix/WWW/intro/detectors/focus/focus_zdc.pdf (2002).
- [31] K. Adcox *et al.*, Nuclear Instruments and Methods in Physics Research Section A: Accelerators, Spectrometers, Detectors and Associated Equipment **499**, 489 (2003), The Relativistic Heavy Ion Collider Project: RHIC and its Detectors.
- [32] K. Adcox *et al.*, Nuclear Instruments and Methods in Physics Research Section A: Accelerators, Spectrometers, Detectors and Associated Equipment **497**, 263 (2003).
- [33] K. Kenichi, *Asymmetries of W^\pm -Boson Production in Polarized pp Collisions at $\sqrt{s_{NN}} = 500\text{GeV}$* , Ph.D. thesis, Kyoto University (2009).
- [34] M. L. Miller, K. Reygers, S. J. Sanders, and P. Steinberg, Annual Review of Nuclear and Particle Science **57**, 205 (2007), <https://doi.org/10.1146/annurev.nucl.57.090506.123020>.
- [35] S. Milov, “Centrality determination using BBC in Au+Au and Cu+Cu collisions at $\sqrt{s_{NN}} = 200 \text{ GeV}$,” (2005), PHENIX internal Analysis Note 461.
- [36] J. Mitchell *et al.*, Nuclear Instruments and Methods in Physics Research Section A: Accelerators, Spectrometers, Detectors and Associated Equipment **482**, 491 (2002).
- [37] A. Sickles, M. P. McCumber, and A. Adare, Phys. Rev. C **81**, 014908 (2010).
- [38] J. Adam *et al.*, Physics Letters B **763**, 238 (2016).

- [39] J. Kapitán, Nuclear Physics A **855**, 412 (2011), Proceedings of the 4th International Conference on Hard and Electromagnetic Probes of High-Energy Nuclear Collisions - HP2010.
- [40] K. Eskola, V. Kolhinen, and C. Salgado, The European Physical Journal C - Particles and Fields **9**, 61 (1999).
- [41] B. G. Zakharov, J. Phys. **G41**, 075008 (2014), arXiv:1311.1159 [hep-ph].
- [42] S. Acharya *et al.*, Phys. Lett. B **793**, 420 (2019).
- [43] Y. Kim, Nuclear Physics A **982**, 955 (2019), The 27th International Conference on Ultrarelativistic Nucleus-Nucleus Collisions: Quark Matter 2018.
- [44] C. Woody, “sPHENIX EMCAL Project Status, Overview of the EMCAL System,” https://indico.bnl.gov/event/5521/contributions/27320/attachments/22128/30720/sPHENIX_Asia_Meeting_EMCAL_3-26-19.pdf (2019), accessed: 2019-07-14.
- [45] E. Meschi *et al.*, “Electron Reconstruction in the CMS Electromagnetic Calorimeter,” (2001), The Compat Muon Solenoid Experiment CMS Note 034.
- [46] F. Reines and C. L. Cowan, Phys. Rev. **92**, 830 (1953).
- [47] M. Gell-Mann, (1961), 10.2172/4008239, tHE EIGHTFOLD WAY: A THEORY OF STRONG INTERACTION SYMMETRY.
- [48] O. W. Greenberg, American Journal of Physics **50**, 1074 (1982), <https://doi.org/10.1119/1.12922>.
- [49] O. W. Greenberg, Phys. Rev. Lett. **13**, 598 (1964).
- [50] J. J. Aubert *et al.*, Phys. Rev. Lett. **33**, 1404 (1974).

- [51] I. J. R. Aitchison and A. J. G. Hey, *Gauge theories in particle physics: A practical introduction. Vol. 1: From relativistic quantum mechanics to QED* (CRC Press, Bristol, UK, 2012).
- [52] G. Hanson *et al.*, Phys. Rev. Lett. **35**, 1609 (1975).
- [53] J. C. Collins *et al.*, Adv. Ser. Direct. High Energy Phys. **5**, 1 (1989), arXiv:hep-ph/0409313 [hep-ph].
- [54] J. C. Collins and M. J. Perry, Phys. Rev. Lett. **34**, 1353 (1975).
- [55] J. Adams *et al.*, Nuclear Physics A **757**, 102 (2005), First Three Years of Operation of RHIC.
- [56] F. Gelis *et al.*, Annual Review of Nuclear and Particle Science **60**, 463 (2010).
- [57] W. Israel and J. M. Stewart, Annals Phys. **118**, 341 (1979).
- [58] Nuclear Physics A **837**, 26 (2010).
- [59] H. Song, S. A. Bass, U. Heinz, T. Hirano, and C. Shen, Phys. Rev. C **83**, 054910 (2011).
- [60] K. Yagi, T. Hatsuda, and Y. Miake, *Quark-Gluon Plasma* (Cambridge University Press, Cambridge, UK, 2005).
- [61] P. Huovinen *et al.*, Physics Letters B **503**, 58 (2001).
- [62] M. Cacciari, G. P. Salam, and G. Soyez, Journal of High Energy Physics **2008**, 063 (2008).
- [63] Y.-S. Lai and B. A. Cole, (2008), arXiv:0806.1499 [nucl-ex].
- [64] M. L. Miller, K. Reygers, S. J. Sanders, and P. Steinberg, Annual Review of Nuclear and Particle Science **57**, 205 (2007).

- [65] T. Matsui and H. Satz, Phys. Lett. **B178**, 416 (1986).
- [66] J. Aubert *et al.*, Physics Letters B **123**, 275 (1983).
- [67] A. Bodek and J. L. Ritchie, Phys. Rev. D **23**, 1070 (1981).
- [68] R. Feynman, R. Field, and G. Fox, Nuclear Physics B **128**, 1 (1977).
- [69] J. W. Cronin *et al.*, Phys. Rev. D **11**, 3105 (1975).
- [70] L. McLerran and R. Venugopalan, Phys. Rev. D **49**, 2233 (1994).
- [71] I. Vitev, Phys. Rev. C **75**, 064906 (2007).
- [72] A. Adare *et al.* (PHENIX Collaboration), Phys. Rev. Lett. **114**, 192301 (2015).
- [73] H. Hahn *et al.*, Nuclear Instruments and Methods in Physics Research Section A: Accelerators, Spectrometers, Detectors and Associated Equipment **499**, 245 (2003), The Relativistic Heavy Ion Collider Project: RHIC and its Detectors.
- [74] M. Allen *et al.*, Nuclear Instruments and Methods in Physics Research Section A: Accelerators, Spectrometers, Detectors and Associated Equipment **499**, 549 (2003), The Relativistic Heavy Ion Collider Project: RHIC and its Detectors.
- [75] C. Adler *et al.*, Nuclear Instruments and Methods in Physics Research Section A: Accelerators, Spectrometers, Detectors and Associated Equipment **499**, 433 (2003), The Relativistic Heavy Ion Collider Project: RHIC and its Detectors.
- [76] M. Aizawa *et al.*, Nuclear Instruments and Methods in Physics Research Section A: Accelerators, Spectrometers, Detectors and Associated Equipment **499**, 508 (2003), The Relativistic Heavy Ion Collider Project: RHIC and its Detectors.
- [77] S. Kudo, “Charged hadron R_{CP} measurement in ${}^3\text{He}+\text{Au}$ collisions at $\sqrt{s_{NN}} = 200$ GeV,” (2017), PHENIX internal Analysis Note 1297.

- [78] N. Novitzky *et al.*, “Neutral meson analysis in Run-15 p+p, p+Au and p+Al collisions,” (2017), PHENIX internal Analysis Note 1269.
- [79] C. Klein-Bösing, *Production of Neutral Pions and Direct Photons in Ultra-Relativistic Au+Au Collisions*, Ph.D. thesis, Universität Münster (2004).
- [80] J. Frantz, *Direct Photon Shine: Direct Photon and π^0 Production in $\sqrt{s_{NN}} = 200$ GeV Au + Au Collisions*, Ph.D. thesis, Columbia University (2005).
- [81] S. S. Adler *et al.* (PHENIX Collaboration), Phys. Rev. D **74**, 072002 (2006).
- [82] J. Osborn, Nuclear Physics A **982**, 591 (2019), The 27th International Conference on Ultrarelativistic Nucleus-Nucleus Collisions: Quark Matter 2018.
- [83] T. Danley, *Photon-Related Elliptic Azimuthal Asymmetry and Photon-Hadron Correlations with an Isolation Cut in Au+Au Collisions at $\sqrt{s_{NN}} = 200$ GeV at RHIC-PHENIX*, Ph.D. thesis, Ohio University (2018).
- [84] G.-L. Ma and X.-N. Wang, Phys. Rev. Lett. **106**, 162301 (2011).
- [85] K. C. Zapp *et al.*, Journal of High Energy Physics **2013**, 80 (2013).
- [86] Z.-Q. Liu *et al.*, The European Physical Journal C **76**, 20 (2016).
- [87] T. Sjöstrand, S. Mrenna, and P. Skands, Journal of High Energy Physics **2006**, 026 (2006).
- [88] T. Sjöstrand, S. Mrenna, and P. Skands, Computer Physics Communications **178**, 852 (2008).
- [89] K. Eskola, H. Paukkunen, and C. Salgado, Journal of High Energy Physics **2009**, 065 (2009).
- [90] H. Lai *et al.*, The European Physical Journal C - Particles and Fields **12**, 375 (2000).

- [91] K. J. Eskola *et al.*, The European Physical Journal C **77**, 163 (2017).
- [92] R. D. Ball *et al.* (NNPDF), Nucl. Phys. **B877**, 290 (2013).
- [93] X.-N. Wang and M. Gyulassy, Phys. Rev. D **44**, 3501 (1991).
- [94] X.-N. Wang and M. Gyulassy, Phys. Rev. Lett. **68**, 1480 (1992).
- [95] X.-N. Wang and M. Gyulassy, Phys. Rev. D **45**, 844 (1992).
- [96] M. Gyulassy and X.-N. Wang, Computer Physics Communications **83**, 307 (1994).
- [97] A. Adare *et al.* (PHENIX), (2015), arXiv:1501.06197 [nucl-ex].
- [98] A. Aprahamian *et al.*, (2015), Reaching for the horizon: The 2015 long range plan for nuclear science.
- [99] “sPHENIX PD23 Review Agenda Page,” <https://indico.bnl.gov/event/6145/>, accessed: 2019-07-29.
- [100] M. McCumber, “Practical Jet Mathematics,” (2007), PHENIX internal Analysis Note 646.
- [101] A. Adare *et al.* (PHENIX Collaboration), Phys. Rev. C **78**, 014901 (2008).
- [102] P. Stankus, “Mathematical Framework for Interpreting Pair Angular Correlations in a Two-Source Model,” (2005), PHENIX internal Technical Note 412.
- [103] “sPHENIX PD23 Review Technical Design Report,” https://indico.bnl.gov/event/6145/attachments/22906/32787/sphenix_tdr_20190513.pdf, accessed: 2019-07-29.
- [104] S. Agostinelli *et al.*, Nuclear Instruments and Methods in Physics Research Section A: Accelerators, Spectrometers, Detectors and Associated Equipment **506**, 250 (2003).
- [105] J. Allison *et al.*, IEEE Transactions on Nuclear Science **53**, 270 (2006).

- [106] J. Allison *et al.*, Nuclear Instruments and Methods in Physics Research Section A: Accelerators, Spectrometers, Detectors and Associated Equipment **835**, 186 (2016).
- [107] “CERN Accelerating Science,” <https://home.cern/science/experiments/cms>, accessed: 2019-08-01.

APPENDIX A: JARGON IN RELATIVISTIC HEAVY ION COLLISIONS

A.1 Transverse Momentum (p_T)

Most of the observables in collision physics are studied as a function of transverse momentum (p_T). Initially, the colliding partons has only longitudinal momentum (without considering intrinsic k_T effect) along the beam axis. Any transverse momentum produced should be due to the interaction during the collision. Also, the momentum conservation demands for the net transverse momentum to be zero.

A.2 Rapidity (y) and Pseudorapidity (η)

The rapidity is defined as,

$$y = \frac{1}{2} \ln \left(\frac{E + p_z}{E - p_z} \right), \quad (\text{A.1})$$

where E and p_z are energy and longitudinal momentum. The rapidity difference is Lorentz invariant. Since the jets are boosted along the beam, the angle between the jets can be expressed in terms of rapidity difference.

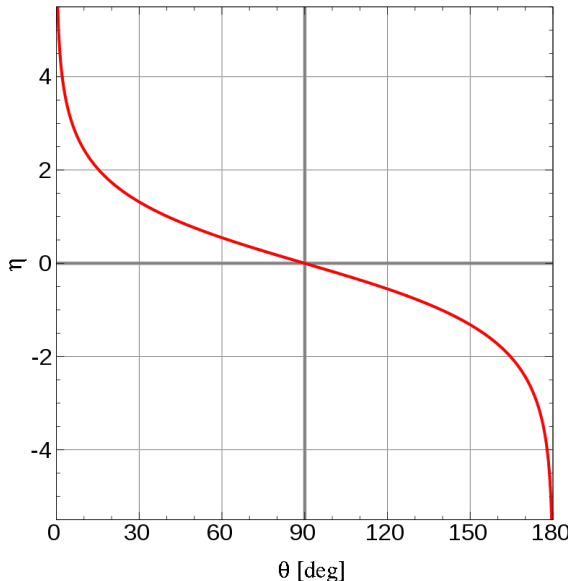


Figure A.1: Pseudorapidity (η) vs polar angle (θ). The normal polar angle (90°) corresponds to zero pseudorapidity.

For highly relativistic particle, $p_z \approx E \cos\theta$. Thus, high relativistic equivalent of rapidity called pseudorapidity is defined as,

$$\eta \equiv -\ln\left(\tan\frac{\theta}{2}\right) \quad (\text{A.2})$$

The pseudorapidity is also Lorentz invariant under longitudinal boosts are used to measure the polar angle of particle. The relation between the polar angle and the pseudorapidity is illustrated in the Figure A.1. The *Midrapidity* region is the region around $\eta = 0$ or $\theta = 90^\circ$ (i.e. perpendicular to the beam direction.). Also the *Forward rapidity (Backward rapidity)* represents the regions with maximum (minimum) rapidity.

A.3 Invariant Mass

The invariant mass (W) of a particle decaying into a system of particles is defined as a

$$(Wc^2)^2 = \left(\sum E\right)^2 - \left\|\sum \mathbf{p}c\right\|^2$$

$$W^2 = \left(\sum E\right)^2 - \left\|\sum \mathbf{p}\right\|^2 \text{ (in natural units } c=1\text{)} \quad (\text{A.3})$$

where $\sum E$ is the sum of energies and $\sum \mathbf{p}$ is the vector sum of momentum of particles. The invariant mass is constant in all frames of reference and hence used in relativistic regime. If the system is at rest, the invariant mass is equal to the total mass of the system divided by c^2 . The invariant mass for one particle in such case is also called *rest mass*.

A.4 Mandelstam Variables

Mandelstam Variables for $1+2 \rightarrow 3+4$ processes are defined as

$$s = (\bar{p}_1 + \bar{p}_2)^2 = (\bar{p}_3 + \bar{p}_4)^2$$

$$t = (\bar{p}_1 - \bar{p}_3)^2 = (\bar{p}_4 - \bar{p}_2)^2$$

$$u = (\bar{p}_1 - \bar{p}_4)^2 = (\bar{p}_3 + \bar{p}_2)^2 \quad (\text{A.4})$$

where s, t and u corresponds to the s -channel, t -channel and u -channel of interaction. The \bar{p}_i 's are the four momentum vectors for the particles. The s -channel represents particles 1, 2 merging to form a intermediate boson and eventually splitting into 3,4 particles. In,

t-channel is a scattering process where particle 1 (2) emits (absorbs) intermediate boson and changes to particle 3 (4). The *u*- channel is equivalent to *t*-channel with role of 3,4 particle being interchanged.

The *t* value is also known as four-momentum transfer. While \sqrt{s} equals to total center of mass energy (invariant mass) available for the interaction.

A.5 Collision Geometry

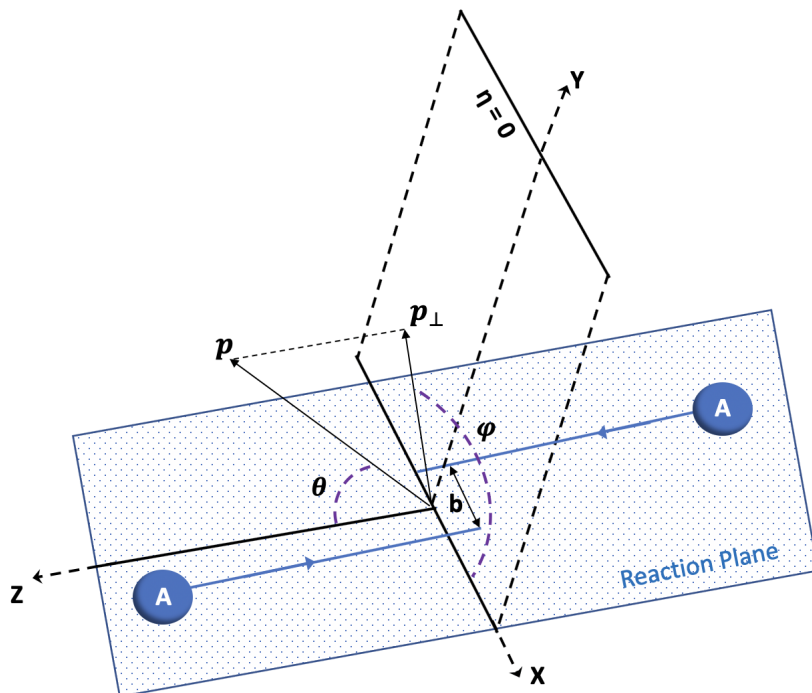


Figure A.2: Cartoon illustration of collision geometry. The green grid plane is the reaction plane with two nuclei colliding along z-axis.

The geometry in heavy-ion collisions showing polar angle (θ), azimuthal angle (ϕ), impact parameter (b), transverse plane and reaction plane is illustrated in Figure A.2. The beam direction is generally taken in Z-axis. Impact parameter is the distance between the centers of two interacting particles. The reaction plane is the plane created by impact

parameter and beam axis. Also, the reaction plane angle is the angle made by reaction plane with X- axis. Reaction plane angle is zero in the Figure A.2 since the impact parameter lies along X-axis.

A.6 Impact parameter and Centrality

In heavy ion collisions, the impact parameter is too small to measure and hence are quantified in terms of centrality. Centrality represents the extent of overlap during collisions. Details about the centrality is discussed in Section 2.4. Smaller the value of centrality more central is the collision. The head on collisions corresponds to most central collision (smaller value) while grazing or non-central collisions corresponds to most peripheral centrality (larger value).

APPENDIX B: 2-PARTICLE CORRELATION MATHEMATICS

In this chapter, I describe some mathematical details especially related to two-particle correlation methods. This chapter is largely adapted from [100].

B.1 Notations

$$[N] = \text{True Counts}$$

$$[\mathbb{N}] = \text{Measured (Raw) Counts}$$

$$[n] = \text{True counts/Event}$$

$$[\mathfrak{n}] = \text{Measured (Raw) Counts/Event} \quad (\text{B.1})$$

$$\left[\frac{dn}{d\Delta\phi} \right] = \text{True Counts/Event/Rad}$$

$$\left[\frac{d\mathfrak{n}}{d\Delta\phi} \right] = \text{Measured Counts/Event/Rad}$$

B.2 Efficiency (ϵ) Definitions

$$[\mathfrak{n}^A] = \epsilon^A n^A$$

$$[\mathfrak{n}^B] = \epsilon^B n^B$$

$$[\mathfrak{n}_{\text{same}}^{AB}] = \epsilon_{\text{same}}^{AB} n_{\text{same}}^{AB}$$

$$[\mathfrak{n}_{\text{mix}}^{AB}] = \epsilon_{\text{mix}}^{AB} n_{\text{mix}}^{AB}$$

where superscripts A corresponds to trigger particle, B to partner particle and AB to trigger-partner pair. Also, the subscripts *same* corresponds to pair from real or same events and *mix* corresponds to that from mixed events.

B.3 Acceptance Correction

From definition,

$$\frac{d\langle \mathfrak{n}_{\text{same}}^{AB} \rangle}{d\Delta\phi} = \frac{\frac{d\langle \mathfrak{n}_{\text{same}}^{AB} \rangle}{d\Delta\phi}}{Acc(\Delta\phi)} \quad (\text{B.3})$$

The acceptance correction follows the shape as the mixed event pair distribution [101].

Hence

$$\begin{aligned} Acc(\Delta\phi) &\propto \frac{d\langle n_{mix}^{AB} \rangle}{d\Delta\phi} \\ &= \alpha \frac{d\langle n_{mix}^{AB} \rangle}{d\Delta\phi} \end{aligned} \quad (B.4)$$

where α is proportionality constant. Putting the value from Equation (B.4) to (B.3) and then integrating Equation (B.3) over $\Delta\phi$,

$$\int \frac{d\langle n_{same}^{AB} \rangle}{d\Delta\phi} d\Delta\phi = \frac{1}{\alpha} \frac{\langle n_{same}^{AB} \rangle}{\langle n_{mix}^{AB} \rangle} \int \frac{\frac{d\langle n_{same}^{AB} \rangle}{d\Delta\phi}}{\frac{d\langle n_{mix}^{AB} \rangle}{d\Delta\phi}} \frac{\langle n_{mix}^{AB} \rangle}{\langle n_{same}^{AB} \rangle} d\Delta\phi \quad (B.5)$$

Now using the definition of correlation function ($C(\Delta\phi)$) and from Equation (B.2), the Equation (B.5) becomes,

$$\frac{\langle n_{same}^{AB} \rangle}{\epsilon_{same}^{AB}} = \frac{1}{\alpha} \frac{\langle n_{same}^{AB} \rangle}{\langle n_{mix}^{AB} \rangle} \int C(\Delta\phi) d\Delta\phi \quad (B.6)$$

From "The Sum Rule of Correlations" [102],

$$\int C(\Delta\phi) d\Delta\phi = \frac{\epsilon_{mix}^{AB}}{\epsilon_{same}^{AB}} \int d\Delta\phi \quad (B.7)$$

Thus from Equation (B.6) and (B.7),

$$\frac{1}{\epsilon_{same}^{AB}} = \frac{1}{\alpha} \frac{1}{\langle n_{mix}^{AB} \rangle} \frac{\epsilon_{mix}^{AB}}{\epsilon_{same}^{AB}} \int d\Delta\phi \quad (B.8)$$

Now from Equation (B.8) and (B.4), acceptance correction can be written as,

$$Acc(\Delta\phi) = \frac{d\langle n_{mix}^{AB} \rangle}{d\Delta\phi} \frac{\epsilon_{mix}^{AB}}{\langle n_{mix}^{AB} \rangle} \int d\Delta\phi \quad (B.9)$$

B.4 Jet Function from Two Source Model

From a two-source model as described in Section 4.1,

$$\frac{d\langle n_{jet}^{AB} \rangle}{d\Delta\phi} = \frac{d\langle n_{same}^{AB} \rangle}{d\Delta\phi} - \frac{d\langle n_{com}^{AB} \rangle}{d\Delta\phi}, \quad (B.10)$$

where $n_{com}^{AB} \equiv n_{bg}^{AB}$. Dividing by number of trigger in both sides for per-trigger yield and writing background in terms of harmonics,

$$\frac{1}{\langle n^A \rangle} \frac{d\langle n_{jet}^{AB} \rangle}{d\Delta\phi} = \frac{1}{\langle n^A \rangle} \left[\frac{d\langle n_{same}^{AB} \rangle}{d\Delta\phi} - \frac{\langle n_{com}^{AB} \rangle}{\int d\Delta\phi} (1 + \langle 2v_2^A v_2^B \rangle \cos(2\Delta\phi)) \right] \quad (B.11)$$

The combinatorial (background) pairs can be approximated by mixed pair with correction from centrality bin bias and the Equation B.11 can be written as,

$$\frac{1}{\langle n^A \rangle} \frac{d\langle n_{jet}^{AB} \rangle}{d\Delta\phi} = \frac{1}{\langle n^A \rangle} \left[\frac{d\langle n_{same}^{AB} \rangle}{d\Delta\phi} - \xi \frac{\langle n_{mix}^{AB} \rangle}{\int d\Delta\phi} (1 + \langle 2v_2^A v_2^B \rangle \cos(2\Delta\phi)) \right] \quad (\text{B.12})$$

Now, putting values from Equation (B.2) and B.3 in Equation (B.12),

$$\frac{1}{\langle n^A \rangle} \frac{d\langle n_{jet}^{AB} \rangle}{d\Delta\phi} = \frac{\epsilon^A}{\langle n^A \rangle} \left[\frac{\frac{d\langle n_{same}^{AB} \rangle}{d\Delta\phi}}{Acc(\Delta\phi)} - \xi \frac{\langle n_{mix}^{AB} \rangle}{\epsilon_{mix}^A \int d\Delta\phi} (1 + \langle 2v_2^A v_2^B \rangle \cos(2\Delta\phi)) \right] \quad (\text{B.13})$$

Putting the value of acceptance correction from Equation (B.9),

$$\frac{1}{\langle n^A \rangle} \frac{d\langle n_{jet}^{AB} \rangle}{d\Delta\phi} = \frac{\epsilon^A}{\langle n^A \rangle} \left[\frac{\frac{d\langle n_{same}^{AB} \rangle}{d\Delta\phi}}{\frac{d\langle n_{mix}^{AB} \rangle}{d\Delta\phi}} \frac{\langle n_{mix}^{AB} \rangle}{\epsilon_{mix}^{AB} \int d\Delta\phi} - \xi \frac{\langle n_{mix}^{AB} \rangle}{\epsilon_{mix}^A \int d\Delta\phi} (1 + \langle 2v_2^A v_2^B \rangle \cos(2\Delta\phi)) \right] \quad (\text{B.14})$$

$$\frac{1}{\langle n^A \rangle} \frac{d\langle n_{jet}^{AB} \rangle}{d\Delta\phi} = \frac{\epsilon^A}{\langle n^A \rangle} \frac{\langle n_{mix}^{AB} \rangle}{\epsilon_{mix}^{AB} \int d\Delta\phi} \left[\frac{\frac{d\langle n_{same}^{AB} \rangle}{d\Delta\phi}}{\frac{d\langle n_{mix}^{AB} \rangle}{d\Delta\phi}} - \xi (1 + \langle 2v_2^A v_2^B \rangle \cos(2\Delta\phi)) \right] \quad (\text{B.15})$$

Above is the "event-normalized" framework (normalization for correlation function). Now, multiplying Equation (B.15) by unity to change into the "pair-normalized" framework,

$$\frac{1}{\langle n^A \rangle} \frac{d\langle n_{jet}^{AB} \rangle}{d\Delta\phi} = \frac{\epsilon^A}{\langle n^A \rangle} \frac{\langle n_{mix}^{AB} \rangle}{\epsilon_{mix}^{AB} \int d\Delta\phi} \left[\frac{\langle n_{same}^{AB} \rangle}{\langle n_{mix}^{AB} \rangle} \frac{\langle n_{mix}^{AB} \rangle}{\langle n_{same}^{AB} \rangle} \left[\frac{\frac{d\langle n_{same}^{AB} \rangle}{d\Delta\phi}}{\frac{d\langle n_{mix}^{AB} \rangle}{d\Delta\phi}} - \xi (1 + \langle 2v_2^A v_2^B \rangle \cos(2\Delta\phi)) \right] \right] \quad (\text{B.16})$$

Now, using the definition of correlation function $C(\Delta\phi) \equiv \frac{\frac{d\langle n_{same}^{AB} \rangle}{d\Delta\phi}}{\frac{d\langle n_{mix}^{AB} \rangle}{d\Delta\phi}} / \langle n_{same}^{AB} \rangle$, the Equation (B.16) becomes,

$$\frac{1}{\langle n^A \rangle} \frac{d\langle n_{jet}^{AB} \rangle}{d\Delta\phi} = \frac{\epsilon^A}{\langle n^A \rangle} \frac{\langle n_{same}^{AB} \rangle}{\epsilon_{mix}^{AB} \int d\Delta\phi} [C(\Delta\phi) - b_0 (1 + \langle 2v_2^A v_2^B \rangle \cos(2\Delta\phi))] \quad (\text{B.17})$$

where $b_0 = \xi \frac{\langle n_{mix}^{AB} \rangle}{\langle n_{same}^{AB} \rangle} = \xi \kappa \frac{\langle n^A \rangle \langle n^B \rangle}{\langle n_{same}^{AB} \rangle}$ is background level. κ is pair-cut survival probability.

$$\frac{1}{\langle n^A \rangle} \frac{d\langle n_{jet}^{AB} \rangle}{d\Delta\phi} = \frac{1}{\epsilon^B \kappa \langle n^A \rangle \int d\Delta\phi} [C(\Delta\phi) - b_0 (1 + \langle 2v_2^A v_2^B \rangle \cos(2\Delta\phi))] \quad (\text{B.18})$$

where $\epsilon_{mix}^{AB} = \kappa \epsilon^A \epsilon^B$.

Thus, the ***working equation*** for two particle correlation method can be written as,

$$J(\Delta\phi) = C(\Delta\phi) - b_0 (1 + \langle 2v_2^A v_2^B \rangle \cos(2\Delta\phi)) \quad (\text{B.19})$$

where $J(\Delta\phi)$ is called the jet function which has only contribution from jet and can be defined as,

$$\frac{1}{\langle n^A \rangle} \frac{d\langle n_{jet}^{AB} \rangle}{d\Delta\phi} = \frac{1}{\epsilon^B \kappa} \frac{\langle n_{same}^{AB} \rangle}{\langle n^A \rangle \int d\Delta\phi} J(\Delta\phi) \quad (\text{B.20})$$

The coefficient (normalization factor) of $J(\Delta\phi)$ in right hand side of the Equation (B.20) can be different with different normalization conditions of correlation function.

APPENDIX C: sPHENIX EMCAL SIMULATION: DESIGN AND CORRELATION STUDIES

Part of my dissertation research also involved analysis of design simulations of the sPHENIX EMCAL [99, 103] in order to optimize its design and tune its simulation for better future physics analysis. The simulation incorporates the GEANT4 [104–106] simulation program to fully implement the geometries and materials of the real sPHENIX detector and to simulate completely particle propagation in all details through the detector. Below I briefly describe this work.

C.1 sPHENIX Electromagnetic Calorimeter (EMCal) Design

The sPHENIX electromagnetic calorimeter [99, 103] is being designed to cover ± 1.1 in η and the full angle (2π) in ϕ . Tungsten powder and epoxy will be used as passive absorber material and scintillating fibers (embedded in the absorber) will serve as the active (light-collecting) detector material. There will be a total of 24576 towers (96×256) with a segmentation of $\Delta\eta \times \Delta\phi \approx 0.025 \times 0.025$. The EMCal will have excellent resolution of $\sigma_E/E < 16\%/\sqrt{E} \oplus 5\%$ providing an electron and hadron separation greater than 100:1. The EMCal will be compact and be fitted inside the sPHENIX solenoid (which is being reused from the BaBar experiment and will create 1.4 T of magnetic field). The precise measurements of jets, photons and Upsilonons (Υ) are among the main physics goal of the sPHENIX EMCAL. The basic EMCal subsystems of sPHENIX are shown in Figure C.1.

Each sector consists of 96 modules (blocks) which in turn consists of 2×2 projective towers. The blocks are tilted at an angle of $\sim 9^\circ$ in both ϕ and η direction. This tilt is designed to minimize the channeling of incident and shower particles along projective lines. The sector design for the sPHENIX EMCAL is shown in Figure C.2.

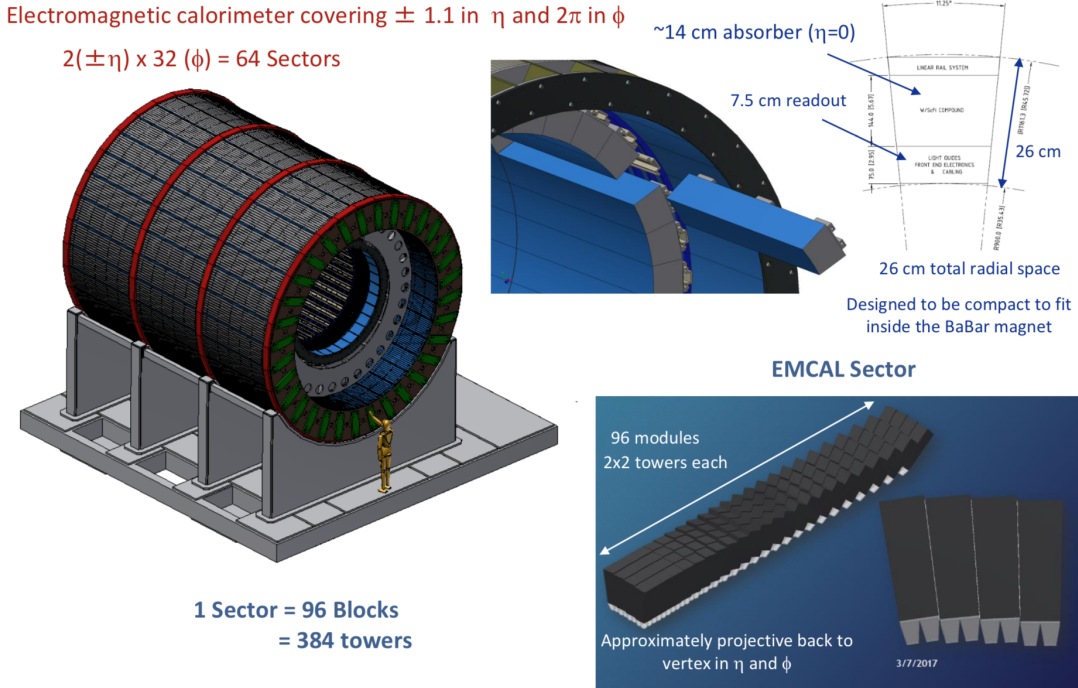


Figure C.1: Electromagnetic Calorimeter subsystem of sPHENIX. The figure is taken from [44].

C.2 EMCAL Software

Among the different software studies related to the EMCAL, I contributed in the following:

- Cluster Reconstruction Performance
- Energy Leakage of EM Clusters
- New Cluster Calibration Framework

C.3 Cluster Reconstruction Performance

As described previously in the detector chapters of this thesis, energy from a single particle, especially a photon or electron, which showers in the EMCAL is spread over several towers. Each tower makes its own independent measurement of a given shower's energy

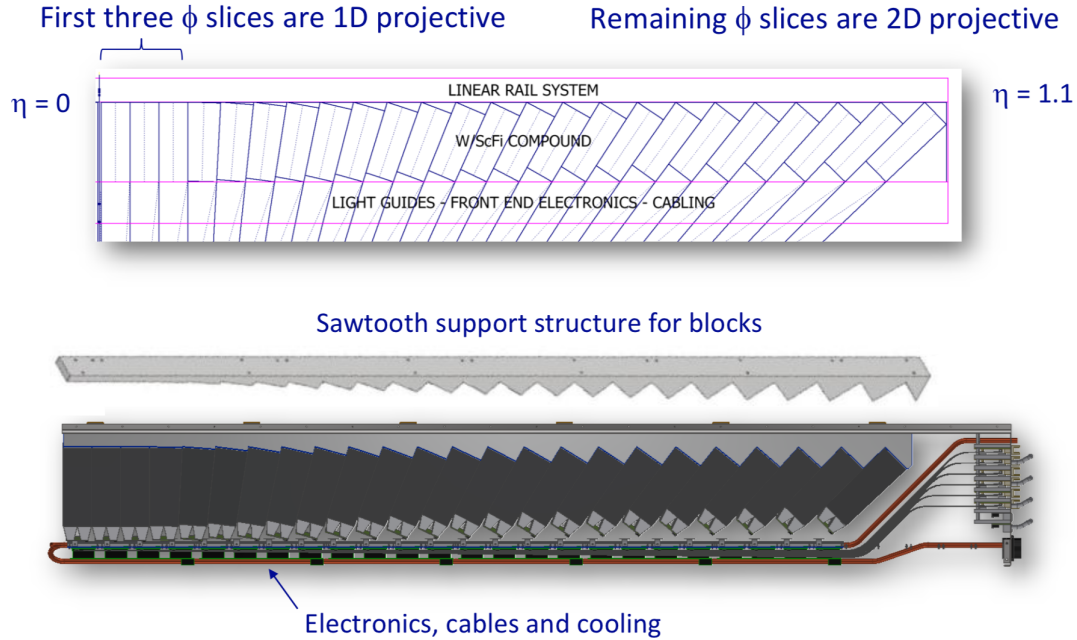


Figure C.2: Electromagnetic Calorimeter subsystem of sPHENIX. The figure is taken from [44].

contribution at its location. Clustering is the action, achieved via various algorithms, of grouping continuous hit towers into the larger groups, clusters, which correspond ideally to the individual particles such as photons. In the high multiplicity environment of sPHENIX, there will be a high probability of shower overlap. So, the calorimeters in sPHENIX require a clustering algorithm which separates the overlapping shower energies. In order to find out the best clustering algorithm for the sPHENIX EMCal, three different clustering algorithms were studied viz; Simplest contiguous, PHENIX and CMS Island [45].

- **Simplest Contiguous:** This clustering algorithm doesn't split the overlapping showers. It simply finds a group of adjacent towers having non-zero energies and assign this group as a cluster.
- **CMS Island:** The island algorithm used earlier in CMS experiment [107] was also studied for sPHENIX detector. This algorithm also separates the two overlapping

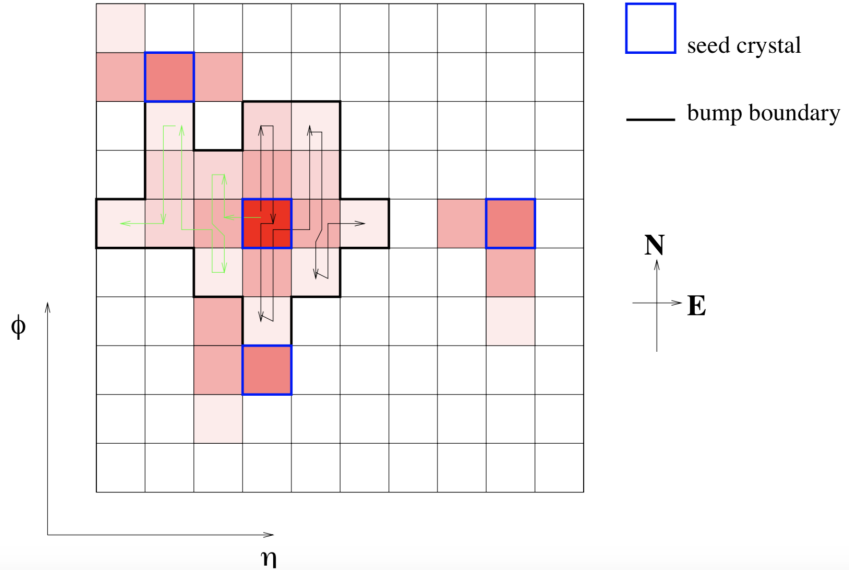


Figure C.3: Illustration of CMS Island algorithm. The figure is taken from [45].

showers. The working of the island algorithm is illustrated in the Figure C.3. The island algorithm follows the basic steps as described below;

1. Find the towers with energy greater than certain threshold energy and store them as "seed".
2. Remove seeds adjacent to higher energy ones
3. Beginning from the seed with highest energy
 - (a) Move along ϕ directions (both sides) until there is rise in energy or there is null energy.
 - (b) Move one step in η and repeat the process in ϕ . And continue this along other η until there is rise in energy or there is null energy.

- **PHENIX:** This algorithm separates (splits) the shower overlaps based on a shower shape fitting where a separate fit template is added for each local maximum in each contiguous/adjacent grouping. The detail is described in Section... The main

difference between the PHENIX clustering algorithm and island is that there is the possibility of two clusters sharing a tower in the PHENIX algorithm.

Different comparative studies for eg. projectiveness (1D vs 2D), ganging of towers, splitting efficiency etc. were done for these three clustering algorithms. The comparison of

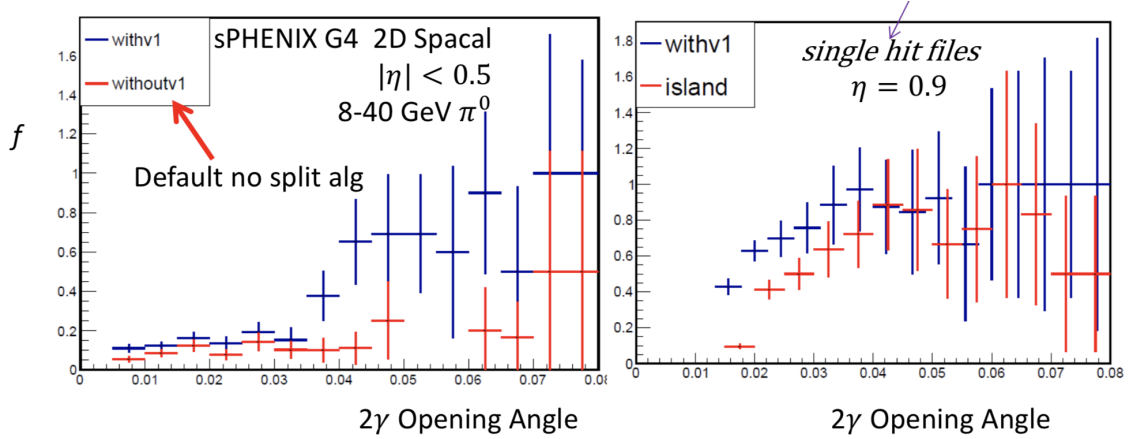


Figure C.4: π^0 cluster splitting fraction with respect to the opening angle of two decaying photons. Here "withv1" corresponds to the PHENIX clustering algorithm while "withoutv1" corresponds to the simple contiguous algorithm.

splitting efficiency for the different clustering algorithms is shown in Figure C.4. From the figure, we can see that the PHENIX clustering algorithm clearly does better compared to other two algorithms.

Figure C.5 shows the GEANT4 simulation result of cluster energy vs. truth energy for single photon (i.e. $p+p$ collision environment). The figure shows the island algorithm under-predicting the energy of the clusters compared to that by the other two clustering algorithms. For the high multiplicity environment (A+A collisions), the GEANT4 simulation study was done to by embedding the photon with previously generated hit files.

The performance of the simple contiguous and PHENIX algorithm in the embedding situation is shown in Figure C.6. From the figure, we can clearly see that the simple contiguous algorithm clearly over predicts the high energy cluster compared to PHENIX

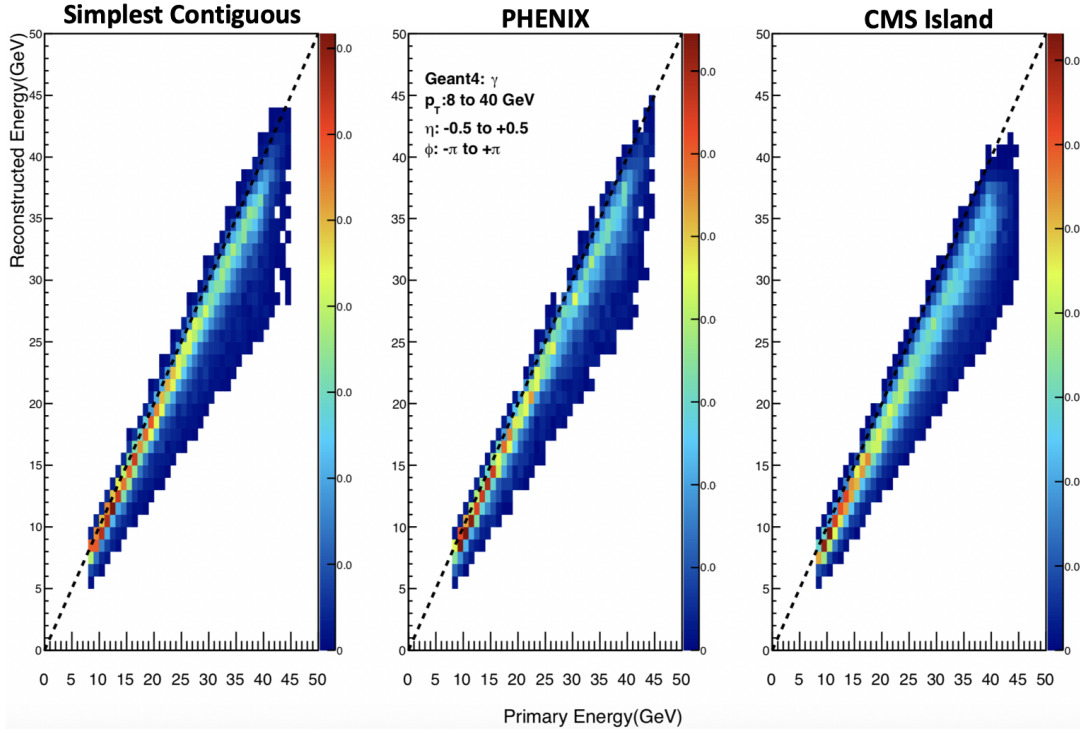


Figure C.5: Reconstructed energy vs truth (primary) energy for single photon simulation in three different clustering algorithm. The dashed line is where the reconstructed energy is equal to the truth or primary energy.

algorithm. This is expected because the simple contiguous algorithm doesn't separate the overlapped showers in high multiplicity environment. Currently, the PHENIX clustering algorithm is being used as the default clustering algorithm in sPHENIX calorimeters.

C.4 Cluster Energy Leakage

During the cluster study for three different clustering algorithms, we discovered cases of very low energy reconstructed energy in the EMCAL for photons and π^0 . Figure C.7 shows the blue triangular band of low energy clusters compared to primary energy. The fraction of low energy clusters ($E_{\text{cluster}}/E_{\text{truth}} < 0.7$) was found to be $\sim 5\text{-}10\%$. In order to find out the possible reasons behind such low energy clusters, we did the simulation study in the very small area of the EMCAL (as small as towers) with a high density of thrown particles in

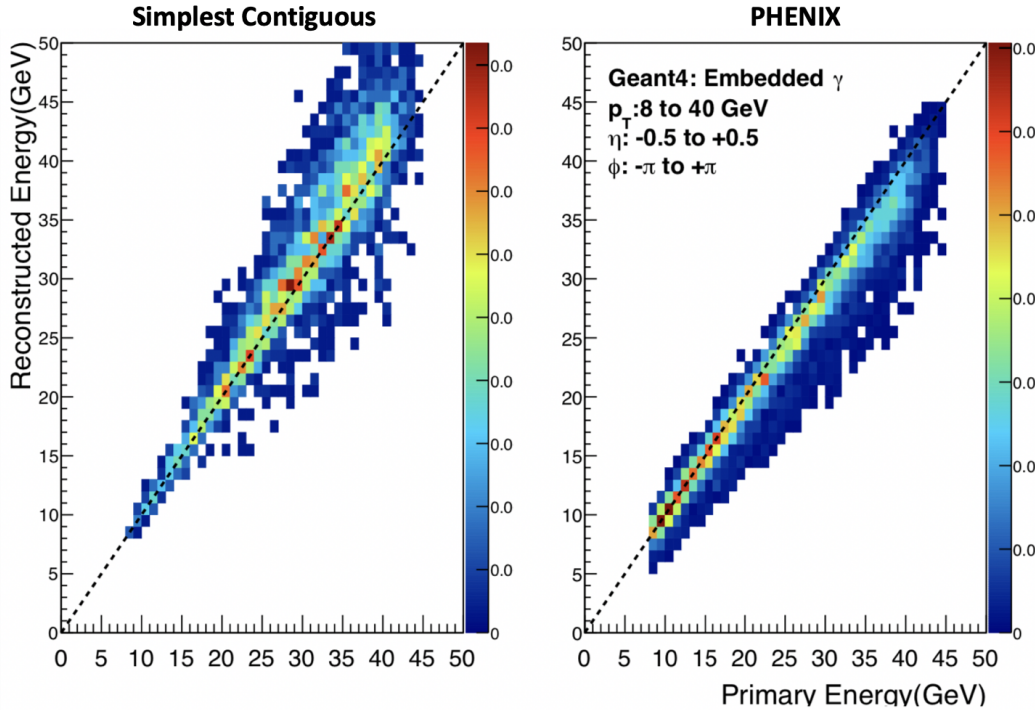


Figure C.6: Reconstructed energy vs truth (primary) energy for embedded photon simulation in two different clustering algorithms. The dashed line is where the reconstructed energy is equal to the truth or primary energy.

this small volume. From the study, we found that the pattern of low energy clusters matched with different geometries of the EMCal subsystems as shown in Figure C.8. The figure shows square pattern of fibers and tower boundaries in $\Delta\eta \times \Delta\phi \sim 0.025 \times 0.025$. Also, it shows the sector boundary around $\eta \approx 0$. So, the photons hitting the fibers and geometrical boundaries directly are showering less and appearing as low energy reconstructed clusters.

In order to deal with this "channeling" problem tilting of EMCal blocks was proposed. This channeling is caused by particles going long ways through only the active fibers which are oriented in the same direction the particles' trajectories and hence never hitting absorber material. The study was done for the various proposed tilting angles. Our simulation

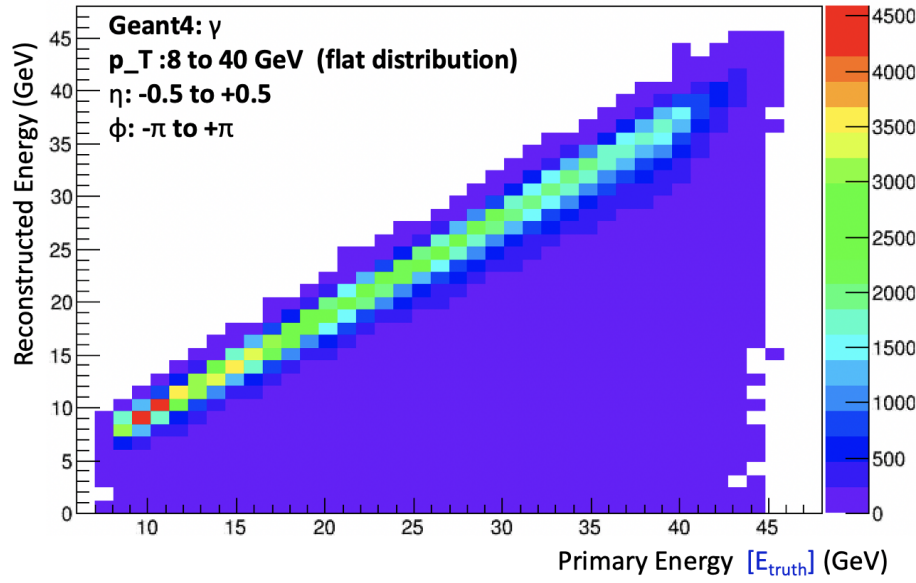


Figure C.7: Reconstructed vs. Primary energy for single photon simulation using PHENIX clustering algorithm.

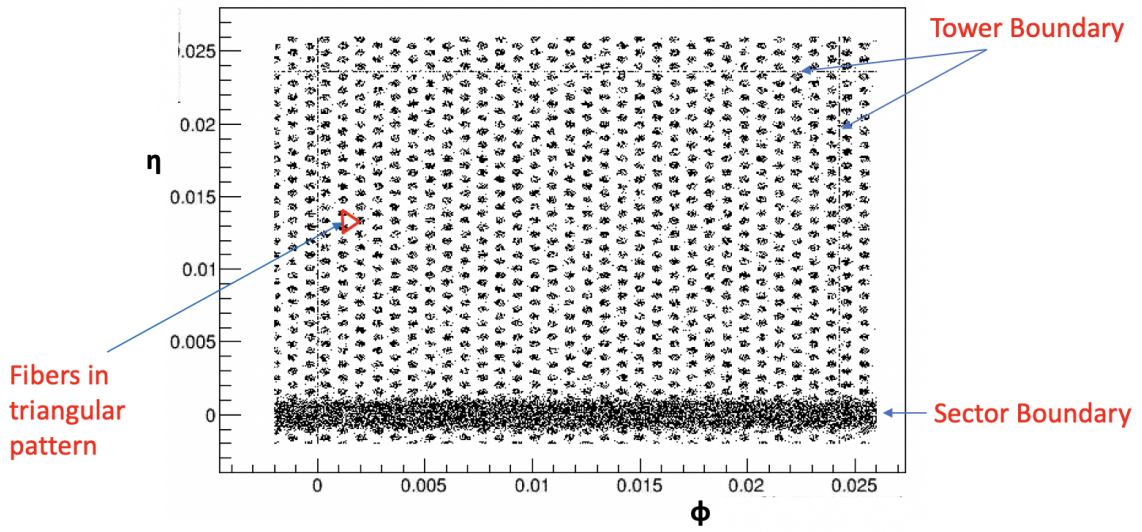


Figure C.8: Patterns of low energy clusters in the single photon GEANT4 simulation. The pattern matches with the fiber positions, tower boundary and sector boundary.

study with different tilting angles confirmed the current tilting angle $\sim 9^0$ as a sufficient value, and optimal given other constraints. The geometrical patterns are removed with the implementation of the current tilt as shown in left of the Figure C.9 and the low reconstructed energy cluster is much reduced to $\sim 2\text{-}3\%$ which is expected to be a typical irreducible limit given typical EMCAL detector geometries such as that of sphenix.

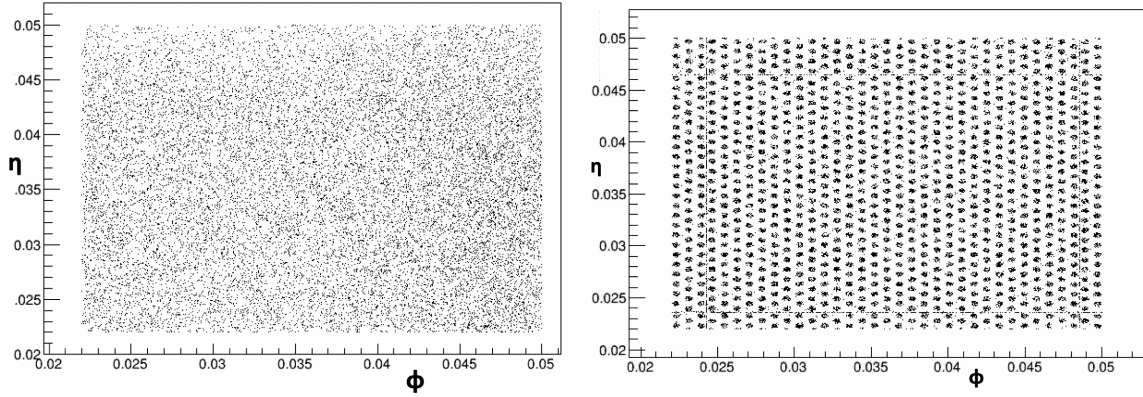


Figure C.9: The low energy clusters before (right) and after (left) 9^0 tilt. Note: the number of events in the left figure is large compared to that in right figure.

C.5 Cluster Energy Position Dependence Study and New Cluster Corrections

After the tilt study, we focused on block edge leakages as one of the possible remaining sources of low reconstructed energy. The pattern should be dependent on η or Z-position of the hit on front face of EMCAL. Thus we switched our position measure using the plain projected z-position of primary photon on front face of EMCAL (ZEMC). For the study following considerations were made;

- GEANT4 single photon with 9^0 tilt
- PHENIX clustering algorithm
- p_T : 8 to 40 GeV/c
- ϕ : 0.2, various ranges

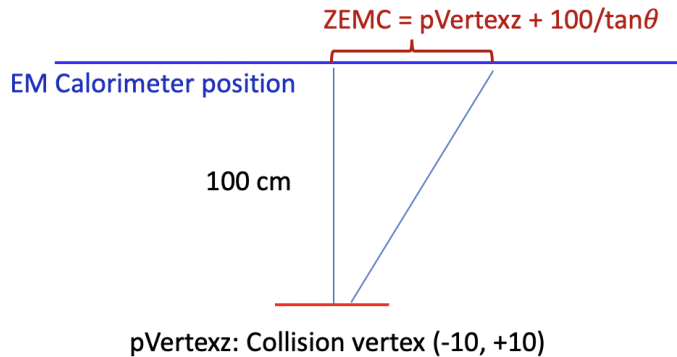


Figure C.10: Pictorial illustration of ZEMC.

- η : 0.1 to 1.0
- Turned off the inner hadronic calorimeter and magnet. Blackhole is just after EMC.
- width of z-vertex distribution: 10.0 cm

The ratio of reconstructed cluster energy as a function of ZEMC is shown in Figure C.11.

Note that even though the detector is designed to have a smooth energy reconstruction performance as a function of pseudorapidity (η) since it is η -projective, not ZEMC projective (which would be typical of the more standard cylindrically symmetric barrel designs) the same non-uniformity is found as a function of *eta* for different z-vertex origin selections. Thus the problem seems to be most conveniently plotted as a function of ZEMC when averaging over all z-vertexes of a realistic event sample.

The figure shows that the average is centered on response of 1 but there are still position dependent variations in the response. Although a position-based calibration was applied, the pattern is not completely unexpected. The current position dependence calibration uses a 2x2 tower block as its unit, duplicating the same block corrections over the entire EMCAL, and hence misses the projectivity of the blocks in different positions.

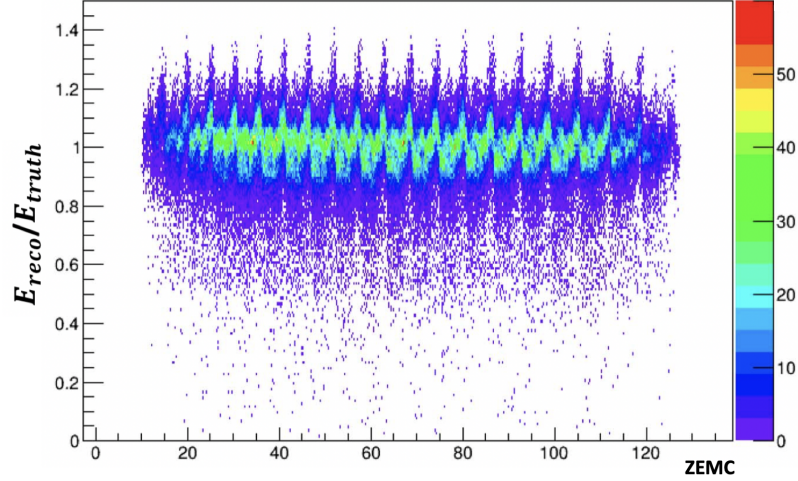


Figure C.11: Reconstruction efficiency as a function of ZEMC.

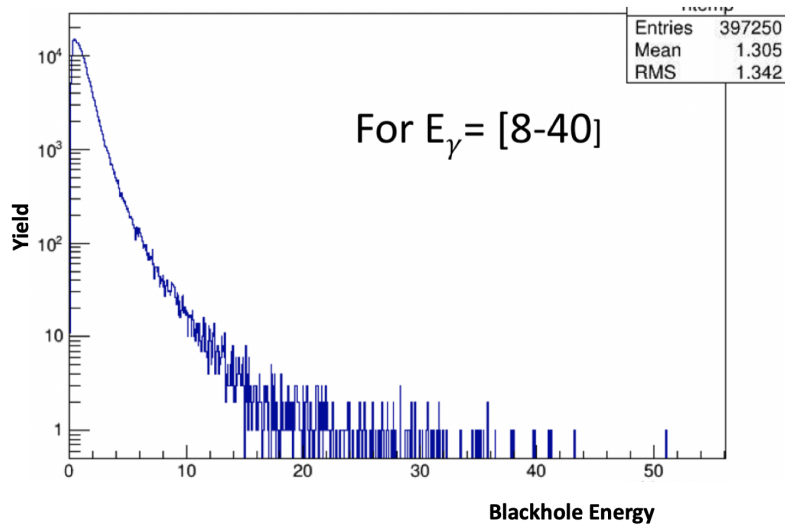


Figure C.12: Blackhole energy just after the EMCAL position.

Figure C.12 shows the yield of leaked energy collected in blackhole just outside of EMCAL. The figure, we can see that all of the clusters thrown have some non-zero leakage. For the study of leakage contribution to the position dependence, we added the leakage energy to the cluster energy and plotted with respect to ZEMC as shown in right of the

Figure C.13. From the figure we can see that the position dependence is still pronounced

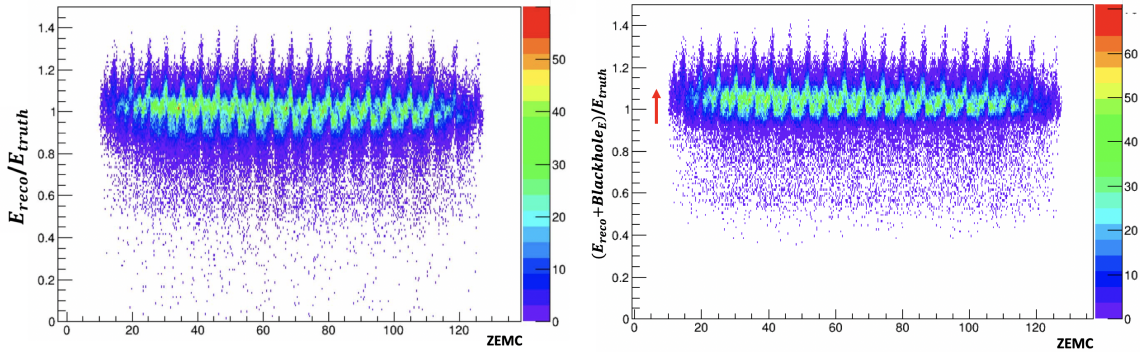


Figure C.13: Reconstruction efficiency without (left) and with (right) including blackhole energy.

even with leakage was included. However, the leakage does make some noticeable changes especially in low side of the peaks and also shift overall scale to upward direction.

C.6 New Calibration Framework

The Ohio University group is currently working in developing the new modular calibration framework for the sPHENIX EMCAL. The framework would provide a more global position dependence correction scheme and with a design to be more modular in that the leakage and other corrections are separated. The leakage corrections should be separated from other corrections, since some analyses will also use the sPHENIX Hadronic Calorimeter that sits behind the EMCAL, and will catch some of the leaked energy thereby recovering it, so for such analyses using the leakage correction could result in double counting.

APPENDIX D: COPY RIGHTS

This Appendix includes the permissions for the figures used in the dissertation taken from other sources. Those figures which are available with under Creative Commons License (Attribution 3.0 Unported (CC BY 3.0)) do not require permission to re-use.



HOME: pdgLive **Summary Tables** **Reviews, Tables, Plots** **Particle Listings**

Figures from 2018 edition of RPP

You have the authors' permission to use these figures as long as credit is given to the PDG citation.

Please use this **CITATION**:
M. Tanabashi et al. (Particle Data Group), Phys. Rev. D **98, 030001 (2018).**

Figures are in EPS format.

Contents

Figures found in the following sections:

- [Introduction](#)
- [Constants, Units, Atomic and Nuclear Properties](#)
- [Standard Model and Related Topics](#)
- [Astrophysics and Cosmology](#)
- [Experimental Methods and Colliders](#)
- [Mathematical Tools](#)
- [Gauge Bosons](#)
- [Leptons](#)
- [Quarks](#)
- [Mesons](#)
- [Baryons](#)
- [Searches](#)

Introduction Figures:

History Plots	Fig. 1
-------------------------------	------------------------

Constants, Units, Atomic and Nuclear Properties Figures:

Electromagnetic relations	Fig. 7.1
---	--------------------------

Standard Model and Related Topics Figures:

Quantum chromodynamics	Fig. 9.1(T)	Fig. 9.1(B)	Fig. 9.2	Fig. 9.3
--	-----------------------------	-----------------------------	--------------------------	--------------------------



Figure D.1: The permission to use Figure 1.5, 1.7, 1.8 and 1.10



24-May-2019

This license agreement between the American Physical Society ("APS") and Abinash Pun ("You") consists of your license details and the terms and conditions provided by the American Physical Society and SciPris.

Licensed Content Information

License Number:	RNP/19/MAY/015126
License date:	24-May-2019
DOI:	10.1103/PhysRevD.90.012007
Title:	Inclusive double-helicity asymmetries in neutral-pion and eta-meson production in $\text{p}+\text{p}$ collisions at $\sqrt{s}=200\text{ GeV}$
Author:	A. Adare et al. (PHENIX Collaboration)
Publication:	Physical Review D
Publisher:	American Physical Society
Cost:	USD \$ 0.00

Request Details

Does your reuse require significant modifications:	No
Specify intended distribution locations:	United States
Reuse Category:	Reuse in a thesis/dissertation
Requestor Type:	Author of requested content
Items for Reuse:	Figures/Tables
Number of Figure/Tables:	1
Figure/Tables Details:	Figure 1.
Format for Reuse:	Print and Electronic
Total number of print copies:	Up to 1000

Information about New Publication:

University/Publisher:	Ohio University
Title of dissertation/thesis:	Abinash Pun
Author(s):	Abinash Pun
Expected completion date:	Jul. 2019

License Requestor Information

Name:	Abinash Pun
Affiliation:	Individual
Email Id:	ap564413@ohio.edu
Country:	United States

Figure D.2: The permission to use Figure 1.11

5/29/2019

RightsLink - Your Account

**THE AMERICAN ASSOCIATION FOR THE ADVANCEMENT OF SCIENCE
LICENSE
TERMS AND CONDITIONS**

May 29, 2019

This Agreement between Ohio University – Abinash Pun ("You") and The American Association for the Advancement of Science ("The American Association for the Advancement of Science") consists of your license details and the terms and conditions provided by The American Association for the Advancement of Science and Copyright Clearance Center.

License Number	4598280121093
License date	May 29, 2019
Licensed Content Publisher	The American Association for the Advancement of Science
Licensed Content Publication	Science
Licensed Content Title	Ab Initio Determination of Light Hadron Masses
Licensed Content Author	S. Dür, Z. Fodor, J. Frison, C. Hoelbling, R. Hoffmann, S. D. Katz, S. Krieg, T. Kurth, L. Lellouch, T. Lippert, K. K. Szabo, G. Vulvert
Licensed Content Date	Nov 21, 2008
Licensed Content Volume	322
Licensed Content Issue	5905
Volume number	322
Issue number	5905
Type of Use	Thesis / Dissertation
Requestor type	Scientist/individual at a research institution
Format	Print and electronic
Portion	Figure
Number of figures/tables	1
Order reference number	
Title of your thesis / dissertation	Study of π^0-h^{\pm} correlation in Light-Heavy Ion Collisions at RHIC-PHENIX
Expected completion date	Jul 2019
Estimated size(pages)	150
Requestor Location	Ohio University 217, Edwards Accelerator Labs

ATHENS, OH 45701
United States
Attn: Ohio University

Total **0.00 USD**

Terms and Conditions

American Association for the Advancement of Science TERMS AND CONDITIONS

Regarding your request, we are pleased to grant you non-exclusive, non-transferable permission, to republish the AAAS material identified above in your work identified above, subject to the terms and conditions herein. We must be contacted for permission for any uses other than those specifically identified in your request above.

The following credit line must be printed along with the AAAS material: "From [Full Reference Citation]. Reprinted with permission from AAAS."

All required credit lines and notices must be visible any time a user accesses any part of the AAAS material and must appear on any printed copies and authorized user might make.

Figure D.3: The permission to use Figure 1.12

**SPRINGER NATURE LICENSE
TERMS AND CONDITIONS**

May 30, 2019

This Agreement between Ohio University -- Abinash pun ("You") and Springer Nature ("Springer Nature") consists of your license details and the terms and conditions provided by Springer Nature and Copyright Clearance Center.

License Number	4598920163103
License date	May 30, 2019
Licensed Content Publisher	Springer Nature
Licensed Content Publication	Journal of High Energy Physics
Licensed Content Title	The QCD equation of state with dynamical quarks
Licensed Content Author	Szabolcs Borsányi, Gergely Endrődi, Zoltán Fodor et al
Licensed Content Date	Jan 1, 2010
Licensed Content Volume	2010
Licensed Content Issue	11
Type of Use	Thesis/Dissertation
Requestor type	academic/university or research institute
Format	print and electronic
Portion	figures/tables/illustrations
Number of figures/tables/illustrations	2
Will you be translating?	no
Circulation/distribution	<501
Author of this Springer Nature content	no
Title	Study of π^0-h^{\pm} correlation in Light-Heavy Ion Collisions at RHIC-PHENIX
Institution name	n/a
Expected presentation date	Jul 2019
Portions	Fig. 11, 12
Requestor Location	Ohio University 217, Edwards Accelerator Labs
	ATHENS, OH 45701 United States Attn: Ohio University
Total	0.00 USD

Figure D.4: The permission to use Figure 1.13

FW: permission to re-use images for dissertation

KJ Koropsak, Jane <jane@bnl.gov>
Today, 09:05 AM
Pun Ahinash ✘

Abi,
Pete forwarded your email to me.
I grant you permission to use these images for your dissertation.
Please note that images may not be altered, except for size. The acknowledgement, "Courtesy Brookhaven National Laboratory" should be included.
Good luck!
-Jane

Jane Koropsak
Brookhaven National Laboratory
Media & Communications
Bldg. 400C
Upton, NY 11973
Tel: 631.344.4909

From: Genzer, Peter A
Sent: Monday, June 17, 2019 11:23 PM
To: Koropsak, Jane <jane@bnl.gov>
Subject: Fw: permission to re-use images for dissertation

Hi Jane,

Could you respond tomorrow?

Thanks,

Pete

Pete Genzer
Deputy Director, Stakeholder and Community Relations Office
Manager, Media & Communications Office
Brookhaven National Laboratory
(631) 344-3174 (office)
(631) 357-1028 (cell)
genzer@bnl.gov

Follow Brookhaven Lab on Twitter: @brookhavenlab

Figure D.5: The permission to use Figure 1.14 and Figure 2.1. Part 1 of 2.

From: Pun, Abinash <ap564413@ohio.edu>
Sent: Monday, June 17, 2019 10:09 PM
To: Genzer, Peter A
Subject: permission to re-use images for dissertation

Dear Peter,

I am a graduate student in the Department of Physics and Astronomy at Ohio University. I am currently working on PHENIX data. I would like to ask permission for re-using a couple of images published on the BNL website for my dissertation.

1. QCD phase diagram in the article "Supercomputing the Transition from Ordinary to Extraordinary Forms of Matter"
2. Ariel photo of RHIC in <https://www.flickr.com/photos/brookhavenlab/7979381212/in/album-72157613690851651/>

Looking forward to your response.

Sincerely,
Abi

=====

ABINASH PUN

Graduate Student

Department of Physics and Astronomy

Ohio University,

Athens OH 45701

Figure D.6: The permission to use Figure 1.14 and Figure 2.1. Part 2 of 2.

From: Franz, Achim <afranz@bnl.gov>
Sent: Friday, June 21, 2019 01:53 PM
To: Pun, Abinash
Subject: Re: permission to re-use images

Hi,

Totally forgot if I replied to you, I was in a multi-day meeting, no problem using the images, if you want to add "Courtesy PHENIX Collaboration"

Achim

From: "Pun, Abinash" <ap564413@ohio.edu>
Date: Tuesday, June 18, 2019 at 11:22
To: "Franz, Achim" <afranz@bnl.gov>
Subject: permission to re-use images

Dear Achim,

I am a graduate student in the Department of Physics and Astronomy at Ohio University. I am currently working on PHENIX data. I would like to ask permission for re-using following images published on the PHENIX drawing website for my dissertation.

1. Run12 PHENIX detector overview "https://www.phenix.bnl.gov/WWW/run/drawing/Phenix_2012_sidebyside"
2. Flow cartoon <https://www.phenix.bnl.gov/WWW/run/drawing/flowcartoon.pdf>
3. Magnetic field lines for two central magnet coils in combined (++) mode https://www.phenix.bnl.gov/WWW/run/drawing/PHNX_Magnet_++_lines.jpg

Looking forward to your response.

Sincerely,
Abi

ABINASH PUN
Graduate Student
Department of Physics and Astronomy
Ohio University,
Athens OH 45701

Figure D.7: The permission to use Figure 1.16, Figure 2.2 and Figure 2.4

 Copyright Clearance Center	
Confirmation Number: 11820788 Order Date: 06/04/2019	
Customer Information	
Customer: Abinash pun Account Number: 3001396211 Organization: Ohio University Email: ap564413@ohio.edu Phone: +1 (740) 541-4420 Payment Method: Invoice	
This is not an invoice	
Order Details	
Journal of Physics G : Nuclear and Particle Physics	
Billing Status: N/A	
Order detail ID: 71915856 ISSN: 0954-3899 Publication Type: Journal Volume: Issue: Start page: Publisher: IOP Publishing Author/Editor: Institute of Physics (Great Britain)	
Permission Status:  Granted Permission type: Republish or display content Type of use: Thesis/Dissertation Order License Id: 4602060938974	
Requestor type Academic institution Format Print, Electronic Portion image/photo Number of images/photos requested 1 The requesting person/organization Abinash Pun Title or numeric reference of the portion(s) Figure 1 Title of the article or chapter the portion is from N/A Editor of portion(s) N/A Author of portion(s) N/A Volume of serial or monograph N/A Page range of portion 150 Publication date of portion July 2019 Rights for Main product Duration of use Current edition and up to 5 years	

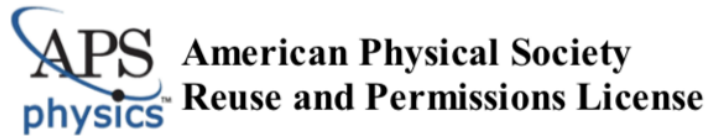
Figure D.8: The permission to use Figure 1.17 and 1.22 (part1 of 2).

Creation of copies for the disabled	no
With minor editing privileges	no
For distribution to	Worldwide
In the following language(s)	Original language of publication
With incidental promotional use	no
Lifetime unit quantity of new product	Up to 499
Title	Study of π^0 - $h^{(\pm)}$ correlation in Light-Heavy Ion Collisions at RHIC-PHENIX
Institution name	n/a
Expected presentation date	Jul 2019
Note: This item was invoiced separately through our RightsLink service . More info \$ 0.00	
Total order items: 1	Order Total: \$0.00

[About Us](#) | [Privacy Policy](#) | [Terms & Conditions](#) | [Pay an Invoice](#)

Copyright 2019 Copyright Clearance Center

Figure D.9: The permission to use Figure 1.17 and 1.22 (part2 of 2).



04-Jun-2019

This license agreement between the American Physical Society ("APS") and Abinash Pun ("You") consists of your license details and the terms and conditions provided by the American Physical Society and SciPris.

Licensed Content Information

License Number:	RNP/19/JUN/015429
License date:	04-Jun-2019
DOI:	10.1103/PhysRevC.75.024909
Title:	High transverse momentum π meson production in $\text{p}+\text{p}, \text{dS}+\text{Au}$, and $\text{Au}+\text{Au}$ collisions at $\sqrt{s_{\text{NN}}} = 200 \text{ GeV}$
Author:	S. S. Adler et al. (PHENIX Collaboration)
Publication:	Physical Review C
Publisher:	American Physical Society
Cost:	USD \$ 0.00

Request Details

Does your reuse require significant modifications:	No
Specify intended distribution locations:	United States
Reuse Category:	Reuse in a thesis/dissertation
Requestor Type:	Student
Items for Reuse:	Figures/Tables
Number of Figure/Tables:	1
Figure/Tables Details:	20
Format for Reuse:	Print and Electronic
Total number of print copies:	Up to 1000

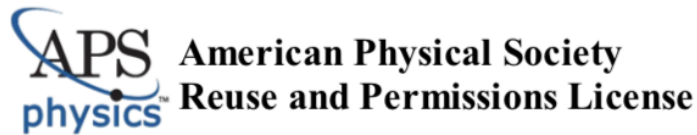
Information about New Publication:

University/Publisher:	Ohio University
Title of dissertation/thesis:	Abinash Pun
Author(s):	Abinash Pun
Expected completion date:	Jul. 2019

License Requestor Information

Name:	Abinash Pun
Affiliation:	Individual
Email Id:	ap564413@ohio.edu
Country:	United States

Figure D.10: The permission to use Figure 1.18



05-Jun-2019

This license agreement between the American Physical Society ("APS") and Abinash Pun ("You") consists of your license details and the terms and conditions provided by the American Physical Society and SciPris.

Licensed Content Information

License Number:	RNP/19/JUN/015476
License date:	05-Jun-2019
DOI:	10.1103/PhysRevLett.91.072304
Title:	Evidence from $\mathrm{d}^3\mathrm{N}/\mathrm{d}p_{\mathrm{T}} \mathrm{d}\eta$ Measurements for Final-State Suppression of High- p_{T} Hadrons in $\mathrm{Au} + \mathrm{Au}$ Collisions at RHIC
Author:	J. Adams et al. (STAR Collaboration)
Publication:	Physical Review Letters
Publisher:	American Physical Society
Cost:	USD \$ 0.00

Request Details

Does your reuse require significant modifications:	No
Specify intended distribution locations:	United States
Reuse Category:	Reuse in a thesis/dissertation
Requestor Type:	Author of requested content
Items for Reuse:	Figures/Tables
Number of Figure/Tables:	1
Figure/Tables Details:	Figure 4
Format for Reuse:	Print and Electronic
Total number of print copies:	Up to 1000

Information about New Publication:

University/Publisher:	Ohio University
Title of dissertation/thesis:	Abinash Pun
Author(s):	Abinash Pun
Expected completion date:	Jun. 2019

License Requestor Information

Name:	Abinash Pun
Affiliation:	Individual
Email Id:	ap564413@ohio.edu
Country:	United States

Figure D.11: The permission to use Figure 1.19.

**ELSEVIER LICENSE
TERMS AND CONDITIONS**

Jun 05, 2019

This Agreement between Ohio University -- Abinash pun ("You") and Elsevier ("Elsevier") consists of your license details and the terms and conditions provided by Elsevier and Copyright Clearance Center.

License Number	4602661024492
License date	Jun 05, 2019
Licensed Content Publisher	Elsevier
Licensed Content Publication	Nuclear Physics A
Licensed Content Title	Jet shape and fragmentation function measurements with CMS
Licensed Content Author	Yaxian Mao
Licensed Content Date	Dec 1, 2014
Licensed Content Volume	932
Licensed Content Issue	n/a
Licensed Content Pages	5
Start Page	88
End Page	92
Type of Use	reuse in a thesis/dissertation
Portion	figures/tables/illustrations
Number of figures/tables/illustrations	1
Format	both print and electronic
Are you the author of this Elsevier article?	No
Will you be translating?	No
Original figure numbers	Fig 2.
Title of your thesis/dissertation	Study of π^0-h^{\pm} correlation in Light-Heavy Ion Collisions at RHIC-PHENIX
Expected completion date	Jul 2019
Estimated size (number of pages)	150
Requestor Location	Ohio University 217, Edwards Accelerator Labs

ATHENS, OH 45701

Figure D.12: The permission to use Figure 1.20.

RE: request for permission to re-use content from your paper

 Eskola, Kari <kari.eskola@jyu.fi>
 Today, 02:51 AM
 Pun, Abinash ✎

You replied on 6/10/2019 08:54 AM.

Reply | v

Dear Abi,

It is OK with me that you use the figure you mentioned, provided of course that you refer to the original paper in the text or in the figure caption.

Thanks for your interest and Best regards,
 Kari Eskola

From: Pun, Abinash <ap564413@ohio.edu>
Sent: perjantai 7. kesäkuuta 2019 0:29
To: kari.eskola@phys.jyu.fi
Subject: request for permission to re-use content from your paper

Dear Kari,

I am a graduate student at the Department of Physics and Astronomy of Ohio University and am currently working at PHENIX data. I am writing my PhD thesis now. I would like you to request your permission to use figure 1 from your paper "*EPS09 — A new generation of NLO and LO nuclear parton distribution functions*" published in JHEP (2009).

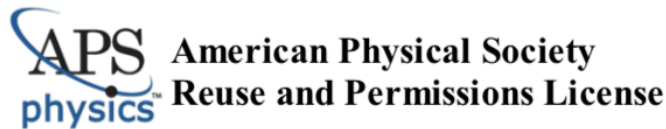
Looking forward to your response.

Sincerely,
 Abi

=====

ABINASH PUN
 Graduate Student
 Department of Physics and Astronomy
 Ohio University,

Figure D.13: The permission to use the Figure 1.23



06-Jun-2019

This license agreement between the American Physical Society ("APS") and Abinash Pun ("You") consists of your license details and the terms and conditions provided by the American Physical Society and SciPris.

Licensed Content Information

License Number:	RNP/19/JUN/015487
License date:	06-Jun-2019
DOI:	10.1103/PhysRevLett.91.072304
Title:	Evidence from $\mathrm{A}^{\mathrm{A}}\mathrm{A}^{\mathrm{B}}$ Measurements for Final-State Suppression of High- p_{T} Hadrons in $\mathrm{A}^{\mathrm{A}}\mathrm{A}^{\mathrm{B}}$ Collisions at RHIC
Author:	J. Adams et al. (STAR Collaboration)
Publication:	Physical Review Letters
Publisher:	American Physical Society
Cost:	USD \$ 0.00

Request Details

Does your reuse require significant modifications:	No
Specify intended distribution locations:	United States
Reuse Category:	Reuse in a thesis/dissertation
Requestor Type:	Student
Items for Reuse:	Figures/Tables
Number of Figure/Tables:	1
Figure/Tables Details:	Figure 3
Format for Reuse:	Print and Electronic
Total number of print copies:	Up to 1000

Information about New Publication:

University/Publisher:	Ohio University
Title of dissertation/thesis:	Abinash Pun
Author(s):	Abinash Pun
Expected completion date:	Jul. 2019

License Requestor Information

Name:	Abinash Pun
Affiliation:	Individual
Email Id:	ap564413@ohio.edu
Country:	United States

Figure D.14: The permission to use Figure 1.24.

 **RightsLink®**

[Home](#) [Create Account](#) [Help](#) 



Title: Multiplicity and transverse momentum dependence of two- and four-particle correlations in pPb and PbPb collisions

Author: S. Chatrchyan, V. Khachatryan, A.M. Sirunyan, A. Tumasyan, W. Adam, T. Bergauer, M. Dragicevic, J. Erö, C. Fabjan, M. Friedl, R. Frühwirth, V.M. Ghete, N. Hörmann, J. Hrubec, M. Jeitler, W. Kiesenhofer, V. Knünz, M. Krammer, I. Krätschmer, D. Liko, I. Mikulec et al.

Publication: Physics Letters B

Publisher: Elsevier

Date: 23 July 2013

Copyright © 2013 CERN. Published by Elsevier B.V.

LOGIN

If you're a copyright.com user, you can login to RightsLink using your copyright.com credentials.

Already a RightsLink user or want to [learn more?](#)

Creative Commons Attribution-NonCommercial-No Derivatives License (CC BY NC ND)

This article is published under the terms of the [Creative Commons Attribution-NonCommercial-No Derivatives License \(CC BY NC ND\)](#).

For non-commercial purposes you may copy and distribute the article, use portions or extracts from the article in other works, and text or data mine the article, provided you do not alter or modify the article without permission from Elsevier. You may also create adaptations of the article for your own personal use only, but not distribute these to others. You must give appropriate credit to the original work, together with a link to the formal publication through the relevant DOI, and a link to the Creative Commons user license above. If changes are permitted, you must indicate if any changes are made but not in any way that suggests the licensor endorses you or your use of the work.

Permission is not required for this non-commercial use. For commercial use please continue to request permission via Rightslink.

[BACK](#)

[CLOSE WINDOW](#)

Copyright © 2019 [Copyright Clearance Center, Inc.](#). All Rights Reserved. [Privacy statement](#). [Terms and Conditions](#).
Comments? We would like to hear from you. E-mail us at customercare@copyright.com

Figure D.15: The permission to use figure (c) of Figure 1.25.



SPRINGER NATURE

Title: Creation of quark-gluon plasma droplets with three distinct geometries
Author: C. Aidala et al
Publication: Nature Physics
Publisher: Springer Nature
Date: Dec 10, 2018
 Copyright © 2018, Springer Nature

LOGIN
 If you're a copyright.com user, you can login to RightsLink using your copyright.com credentials.
 Already a RightsLink user or want to learn more?

Author Request

If you are the author of this content (or his/her designated agent) please read the following. If you are not the author of this content, please click the Back button and select no to the question "Are you the Author of this Springer Nature content?".

Ownership of copyright in original research articles remains with the Author, and provided that, when reproducing the contribution or extracts from it or from the Supplementary Information, the Author acknowledges first and reference publication in the Journal, the Author retains the following non-exclusive rights:

To reproduce the contribution in whole or in part in any printed volume (book or thesis) of which they are the author(s).

The author and any academic institution, where they work, at the time may reproduce the contribution for the purpose of course teaching.

To reuse figures or tables created by the Author and contained in the Contribution in oral presentations and other works created by them.

To post a copy of the contribution as accepted for publication after peer review (in locked Word processing file, or a PDF version thereof) on the Author's own web site, or the Author's institutional repository, or the Author's funding body's archive, six months after publication of the printed or online edition of the Journal, provided that they also link to the contribution on the publisher's website.

Authors wishing to use the published version of their article for promotional use or on a web site must request in the normal way.

If you require further assistance please read Springer Nature's online [author reuse guidelines](#).

For full paper portion: Authors of original research papers published by Springer Nature are encouraged to submit the author's version of the accepted, peer-reviewed manuscript to their relevant funding body's archive, for release six months after publication. In addition, authors are encouraged to archive their version of the manuscript in their institution's repositories (as well as their personal Web sites), also six months after original publication.

v1.0

Figure D.16: The permission to use Figure 1.26.

2/1/2019

RightsLink Printable License

**ELSEVIER LICENSE
TERMS AND CONDITIONS**

Feb 01, 2019

This Agreement between Ohio University -- Abinash Pun ("You") and Elsevier ("Elsevier") consists of your license details and the terms and conditions provided by Elsevier and Copyright Clearance Center.

License Number	4520380769066
License date	Feb 01, 2019
Licensed Content Publisher	Elsevier
Licensed Content Publication	Nuclear Instruments and Methods in Physics Research Section A: Accelerators, Spectrometers, Detectors and Associated Equipment
Licensed Content Title	PHENIX magnet system
Licensed Content Author	S.H. Aronson, J. Bowers, J. Chiba, G. Danby, A. Drees, O. Fackler, A. Franz, J.P. Freidberg, W. Guryan, A. Harvey, T. Ichihara, J. Jackson, R. Jayakumar, S. Kahn, V. Kashikhin, P.J. Kroon, M. Libkind, M.D. Marx, W.Z. Meng, F. Messer, S. Migliolio, I.D. Ojha, R. Prigl et al.
Licensed Content Date	Mar 1, 2003
Licensed Content Volume	499
Licensed Content Issue	2-3
Licensed Content Pages	9
Start Page	480
End Page	488
Type of Use	reuse in a thesis/dissertation
Portion	figures/tables/illustrations
Number of figures/tables/illustrations	1
Format	both print and electronic
Are you the author of this Elsevier article?	No
Will you be translating?	No
Original figure numbers	figure 1
Title of your thesis/dissertation	Study of π^0-h^{\pm} correlation in Light-Heavy Ion Collisions at RHIC-PHENIX
Expected completion date	Jul 2019
Estimated size (number of pages)	150
Requestor Location	Ohio University 217, Edwards Accelerator Labs
Publisher Tax ID	ATHENS, OH 45701 United States Attn: Ohio University

<https://s100.copyright.com/AppDispatchServlet>

1/6

Figure D.17: The permission to use Figure 2.3.



Mickey Chiu <chiu@bnl.gov>

Today, 01:35 PM

Pun, Abinash



Hi Abinash,

I don't think you need my permission, so feel free to go ahead and use that image.

Sincerely,

Mickey

--

Building 510C
 Department of Physics
 Brookhaven National Laboratory
 Upton, NY 11973
 Phone: 631-344-8428

On Jun 18, 2019, at 1:18 PM, Pun, Abinash <ap564413@ohio.edu> wrote:

Dear Chiu

I am a graduate student in the Department of Physics and Astronomy at Ohio University. I am currently working on PHENIX data. I would like to ask permission for re-using sketch of the *location of ZDC* (slide 4) from your presentation titled "[RHIC Zero Degree Calorimeter](#)".

Looking forward to your response.

Sincerely,
 Abi

ABINASH PUN
 Graduate Student
 Department of Physics and Astronomy
 Ohio University,
 Athens OH 45701

Figure D.18: The permission to use Figure 2.7.

1/22/2019

Rightslink® by Copyright Clearance Center

Title: PHENIX central arm tracking detectors

Author: K. Adcox,N.N. Ajitanand,J. Alexander,D. Autrey,R. Averbeck,B. Azmoun,K.N. Barish,V.V. Baublis,R. Belkin,S. Bhagatula,J.C. Biggs,D. Borland,S. Botelho,W.L. Bryan,J. Burward-Hoy,S.A. Butsyk,W.C. Chang,T. Christ,O. Dietzsch,A. Drees,R. du Rietz et al.

Publication: Nuclear Instruments and Methods in Physics Research Section A: Accelerators, Spectrometers, Detectors and Associated Equipment

Publisher: Elsevier

Date: 1 March 2003

Copyright © 2002 Published by Elsevier B.V.

Logged in as:
Abinash pun
Ohio University
[LOGOUT](#)

Order Completed

Thank you for your order.

This Agreement between Ohio University -- Abinash pun ("You") and Elsevier ("Elsevier") consists of your license details and the terms and conditions provided by Elsevier and Copyright Clearance Center.

Your confirmation email will contain your order number for future reference.

printable details

License Number	4514330410736
License date	Jan 22, 2019
Licensed Content Publisher	Elsevier
Licensed Content Publication	Nuclear Instruments and Methods in Physics Research Section A: Accelerators, Spectrometers, Detectors and Associated Equipment
Licensed Content Title	PHENIX central arm tracking detectors
Licensed Content Author	K. Adcox,N.N. Ajitanand,J. Alexander,D. Autrey,R. Averbeck,B. Azmoun,K.N. Barish,V.V. Baublis,R. Belkin,S. Bhagatula,J.C. Biggs,D. Borland,S. Botelho,W.L. Bryan,J. Burward-Hoy,S.A. Butsyk,W.C. Chang,T. Christ,O. Dietzsch,A. Drees,R. du Rietz et al.
Licensed Content Date	Mar 1, 2003
Licensed Content Volume	499
Licensed Content Issue	2-3
Licensed Content Pages	19
Type of Use	reuse in a thesis/dissertation
Portion	figures/tables/illustrations
Number of figures/tables/illustrations	2
Format	both print and electronic
Are you the author of this Elsevier article?	No
Will you be translating?	No
Original figure numbers	figures 2 and 3
Title of your	Study of π^0-h^{\pm} correlation in Light-Heavy Ion Collisions at RHIC-PHENIX

<https://s100.copyright.com/AppDispatchServlet>

1/2

Figure D.19: The permission to use Figure 2.8 and Figure 2.9. Part 1 of 2.

1/22/2019 Rightslink® by Copyright Clearance Center
thesis/dissertation
Expected completion date Jul 2019
Estimated size (number of pages) 150
Requestor Location Ohio University
217, Edwards Accelerator Labs

ATHENS, OH 45701
United States
Attn: Ohio University
Publisher Tax ID 98-0397604
Total 0.00 USD

[ORDER MORE](#) [CLOSE WINDOW](#)
Copyright © 2019 [Copyright Clearance Center, Inc.](#), All Rights Reserved. [Privacy statement](#). [Terms and Conditions](#).
Comments? We would like to hear from you. E-mail us at customercare@copyright.com

Figure D.20: The permission to use Figure 2.8 and Figure 2.9. Part 2 of 2.

1/24/2019

RightsLink Printable License

**ELSEVIER LICENSE
TERMS AND CONDITIONS**

Jan 24, 2019

This Agreement between Ohio University -- Abinash Pun ("You") and Elsevier ("Elsevier") consists of your license details and the terms and conditions provided by Elsevier and Copyright Clearance Center.

License Number	4515420071499
License date	Jan 24, 2019
Licensed Content Publisher	Elsevier
Licensed Content Publication	Nuclear Instruments and Methods in Physics Research Section A: Accelerators, Spectrometers, Detectors and Associated Equipment
Licensed Content Title	Construction and performance of the PHENIX pad chambers
Licensed Content Author	K. Adcox, J. Ajitanand, J. Alexander, J. Barrette, R. Belkin, D. Borland, W.L. Bryan, R. du Rietz, K. El Chenawi, A. Cherlin, J. Fellenstein, K. Filimonov, Z. Fraenkel, D. Gan, S. Garpman, Y. Gil, S.V. Greene, H.-Å. Gustafsson, W. Holzmann, M. Issah, U. Jagadish et al.
Licensed Content Date	Feb 1, 2003
Licensed Content Volume	497
Licensed Content Issue	2-3
Licensed Content Pages	31
Start Page	263
End Page	293
Type of Use	Reuse in a thesis/dissertation
Portion	Figures/Tables/Illustrations
Number of figures/tables/illustrations	1
Format	Both print and electronic
Are you the author of this Elsevier article?	No
Will you be translating?	No
Original figure numbers	Figure 6
Title of your thesis/dissertation	Study of π^0-h^{\pm} correlation in Light-Heavy Ion Collisions at RHIC-PHENIX
Expected completion date	Jul 2019
Estimated size (number of pages)	150
Requestor Location	Ohio University 217, Edwards Accelerator Labs
Publisher Tax ID	ATHENS, OH 45701 United States Attn: Ohio University

<https://s100.copyright.com/AppDispatchServlet>

1/6

Figure D.21: The permission to use Figure 2.10.

2/1/2019

RightsLink Printable License

**ELSEVIER LICENSE
TERMS AND CONDITIONS**

Feb 01, 2019

This Agreement between Ohio University -- Abinash Pun ("You") and Elsevier ("Elsevier") consists of your license details and the terms and conditions provided by Elsevier and Copyright Clearance Center.

License Number	4520390191075
License date	Feb 01, 2019
Licensed Content Publisher	Elsevier
Licensed Content Publication	Nuclear Instruments and Methods in Physics Research Section A: Accelerators, Spectrometers, Detectors and Associated Equipment
Licensed Content Title	PHENIX calorimeter
Licensed Content Author	L Aphecetche, T.C Awes, J Banning, S Bathe, A Bazilevsky, S Belikov, S.T Belyaev, C Blume, M Bobrek, D Bucher, V Bumazhnov, H Büsching, S Chernichenkov, V Ciaciolo, M Cutshaw, D.G D'Enterria, S Daniels, G David, H Delagrange, A Denisov, A Durum, Y.V Efremenko et al.
Licensed Content Date	Mar 1, 2003
Licensed Content Volume	499
Licensed Content Issue	2-3
Licensed Content Pages	16
Start Page	521
End Page	536
Type of Use	reuse in a thesis/dissertation
Intended publisher of new work	other
Portion	figures/tables/illustrations
Number of figures/tables/illustrations	2
Format	both print and electronic
Are you the author of this Elsevier article?	No
Will you be translating?	No
Original figure numbers	figure1 and figure 10
Title of your thesis/dissertation	Study of π^0-h^{\pm} correlation in Light-Heavy Ion Collisions at RHIC-PHENIX
Expected completion date	Jul 2019
Estimated size (number of pages)	150
Requestor Location	Ohio University 217, Edwards Accelerator Labs

ATHENS, OH 45701

<https://s100.copyright.com/AppDispatchServlet>

1/6

Figure D.22: The permission to use Figure 2.11 and Figure 2.12.

 Copyright Clearance Center

Confirmation Number: 11791211
Order Date: 02/14/2019

Customer Information

Customer: Abinash pun
Account Number: 3001396211
Organization: Ohio University
Email: ap564413@ohio.edu
Phone: +1 (740) 541-4420
Payment Method: Invoice

This is not an invoice

Order Details

Annual review of nuclear and particle science	Billing Status: N/A
--	--------------------------------------

Order detail ID:	71809423	Permission Status:	 Granted
ISSN:	1545-4134	Permission type:	Republish or display content
Publication Type:	e-Journal	Type of use:	Thesis/Dissertation
Volume:		Order License Id:	4527800067150
Issue:		Requestor type	Academic institution
Start page:		Format	Print, Electronic
Publisher:	ANNUAL REVIEWS	Portion	chart/graph/table/figure
		Number of charts/graphs/tables/figures	1
		The requesting person/organization	Abinash Pun/Ohio University
		Title or numeric reference of the portion(s)	Figure 8
		Title of the article or chapter the portion is from	Experimental Details
		Editor of portion(s)	N/A
		Author of portion(s)	N/A
		Volume of serial or monograph	N/A
		Page range of portion	150
		Publication date of portion	July 2019
		Rights for	Main product
		Duration of use	Life of current edition
		Creation of copies for	yes

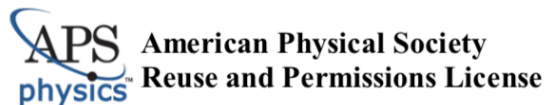
Figure D.23: The permission to use Figure 2.15. Part 1 of 2.

the disabled	
With minor editing privileges	yes
For distribution to	United States
In the following language(s)	Original language of publication
With incidental promotional use	no
Lifetime unit quantity of new product	Up to 499
Title	Study of π^0 - $h^{(\rho)}$ correlation in Light-Heavy Ion Collisions at RHIC-PHENIX
Institution name	n/a
Expected presentation date	Jul 2019
Note: This item was invoiced separately through our RightsLink service . More info	
\$ 0.00	
Total order items: 1	
Order Total: \$0.00	

[About Us](#) | [Privacy Policy](#) | [Terms & Conditions](#) | [Pay an Invoice](#)

Copyright 2019 Copyright Clearance Center

Figure D.24: The permission to use Figure 2.15. Part 2 of 2.



08-Apr-2019

This license agreement between the American Physical Society ("APS") and Abinash Pun ("You") consists of your license details and the terms and conditions provided by the American Physical Society and SciPris.

Licensed Content Information

License Number:	RNP/19/APR/013716
License date:	08-Apr-2019
DOI:	10.1103/PhysRevC.81.014908
Title:	Extraction of correlated jet pair signals in relativistic heavy ion collisions
Author:	Anne Sickles, Michael P. McCumber, and Andrew Adare
Publication:	Physical Review C
Publisher:	American Physical Society
Cost:	USD \$ 0.00

Request Details

Does your reuse require significant modifications:	No
Specify intended distribution locations:	United States
Reuse Category:	Reuse in a thesis/dissertation
Requestor Type:	Author of requested content
Items for Reuse:	Figures/Tables
Number of Figure/Tables:	1
Figure/Tables Details:	Figure 1
Format for Reuse:	Print and Electronic
Total number of print copies:	Up to 1000

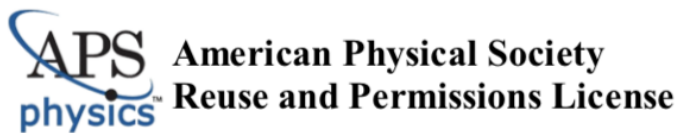
Information about New Publication:

University/Publisher:	Ohio University
Title of dissertation/thesis:	Jet Related Two-Particle Correlations in He3+Au
Author(s):	Abinash
Expected completion date:	Jul. 2019

License Requestor Information

Name:	Abinash Pun
Affiliation:	Individual
Email Id:	ap564413@ohio.edu
Country:	United States

Figure D.25: The permission to use Figure 4.2



08-Apr-2019

This license agreement between the American Physical Society ("APS") and Abinash Pun ("You") consists of your license details and the terms and conditions provided by the American Physical Society and SciPris.

Licensed Content Information

License Number:	RNP/19/APR/013716
License date:	08-Apr-2019
DOI:	10.1103/PhysRevC.81.014908
Title:	Extraction of correlated jet pair signals in relativistic heavy ion collisions
Author:	Anne Sickles, Michael P. McCumber, and Andrew Adare
Publication:	Physical Review C
Publisher:	American Physical Society
Cost:	USD \$ 0.00

Request Details

Does your reuse require significant modifications:	No
Specify intended distribution locations:	United States
Reuse Category:	Reuse in a thesis/dissertation
Requestor Type:	Author of requested content
Items for Reuse:	Figures/Tables
Number of Figure/Tables:	1
Figure/Tables Details:	Figure 1
Format for Reuse:	Print and Electronic
Total number of print copies:	Up to 1000

Information about New Publication:

University/Publisher:	Ohio University
Title of dissertation/thesis:	Jet Related Two-Particle Correlations in He3+Au
Author(s):	Abinash
Expected completion date:	Jul. 2019

License Requestor Information

Name:	Abinash Pun
Affiliation:	Individual
Email Id:	ap564413@ohio.edu
Country:	United States

Figure D.26: The permission to use Figure 4.4

**ELSEVIER LICENSE
TERMS AND CONDITIONS**

Jun 21, 2019

This Agreement between Ohio University -- Abinash Pun ("You") and Elsevier ("Elsevier") consists of your license details and the terms and conditions provided by Elsevier and Copyright Clearance Center.

License Number	4613760039494
License date	Jun 21, 2019
Licensed Content Publisher	Elsevier
Licensed Content Publication	Nuclear Physics A
Licensed Content Title	Jet studies in 200 GeV p+p and d+Au collisions from the STAR experiment at RHIC
Licensed Content Author	Jan Kapitán
Licensed Content Date	Apr 1, 2011
Licensed Content Volume	855
Licensed Content Issue	1
Licensed Content Pages	4
Start Page	412
End Page	415
Type of Use	reuse in a thesis/dissertation
Portion	figures/tables/illustrations
Number of figures/tables/illustrations	1
Format	both print and electronic
Are you the author of this Elsevier article?	No
Will you be translating?	No
Original figure numbers	Figure 3
Title of your thesis/dissertation	Study of π^0-h^{\pm} correlation in Light-Heavy Ion Collisions at RHIC-PHENIX
Expected completion date	Jul 2019
Estimated size (number of pages)	150
Requestor Location	Ohio University 217, Edwards Accelerator Labs
	ATHENS, OH 45701 United States Attn: Ohio University
Publisher Tax ID	98-0397604
Total	0.00 USD
Terms and Conditions	

Figure D.27: The permission to use Figure 5.16



Confirmation Number: 11827766
Order Date: 06/28/2019

Customer Information

Customer: Abinash pun
Account Number: 3001396211
Organization: Ohio University
Email: ap564413@ohio.edu
Phone: +1 (740) 541-4420
Payment Method: Invoice

This is not an invoice

Order Details

Journal of Physics G : Nuclear and Particle Physics

Billing Status:
N/A

Order detail ID:	71934173	Permission Status:	Granted
ISSN:	0954-3899	Permission type:	Republish or display content
Publication Type:	Journal	Type of use:	Thesis/Dissertation
Volume:		Order License Id:	4617800864880
Issue:		Requestor type	Academic institution
Start page:		Format	Print, Electronic
Publisher:	IOP Publishing	Portion	image/photo
Author/Editor:	Institute of Physics (Great Britain)	Number of images/photos requested	1
		The requesting person/organization	Abinash pun
		Title or numeric reference of the portion(s)	Fig 5.
		Title of the article or chapter the portion is from	Parton energy loss in the mini quark-gluon plasma and jet quenching in proton-proton collisions
		Editor of portion(s)	N/A
		Author of portion(s)	N/A
		Volume of serial or monograph	N/A
		Page range of portion	150
		Publication date of portion	July 2019
		Rights for	Main product
		Duration of use	Life of current edition

Figure D.28: The permission to use Figure 5.27. Part 1 of 2.

Creation of copies for the disabled	no
With minor editing privileges	no
For distribution to	Worldwide
In the following language(s)	Original language of publication
With incidental promotional use	no
Lifetime unit quantity of new product	Up to 499
Title	Study of π^0 - $h^{(\pm)}$ correlation in Light-Heavy Ion Collisions at RHIC-PHENIX
Institution name	n/a
Expected presentation date	Jul 2019
Note: This item was invoiced separately through our RightsLink service . More info \$ 0.00	
Total order items: 1	Order Total: \$0.00

[About Us](#) | [Privacy Policy](#) | [Terms & Conditions](#) | [Pay an Invoice](#)

Copyright 2019 Copyright Clearance Center

Figure D.29: The permission to use Figure 5.27. Part 2 of 2.